William R. Wiley

EMSL

Environmental Molecular Sciences Laboratory

Annual Report 2000

Interfacial Chemistry and Engineering

August 2001

Pacific Northwest National Laboratory

Operated by Battelle for the
U.S. Department of Energy

Cover photo: *Structural and energetic model of Cs⁺ exchange with K⁺ in a layer lattice silicate mineral (e.g., muscovite). Muscovite is a 2:1 layer silicate containing structural layers of octahedrally coordinated Al(III) over- and underlain by layers of tetrahedrally coordinated Si(IV). Isomorphic substitutions in these layers lead to charge imbalance and a cation exchange capacity. These types of exchange reactions control the migration velocity of radio-cesium beneath leaked single shell tanks at Hanford and other DOE sites.*

Environmental Dynamics and Simulation researchers have 1) developed molecular models of this exchange reaction; 2) identified the key layer lattice silicates in Hanford sediments controlling Cs⁺ exchange using advanced spectroscopic techniques such as synchrotron X-ray microscopy; 3) studied the thermodynamics and kinetics of Cs⁺ adsorption and desorption on Hanford sediments; and 4) collaborated on the development of a multi-component reactive transport model to forecast Cs migration velocities beneath leaked high level waste tanks at Hanford.

Annual Report 2000

Interfacial Chemistry and Engineering

J. W. Grate, Interim Associate Director
and the Staff of the Interfacial Chemistry
and Engineering Program

August 2001

Contents

1. Introduction

2. Oxide and Mineral Films and Surfaces

3. Electronic and Catalytic Materials

4. Nanoscale Materials

5. Interfacial Properties and Reactivity

6. Microanalytical Separations and Sensing

9. Appendix

1. Introduction

This annual report describes the research and accomplishments in 2000 of the Interfacial Chemistry and Engineering Program, one of six research programs at the William R. Wiley Environmental Molecular Sciences Laboratory (EMSL) – a multidisciplinary, national scientific user facility and research organization (Figure 1.1). EMSL is operated by Pacific Northwest National Laboratory (PNNL) for the U.S. Department of Energy's (DOE's) Office of Biological and Environmental Research. The resources and opportunities within the facility are an outgrowth of DOE's commitment to fundamental research on the physical, chemical, and biological processes that are the foundation for understanding and resolving environmental and other critical scientific issues. Currently, over 100 instrument systems are available to the scientific community, which includes EMSL's resident research staff and their collaborators as well as external users.

The EMSL complex evolved from a 1986 vision by the late Dr. William R. Wiley, director of Pacific Northwest National Laboratory, to build an innovative multipurpose user facility providing synergism between the physical, mathematical, and life sciences. Dr. Wiley and others believed that molecular-level research was essential for attacking problems in environmental cleanup, energy efficiency, health, and other areas. From this belief grew a concept for a center for molecular science that would bring together theoreticians with expertise in computer modeling of molecular processes and experimentalists from the physical and life sciences (Figure 1.1).

EMSL's resident research staff conducts fundamental research in areas relevant to DOE missions and affords expert assistance to users, who include university professors, graduate and undergraduate students, and postdoctoral fellows, and scientists from industry, national laboratories, and DOE contractors. Their research programs and collaborative efforts are providing a scientific basis for evaluating a number of social and technical factors associated with environmental issues—factors such as transformation and migration of contaminants in soils and groundwater; cell response to environmental contaminants; reaction of important tropospheric molecules—and a technical basis for waste retrieval and processing.

The Interfacial Chemistry and Engineering (IC&E) Program is helping to address national needs in environmental restoration, waste management, pollution prevention, energy, and national security through research that specializes in preparation, characterization, interactions, and reactivity of interfaces. IC&E's highly diversified staff and instrumentation conduct research in areas ranging from dissolution of environmentally relevant mineral interfaces, molecular beam epitaxy of metal oxides, heterogeneous catalysis, and photopatterned polymer film materials to nuclear waste form materials, NOx reduction, microreactors, and sensors for chemical, radiochemical, and biological detection. Research in these areas span the range from fundamental studies to near-deployment engineering.

Figure 1.1. As a national scientific user facility, the EMSL supports both open and proprietary research. More information and specific procedures for becoming a user are available on the EMSL website at http://www.emsl.pnl.gov/.

EMSL Director's Office
J.H. Futrell, Director
Telephone: (509) 376-0223
Facsimile: (509) 376-6742
Email: jean.futrell@pnl.gov

- -

A.A. Campbell, Deputy Director
Telephone: (509) 376-6688
Facsimile: (509) 376-6742
Email: allison.campbell@pnl.gov

D. Ray, Deputy Director
Telephone: (509) 376-8069
Facsimile: (509) 376-6742
Email: dray@pnl.gov

Chemical Structure & Dynamics
S.D. Colson, Associate Director
Telephone: (509) 376-4598
Facsimile: (509) 376-0846
Email: steven.colson@pnl.gov

Computing & Information Sciences
M.J. Peterson, Acting Deputy Director
Telephone: (509) 376-0301
Facsimile: (509) 376-0420
Email: marty.peterson@pnl.gov

Environmental Dynamics & Simulation
J.M. Zachara, Associate Director
Telephone: (509) 376-3254
Facsimile: (509) 376-3650
Email: john.zachara@pnl.gov

Interfacial Chemistry & Engineering
J.W. Grate, Interim Associate Director
Telephone: (509) 376-1833
Facsimile: (509) 376-5106
Email: jwgrate@pnl.gov

Macromolecular Structure & Dynamics
D.W. Koppenaal, Associate Director
Telephone: (509) 376-0368
Facsimile: (509) 376-2303
Email: david.koppenaal@pnl.gov

Theory, Modeling & Simulation
D.A. Dixon, Associate Director
Telephone: (509) 372-4999
Facsimile: (509) 375-6631
Email: david.dixon@pnl.gov

Figure 1.2. Contact information for EMSL research organizations

Interfacial Chemistry and Engineering Program

The Interfacial Chemistry and Engineering (IC&E) Program focuses on innovative research in the areas of surface and interfacial chemistry, advanced materials synthesis and characterization, and microanalytical science. Our activities emphasize research relevant to the four DOE mission areas – basic science, energy, the environment, and national security – and operation of a world-class user facility for scientific problem solving. Our staff also plays a major role in the EMSL by providing support, training, and collaboration to onsite users. Last year we hosted 94 external users from 34 different academic, private, and research laboratories; and 36 students at high school, undergraduate, and graduate levels, 11 postdoctoral fellows, and 5 visiting faculty members.

The IC&E directorate has undergone a number of changes over the past years. The merger of the Materials and Interfaces and Processing Science groups resulted in the Interfacial and Processing Sciences (I&PS) directorate. At the end of last year, individual technical groups within I&PS were reorganized and the directorate name changed to more clearly reflect the overall research expertise.

The range of scientific expertise and instrumentation within IC&E provides a unique environment for research in areas such as nanoscience and nanotechnology; heterogeneous catalysis; environmental interfaces, including aerosols and minerals; materials interfaces, and chemoselective interfaces; and areas within microanalytical science, such as chemical sensing and microfluidics. The combination under one roof of surface and interface characterization techniques that provide high spatial, depth, and energy resolution for a broad array of methods is unmatched anywhere in the world. Many systems are coupled directly to growth chambers, and samples can be moved among 16 different systems without exposure to air.

Another source of advanced research support is the instrumentation available for chemical synthesis, analytical chemistry, separations, electrochemistry, thin film deposition, catalytic reactors, ion beam processing, and microfabrication. Capabilities include a 3.4 MeV ion beam facility for interface

characterization; scanning probe microscopies, spectroelectrochemistry, electron microscopy and x-ray analysis; high-spatial/energy resolution surface analysis; catalyst preparation, characterization and reaction engineering; a fully equipped Class 1000 clean room for microfabrication, microanalytical systems development and testing laboratories; inorganic, organic, polymer, and biochemical synthesis and characterization facilities; a full complement of thin film deposition and characterization facilities; and fully equipped analytical support laboratories.

This annual report describes our research and accomplishments in fiscal year 2000. Individual papers within the report represent four research groups, summarized below: Films and Interphases; Microsensors and Microfluidics; Surface Chemistry and Catalysis; and Materials Interfaces. Because much of the research in IC&E is highly interdisciplinary, program and user research summaries are organized into the following sections:

- Oxide and Mineral Films and Surfaces

- Electronic and Catalytic Materials

- Nanoscale Materials

- Interfacial Properties and Reactivity

- Microanalytical Separations and Sensing

- Environmental Studies — Waste Separations, Forms, and Chemistry

- Analysis and Characterization

Films and Interphases. The physical and chemical properties of the region between single phases of material (the interphase) have a major influence on many characteristics of the material, including stability, electronic properties, atomic and ionic transport, and chemical reactivity. Research programs include the synthesis of thin films and nanostructured materials, both of which contain a high concentration of interphase regions. The research activities also involve studies of solid/solid, solid/liquid and solid/gas (or vacuum) interphase regions. Although most studies are focused on inorganic materials and interphases, organic and

biological systems are becoming an increasingly large part of our work.

Many of the studies involving solid/liquid interfaces focus on materials stability, including corrosion of ancient materials, cracking of lightweight alloys, the durability of waste storage glasses, and the dissolution and growth of mineral surfaces. Programs related to solid/solid regions generally involve the creation of materials with new or unique properties. These studies involve, for example, the control of electronic structures by interfacial engineering, the influence of interface structure on the properties of ferroelectric and thin films, and the use of surface structures to stabilize nanoclusters. Solid/gas interface studies include gas reaction of mineral surfaces, studies of atmospheric aerosols, and remote methods of material removal for analysis. A research program using laser ablation mass spectrometry focuses on remote analysis of materials ranging from nuclear waste to the dating of Martian rocks. A critical component of this program is to understand the basic physical and chemical processes that occur at the interface between the solid sample material and the laser-induced plasma. Our interface and surface analysis laboratory capabilities are used to perform a wide range of tests in support of user research, from characterization of self-assembled monolayer (SAM) films to analysis of chemical damage on fruit skins.

Microsensors and Microfluidics
. Common themes in this multidisciplinary area involve combining microfabricated structures or microfluidic systems with materials and chemical processes to investigate molecular interactions, and developing new microanalytical principles, tools, and techniques. Methods from information science are used to explore and process multivariate analytical data. Included in this work is chemical microsensor development with a focus on acoustic wave sensor arrays and optical sensing. Key areas of science in this effort include rational design of polymeric sensing materials, linear free energy models for vapor/polymer interactions, organic thin films, integrated sensor system development, and multivariate data analysis. New chemometric methods are being designed to incorporate knowledge of molecular interactions into the analysis to extract more information from analytical data.

Microfluidic analytical tools and methods are being developed in two main areas, radiochemistry and bioanalytical chemistry. Through the use of renewable surface techniques, fresh microbeads with interactive surfaces can be delivered to a separation, reaction, or sensing zone for each measurement. Thus, the interactive surface is renewed for every microanalytical procedure. Automated microanalytical separations in radiochemistry have been developed for nuclear waste characterization and medical isotope separations. Novel radionuclide sensors for water monitoring are under investigation. Bioanalytical methods are being developed for complete automated sample handling and delivery to a deoxyribonucleic acid (DNA) detector or oligonucleotide array. Sample preparation entails several steps, including selective capture methods for cells or DNA segments from a variety of sample matrices, as well as DNA processing upstream from a chip or detector. In addition, we are developing microfluidic renewable surface techniques as a method for observing and investigating biomolecular interactions.

Surface Chemistry and Catalysis
. Fundamental and applied studies of a variety of chemical conversion processes are being conducted with a strong emphasis on processes that occur on the surface of heterogeneous catalysts. In fact, chemical reactions taking place on the surfaces of materials underlie many processes of environmental concern. For example, the speed with which contaminants migrate in the subsurface depends markedly on reactions between these chemical species and the surfaces of soils. Other technological areas where surface chemistry plays a profound role include the development of advanced chemical sensors able to function in extremely harsh environments; predictions of long-term stability of waste containment vessels; and the development of stable, selective materials for separating the most hazardous species from toxic wastes. As such, while our primary focus is on the surface chemistry of heterogeneous catalysts, we apply our fundamental understanding of surface chemical processes in a wide range of areas.

Understanding the surface chemistry of oxide materials is important because, compared to metals and semiconductors, far less is known about oxide surfaces at the molecular level. Basic research is carried out with the simplest, most well-defined, environmentally relevant crystallographic structures (mineral carbonates, metal oxides) where molecular theory and spectroscopy are immediately applicable. The work then progresses to materials with more complex structures, such as iron and titanium oxides with substitutional impurities. For example, fundamental studies of the oxygen storage and release properties of pure and zirconium-doped ceria single crystal thin films are aimed at understanding how these "oxygen storage materials" perform in an automobile exhaust catalytic converter. New and unique molecular beam epitaxy (MBE) and chemical vapor deposition (CVD) facilities dedicated to the synthesis of oxide thin film materials make these studies possible.

In addition to fundamental surface chemistry research, we are developing materials and reactor designs for a number of heterogeneous catalytic processes. One study involves synthesizing, characterizing, and testing a group of novel, mesoporous silica-supported, solid-acid catalysts for use in petroleum refining processes. In addition, we are developing a plasma-assisted catalysis process for the removal of NOx from the emissions of "lean-burn" engines such as light duty diesels. This program resulted in a new class of highly active zeolite-based materials that are particularly well suited for catalytic NOx reduction of the gas stream exiting a non-thermal plasma reactor.

Another primary thrust area is microtechnology, or the process intensification of chemical reactor hardware. Microreactor systems are being developed for compact fuel processing applications, including automotive power generation, man-portable power, and ultra-small power generation for microelectro-mechanical systems (MEMS) devices at the MEMS scale. Our work in this area was recognized in FY 1999 with an R&D 100 Award from Research and Development Magazine for the Compact Microchannel Fuel Vaporizer. This breakthrough technology integrated novel catalysts into a compact microchannel reactor design before deploying the

technology for industrial use. The reactor was more than an order of magnitude smaller than competing technology and is one critical component of an automotive fuel processing system.

Materials Interfaces. Interfaces in materials, solid-state devices, and large-scale materials applications have a major influence on the many properties of the materials, solid-state atomic and ionic transport, the performance of many devices, and the success of large-scale applications. Interfaces in materials generally refer to the few-atom layers between single and dissimilar phase materials (e.g., grain boundaries, multi-layer films, metal-insulator contacts). Such interfaces may be intentionally formed, as in multi-layer devices or nanocomposites, or naturally formed, as in many natural minerals. Interfaces can also form during radiation-induced phase transformations in nuclear waste materials or as an advanced materials treatment using ion-beam modification techniques.

Studies are being conducted on solid/solid interfaces in a wide variety of materials, radiation effects in materials, fundamental defect properties and interactions, atomic and ionic transport, and aerosol characterization. Included in these research projects is the application of ion-beam analysis, transmission electron microscopy, x-ray diffraction, and computer simulation techniques. Many of the studies on solid/solid interfaces involve 1) the characterization of interfaces between thin films and substrates, between ion-beam-modified surfaces and original substrate, or between nanoclusters and host matrices; 2) the segregation or diffusion of point defects, impurities, dopants, or gas atoms to or away from such interfaces; 3) the transport of hydrogen, oxygen, or other gases across such interfaces; 4) the formation or destruction of such interfaces from radiation damage processes, and 5) the stability of interfaces under a wide range of environmental conditions. Studies on radiation effects include experimental research on materials for immobilization of nuclear waste and plutonium, as well as materials for next-generation nuclear power production, and multiscale computer simulations of damage production processes, defect diffusion, and microstructure evolution.

Fundamental studies of ion-implantation damage in wide-band-gap semiconductors, such as silicon carbide and gallium nitride, are also being performed. Studies on atomic and ionic transport include ion-exchange processes in nuclear waste glasses, hydrogen storage and transport in materials, and oxygen transport in fast ion conductors. In many of these studies, crystalline quality, interfacial stresses, crystallographic orientation, phase identification, and structural information are obtained by x-ray diffraction, electron microscopy, and ion-beam analysis techniques. An overall theme of the more fundamental research projects is the integration of experimental and computer simulation methods to provide atomic-level understanding of the physical processes, as well as atomic-level interpretation of experimental data.

2. Oxide and Mineral Films and Surfaces

Surface Structure and Reactivity of Anatase (001)

E. I. Altman[(a,b)], Y. Liang, and S. A. Chambers

(a) Department of Chemical Engineering, Yale University.
(b) EMSL User.

The anatase polymorph of TiO_2 is commonly used as a catalyst support, and as such it has been found to enhance the reactivity of supported metals and oxides. In addition, anatase is of interest for its own catalytic properties as a photocatalyst to split water. Therefore, we have worked with EMSL staff to characterize the surface structure and reactivity of epitaxial anatase (001) films and single crystals. It was previously found by the EMSL group that films grown on Nb-doped $SrTiO_3$ (001) display a (4x1) reconstruction observable by RHEED, LEED, and STM even when the surfaces are fully oxidized. This reconstruction is unusual because the (1x1) surface is autocompensated, so the reconstruction is not driven by the need to create a non-polar surface. As shown in the STM image in Figure 2.1a, we found that single crystals display the same reconstruction, eliminating strain due to the 3.7%

lattice mismatch between anatase and $SrTiO_3$ as the source of the reconstruction. Figure 2.1a also indicates that the stripes due to the reconstruction rotate by 90° when a single height atomic step is descended, resulting in (4x1) and (1x4) domains. This is a consequence of the bulk crystal structure, which dictates that the bond directions rotate 90° in alternating layers. On crystals misoriented by 2°, we found that one of the domains is suppressed, resulting in double-height steps running parallel to the (001) direction of the reconstruction as shown in Figure 2.1b. This observation—that there is energy reduction when the steps running parallel to the reconstruction stripes double in height—provides valuable information about relative surface energies and resulting structures.

To further characterize the surface structure, we have studied the adsorption of formic acid on anatase (001). On studies of the rutile polymorph of TiO_2, formate anions were observed to bond to exposed undercoordinated Ti ions on the surface in a bidendate manner. Assuming formate bonds in a similar way to anatase, the location of the formate anions in STM images provides the location of the undercoordinated Ti atoms on the reconstructed surface. Figure 2.2 shows STM images with low coverages of formic acid after adsorption at 300 K (Figure 2.2a) and annealing to 850 K (Figure 2.2b).
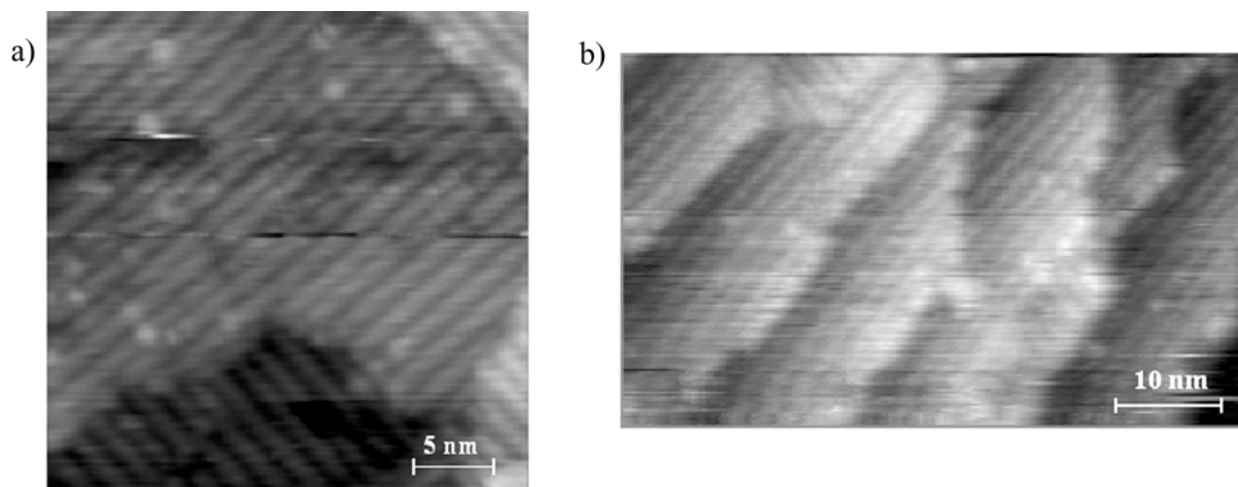
Figure 2.1. STM images of (001) oriented anatase single crystal surfaces. (a) The stripes are due to the (4x1) reconstruction, and the direction of the stripes rotates by 90° when the ~3.8-Å-high, single-height step at the bottom of the image is descended. (b) In areas where the step density is high, double-height steps are observed, thus suppressing one of the domains and leaving the stripes running parallel to the steps.
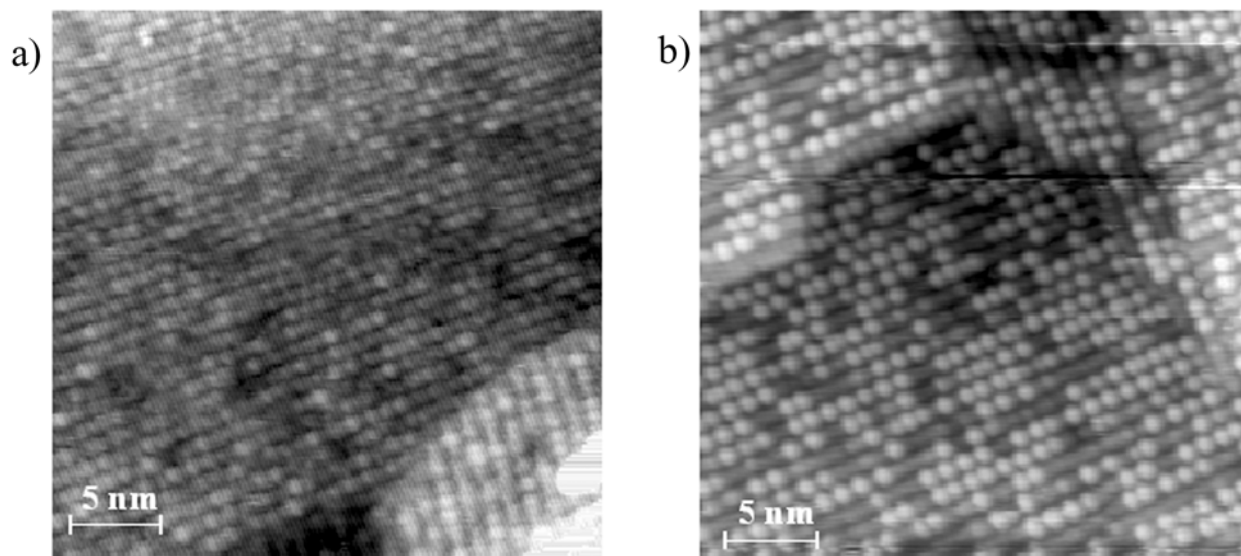
Figure 2.2. STM images obtained before (a) and after (b) annealing an adsorbed formic acid layer to 850 K. The annealing desorbs water and some of the adsorbed acid as CO_2 and CO, and improves the resolution. The bright spots are due to the adsorbed species. The image in (b) clearly shows the molecules symmetrically centered on the bright rows, a minimum distance of 2x apart.

The bright spots are attributed to adsorbed molecules that are centered on the tops of the bright rows indicating that the undercoordinated Ti atoms are centered atop the row. In addition, the minimum distance between molecules is 2×, as would be expected for bidendate formate. This eliminates models that have been proposed that have pairs of undercoordinated Ti atoms straddling the bright row, and other models that suggest that the lowest coordinated Ti atoms are in the trough. We are currently looking at higher coverages to determine if there are less reactive sites in the trough that also expose coordinatively unsaturated Ti atoms. Through this work, we are developing models of the surface structure and how this structure determines the types of sites available for reaction on the surface.

The Effect of the Chemical Identity of M(IV) Dopants on the Reduction of Oxygen at Hematite Surfaces

B. A. Balko[a,b] and K. M. Clarkson[a,c]

Supported by the Lewis & Clark College John S. Rogers Summer Science Program.
(a) Lewis & Clark College.
(b) EMSL User.
(c) Student.

The association of Fe(II) sites with Fe(III)-containing iron oxides increases the reducing capabilities of these oxides (Haderlein and Pecher 1998, Klausen et al. 1995). Because Fe(III)-containing oxides are widespread in natural as well as in anthropogenic systems (e.g., iron passive films), changes in the numbers of Fe(II) sites in these iron oxides can have a significant impact on the biogeochemistry of natural systems and on the continued corrosion of iron structures. One way to introduce Fe(II) sites into Fe(III)-containing iron oxides is via M(IV) dopants. Iron oxides found in natural and anthropogenic systems are likely to be impure and therefore, in essence, doped. Impurities are incorporated into minerals during their formation and, likewise, passive films may be doped with alloying elements (Schmuki et al. 1998, Piao and Park 1997, Hakiki et al. 1998) and/or ions in solution (Shimizu 1993). Thus, it is important to examine the details of how the introduction of dopants affects the reactivity of Fe(III)-containing oxides. The reactive system that we chose to focus on is the reduction of oxygen on hematite. Our research addresses two issues: 1) the effect that the identity of the dopant has on the rate of reduction and 2) how the increase in reactivity is related to the increase in dopant concentration.

At Lewis & Clark College, we prepared hematite doped with Sn(IV) and Ti(IV) at two different doping levels. We compared the reactivity of the doped electrodes toward oxygen reduction by examining the open circuit potential (V_{oc}), cathodic transfer coefficient (β) and exchange current density (J_o), which were extracted from a Tafel plot (plot of log [current density] versus applied voltage). In order to conclude that the reactivity differences we observed could be attributed to the chemical identity of the dopants, it was important to quantify the dopant concentrations in our samples. Because the doping levels were so low

($\sim 0.06 – 0.9$ %), this quantification could not be done with the instrumentation available to us at Lewis & Clark College.

The actual doping levels in the pellets were quantified with a time-of-flight secondary ion mass spectrometer (TOF-SIMS) (Physical Electronics Instruments Model T2100) and an ultrahigh resolution x-ray photoelectron spectrometer (XPS) (Physical Electronics Instruments Quantum 2000) at the EMSL. The TOF-SIMS was used to compare relative dopant levels for the Ti- and Sn-doped electrodes and to examine how the dopants were distributed in the pellets. Maps of the TOF-SIMS Ti and Sn signals (250-nm beam spot; 25 keV; nominally 60-pA beam; 7-keV extractor; 100-micron raster size) showed that the dopants are distributed uniformly throughout the sample; there was no obvious concentration of dopants at the grain boundaries. TOF-SIMS analyses over the cross section of fractured pellets did not show a significant difference between the concentration of dopants at the outer and inner layers of the pellets. The XPS analysis (23.5-eV beam energy) was used with the TOF-SIMS to determine the concentration of dopant in our samples.

Our results show that the reactivity of doped hematite towards the reduction of oxygen is primarily determined by the concentration of the dopant rather than by its identity. The greatest effect that the identity of the dopant had was on the apparent cathodic transfer coefficient; βn for the Sn-doped electrodes was smaller than for the Ti-doped electrodes, indicating that the density of interface states is greater in the Sn-doped electrodes. The Ti(IV) dopant may lead to fewer interface states because it is better accommodated in the hematite lattice. The measured ion exchange current densities showed that increasing the doping density increased the rate of oxygen reduction as expected. The increase in reactivity, however, was significantly less than the increase in dopant concentration. This result suggests that catalytic surface Fe(II) sites play an important role in the reduction of oxygen at hematite electrodes. This finding, however, may also be attributed to bandgap states associated with the dopants that act as electron traps, the fact that not all the dopants present in the electrodes lead to Fe(II) sites, and/or that stray anodic current made a greater contribution to the exchange current density in the lower doped electrodes.

This work will be published in the February 2001 issue of the *Journal of the Electrochemical Society.*

References

Haderlein, S. B. and K. Pecher, in *Mineral-Water Interfacial Reactions: Kinetics and Mechanisms*, D. L. Sparks and T. J. Grundl, eds., Vol. 715, p. 438, American Chemical Society, Washington, D.C. (1998).

Hakiki, N. E., M. D. C. Belo, A. M. P. Simões and M. G. S. Ferreira, *J. Electrochem. Soc.*, 145, 3821 (1998).

Klausen, J., S. P. Trober, S. B. Haderlein and R. P. Schwarzenbach, *Environ. Sci. Technol.*, 29, 2396 (1995).

Piao, T. and S.-M. Park, *J. Electrochem. Soc.*, 144, 3371 (1997).

Schmuki, P., S. Virtanen, H. S. Isaacs, M. P. Ryan, A. J. Davenport, H. Böhni and T. Stenberg, *J. Electrochem. Soc.*, 145, 791 (1998).

Shimizu, K., *Corrosion Science*, 35, 247 (1993).

Electronic Structure of Pure and Al-Doped TiO$_2$

L. J. Brillson[a], S. H. Goss[a], and S. A. Chambers

Supported by U.S. Department of Energy, Office of Science.

(a) Departments of Electrical Engineering and Physics, Ohio State University.

We used low energy electron-excited nano-luminescence (LEEN) spectroscopy to measure the deep levels, due to lattice imperfections, impurities, and chemical reactions, in high purity TiO$_2$ grown by molecular beam epitaxy (MBE) on TiO$_2$ substrates. We observed a dominant defect emission at ~1.5 eV within the semiconductor band gap that corresponds to lattice point defects intrinsic to the pure material.

We performed these LEEN experiments to establish the intrinsic or extrinsic nature of emission at 1.5 eV that we observed previously in Al-doped TiO$_2$ epilayers. To address this question, we studied a TiO$_2$ single crystal grown epitaxially at the EMSL by Dr. S. A. Chambers. The growth involved O-rich conditions, so that the resulting crystal was clear. This clear appearance is characteristic of TiO$_2$ with low densities of deep level defects. Specifically, a defect with optical emission at 2.5 eV can impart a blue color to TiO$_2$ and is believed to be due to an O deficiency. We employed an incident electron beam of kinetic energy in the 0.5 to 5 keV range to produce depth-dependent free electron-hole pair recombination with a resolution on a scale of tens of nm or less. LEEN spectroscopy permits detection of defect and impurity concentrations as low as 10^{11} cm^{-2} or 10^{15} cm^{-3}, which is well below the sensitivity of conventional surface science probes. The experiments are performed in an ultrahigh vacuum (UHV) environment in order to maintain clean surface conditions that could otherwise introduce extrinsic electronic effects.

Figure 2.3 shows a set of LEEN spectra at incident energies E_B ranging from 0.5 to 5 keV, which corresponds to total excitation depths ranging from 4 nm to 160 nm. For the 100-nm thick TiO$_2$ under investigation, therefore, it is possible to contrast emission from the epilayer at low voltage (0.5 to 2 keV) with emission from the underlying substrate at high

Power corrected: TiO$_2$ on TiO$_2$ with 0.9 nm of Al
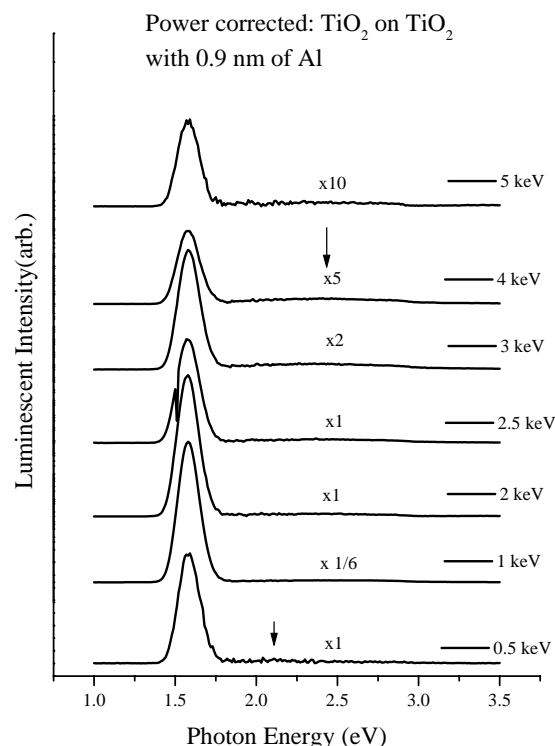
Figure 2.3. LEEN spectra versus incident beam energy from 0.5 to 5 keV for high purity TiO$_2$ grown by MBE on TiO$_2$. The dominant peak at 1.5 eV is strong within epilayer depths, whereas the weak 2.5-eV emission grows only near the substrate. A metal-induced emission feature appears at 2.2 eV, localized to the top few nanometers of the surface.

voltage (3.5 keV and higher). The energy-dependent spectra show a dominant spectral feature at 1.5 eV (1.44 eV after correction for the optical train) that is strongest in the low-energy spectra. Hence, this feature corresponds to states within the band gap of the epilayer. Since this layer is believed to be of high purity, we conclude that the 1.5-eV feature—roughly at the middle of the 3-eV band gap—is intrinsic to the TiO$_2$ and is not due to an impurity. Since emission from this defect is strong for O-rich conditions, we conclude that it is due to a Ti deficiency, perhaps a Ti vacancy or a vacancy complex. Our previous work showed that this peak increases as a TiO$_2$ surface is oxidized, along with a decrease in the 2.5-eV peak. This suggests a competition between carriers for recombination via the two different defect pathways or a conversion of one type of defect into another.

Conversely, the broad weak hump at ~2.5 eV increases with E_B, indicating a defect that is largely absent in the epilayer but that becomes more evident near or in the TiO_2 substrate. The low intensity of this feature in the epilayer is consistent with the clear color of the crystal. This 2.5-eV emission is much weaker than similar features observed in previous TiO_2 specimens, where growth conditions were less O-rich. Since this 2.5-eV feature and blue color is associated with n-type doping, we associate this spectral feature with a transition involving a level at least 2.5 eV above the valence band edge. Figure 2.3 also shows a decrease in the 1.5-eV feature as the 2.5-eV peak begins to increase. This is again consistent with our previous data for oxidized TiO_2 surfaces.

Finally, we observe new emission at ~2.2 eV that is due to a 0.9-nm layer of Al deposited by thermal evaporation in UHV on the free TiO_2 surface. This layer is intended primarily to provide a discharge path for the otherwise highly insulating specimen. However, in addition, the Al layer can bond with O in the TiO_2 selvedge, producing new electronic states. Such states are evident from the 2.2-eV emission localized within a few nanometers of the free surface. This observation confirms that studies of metal-induced interface states are feasible for TiO_2 and that correlations are possible between deep levels within the TiO_2 band gap measured via LEEN spectroscopy vs. chemical shifts of core levels measured either via x-ray photoemission or Auger electron spectroscopies. Experiments are planned to use our high resolution hemispherical analyzer to perform AES N(E) spectra from metal-TiO_2 interfaces to establish such correlations. Delivery of this equipment is anticipated in early 2001.

Controlled Deposition of Indium Tin Oxide on Plastic Substrates

C. Bonham[a,b], P. E. Burrows[b,c],
G. L. Graff[b,c], M. E. Gross[b,c],
P. M. Martin[b], M. Hall[b],
E. Mast[b], and W. Bennett[b]

Many of the properties of plastic are desirable in the flat-panel display industry, where the demand for remote information access is driving the development of rugged, lightweight, power-efficient displays. Organic light-emitting displays (OLEDs) began to achieve low-voltage operation in the late 1980s (Tang and VanSlyke 1987) and have recently demonstrated the potential for luminous efficiencies in excess of 40 lm/W (Baldo et al. 1999). Furthermore, the intrinsic properties of organic semiconductors render them ideal candidates for novel display applications. Many of the materials used in polymeric OLEDs (Burroughs et al. 1990) are intrinsically flexible. However, similar flexibility occurs in small molecule, vacuum deposited OLEDs (Gu et al. 1997), due to the relatively weak nature of the van der Waals force responsible for intermolecular bonding in these systems.

Two major impediments to the realization of plastic displays are the moisture permeability of plastics and the need for a transparent conductive oxide anode. While the former is effectively solved by Battelle's Barix moisture barrier technology, the latter are normally deposited at high substrate temperatures to achieve the correct film stoichiometry for high transparency and conductivity. To achieve similar effects at room temperature requires understanding the physics of film growth and oxygen vacancy generation in complex ternary oxide systems.

We used the thin film deposition facilities in the EMSL to deposit thin films of the transparent conductor indium tin oxide (ITO) on room temperature polyethylene terephthalate substrates using reactive

sputtering from a pressed ITO target with an Ar plasma with a low concentration of O_2 to control the O_2 defect density. By systematically controlling the chamber base pressure, deposition rate, and $Ar:O^2$ ratio, we successfully and reproducibly deposit films with a sheet resistivity of 40Ω/square ITO and a transparency of > 80% across the visible spectral region, as shown in Figure 2.4.

We have also developed post-deposition surface treatment techniques to optimize charge injection from the ITO into a hole-transporting organic semiconductor for application to efficient, low-voltage, flexible light-emitting organic displays (FOLEDs). Figure 2.5 shows results from an organic light-emitting pixel grown on our optimized low-temperature anode as compared to an identical device grown on a conventional glass substrate. While the operating voltages of the two devices are similar, the efficiency of the device on plastic exceeds that of the conventional, glass-based device.

Current work involves applying ion beam and more sophisticated post-deposition processes to further optimize our deposition process while understanding the physics of charge transport across structured organic-inorganic heterojunctions.
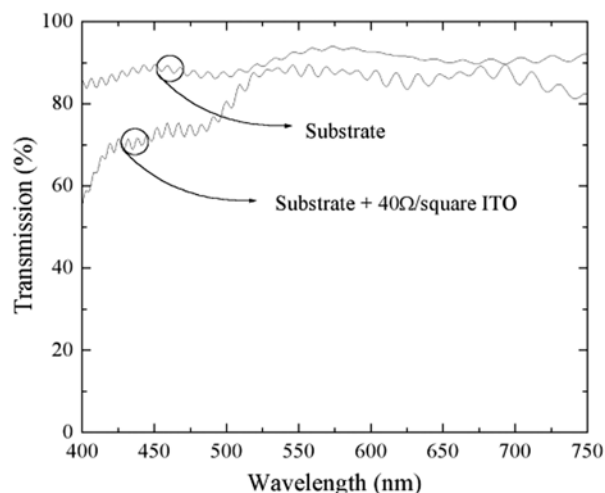
Figure 2.4. Transparency as a function of wavelength of an ITO coating produced using our optimized process, compared to the transparency of the bare substrate.
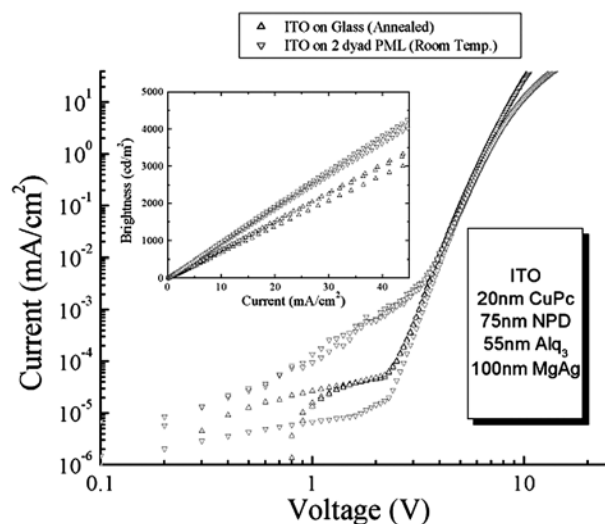
Figure 2.5. Current-voltage characteristics of a vacuum-deposited FOLED grown on the Barix-engineered substrate. Inset: Brightness of the FOLED as a function of drive current. The device grown on low-temperature ITO shows comparable operating voltage but higher efficiency as compared to the conventional device on glass.

References

Baldo, M. A., S. Lamansky, P. E. Burrows, M. E. Thompson and S. R. Forrest, *Appl. Phys. Lett.* **75,** 4 (1999).

Burroughs, J. H., D. D. C. Bradley, A. R. Brown, R. N. Marks, K. MacKay, R. H. Friend, P. L. Burn and A. B. Holmes, *Nature* (London) **347,** 539 (1990).

Gu, G., P. E. Burrows, S. Venkatesh and S. R. Forrest, *Optics Letters*, **22,** 172 (1997).

Tang and VanSlyke, *Appl. Phys. Lett.* **51,** 913 (1987).

Scanning Tunneling Microscopy Investigation of the TiO$_2$ Anatase (101) Surface

W. Hebenstreit[(a,b)], *N. Ruzycki*[(a,b)],
G. S. Herman, Y. Gao, and
U. Diebold[(a,b)]

Supported by National Science Foundation-
CAREER, EPSCoR, and PNNL Laboratory
Directed Research and Development funding.
(a) Department of Physics, Tulane University.
(b) EMSL User.

We have measured and reported the first scanning tunneling microscopy (STM) study of single-crystalline anatase. Atomically-resolved images of the (101) surface are consistent with a bulk-truncated (1x1) termination. Step edges run predominantly in [010], [111], and [111] directions. The surface is stable with very few point defects. Fourfold coordinated Ti atoms at step edges are preferred adsorption sites and allow the identification of tunneling sites in STM.

Titanium dioxide (TiO$_2$) is a versatile material that finds uses as a promoter in heterogeneous catalysis, gas sensors, protective and optically active coatings, as a pigment in paints, and most importantly, as a promising photoactive material in the photocatalytic degradation of environmental pollutants (Serpone and Pelizetti 1989, Linsebigler et al. 1995) and in solar cells (O'Regan and Grätzel 1991). TiO$_2$ exists in the three common crystallographic phases: rutile, anatase, and brookite. Commercial TiO$_2$ powder catalysts are a mixture of rutile and anatase and, for reasons not yet completely understood, anatase is the more photocatalytically active form (Serpone and Pelizetti 1989). Many detailed surface investigations have been performed on single-crystalline rutile TiO$_2$ in order to understand, and ultimately control, the surface chemistry underlying all these applications. A rather complete understanding of the surface properties of rutile has evolved (Henrich and Cox 1994). In comparison, relatively little is known about the surface properties of the technologically more important anatase phase, mainly for lack of appropriate single-crystalline specimens.
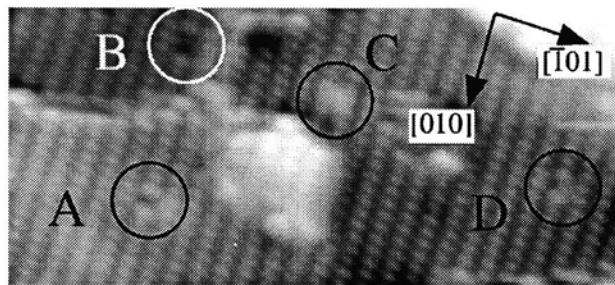
Figure 2.6. STM image (*V sample* 511.22 V, *I tunnel* 51.23 nA, 130 360 Å 2) of an anatase (101) surface. Four features could possibly be representative of oxygen vacancies; single black spots (A),double black spots (B), bright spots (C), and half black spots (D).

We have used scanning tunneling microscopy to examine the surface geometry, defect, and electronic structure of the anatase (101) surface. An unreconstructed (1x1) termination is obtained through sputtering and annealing in UHV. Atomically resolved STM images support a model for an autocompensated, bulk-terminated surface. Preferred step orientations have been identified (Figure 2.6).

They contain fourfold-coordinated Ti atoms that are active centers for adsorption. Depending on the tunneling conditions, twofold-coordinated oxygen atoms can be distinguished in empty-state STM images. The surface is surprisingly stable and appears to have little tendency to form point defects.

These results have been completely reported in *Physical Review B*, *Rapid Communications* 64 (24) (2000).

References:

Henrich, V. E. and P. A. Cox, *The Surface Science of Metal Oxides* (Cambridge University Press, Cambridge, 1994).

Linsebigler, A. L., G. Lu, and J. T. Yates, Jr., *Chem. Rev.* 95, 735 (1995).

O'Regan, B. and M. Grätzel, *Nature* (London) 353, 737 (1991).

Serpone, N. and E. Pelizetti (editors). *Photocatalysis Fundamentals and Applications* (Wiley, New York, 1989).

The Influence of the Bulk Reduction State on the Surface Structure and Morphology of Rutile TiO$_2$ (110) Single Crystals

M. Li[a], W. Hebenstreit[a], U. Diebold[a,b],
A. M. Tyryshkin, M. K. Bowman,
G. C. Dunham, and M. A. Henderson

Supported by the U.S. Department of Energy Office of Basic Energy Sciences.
(a) Department of Physics, Tulane University.
(b) EMSL User.

We have investigated the relationship between different types and amounts of bulk defects and the surface morphology of TiO$_2$ (110) single crystals prepared by annealing in ultrahigh vacuum and in oxygen. Rutile TiO$_2$(110) specimens were cut from the same crystal, and were heated in a furnace to different temperatures, which resulted in different states of reduction (colors of the crystals). After characterization of the bulk defects with electron paramagnetic resonance (EPR) spectroscopy, the specimens were studied with scanning tunneling microscopy (STM), low-energy He$^+$ ion scattering (LEIS), and work function measurements. EPR reveals that darker rutile crystals exhibit higher concentrations of extended Ti^{3+} related bulk defects such as crystallographic shear planes (CSP), with a decrease in substitutional and interstitial defects as compared to lighter crystals. Surface structures with (1x2) features are preferably formed upon UHV annealing on these darker crystals. LEIS measurements show that all of the crystals' (110) surfaces are reoxidized upon annealing in $^{18}O_2$ (573 K, 1x10^{-6} mbar, 10 minutes) and that the ^{18}O surface content is proportional to the bulk reduction state. UV-visible adsorption spectra and resistivity measurements also scale with the reduction states of crystals. Only the (1x1) structure is observed on the surface of slightly reduced crystals. Annealing in oxygen induces additional metastable structures (i.e., TiO$_2$ clusters on blue crystals and rosette networks on dark blue crystals).

Surface Reconstructions of Fe$_3$O$_4$(001)

B. Stanka[a], W. Hebenstreit[a],
U. Diebold[a,b], and
S. A. Chambers

Supported by National Science Foundation.
(a) Department of Physics, Tulane University.
(b) EMSL User.

We investigated the surface termination, structure, morphology, and composition of Fe$_3$O$_4$(001) using scanning tunneling microscopy (STM), low-energy electron diffraction (LEED), low-energy He$^+$ ion scattering (LEIS), and x-ray photoelectron spectroscopy (XPS). The samples consisted of ~5000-Å-thick epitaxial films of Fe$_3$O$_4$ (001) grown by oxygen-plasma-assisted molecular beam epitaxy (OPA-MBE) on MgO(001) substrates. The ($\tilde{A}$2 x $\tilde{A}$2)R45° surface reconstruction present on the as-grown surface was recovered by heating the sample in oxygen (10^{-6} to 10^{-7} mbar) at temperatures between 520 K and 770 K after a through-air transfer from the MBE chamber.

STM results were interpreted assuming an autocompensated B-layer termination, which consists of a layer of octahedrally-coordinated Fe and tetrahedrally-coordinated O, along with one O vacancy per unit cell. Evidence for a vacancy-induced lateral relaxation of the adjacent octahedral Fe ions was found. Further annealing in UHV caused a transformation to either a (1 x n) or a (2$\tilde{A}$2 x $\tilde{A}$2)R45° structure. These surfaces can be reproducibly transformed back to the ($\tilde{A}$2 x $\tilde{A}$2)R45° reconstruction by annealing in oxygen. Interestingly, at no time did we observe the other autocompensated termination, which consists of one-half monolayer of tetrahedrally coordinated Fe(III), despite its observation on the as-grown surface. Thus, it appears that the surface termination is critically dependent on the method of surface preparation.

Results published in B. Stanka, W. Hebenstreit, U. Diebold and S. A. Chambers, "Surface Reconstructions of Fe$_3$O$_4$(001)", *Surface Science* 448 (1) 49 (2000).

Effects of Oxygen Plasma and Thermal Treatments on the Atomic Structures of the TiO₂(110) Surface

S. Gan[a], Y. Liang, and D .R. Baer

(a) Postdoctoral Research Fellow.

The surface of transition metal oxides plays an important role in a variety of technological applications ranging from sensors and electronic devices to catalyst development. As a model system, the surface of TiO₂ is key to understanding surface physics and chemistry of the metal oxides. Recently a great deal of work has been carried out to investigate surface structures of TiO₂ and preparation of TiO₂ surfaces with controlled structure and stoichiometry. This has significantly enhanced our understanding of the physical and chemical properties of TiO₂ surfaces. However, atomic control of TiO₂ remains a difficult art, and preparation of well-defined, clean, and reproducible surfaces for different crystals remains a tedious and somewhat random process. We investi-

gated the effects of oxygen plasma treatment and annealing in ultra-high vacuum (UHV) on the atomic structures, stoichiometry, and chemical properties of the TiO₂(110) surface. We found that annealing TiO₂ crystals in oxygen plasma could effectively remove calcium and carbon contaminants, and dramatically improve the surface morphology and stoichiometry. In contrast, annealing the surface in UHV was found to have a profound effect on the dynamics of surface atomic steps, and consequently, affect the atomic structures of the resulting surface (Gan et al. 2000, Gan et al., in press).

Figure 2.7 is an XPS determination of the dependence of the calcium coverage on the temperature of annealing the TiO₂ crystals in oxygen plasma. Also shown in the figure is the effect of temperature and time on the segregation of calcium during heating in UHV. The calcium coverage (Ca 2p/Ti 2p) is calculated from the ratios of Ca 2p and Ti 2p peak areas in XPS spectra divided by their corresponding atomic sensitivity factors. Results show that annealing TiO₂ crystals in oxygen plasma at above 500° C effectively removed calcium and carbon contaminants. In addition, STM of the resulting surface showed a dramatic
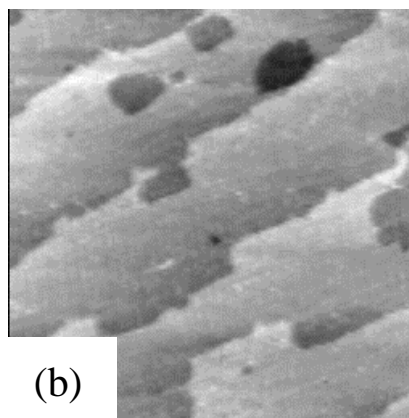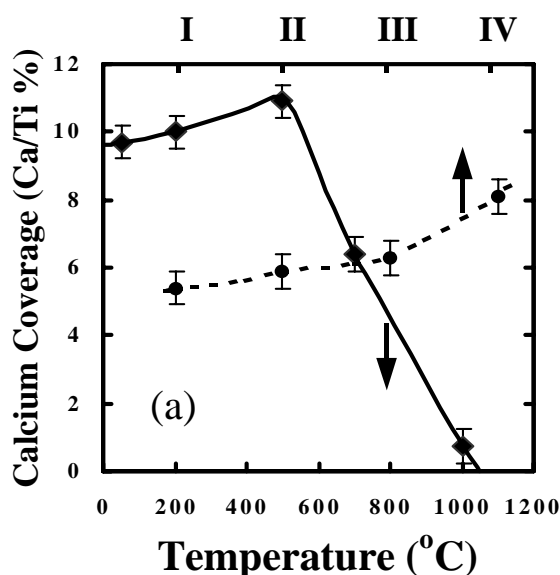
Figure 2.7. The effect of the surface temperature on the calcium coverage during oxygen plasma treatments (solid line) and vacuum annealing (dashed line). The upper labels on the x-axis (I to IV) refer to the corresponding surface conditions [i.e., the freshly loaded sample surface (I) was heated in UHV at 300° C for 15 min (II), for 30 min (III), and at 500° C for 15 min (IV), respectively]. (b) Scanning tunneling micrograph of the TiO₂(110) surfaces after oxygen plasma treatment at 800° C and annealing the surface at 500° C. The image area is 0.65x0.65 μm².

improvement on the morphology with terraces as wide as a few thousand angstroms.

In addition to the oxygen plasma treatment, the effects of annealing in UHV on surface structures, particularly the dynamic behavior of steps on the $TiO_2(110)$ surface structure and phase transformation from (1x1) to the (1x2) were also investigated. We found that two types of steps dominate the transformation process: 1) [001]-type—defined as steps that run along the [001] direction and 2) $[1\bar{1}0]$-type—defined as steps that run parallel to the $[1\bar{1}0]$ direction. The stoichiometric (1x1) surface contained mostly [001]-steps. Reducing this surface caused nearly half the [001]-steps to be gradually converted to $[1\bar{1}0]$-steps. This evolution in step structure was accompanied by a growth of reconstructed (1x2) domains initiated mostly at the $[1\bar{1}0]$-step edges. On the (1x2) domains, the lengths of the [001]- and $[1\bar{1}0]$-steps were approximately equal. The total step length (L) and the ratio of the [001]- and $[1\bar{1}0]$-step lengths $(L_{[001]}/L)_{[1\bar{1}0]}$ are plotted in Figure 2.8. The overall step direction, θ, was determined by the angle of all the steps in each image with respect to the [001] surface, calculated by $\theta = \tan^{-1} L_{[001]}/L_{[1\bar{1}0]}$, where $L_{[001]}$ and $L_{[1\bar{1}0]}$ are the total lengths of the [001]- and $[1\bar{1}0]$-steps in the image. The population of the (1x2) structure calculated based on the surface area it occupied also is shown in Figure 2.8.

Our results showed that the overall step orientation evolved from the initial [001] direction to the $[1\bar{1}0]$ direction with the increase in the annealing temperature. As a result, more $[1\bar{1}0]$-steps were generated at the expense of [001]-steps. The change of step
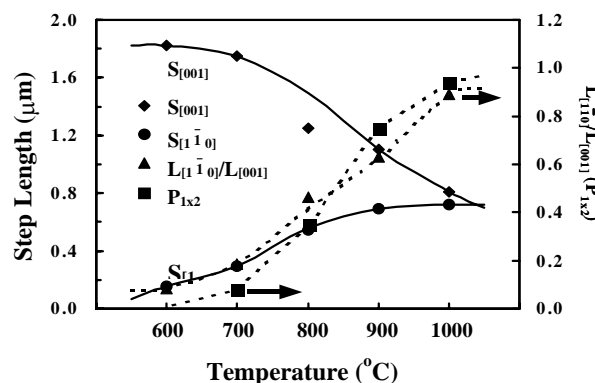
Figure 2.8. The dependence of step orientation and (1x2) population upon the temperature.

orientation and relative population also was accompanied by the surface transformation from the initial (1x1) phase to the (1x2) phase, indicating some correlations between step dynamics and the formation of the (1x2) phase. As shown in Figure 2.8, the initial (1x1) surface was comprised of more than 95% A-steps, the length of which reduced rapidly with the increase of the (1x2) population. The results of this work shed light on the step structure and correlation between the step energetics and the surface phase transformations on the $TiO_2(110)$ surface.

References

Gan, S., Y. Liang, D. R. Baer, "Atomic control of $TiO_2(110)$ surface by oxygen plasma treatment", *Surf. Sci. Lett.*. 459, L498 (2000).

Gan, S., Y. Liang, D. R. Baer, "The interplay between step anisotropy and surface phase transformation on $TiO_2(110)$", *Phys. Rev. B.*, in press.

Surface Studies on TiO₂(111)

*H. Uetsuka[a], A. Sasahara[a], H. Onishi[a,b],
and M. A. Henderson*

Supported by Kanagawa Academy of Science and
Technology.
(a) Kanagawa Academy of Science and
Technology, Japan.
(b) EMSL User.

The aim of the project is to conduct fundamental
surface studies on the adsorption, desorption, and
reactions of small probe molecules on the
(111) surface of TiO₂ rutile. When we assume the
stoichiometric and most coordinatively saturated trun-
cation on TiO₂ (111), fivefold Ti atoms are separated
from each other by 546 pm or more (Figure 2.9).
Chemistry on this surface, with the Ti atoms as
isolated reaction centers, should be different from that
on the well-studied (110) surface, where fivefold Ti
atoms aligned at intervals of 296 pm form one-
dimensional rows of reaction centers.

Our focus was on the relationship between the struc-
ture of the oxide surface and the chemical properties
of the adsorbates. Formate (HCOO) was used as a
probe molecule to determine the relationship. The
molecular vibration of the formate was observed by
high-resolution electron energy-loss spectroscopy
(HREELS) at the EMSL, while high-resolution imag-
ing by scanning tunneling microscopy (STM)
(Uetsuka et al. 2000) was performed at the User site.
The results obtained at both ends suggest that a certain
fraction of formates are adsorbed in a monodentate
geometry on TiO₂(111). Thermal desorption (TPD)
experiments at the EMSL showed the decomposition
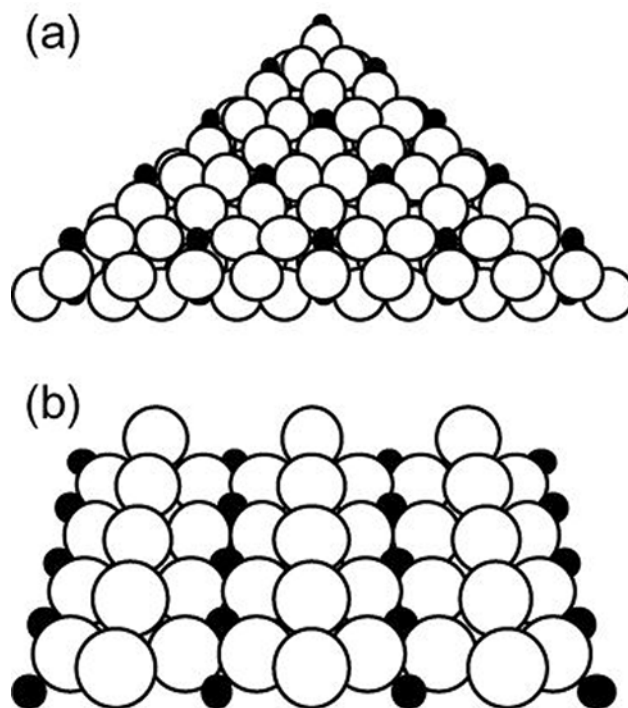
Figure 2.9. Stoichiometric truncations of rutile TiO₂
normal to the (a) (111) and (b) (110) direction. Filled
and open balls represent Ti and O atoms.

reactivity of the formate was not sensitive to the
substrate structure (Uetsuka et al., to be submitted).

References

Uetsuka, H., A. Sasahara, and H. Onishi, "Scanning
Tunneling Microscopy Study of Surface
Reconstructions of Rutile TiO2(111)", *Japanese
Journal of Applied Physics*, 39 3769-3772 (2000).
Uetsuka, H., A. Sasahara, H. Onishi and
M. A. Henderson, to be submitted.

Surface Chemistry Controlled Nucleation, Growth, and Formation of Calcium Phosphate

X. S. Li[(a,b)], D. Stevens[(a)], and A. Campbell

(a) PNNL Energy Science and Technology Division.
(b) EMSL User.

The objective of this study was to investigate calcium phosphate nucleation, growth, and formation on two-dimensional substrates with different functional groups, such as OH, OOH, and SOH_3, to understand the roles of surface chemistry on crystal nucleation kinetics and film formation.

The surface-induced mineralization (SIM) process was used for the deposition of calcium phosphate coatings. The crystal nucleation induction time and growth rate was determined by measuring the Ca or P concentration change in the solution before and after the deposition. The Ca and P concentration of the solution was analyzed with inductively coupled plasma. The formation of coatings was characterized using XRD and SEM. The results of our investigations are shown in Figure 2.10.
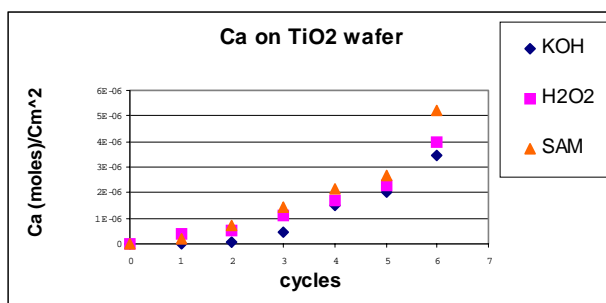
Figure 2.10. Shows calcium phosphate growth on different surfaces.

X-Ray Photoelectron Diffraction of Polar MgO(111)-(1×1) Surface

M. Gajdardziska-Josifovska[a,b],
R. A. Plass[a,b,c], *M. Pauli*[a],
D. K. Saldin[a], *and S. A. Chambers*

Supported by National Science Foundation.
(a) Department of Physics and Laboratory for Surface Studies, University of Wisconsin-Milwaukee.
(b) EMSL User.
(c) Currently at Sandia National Laboratory.

The stability of polar oxide surfaces has long been a problematic question in surface science. A bulk-terminated polar surface has an infinite surface energy because alternating layers of oppositely charged ions produce a dipole moment perpendicular to the surface. Theoretical studies have proposed four different mechanisms for the stabilization of polar oxide surfaces with the rocksalt structure: 1) microscopic faceting into neutral {100} planes, 2) surface reconstruction, 3) adsorption of charged species, and 4) charge transfer. The last two mechanisms allow for a (1×1) structure stabilized by hydrogen (3) or by surface metalization (4).

Our NSF-funded project on polar oxide surfaces aims to provide experimental tests of these stabilization mechanisms, using MgO(111) as a model surface. Microscopy was used to eliminate the neutral-faceting model (Plass et al. 1998a, Giese et al. 2000), and transmission high-energy electron diffraction (THEED) was used to generate the first structure solutions for reconstructed MgO(111) surfaces created at high annealing temperatures (>1450° C) (Plass et al. 1998b). At lower annealing temperatures, THEED reveals (1×1) patterns, but this technique is not suitable for quantitative determination of interlayer relaxations. The user project at PNNL aims to determine the stabilization mechanism of the polar MgO(111)-(1×1) surface from x-ray photoelectron diffraction (XPD) and spectroscopy (XPS) experiments.

The specimens were two bulk single crystals (from Commercial Crystals Lab) that were mechanically polished and cleaned with acetone and methanol solvents. One crystal then was etched in hot concentrated nitric acid and furnace annealed in air to 800° C. Once in UHV, both crystals were further cleaned with an oxygen plasma at room temperature, followed by vacuum annealing at 800° C. Upon cooling to room temperature, *in situ* low-energy electron diffraction (LEED) and reflection high-energy electron diffraction (RHEED) showed (1×1) patterns, in agreement with the *ex situ* THEED observations from thinned single crystals. This result marks the first observation of the MgO(111)-(1×1) structure on a bulk crystal.

Scanned-angle XPD was used to measure O 1s and Mg KLL azimuthal angular distributions at low take-off angles (Figure 2.11), as well as polar scans in high-symmetry azimuths. The surface termination was determined by noting the increase in O 1s/Mg KLL intensity ratio with decreasing emission angle in all polar scans (shown in 1999 report). An O-terminating layer is needed for OH stabilization, and is one of the two possible surface-metalization options (Pojani et al. 1997).

To test for interlayer relaxation, single- and multiple-scattering theories were used to simulate the azimuthal scans for MgO(111)-(1×1) surfaces. Single scattering analysis confirmed the preference for O termination over Mg termination, and for contraction of the topmost layer, but did not fit all experimental peaks. We are now performing multiple-scattering calculations, in a cluster configuration, to test the two essential models of bulk-terminated and contracted MgO(111)-(1×1)O surfaces. The results of these calculations are compared to the experimental data in Figure 2.11.

These results indicate little difference between the two models, and some data peaks remain unfitted by the models currently under consideration. Hence, the surface-metalization model remains unconfirmed by this XPD experiment.
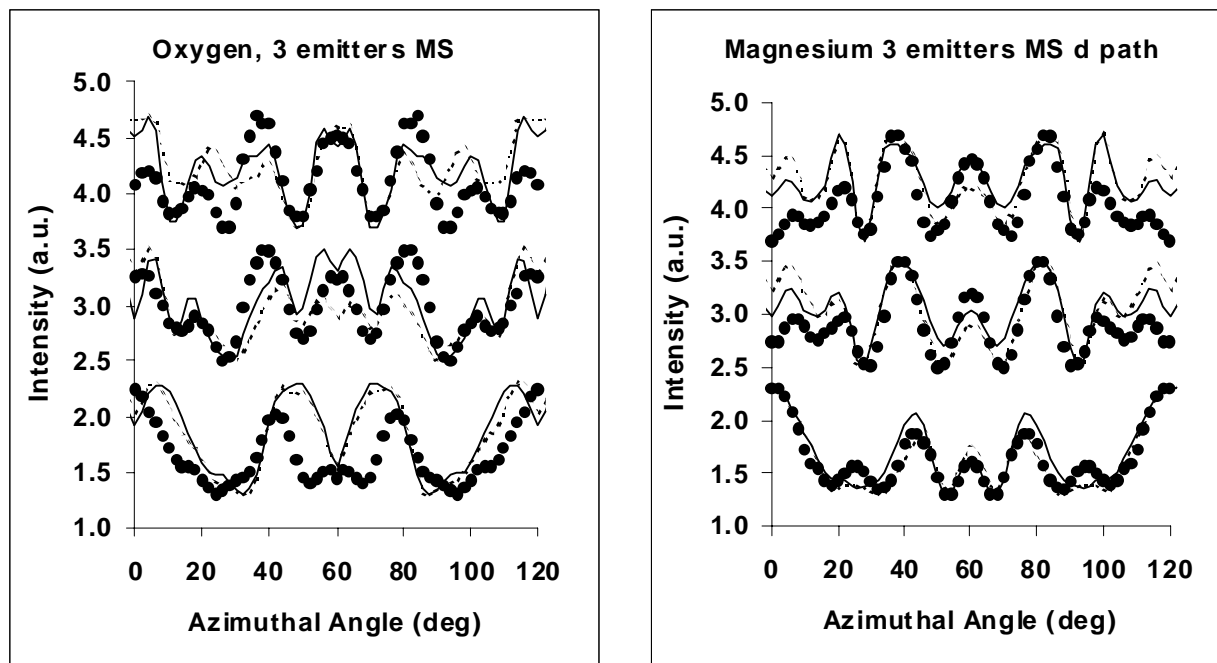
Figure 2.11. XPD azimuthal scans at three fixed polar angles (θ=7, 11 and 16) of O 1s (a) and Mg KLL (b) photoelectrons. Experimental data (circles) and results from multiple-scattering simulations for bulk-terminated MgO (111)-(1x1)O model (solid line) and contracted MgO (111)-(1x1)O model (dashed line).

High-energy-resolution O1s spectra, obtained at normal emission (θ=90°) and grazing emission (θ=10°), reveal that the terminal oxygen layer is bonded to hydrogen (shown in 1999 report). The presence of a monolayer of H associated with the terminal layer of oxygen removes the surface dipole and stabilizes the surface, independent of surface relaxation.

Further calculations are needed to extract the structural model from analysis of the XPD azimuthal scans. However, it appears that the fundamental issue of surface termination and surface dipole is answered by the presence of a terminal OH layer.

References

Giese, D. R., F. J. Lamelas, H. A. Owen, R. Plass and M. Gajdardziska-Josifovska, *Surf. Sci*. 457, 326 (2000).

Plass, R., J. Feller and M. Gajdardziska-Josifovska, *Surf. Sci*. 414, 26 (1998a).

Plass, R., K. Egan, C. Collazo-Davila, D. Grozea, E. Landree, L. D. Marks, M. Gajdardziska-Josifovska, *Phys. Rev. Lett*. 81, 4891 (1998b).

Pojani, A., F. Finocchi, J. Goniakowski, C. Noguera, *Surf. Sci*. 387, 354 (1997).

Spin Polarized Photoemission Study of Half Metallic Magnetite Films

S. Morton[a], G. D. Waddill[a],
J. G. Tobin[b], S. Kim[c], I. Schuller[c],
and S. A. Chambers

Supported by U.S. Department of Energy Office of Basic Energy Sciences, Division of Materials Science.
(a) University of Missouri.
(b) Lawrence Livermore National Laboratory.
(c) University of California at San Diego.

Many materials such as Heusler alloys, manganites, metallic oxides, and perovskites have been predicted theoretically to be half metallic, displaying a co-existence of metallic character for one electron spin population and insulating character for the other, and hence 100% spin polarization at the Fermi level (Figure 2.12). Such materials could possibly be used in the data storage and semiconductor industries as pure spin sources in spintronic devices. However, despite extensive study of such candidate materials, remarkably little truly definitive experimental evidence for half-metallic characteristics has emerged, and the evidence that has emerged has been frequently somewhat contradictory.

One technique that can potentially yield a definitive answer to this question is spin-polarized photoemission, as this technique allows us to directly probe the majority and minority densities of states in the valence band and near the Fermi edge region. It is from this technique that the best evidence to date for half-metallic character has emerged (Park et al. 1998a,b). However, such experiments are frequently hampered by the difficulty in producing clean stoichiometric surfaces with a polarization that is truly representative of that of the bulk material.

We have used the spin-resolving photoelectron spectrometer of the Spectromicroscopy Facility at the Advanced Light Source (ALS) (Tobin et al. 1998) to study the half-metallic candidate material magnetite, (Fe_3O_4). The epitaxial films were grown at the EMSL by oxygen-plasma-assisted molecular beam epitaxy on MgO (100) substrates with precise control of atom fluences and substrate temperature. The properties of the films were determined *in situ* by RHEED, XPS,
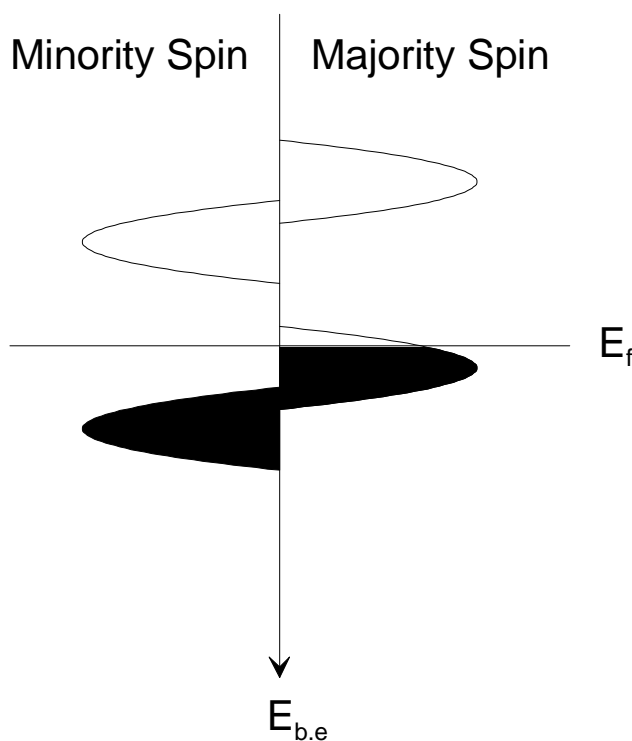
Figure 2.12. Schematic band structure of a hypothetical half metal showing the co-existence of metallic and insulating characteristics in the majority and minority density of states.

and LEED and were comparable to surfaces obtained from *in situ* cleaving of bulk single crystals. After growth and characterization, the samples were transferred *ex situ* to the ALS in an evacuated vessel (total exposure time to atmosphere during sample transfer was approximately 5 minutes). Analysis of the *ex situ* transferred samples at the ALS showed initial surface contamination levels of ~ 50%. By conducting spin-resolved photoemission measurements on these "as-received" samples, we have demonstrated that cleaning by standard techniques such as ion bombardment will result in the loss of spin polarization within minutes (Figure 2.13). However, our ability to perform spin-resolved experiments at higher photon energies than is possible at most other facilities (as a direct result of the high brightness of the third generation synchrotron source), has enabled us to successfully study the near Fermi edge polarization of the "as received" samples without having to resort further to such potentially destructive cleaning techniques. By measuring polarization as a function of emission angle and photon energy, and combining these measurements with a substrate/ overlayer attenuation model,
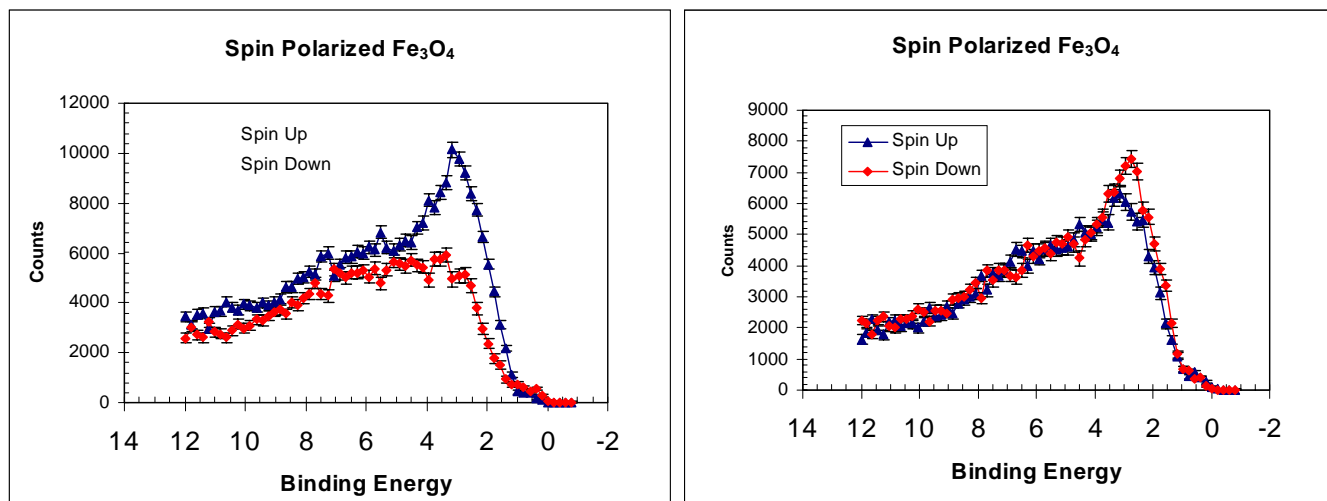
Figure 2.13. Spin-polarized valence band spectra of MBE-grown Fe_3O_4 as received (a), and after 5 minutes sputtering with Ne ions, demonstrating almost complete loss of polarization (b).

we have been able to extract the underlying polarization of the bulk material and have demonstrated that it is significantly higher than the 30% initially observed in the "as-received" samples and may indeed be up to 100%. Furthermore, our spin-resolved spectra demonstrate close agreement with simulated spectra derived from theoretical one-electron density-of-states calculations (Zhang and Satpathy 1991). Further experiments are in progress.

References

Park et al., *Nature* **392**, 794 (1998a); *Phys. Rev. Lett.* **81**, 1953 (1998b).

Tobin, J. G. et al., *MRS Symp. Proc.* **524**, 185 (1998).

Zhang, Z. and S. Satpathy, *Phys. Rev. B.* **44**, 13319 (1991).

Surface Structure Determination of Yttria-Stabilized ZrO$_2$(001) Surface Using X-Ray Photoelectron Diffraction

S. Thevuthasan, Y. J. Kim[a,b],
S. I. Yi[c], V. Shutthanandan,
S. A. Chambers, and C. H. F. Peden

(a) EMSL User.
(b) Department of Chemical Technology, Taejon National University of Technology, South Korea.
(c) Postdoctoral Research Fellow.

The structure and composition of oxide surfaces strongly influence their surface chemical, magnetic, and mechanical properties. Thus, there is a growing interest in determining the termination, reconstruction and relaxation of oxide surfaces. However, surface structures are known accurately for only a few of the more common oxides. The yttrium-stabilized ZrO$_2$(001) surface can be in principle either O-terminated or Zr-terminated. However, neither of these surfaces is charge neutral as a (1x1) structure. It was recently reported that the CeO$_2$(001)surface, which is similar to ZrO$_2$(001), is terminated with 0.5 monolayers of oxygen. The goal of the present work is to perform an experimental determination of the surface structure of a pure yttria-stabilized, single-crystal ZrO$_2$(001) surface. The method we have used is scanned-angle, high-energy photoelectron diffraction at low take-off angles. The rationale behind this approach is that azimuthal intensity scans at the lowest possible take-off angles can provide the highest degree of surface sensitivity. Surface-sensitive, high-energy (AlKα-excited) photoelectron diffraction has been used recently to determine the surface structures of single crystal magnetite and hematite thin films grown on MgO(001) and α-Al$_2$O$_3$(0001). Our goal is to extend this technique to obtain the surface structure by going to the lowest possible take-off angles. By comparing the experimental data to the theoretical simulations using quantum mechanical scattering theory and R-factor analysis, surface structures can be determined.

Figure 2.14 shows aligned and random Rutherford backscattering spectra from a clean, yttria-stabilized ZrO$_2$(001). The minimum yield for Zr was determined to be about 4%, and further investigations indicate that the minimum yield is higher compared to most single-crystal oxides due to the point defects related to yttria stabilization. The amount of yttrium that is substitutional to Zr was determined to be 14 atomic %. Although the aligned spectrum shown in Figure 2.14 qualitatively shows that Y substitutes for Zr, the Zr 3d and Y 3d azimuthal scans at many take-off angles (the scans at $\theta =21^o$ are shown in Figure 2.15) clearly demonstrate that Y occupies the same lattice site as Zr.

Figure 2.16 shows the four structures that are considered for the simulations. The results indicate that the surface termination is ½ monolayer O (S1), and the simulations to determine the surface relaxations are currently in progress.
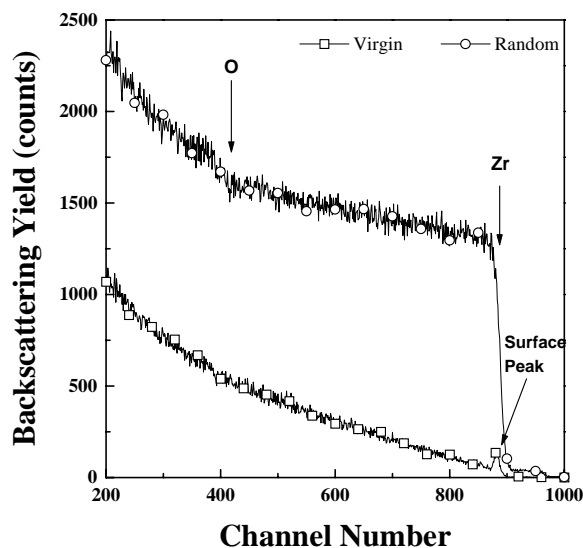
Figure 2.14. Aligned and random spectra from a clean Y-ZrO$_2$(100) single-crystal surface.

Comparison of Experimental Zr 3d and Y 3d Azimuthal Scans

$\theta = 21°$

**Y 3d
K.E. = 1330 eV**

[010]

[110]

**Zr 3d
K.E. = 1307 eV**

Intensity (Arb. Unit)
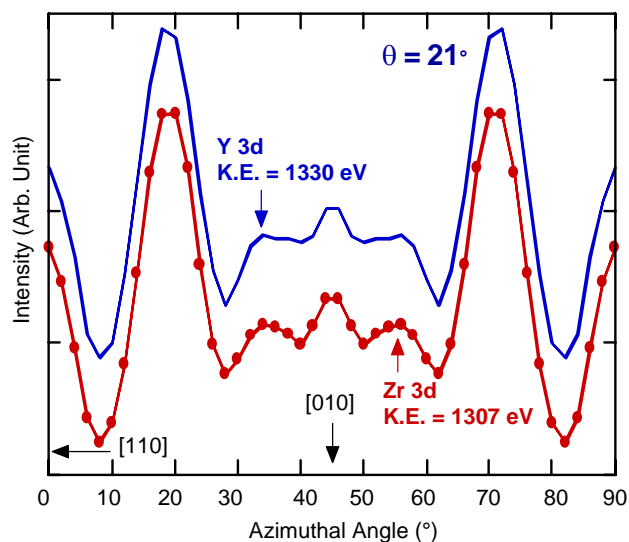
Azimuthal Angle (°)

Figure 2.15. Y 3d and Zr 3d azimuthal scans at takeoff angle, $\theta = 21°$

Y-ZrO$_2$(001)
Considered Surface Terminations

S1 => O Terminated, 0.5 ML
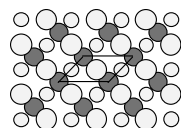
O = 2 dangling bonds
Zr= 2 dangling bonds
Charge Neutral

S2 => O Terminated, 1.0 ML

[010]

[100]
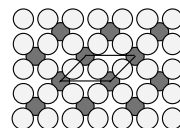
O = 4 dangling bonds
Zr= 0 dangling bonds
Not Charge Neutral
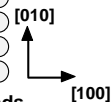
S3 => Zr Terminated, 1.0 ML
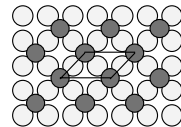
O = 0 dangling bonds
Zr= 4 dangling bonds
Not Charge Neutral

S4 => Zr Terminated, 0.5 ML

[010]

[100]
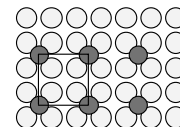
O = 4 dangling bonds
Zr= 4 dangling bonds
Charge Neutral
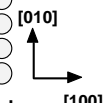
Figure 2.16. The four surface structures that are considered for x-ray photoelectron diffraction simulations.

3. Electronic and Catalytic Materials

Growth of Thin Film Model Oxide Catalysts

E. I. Altman[a,b], T. Droubay[c], and S. A. Chambers

Supported by the U.S. Department of Energy, Office of Basic Energy Sciences, Division of Chemical Sciences.
(a) Department of Chemical Engineering, Yale University.
(b) EMSL User.
(c) Postdoctoral Research Fellow.

Although oxides are widely used to catalyze partial oxidation reactions and the selective reduction of NO, the relationship between oxide catalytic activity and structure remains poorly understood. A major reason for this lack of fundamental insight into oxide catalysis is the dearth of well-ordered, macroscopic, single-crystal oxide catalysts that can be characterized using the full suite of surface science techniques that are routinely applied to metal and semiconductor surfaces. For example, molybdena and related molybdates are important partial oxidation catalysts. Yet all prior detailed work on surface characterization of molybdena has focused on the largely unreactive α-MoO_3 phase, primarily because this is the only phase for which bulk macroscopic single crystals can be readily synthesized. Therefore, we have been working on growing epitaxial β-MoO_3, which is known to be a highly active catalyst for formaldehyde synthesis, and can be considered the parent phase for many mixed molybdate catalysts. The β phase is also of interest to us because it is isostructural with WO_3, a material that is under study at Yale. Comparison of reaction properties for the two surfaces will reveal how the metal cation affects catalytic activity and function *without changing the surface structure.*

In collaboration with EMSL staff, we have grown and characterized β-MoO_3 epitaxial films, using EMSL research capabilities. In particular, we used *in situ* reflection high energy electron diffraction (RHEED) to characterize the growth mode, crystallinity, and orientation of the molybdena films; x-ray photoelectron spectroscopy (XPS) to characterize the film composition and Mo oxidation state; atomic force microscopy (AFM) to characterize the film morphology; and x-ray diffraction (XRD) to determine the

bulk crystal phase of the film. We have shown that fully oxidized MoO_3 films can be grown by oxygen-plasma-assisted molecular beam epitaxy. Further, we have demonstrated in-plane lattice matching of MoO_3 to $LaSrAlO_4$ (001). When the films are grown at 400° C, XRD indicates the presence of a new tetragonal MoO_3 phase. AFM images of these films suggest columnar growth with terraces over 100 nm in width. We have investigated how the phase and growth mode can be manipulated by varying the substrate temperature, growth rate, and other growth parameters. Results indicated that smoother films of a different epitaxial MoO_3 phase could be formed by cycling the growth and annealing temperatures between $\sim300^o$ C and 400° C after forming an initial template layer at 400° C. Examination of the RHEED pattern during growth showed that annealing tended to smooth the films and avoid the appearance of diffraction features associated with the undesirable α phase. Post-growth characterization by XRD, however, revealed the presence of the α phase, which was not consistent with the RHEED pattern. AFM images of the film revealed the presence of some small rectangular clusters on a surface with a different characteristic morphology as shown in Figure 3.1. The rectangular shape is consistent with the orthorhombic α phase suggesting that the surface may contain a minority α phase.
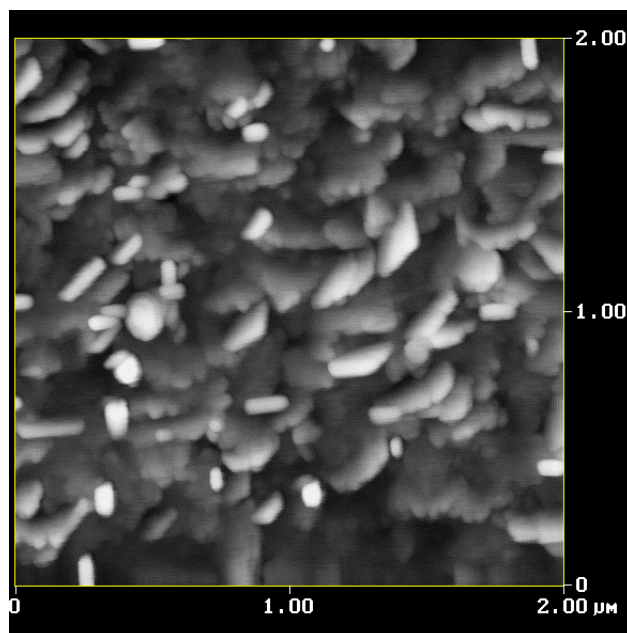
Figure 3.1. Contact AFM image of epitaxial MoO_3 film grown on $SrLaAlO_4$(001).

At Yale, we have been working on characterizing the films with low-energy electron diffraction (LEED) to complement the RHEED work, and on determining the local structure of the films using atomic resolution scanning tunneling microscopy (STM). Some of the results obtained thus far are shown in Figure 3.2. The square symmetry of the LEED pattern in Figure 3.2a is consistent with the RHEED results and again suggests that most of the surface may be in the β phase. The extra spots in the pattern are associated with surface faceting. The STM image in Figure 3.2b shows a large square terrace on the surface raised by a multi-atom height step above the rest of the surface. The image in Figure 3.2c highlights the area to the right of the cluster and shows a single-atom-high step. The step height is ~4 Å, which is the expected height for β-MoO_3 (001) but much less than the α step height of >12 Å. Again, this result is consistent with the surface exposing the β phase. We are now working on obtaining lateral atomic-resolution images to confirm the structure. We will soon start working on characterizing the surface chemistry of the material.
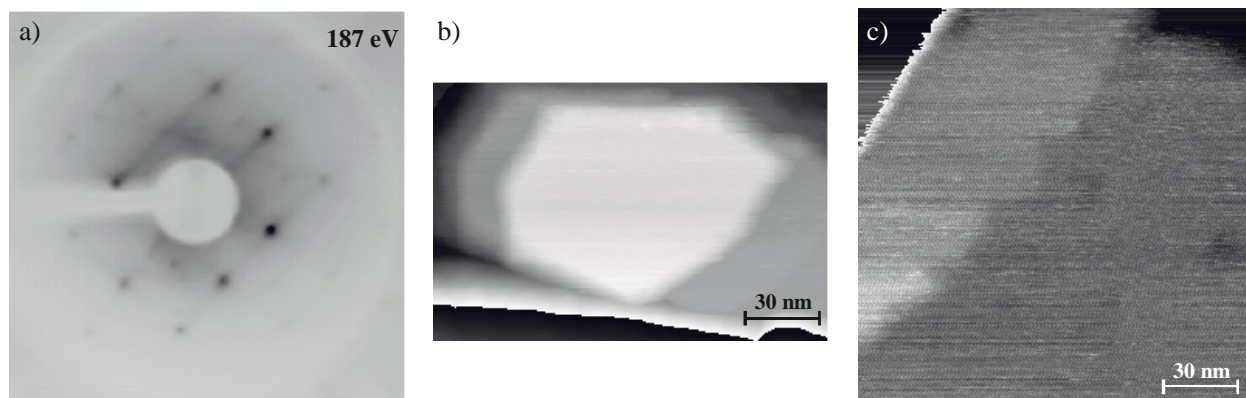
Figure 3.2. (a) LEED pattern obtained for the epitaxial MoO_3 grown on $LaSrAlO_4$(001). (b) Wide-range STM image of the film showing a large, flat terrace and multi-atom-high steps. (c) Higher resolution STM image of the lower terrace in (b). In this image, the step height is ~4 Å, which closely matches that expected for β-MoO_3(001).

MBE Growth and Magnetic Properties of Epitaxial Co Ferrite on MgO(001)

R. F. C. Farrow[a,b], *L. Folks*[a],
M. Toney[a]*, and S. A. Chambers*

Supported by IBM Internal Research and
Development funding.
(a) IBM Almaden Research Center, San Jose, CA.
(b) EMSL User.

For the first time, we have grown stoichiometric thin ($\leq$ ~100 nm) epitaxial films of cobalt ferrite ($Co_1Fe_2O_4$) on MgO(001) by oxygen-plasma-assisted molecular beam epitaxy (OPA-MBE). This material is of considerable interest to the magnetics community because of its superior magnetic properties, which include high magnetic anisotropy and magneto-striction and low conductivity and eddy currents. In bulk $CoFe_2O_4$, Co assumes a +2 formal oxidation state. Ideally, Co^{+2} would occupy octahedral sites, resulting in a perfect inverse spinel structure. How-ever, the high density of interstitial sites in the spinel lattice makes possible cation migration, which has been shown to result in variations in the magnetic properties (Sawatzky et al. 1968, 1969). $CoFe_2O_4$ is of significant interest because of its very high magnetocrystalline anisotropy relative to other magne-tic spinels (~20 and ~30 times larger than that of Fe_3O_4 and $NiFe_2O_4$, respectively). The origin of the unusually high magnetic anisotropy in $CoFe_2O_4$ has to do with the magnetic properties of Co itself, in addi-tion to the crystalline environment of the spinel lattice. In contrast to Fe and Ni, Co has a large unquenched orbital magnetic moment, which enhances its magne-tic properties in all crystals, including the pure metal. In addition, the orbital moment is especially enhanced when Co^{+2} is placed at octrahedral sites in Fe_3O_4. Years ago, Slonczewski (Slonczewski 1958) success-fully developed a model to explain this behavior in terms of the interaction of an isolated Co ion with the local molecular field at cation sites in Fe_3O_4. Later, Tachiki (Tachiki 1960) predicted the magnetic anisotropy of $Co_xFe_{3-x}O_4$ alloys for x up to 1 by con-sidering the change in symmetry of the crystal field brought about by Co substitution for Fe. The magne-tic anisotropy of $CoFe_2O_4$ is further altered and enhanced by strain fields when the material is grown as an epitaxial film. Suzuki and coworkers (Suzuki et al. 1996a,b, 1999; Gu et al. 2000) have used pulsed laser deposition to grow thick films of $CoFe_2O_4$ on a variety of substrates, resulting in various strain config-urations. These workers have found evidence for strain-dependent magnetic anisotropy.

We have also found clear evidence for strain-dependent magnetic anisotropy. High-resolution, core-level measurements for these films reveal that all Co is in the +2 formal oxidation state, as shown in Figure 3.3. We are currently conducting EXAFS measurements at Stanford Synchrotron Radiation Laboratory in collaboration with Professor Gordon Brown, Jr. of Stanford University to determine the site occupancy (tetrahedral, octahedral, or interstitial) for Co^{+2} in the spinel lattice. The lattice mismatch is -0.38% for this system. Very recent results for two of our films of different thickness reveal a strong correla-tion between strain, as measured by XRD, and
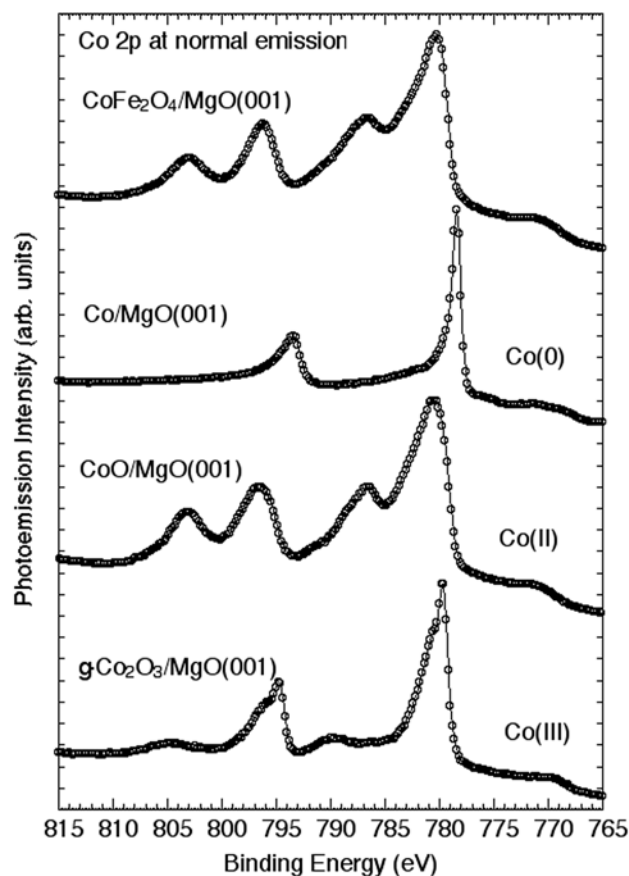
Figure 3.3. Co 2p photoemission spectra for MBE grown $CoFe_2O_4(001)$ on MgO(001), along with appropriate standards, also grown as epitaxial films. A comparison of the line shapes reveals that Co is in the +2 form oxidation state in $CoFe_2O_4$.

magnetic anisotropy, as measured by the magneto-optic Kerr effect (MOKE) and SQUID. A 55-nm-thick film was found to be partially strained, with (a_{film} - a_{bulk})/a_{bulk} = +0.29% and c/a – 1 = -0.6%. MOKE and SQUID measurements revealed a substantial out-of-plane component to the magnetic moment. In contrast, a 110-nm-thick film was either fully relaxed or slightly *compressively* strained [(a_{film} - a_{bulk})/a_{bulk} = -0.05% and c/a – 1 = +1.1%] and exhibited a moment that was oriented entirely in plane, with the easy axis oriented along [100].

References

Hu, G., J. H. Choi, C. B. Eom, V. G. Harris, and Y. Suzuki, *Phys. Rev.* **B62**, R779 (2000).

Sawatzky, G. A., F. van der Woude, and A. H. Morrish, *J. Appl. Phys.* **39**, 1204 (1968).

Sawatzky, G. A., F. van der Woude, and A. H. Morrish, *Phys. Rev.* **187**, 747 (1969).

Slonczewski, J. C., *Phys. Rev.* **110**, 1341 (1958).

Suzuki, Y., G. Hu, R. B. van Dover, and R. J. Cava, *J. Mag. Mag. Matl.* **191**, 1 (1999).

Suzuki, Y., R. B. van Dover, E. M. Gyorgy, J. M. Phillips, V. Koreinvski, D. J. Werder, C. H. Chen, R. J. Cava, J. J. Krajewski, W. F. Peck, Jr. and K. B. Do, *Appl. Phys. Lett.* **68**, 714 (1996).

Suzuki, Y., R. B. van Dover, E. M. Gyorgy, J. M. Phillips and R. J. Felder, *Phys. Rev.* **B53**, 14016 (1996).

Tachiki, M., *Progr. Theoret. Phys.* (Kyoto) **23**, 1055 (1960).

Channeling Study of Barium Titanate Irradiated with Au²⁺ Ions

W. Jiang[a,b], W. J. Weber[a,c], and S. Thevuthasan

Supported by the U.S. Department of Energy, Office of Basic Energy Sciences.
(a) EMSL User.
(b) Postdoctoral Research Fellow.
(c) PNNL Energy Science and Technology Division.

Barium titanate ($BaTiO_3$) has been studied for extensive applications, including the fabrication of ferroelectric, dielectric, semiconducting, and optical devices. Recent investigations of irradiation effects on $BaTiO_3$ have focused on the thermal phase transitions and the temperature dependence of the amorphization dose (Meldrum et al. 1998; Weber et al. 2000), as well as the damage accumulation and recovery (Jiang et al. 2000a). In this study, both ion irradiation and ion-beam analysis have been performed within the EMSL. Single-crystal $BaTiO_3$ wafers were cut and polished along the (110) plane. The samples were irradiated 60° off normal with 1 MeV Au^{2+} ions over fluences ranging from 0.03 to 0.19 ions/nm^2 at 170 and 300 K. The disorder has been analyzed using 2 MeV He^+ Rutherford backscattering spectrometry in channeling geometry (RBS/C). Isochronal annealing experiments (20 min) have been carried out in the temperature range from 300 to 870 K for the irradiated specimens.

A sequence of *in situ* RBS/C spectra for $BaTiO_3$ irradiated at 170 K is shown in Figure 3.4. A random spectrum corresponds to the backscattering yield for amorphous $BaTiO_3$. The high yield of the virgin spectrum indicates that there is measurable pre-existing damage in the near-surface region. This damage overlaps the disorder profiles produced by the Au^{2+} ions, and hinders the determination of the irradiation-induced disorder at the damage peak (~36 nm or channel 896 for Ba). To minimize this interference, disorder on both the Ba and Ti sublattices has been evaluated at a depth of 47 nm (channel 890 for Ba), where the pre-existing damage is relatively low. Since oxygen damage is not
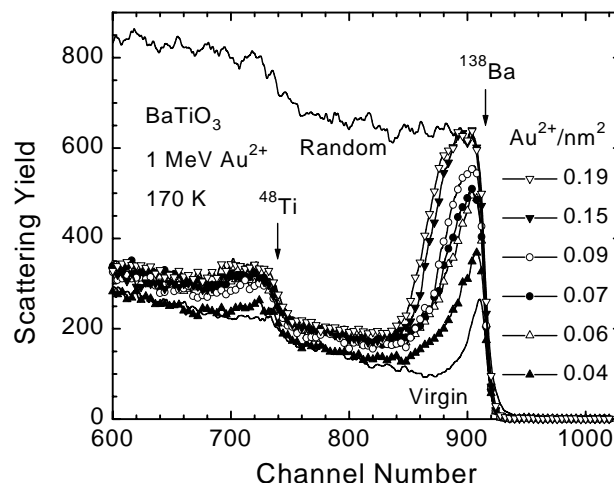
Figure 3.4. A sequence of *in situ* 2 MeV He⁺ RBS/channeling spectra for <110>-oriented $BaTiO_3$ wafers irradiated at 170 K with Au^{2+} ions. Also included are random-equivalent and channeling spectra from a virgin area.

resolvable, it has not been included in the spectra shown. At 0.15 and 0.19 Au^{2+}/nm^2, it appears that a continuous amorphous layer originating at the surface is produced.

The accumulated disorder, at a depth of 47 nm, on the Ba and Ti sublattices is shown in Figure 3.5 as a function of dose in displacements per atom (dpa) for $BaTiO_3$ irradiated at 170 and 300 K. The pre-existing damage is on the order of 0.1 (full amorphization corresponds to 1). The results at 170 and 300 K are indistinguishable within the experimental error (~10%), indicating a low rate of dynamic recovery during irradiation at room temperature. These data are consistent with previous results obtained using *in situ* transmission electron microscopy (TEM) (Meldrum et al. 1998; Weber et al. 2000), but are in contrast to results for GaN (Jiang et al. 2000b) and SiC (Jiang et al. 2000c), where significant shifts to higher doses were observed at room temperature. From Figure 3.5, the amorphization dose at 170 and 300 K is nearly the same and is equal to ~0.5 dpa. This amorphization dose is in good agreement with that determined by *in situ* TEM (Meldrum et al. 1998; Weber et al. 2000). Compared with the similarly structured $SrTiO_3$, where the amorphization dose under similar conditions is on the order of 1 dpa (Weber et al. 2000), $BaTiO_3$ shows a slightly lower radiation resistance.
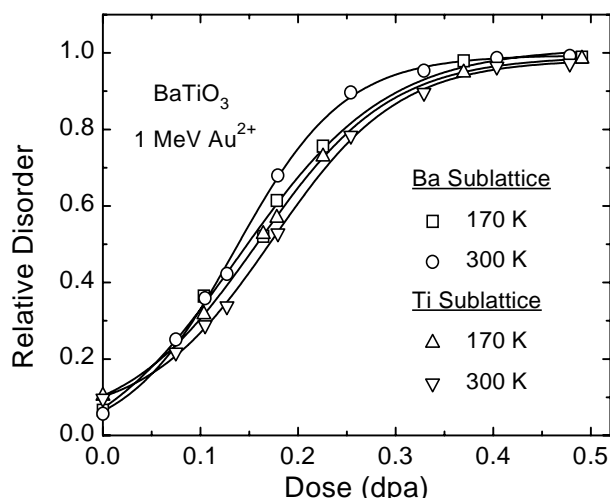
Figure 3.5. Relative disorder as a function of dose (dpa) at a depth of 47 nm (damage peak is located at 36 nm) for 1-MeV Au^{2+} irradiated $BaTiO_3$ at 170 and 300 K. Sigmoidal fitting lines are intended to aid the eye.

The isochronal annealing results for the irradiated $BaTiO_3$ are shown in Figure 3.6. Similar recovery on the Ba and Ti sublattices is observed. Since significant recovery occurs below 300 K at the lowest fluence (0.06 Au^{2+}/nm^2), but does not occur until above 300 K at a slightly higher fluence (0.07 Au^{2+}/nm^2), two separate recovery stages (A and B)
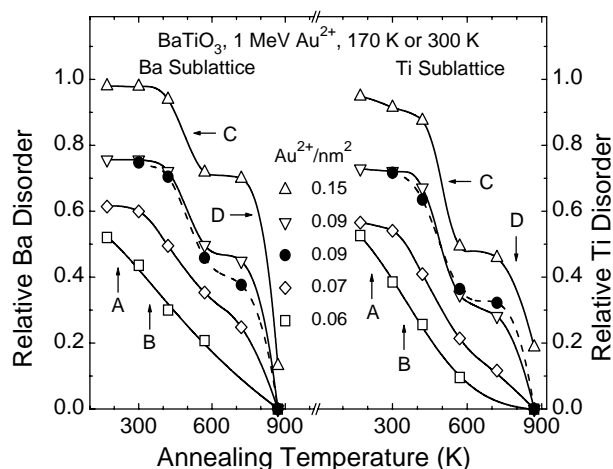
Figure 3.6. Isochronal recovery (20 min) of relative disorder in Au^{2+}-irradiated $BaTiO_3$ as a function of annealing temperature. Open and filled symbols are for samples irradiated at 170 and 300 K, respectively.

are expected to be active between 170 and 420 K, which are not resolvable due to the large temperature increment (150 K) used in this study. The recovery below room temperature suggests that some irradiation-induced defects in $BaTiO_3$ are mobile at these low temperatures. For fluences below 0.09 Au^{2+}/nm^2, complete recovery of the irradiation-induced disorder is achieved by annealing at 870 K. This recovery process also fully removes the pre-existing damage at the selected analysis depth (~47 nm). In addition, two distinct recovery stages (C and D) are observed on both the Ba and Ti sublattices in Figure 3.6. The recovery processes in stage C between 420 and 570 K are believed to be associated with the recovery of defects or defect complexes, which gives rise to the critical temperature for amorphization (550 K) observed in $BaTiO_3$ (Meldrum et al. 1998; Weber et al. 2000). Recovery stage D between 720 and 870 K may be associated with thermal epitaxial recrystallization processes (Jiang et al. 2000a).

References

Jiang, W., W. J. Weber, and S. Thevuthasan, "Damage Accumulation and Recovery in Gold-Ion-Irradiated Barium Titanate", *Nucl. Instr. and Meth. B* (2000a), in press.

Jiang, W., W. J. Weber, and S. Thevuthasan, "In Situ Ion Channeling Study of Gallium Disorder and Gold Profiles in Au-Implanted GaN", *J. Appl. Phys.* **87,** 7671 (2000b).

Jiang, W., W. J. Weber, S. Thevuthasan, and V. Shutthanandan, "Accumulation and Recovery of Disorder on Silicon and Carbon Sublattices in Ion-Irradiated 6H-SiC", *J. Nucl. Mater.* (2000c), in press.

Meldrum, A., L. A. Boatner, and R. C. Ewing, "Effects of Ionizing and Displacive Irradiation on Several Perovskite-Structure Oxides", *Nucl. Instr. and Meth.* **B 141,** 347 (1998).

Weber, W. J., W. Jiang, S. Thevuthasan, and R. E. Williford, "Ion-Beam-Induced Defects and Defect Interactions in Perovskite-Structure Titanates", in *Defects and Surface-Induced Effects in Advanced Perovskites,* G. Borstel, A. Krumins, and D. Millers (eds.), NATO Science Series, Kluwer Academic Publishers, p. 317 (2000).

Disorder Accumulation and Implant Migration in Au²⁺-Irradiated GaN

W. Jiang[a], W. J. Weber[a,b], and S. Thevuthasan

Supported by the U.S. Department of Energy, Office of Basic Energy Sciences.
(a) Postdoctoral Research Fellow.
(b) PNNL Energy Science and Technology Division.

Considerable effort has been devoted recently to the study of gallium nitride (GaN) and related materials worldwide, primarily because of their potential for applications in advanced electronics and opto-electronics. Ion implantation is a crucial process in the device fabrication. A fundamental understanding of implantation damage and dopant behavior in GaN is important to effectively utilize the technique. In this study, GaN single-crystal films (~2-μm thick) on sapphire were irradiated 60° off surface normal at either 180 or 300 K with 1 MeV Au²⁺ ions. Typical fluxes were on the order of 10^{12} Au²⁺/cm²/sec with fluences ranging from 0.4 to 53.8 ions/nm². The disorder on the Ga sublattice and depth profiles of Au implants in GaN were analyzed within the EMSL using *in situ* 2 MeV He⁺ Rutherford backscattering spectrometry in <0001>-axial channeling (RBS/C) direction and random geometry, respectively. *In situ* annealing experiments were performed at 870 K for 20 min, and a similar ion beam analysis was conducted for the annealed samples. Further experimental conditions and procedures for the data analysis have been described elsewhere (Jiang et al. 2000a). The equivalent dose in displacements per atom (dpa) at the damage peak has been evaluated based on the SRIM97 simulations under the assumptions of a threshold displacement energy of 25 eV for both Ga and N sublattices.

A sequence of *in situ* RBS/C spectra for GaN irradiated at 300 K to various Au²⁺ fluences are shown in Figure 3.7, along with random and <0001>-aligned virgin spectra. The Au spectrum (not shown) appears in a background-free region that is well resolved from the Ga signals (Jiang et al. 2000a). The random spectrum is equivalent to that for completely amorphized GaN, while the virgin spectrum corresponds to that for an essentially damage-free crystal. Data in Figure 3.7 indicate that there is a preferential accumulation of
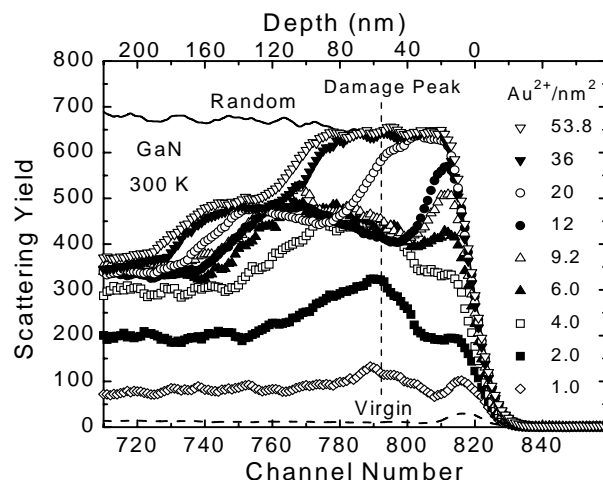
Figure 3.7. A sequence of 2-MeV He⁺ RBS/C spectra taken *in situ* for a <0001>-oriented GaN film (~2-μm thick) on sapphire irradiated 60° off surface normal with 1-MeV Au²⁺ ions at 300 K. Also included are random and <0001>-aligned spectra taken at 300 K from a virgin area.

Ga disorder in the near-surface region. Full amorphization first starts at surface and then extends to the deeper region with the increase of dose. A similar result has been reported for GaN irradiated at 77 and 300 K (Kucheyev et al. 2000). This unusual behavior is attributed to the high mobility of defects in GaN that results in substantial dynamic defect recovery at the damage peak and considerable defect migration into the surface region where the defects are trapped.

The dose dependence of the relative Ga disorder at the damage peak in Au²⁺-irradiated GaN is shown in Figure 3.8. Full amorphization (180 K) occurs at ~10 dpa. This value is about 30 times higher than for SiC under similar irradiation conditions (Jiang et al. 2000b). The damage accumulation at 300 K exhibits four distinct stages. There is a gradual accumulation of disorder below a dose of ~1.0 dpa, followed by a rapid increase in disorder at doses up to ~6 dpa. An intermediate saturation stage emerges at a disorder level of ~0.6 for doses between ~6 and ~20 dpa, and finally a rapid amorphization process occurs at higher doses. Note that the full amorphization at the damage peak is due to the extension of the amorphous surface layer, as discussed above. Also included in Figure 3.8 are the results (Jiang et al. 2000a; Jiang et al. 1999) for GaN irradiated at ~200 K with O⁺ ions, which show a similar saturation level over a comparable dose range. Recent TEM results
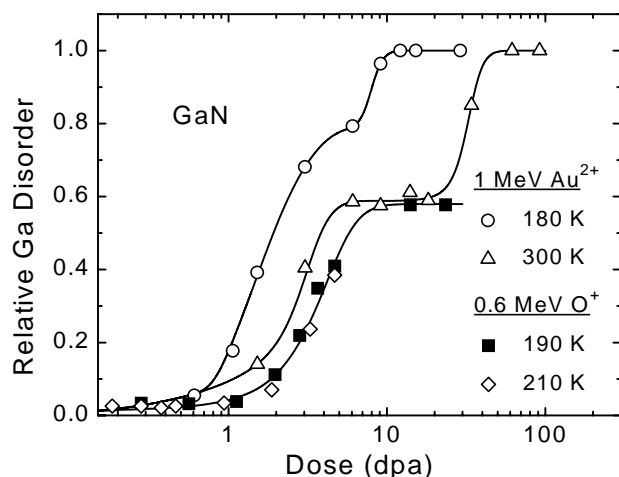
Figure 3.8. Relative Ga disorder at the damage peak as a function of dose for Au^{2+} irradiated GaN at 180 and 300 K. Also included are the data for 0.6-MeV O^+ irradiated GaN at 190 and 210 K.

for C^+- and Au^+-implanted GaN indicate that the formation of point-defect clusters and planar defects is associated with this saturation regime (Kucheyev 2000).

Figure 3.9 shows the depth profiles of Au atoms in GaN irradiated to 20 Au^{2+}/nm^2 at 300 K and annealed
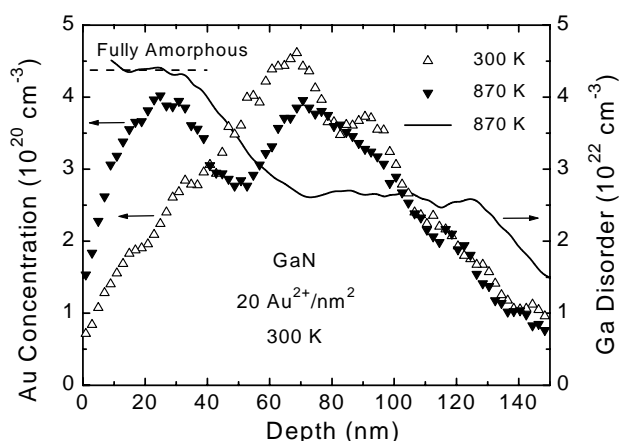
Figure 3.9. Depth profiles of Au atoms implanted into GaN at 300 K to 20 Au^{2+}/nm^2 and after annealing at 870 K for 20 min. Also included is the depth profile of Ga disorder in the annealed GaN.

at 870 K for 20 min. Also included in Figure 3.9 is the Ga disorder profile in the annealed sample, which shows two steps consisting of an amorphous state near the surface and a disorder saturation state at depths from 70 to 120 nm. The as-implanted Au profile exhibits two closely-spaced peaks; the larger one corresponds to the predicted peak in the implant profile. After annealing at 870 K, the Au profile evolves into a well-defined, double-peak structure. One maximum is located in the amorphous surface region (~30 nm), and the other is located near the mean projected range (~66 nm) for the Au. This result suggests that some Au readily diffuses into the amorphous surface region. The remaining Au is trapped in the damaged crystal structure. This behavior is not very surprising because the Au concentration is relatively small (< 2%) compared to the number of Ga defects in the damaged region (Figure 3.9). Thus, the Au may readily recombine with Ga vacancies to form substitutional atoms, similar to behavior observed for Hf^+ implanted GaN (Alves et al. 1999).

References

Alves, E., M. F. da Silva, J. G. Marques, J. C. Soares, and K. Freitag, "Annealing Behavior and Lattice Site Location of Hf Implanted GaN", *Mater. Sci. Eng. **B** 59*, 207 (1999).

Jiang, W., W. J. Weber, and S. Thevuthasan, "*In Situ* Ion Channeling Study of Gallium Disorder and Gold Profiles in Au-Implanted GaN", *J. Appl. Phys.* **87,** 7671 (2000a).

Jiang, W., W. J. Weber, S. Thevuthasan, and V. Shutthanandan, "Accumulation and Recovery of Disorder on Silicon and Carbon Sublattices in Ion-Irradiated 6H-SiC", *J. Nucl. Mater.* (2000b).

Jiang, W., W. J. Weber, S. Thevuthasan, G. J. Exarhos, and B. J. Bozlee, "Effect of Oxygen Ion Implantation in Gallium Nitride", *Mat. Res. Soc. Symp. Proc.* **537,** G6.15.1 (1999).

Kucheyev, S., J. S. Williams, C. Jagadish, J. Zou, and G. Li, "Damage Buildup in GaN under Ion Bombardment", *Phys. Rev. **B** 62,* 7510 (2000).

Disordering and Annealing Processes in Ion-Irradiated 6H-SiC

*W. Jiang[a,b], W. J. Weber[a,c], S. Thevuthasan, and V. Shutthanandan*

Supported by the U.S. Department of Energy, Office of Basic Energy Sciences.
(a) EMSL User.
(b) Postdoctoral Research Fellow.
(c) PNNL Energy Science and Technology Division.

Because of its outstanding properties, silicon carbide (SiC) is a promising candidate material for advanced electronic devices and a variety of nuclear applications. A fundamental understanding of the accumulation and recovery of irradiation-induced damage in SiC is needed to advance its technological applications. In this paper, irradiation experiments on the <0001>-oriented 6H-SiC were performed 60° off surface normal using 2 MeV Au^{2+} over a fluence range from 0.02 to 0.8 ions/nm^2 at 170 and 300 K. The low-energy (50 keV) He^+ irradiation was conducted close to the surface normal and over fluences ranging from 7.5 to 200 ions/nm^2 at 100 and 300 K. Both *in situ* and *ex situ* analyses of disorder in the Au^{2+}- and He^+-irradiated specimens, respectively, have been carried out in the EMSL. Simultaneous determination of disorder on the Si and C sublattices has been achieved based on the 0.94 MeV D^+ Rutherford backscattering spectrometry (RBS) and nuclear reaction analysis (NRA) in channeling geometry (Jiang et al. 2000). *In situ* isochronal annealing (20 min) was used for the Au^{2+}- and He^+-irradiated SiC in a range of temperatures. The ion fluence has been converted to an equivalent dose in units of displacements per atom (dpa) at the damage peak using SRIM-97 simulations under the assumption of threshold displacement energies of 20 eV and 35 eV for the C and Si sublattices, respectively (Devanathan and Weber 2000).

A series of *in situ* channeling spectra for 6H-SiC irradiated with 2 MeV Au^{2+} at 170 K to various ion fluences are shown in Figure 3.10. Also included in Figure 3.10 are random and <0001>-aligned spectra from a virgin area, which respectively define the upper and lower levels of the scattering yields from the amorphous and essentially defect-free SiC
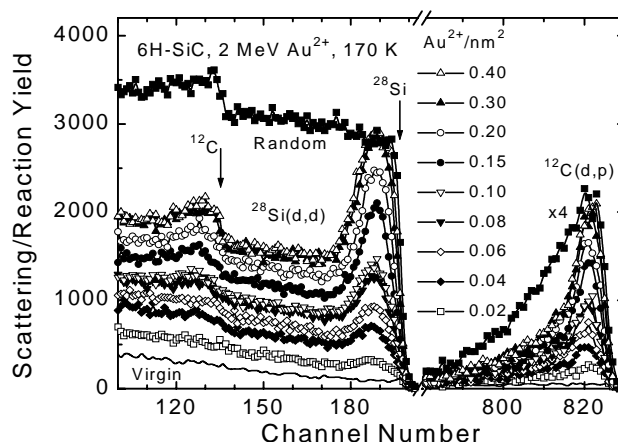
Figure 3.10. A sequence of *in situ* 0.94-MeV D^+ RBS and NRA channeling spectra for <0001>-oriented 6H-SiC wafers irradiated 60° off surface normal at 170 K with 2.0-MeV Au^{2+} ions. Also included are random-equivalent and channeling spectra from a virgin area.

materials. From Figure 3.10, the Si damage peaks for the irradiated specimens are readily measurable from the D^+ RBS channeling. There are also spectra for the C sublattice that arise from $^{12}C(d,p)$ reaction and are well resolved from the RBS spectra. This condition allows simultaneous analysis of disorder on the Si and C sublattices from one experiment.

The accumulated disorder at the damage peak for both the Si and C sublattices is shown in Figure 3.11 as a function of dose (dpa) for 6H-SiC irradiated with Au^{2+} at 170 and 300 K and with He^+ at 100 and
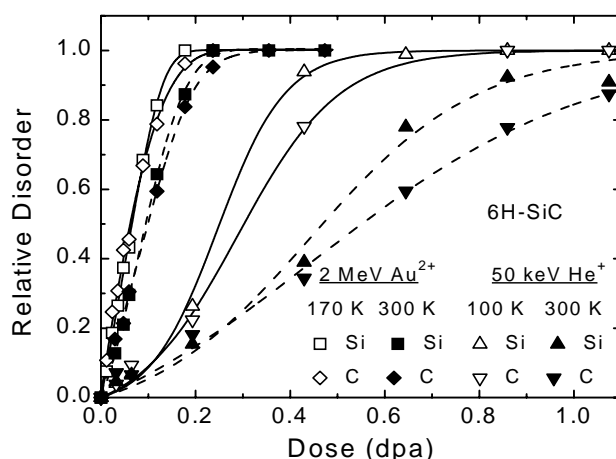
Figure 3.11. Relative disorder as a function of dose at the damage peak for Au^{2+}-irradiated 6H-SiC at 170 and 300 K and He^+-irradiated 6H-SiC at 100 and 300 K.

300 K. From Figure 3.11, the 6H-SiC becomes fully amorphous at ~0.85 dpa under He$^+$ irradiation at 100 K and at ~0.24 dpa under Au^{2+} irradiation at 170 K, which indicates an increasing rate of disordering with increasing ion mass. For both the Au^{2+} and He$^+$ irradiations, the C disorder is slightly higher at low doses (Jiang et al. 2000). This behavior is consistent with a smaller threshold displacement energy on the C sublattice, as reported for molecular dynamics (MD) simulations (Devanathan and Weber 2000) and other experimental measurements (Gao et al. 2000). At higher doses, the residual disorder on the Si sublattice appears to be in excess of that on the C sublattice, suggesting that a slightly higher recovery rate may be occurring on the C sublattice than on the Si sublattice. Irradiation with Au^{2+} and He$^+$ at 300 K indicates that the rate of disordering has decreased with the increase in irradiation temperature for both the Au^{2+} and He$^+$. From Figure 3.11, the amorphization dose at 300 K increases to ~0.35 dpa and > 1.1 dpa for the Au^{2+} and He$^+$, respectively. This decrease in disordering rate is primarily attributed to a higher dynamic recovery rate at the higher irradiation temperature (300 K).

The isochronal annealing results for SiC irradiated at 170 K with Au^{2+} are shown in Figure 3.12 and exhibit similar recovery behavior on the Si and C
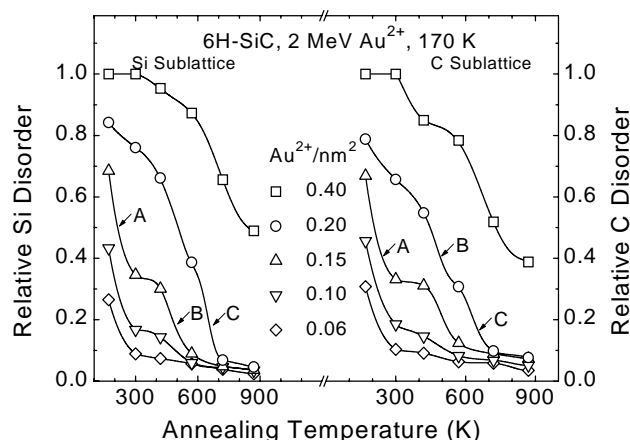
sublattices. Significant recovery processes on both the sublattices occur below room temperature (Stage A), between 420 and 570 K (Stage B), and above 570 K (Stage C). The activation energies for stages A, B, and C on the Si sublattice have been estimated (Weber et al. 2000) to be on the order of 0.3 ± 0.15 eV, 1.3 ± 0.25 eV, and 1.5 ± 0.3 eV, respectively. A complete recovery of disorder is not observed on either the Si or C sublattices for anneals up to 870 K. This may be attributed to the cluster formation and in-cascade amorphization in Au^{2+}-irradiated SiC, as suggested by recent MD simulations (Gao et al. 2000). The clusters and amorphous domains are expected to be relatively stable up to ~1300 K (Snead et al. 1998). Similar thermal recovery behavior was also observed on the Si and C sublattices in He$^+$-irradiated 6H-SiC at ~100 K, where distinct recovery stages are not apparent partly due to the He trapping at defects that inhibit defect migration and recombination (Jiang et al. 2000).

References

Devanathan, R. and W. J. Weber, "Displacement Energy Surface in 3C and 6H SiC", *J. Nucl. Mater.* **278,** 258 (2000).

Gao, F., W. J. Weber, and W. Jiang, "The Primary Damage States Produced by Si and Au Recoils in SiC: A Molecular Dynamics and Experimental Investigation", *Phys. Rev. B* (2000), submitted.

Jiang, W., W. J. Weber, S. Thevuthasan, and V. Shutthanandan, "Accumulation and Recovery of Disorder on Silicon and Carbon Sublattices in Ion-Irradiated 6H-SiC", *J. Nucl. Mater.* (2000), in press.

Snead, L. L., S. J. Zinkle, J. C. Hay, and M. C. Osborne, "Amorphization of SiC under Ion and Neutron Irradiation", *Nucl. Instr. and Meth. B* **141,** 123 (1998).

Weber, W. J., W. Jiang, and S. Thevuthasan, "Accumulation, Dynamic Annealing and Thermal Recovery of Ion-Beam-Induced Disorder in Silicon Carbide", *Nucl. Instr. and Meth. B* (2000), in press.

Zinkle, S. J. and C. Kinoshita, "Defect Production in Ceramics", *J. Nucl. Mater.* **251,** 200 (1997).

Figure 3.12. Isochronal recovery (20 min) of relative disorder on the Si and C sublattices in Au^{2+}-irradiated 6H-SiC as a function of annealing temperature.

Characterization of Low Temperature Buffer Layer Deposition of GaN Thin Films Using Low Pressure MOCVD

M. C. Johnson[a,b], K. Poochinda[a,b], and N. L. Ricker[c]

In the last decade there has been considerable research in the production and characterization of the III-nitrides. This recent emergence of interest in these nitride systems is due to their potential for producing surface acoustic wave devices, blue lasers, and light emitting diodes (LEDs). Past research of nitride growth was greatly hampered by the lack of a suitable bulk-crystal technology for producing GaN substrates. Epitaxy was performed on highly lattice and thermal-expansion mismatched substrates such as silicon, GaAs, and sapphire. The resulting heteroepitaxial films were highly defective and highly conducting due to the defects and impurities.

In the late 1980s, the problems of lattice mismatch began to be overcome due to the efforts of Amano and coworkers (Amano et al. 1986). The use of thin AlN and GaN low-temperature buffer layers facilitated the growth of high-quality GaN films, specular and free of cracks, on sapphire substrates using MOCVD. As a result of these findings, nitride research has exponentially progressed since the early 1990s with the demonstration and commercialization of high-brightness blue and green double heterostructure and single quantum well LEDs, as well as the first blue and violet continuous wave laser diodes.

Our research involves the low-temperature deposition of AlN and GaN layers on Si(100) substrates. AlN and GaN layers are grown using an MOCVD reactor (Crystal Specialities 425) at different operating conditions. These layers are then characterized using Auger electron spectroscopy (AES), scanning electron microscopy (SEM), and x-ray diffraction (XRD). By characterizing the films grown at different conditions, knowledge will be gained for growing low-temperature layers for different systems and their alloys that can be utilized for buffer-layer deposition. AES was used to give compositional and thickness information for each film. A survey was first taken to give surface composition. Then the film was sputtered for a short duration using an Argon sputtering gun, and AES was performed again to give the resulting compositional make-up at that depth. This process was repeated until a complete depth profile was gained. From this, a growth rate (μm/h) and a growth efficiency (μm/μmole reactant) could be determined. Figure 3.13 shows a common depth profile using AES for an AlGaN compound.
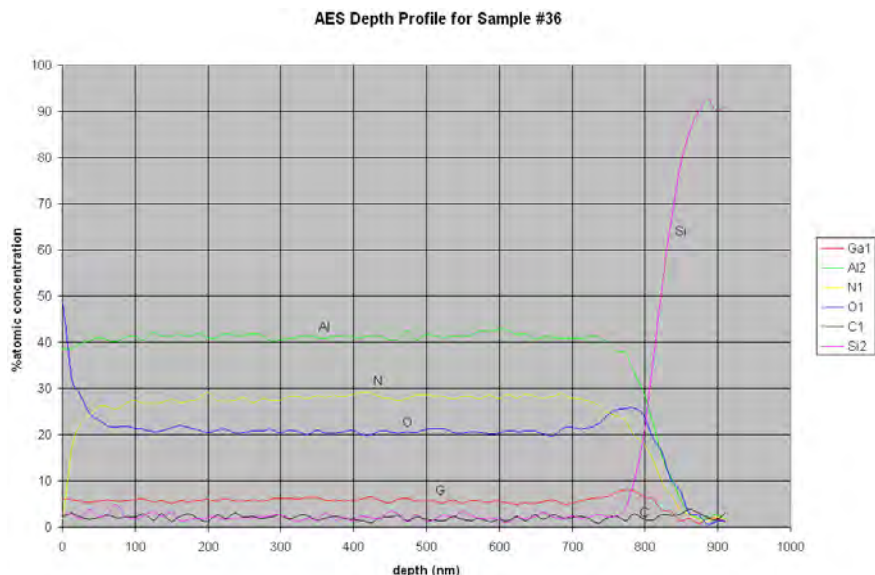
Figure 3.13. AES depth profile for AlGaN thin film grown at 475 $^{\circ}$ C and 200Torr.
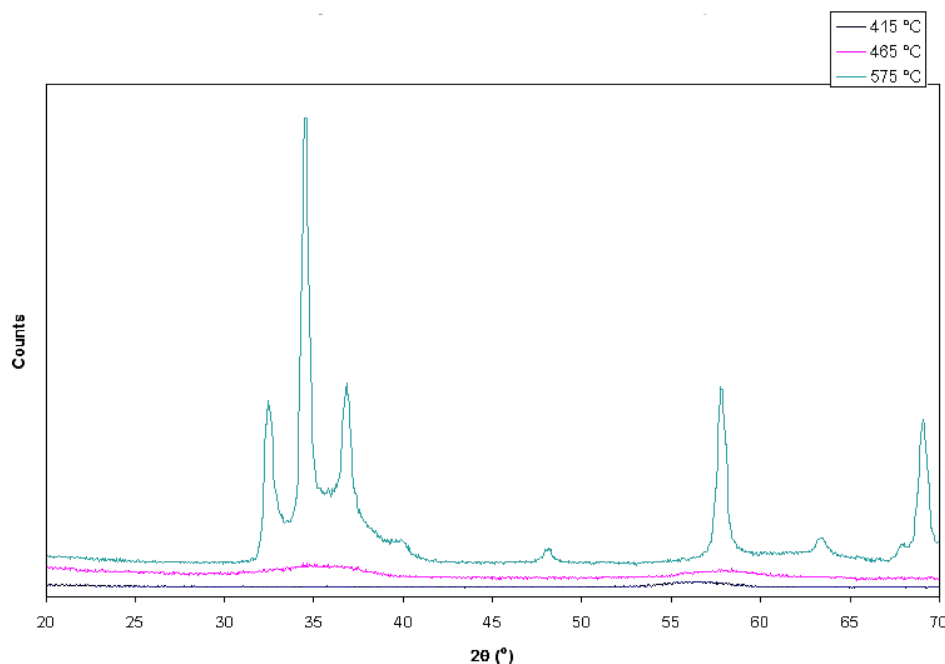
Figure 3.14. Comparison of XRD θ-2θ for increasing temperature for GaN.

We found that this film had a large amount of oxygen impurity, caused by a large amount of water from the carrier gas (H_2) due to improper purification from old equipment.

The GaN films also were analyzed using XRD to determine the effect of growth temperature on crystal structure. The Philips X'Pert MPD was set up for phase identification of polycrystalline thin films. The radiation used was Cu Kα. The 2θ scans were carried out with a fixed incidence angle, θ, of 5°. The XRD θ-2θ scans are demonstrated in Figure 3.14. The intensity of the peaks increases with increasing temperature, which corresponds to better crystallinity. The GaN film grown at 415°C is essentially amorphous since the peaks are very broad. The GaN film grown at 465°C is polycrystalline with an average crystallite size of 2.5 nm, according to the Scherrer formula. The major peaks from the film grown at 575°C appear at 32.5, 34.7, 37.0, 48.3, 58.0, 63.7, 68.0, and 69.3 degrees. These peaks correspond to planes (100), (002), (101), (102), (110), (103), (200)

and (112) of wurtzite GaN, respectively. Thus, the film has the highly oriented polycrystalline wurtzite structure.

Gallium and nitrogen atoms need a high thermal energy for the arrangement of the surface atoms in order to form a continuously well-ordered structure. For example, single-crystal GaN is typically grown above 1000°C on sapphire under normal MOCVD growth conditions. Although Si (100) is a cubic substrate, which provides the compatibility for the growth of zincblende GaN, wurtzite GaN is the more thermodynamically stable phase. It is obvious that the geometrical effect cannot overcome the thermo-dynamic effect at these low temperatures.

Reference

Amano, H. et al., "Metalorganic Vapor Phase Epitaxial Growth of a High Quality GaN Film Using an AlN Buffer Layer", *Appl. Phys. Lett.,* **48**, p. 353 (1986).

Isotopic Labeling in the Dry Reforming of Methane

D. C. LaMont[a,b], A. S. Chellappa[a],
W. J. Thomson[a], and M. L. Balmer

Supported by funding from InnovaTek, Inc.
(a)   Washington State University.
(b)   EMSL User.

Molybdenum Carbide (Mo_2C) is known to be active for steam reforming, dry reforming, and partial oxidation (York et al. 1997a/b, Claridge et al. 1998). However, very little is known about the reaction mechanisms that prevail on these catalysts. For this reason, a preliminary isotopic study was carried out using dry reforming as a model reaction:

$$CH_4 + CO_2 \rightarrow 2CO + 2H_2$$
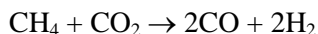
In this study, a synthesized sample of Mo_2C and a commercially available Mo_2C were compared under identical conditions. Both catalysts contained carbon in their bulk structure, and both catalysts had varying amounts of excess carbon on the surface. In addition, both feed gases contained carbon, so there existed within the system a total of four types of carbon to monitor during reforming. The method used in this study was to reform isotopically-labeled methane (99% $^{13}CH_4$) with standard CO_2. Mass spectrometry was used to quantitatively monitor and compare the gaseous ^{13}C- and ^{12}C-containing products leaving the system.

The results indicated that reforming was not the only reaction occurring at the tested conditions. Coking, as well as coke gasification by CO_2 and H_2, occurred at rates significant enough to alter the product distribution from what would be expected for reforming alone. Water gas shift was also observed, a result that has been observed elsewhere (Patt et al. 2000). Additionally, it is now believed that the bulk carbon in the carbide is essentially immobile, while the form and amount of excess carbon on the fresh catalyst heavily influences the behavior of both the CH_4 and the CO_2 at reforming conditions.

References

Claridge, J. B. et al., *J. Catal.*, **180**, 85-100 (1998).
Patt, J., D. J. Moon, C. Phillips, and L. Thompson, *Catal. Ltr.*, **65** 193-195 (2000).
York, A.P.E. et al., *Chem. Comm.*, **1**, 39-40 (1997a).
York, A.P.E. et al., 3rd World Congress on Oxidation Catalysis, R. K. Grasselli et al. Eds. *Elsevier*, 711-720 (1997b).

Interplay Between Interfacial Properties and Dielectric and Ferroelectric Behaviors of Barium Strontium Titanate Thin Films

D. Baer, S. Chambers, S. Gan[a], D. McCready, Y. Liang, V. Shutthanandan, S. Thevuthasan, Z. Yu[b,c], R. Droopad[b,c], J. Ramdani[b,c], and K. Eisenbeiser[b,c]

Supported by the U.S. Department of Energy LTR program.
(a) Postdoctoral Research Fellow.
(b) EMSL User.
(c) Motorola, Inc.

The objective of this project is to gain a fundamental understanding of how interfaces affect the dielectric and ferroelectric properties of barium strontium titanate ($Ba_{1-x}Sr_xTiO_3$ or BST) thin films, and to use such knowledge to improve the design and processing of BST thin-film-based devices. The project addresses two specific issues of significant concern in BST thin-film technology: 1) the effect of interfacial chemistry and stress on the dielectric and ferroelectric properties of BST thin films, and 2) ferroelectric behavior at the nano-scale level. Molecular beam epitaxy and several state-of-the-art surface and interface techniques have been used to synthesize and characterize the surface and interface of BST films, particularly during the initial stage of film growth. By linking the surface and interface properties to the performance of BST films, the interplay between interfacial properties and dielectric and ferroelectric behavior of BST thin films can be extracted.

1. Initial Stage of SrTiO₃ Growth on Si: Structural, Chemical, and Electronic Properties of Strontium Silicate on Si(001)

S. Gan, Y. Liang, V. Shutthanandan, and S. Thevuthasan

Recent work showed that crystalline oxides such as $SrTiO_3$ (STO) are promising as an alternative to SiO_2 in MOSFET. One of the most important issues in this approach is the interfacial template layer that needs to possess favorable structural and chemical properties for growth of crystalline STO on Si. Using scanning tunneling microscopy (STM), x-ray photoelectron spectroscopy (XPS), low-energy electron diffraction (LEED), and Rutherford backscattering (RBS), we investigated the interfacial structure of each strontium-based template grown on Si *in situ*. We found that, depending on the surface strontium coverage, the strontium-covered Si surfaces exhibited a series of reconstructions. These reconstructions not only had different atomic structures but also different stability against oxidation. For instance, upon exposure to oxygen, the (3x2) reconstruction was converted to a disordered (1x1) surface while the Sr/Si-(1x2) reconstruction remained intact. For the growth of oxides, the (1x2) structure was found to provide the most stable interface, as evidenced by a uniform layer in angular dependence XPS results, the lack of interfacial SiO_2 layer, and the ability to form single-crystal SrO films on this structure. By combining results obtained from STM, XPS, RBS, and LEED, we correlated the interface structures with film properties, which allowed us to identify suitable interfacial templates for optimized growth of STO.

2. Band Discontinuities at Epitaxial SrTiO₃/Si(001) Heterojunctions

S. A. Chambers, Y. Liang, D. McCready, Z. Yu, R. Droopad, J. Ramdani, and K. Eisenbeiser

We used photoemission methods to directly measure the valence and conduction band offsets at $SrTiO_3$/Si(001) interfaces, as prepared by molecular beam epitaxy. Within experimental error, the measured values are the same for growth on *n*- and *p*-Si, with nearly the entire discontinuity of 2.1 eV occurring at the valence band edge. In addition, we found that the amount of bending at the $SrTiO_3$/n-Si interface was approximately four times smaller than that at the $SrTiO_3$/p-Si interface. These results are summarized in Figure 3.15. The observed high (low) electron (hole) leakage currents and the asymmetry in drain current for CMOS devices with $SrTiO_3$ as gate oxides are now understood in light of these results (Chambers et al. 2000).
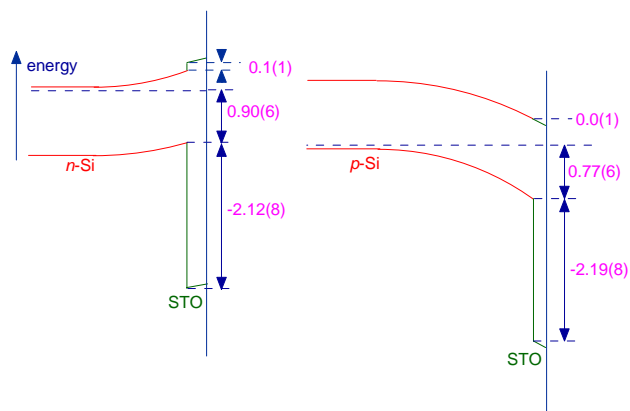
Figure 3.15. Valence and conduction band offsets at SrTiO₃/Si (001) interfaces.

3. Interface Analysis of SrTiO₃/Si Using High-Energy Ion Beam Methods

S. Thevuthasan, V. Shutthanandan, Y. Liang, Z. Yu, R. Droopad, J. Ramdani, and K. Eisenbeiser

RBS and high-energy ion channeling are powerful techniques for investigating film quality, defects,
interfacial structure, and stoichiometry of films. We used ion channeling to examine the crystallinity and interfacial structure of SrTiO₃/Si with different SrTiO₃ film thickness. High-energy ion channeling shows that SrTiO₃ films grown on Si substrates have very good crystallinity with approximately 3% minimum yield for both Sr and Ti. However, ion channeling also indicates a disordered silica layer at the interface of SrTiO₃/Si. Such a layer was likely formed due to a small amount of oxygen diffused across the SrTiO₃/Si interface that reacted with Si during the growth of the SrTiO₃ films. In addition, the thermal stability of SrTiO₃/Si under different annealing conditions (vacuum, oxygen, and hydrogen) also has been investigated using ion channeling. Results showed that an increased disordering associated with O and Sr occurred when SrTiO₃/Si systems were annealed in vacuum condition.

Reference

Chambers, S. A., Y. Liang, D. McCready, Z. Yu, R. Droopad, J. Ramdani, and K. Eisenbeiser, "Band discontinuities at epitaxial SrTiO₃/Si(001) heterojunctions", *App. Phys. Lett*. **77**, 1662 (2000).

Channeling Studies of CeO$_2$ and Ce$_{1-x}$Zr$_x$O$_2$ Films on Yttria-Stabilized ZrO$_2$(111)

V. Shutthanandan, S. Thevuthasan,
Y. J. Kim[a], and C. H. F. Peden

Supported by the U.S. Department of Energy Office of Basic Energy Sciences, and Taejon National University of Technology, South Korea.

(a) EMSL User, Taejon National University of Technology, South Korea.

Cerium oxide and Ce$_{1-x}$Zr$_x$O$_2$ have received much attention in the recent past because of their technological applications in novel metal/alumina-based automotive exhaust catalysts. Pure CeO$_2$ has the ability to store and release oxygen under reaction conditions, and its thermal stability, as well as its storage and release ability, can be tremendously improved by adding ZrO$_2$ into it. In addition, CeO$_2$ is an attractive candidate for high-dielectric materials on semiconductors because of its large band gap and high dielectric constant. Recently, several high-quality, well-oriented, single-crystal CeO$_2$ and Ce$_{1-x}$Zr$_x$O$_2$ films with various stoichiometries and thickness have been synthesized using molecular beam epitaxial (MBE) growth methods. The theme of the present work is to investigate the crystalline quality and nature of the film/substrate interface in CeO$_2$ and Ce$_{1-x}$Zr$_x$O$_2$ thin films grown on yttria-stabilized ZrO$_2$ substrates using Rutherford backscattering spectroscopy and channeling (RBS/C) techniques.

The samples were grown in the MBE facility at the EMSL. RBS and channeling measurements were carried out at a sample temperature close to 300 K using 2.04 MeV He$^+$ ions at normal incidence. The backscattering spectra were collected using a silicon surface barrier detector at a scattering angle of 150°. The SIMNRA program was used to simulate the experimental RBS spectra and determine the thickness and stoichiometry of the films.

In Figure 3.16, we present the channeling and random spectra of a pure CeO$_2$ film grown on yttria-stabilized ZrO$_2$(111). SIMNRA was used to simulate (solid line) the random spectrum of the film. The stoichiometry and thickness of the film were determined to be Ce:O=1:2 and 270 nm, respectively,
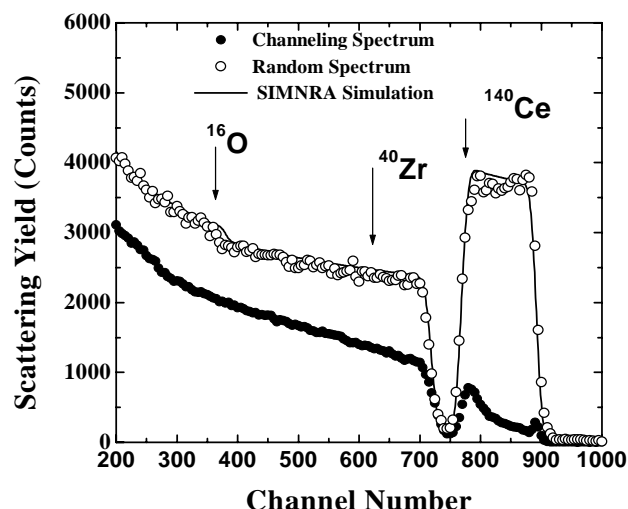
Figure 3.16. Channeling and random RBS spectra for an epitaxially-grown CeO$_2$ film on yttria-stabilized ZrO$_2$(111).

using SIMNRA simulation. The surface peak of the Ce is clearly visible in the channeling spectrum. A small energy window just behind the surface peak of Ce was used to calculate the minimum yield (χ_{min}) of Ce. Another small energy window near the substrate Zr edge was used to calculate the minimum yield for Zr in the substrate. The minimum yield is the ratio of the yield in the channeling geometry to that for a random geometry. A high crystalline quality of the film is evident from the 4.7% minimum yield, χ_{min}, obtained for Ce.

The second peak observed (low energy side of the signal related to Ce) in the channeling spectrum of the CeO$_2$ film is due to the disordering at the interface. Because of the strain associated with the lattice mismatch (5.3%), some Ce atoms at the interface appear to be slightly displaced from their lattice positions. These disordered Ce atoms from the Ce atomic rows are now visible to the incident ion beam since the ion beam is well aligned along the (111) direction of the film. When the interface layer exceeds some critical thickness, the strain associated with the lattice mismatch appears to be relieved somewhat and, as a result, the disorder seems to decrease, allowing a good quality single-crystal CeO$_2$ film to be grown. Because of this disorder at the interface and the high dechanneling in the film, the minimum yield (χ_{min} =52%) of Zr in the substrate is very high.

Figure 3.17 shows the channeling and random spectra for the $Ce_{1-x}Zr_xO_2$ film. As in the case of the CeO_2 film, this film also shows a good crystalline quality as evident from the channeling spectrum. For the film, χ_{min} for Ce is calculated to be 12.1%. This minimum yield is a little higher compared to the minimum yield calculated from the pure CeO_2 film. This increase may be due to the lattice distortion caused by the mismatch of the metal-oxygen bond lengths between Zr-O and Ce-O. The minimum yields for film and substrate Zr were determined to be 22.3% and 55%, respectively. As in the case of the pure CeO_2 film, the $Ce_{1-x}Zr_xO_2$ film also shows a significant amount of disorder at the interface as evident from the second peak in the Ce channeling spectrum. SIMNRA simulation was performed on the random spectrum and the film stoichiometry (Zr: Ce: O of 0.3:0.7:2) and film thickness (about 106 nm) were obtained.

The backscattering signal from the mixed Zr atoms in the $Ce_{1-x}Zr_xO_2$ film is very small in the channeling spectrum compared to the random spectrum, possibly due to the shadowing of Zr atoms by Ce atoms in the film. This observation indicates that Zr atoms in the film are mostly substituting for Ce atoms. Normalized angular yield curves shown in Figure 3.18 in the [111]

Figure 3.18. Angular yield curves with respect to [111] direction for Ce in the film, Zr in the film, and Zr in the substrate for $Ce_{1-x}Zr_xO_2$ film.

direction for Ce, Zr in the film, and Zr in the substrate are also consistent with the Zr substitution for Ce in the film. Again, the variation of yield as a function of polar angle is similar for both Ce and Zr in the substrate, and it is clear that the atomic rows of Ce in the film are parallel to the atomic rows of Zr in the substrate. In addition, the change of angular yields as a function of polar angles for Ce and Zr in the film is identical. For the first order, the fraction of dopant atoms incorporated in the substitutional sites in the film can be calculated from the following equation:

$$S=(1- \chi_{impurity})/(1-\chi_{host}) \qquad (1)$$

where S is the fractional substitution, $\chi_{impurity}$ is the minimum yield of the impurity or dopant atoms, and χ_{host} is the minimum yield of the host atoms. Using the values of χ_{min} obtained from the channeling measurements, the fraction of Zr substitution was calculated to be approximately 88%. This shows that about 88% of Zr atoms substitutionally occupy the cation sites in the CeO_2 lattice.

Figure 3.17. Channeling and random RBS spectra for an epitaxially-grown $Ce_{1-x}Zr_xO_2$ film on yttria-stabilized ZrO_2.

Hydrogen-Damage Interactions in Yttria-Stabilized Zirconia

V. Shutthanandan, S. Thevuthasan, J. S. Young, T. M. Orlando, and W. J. Weber[(a,b)]

Hydrogen embrittlement of Zr metals and Zr alloys has been extensively studied in the past, and it is believed that the hydrogen embrittlement in zirconium and its alloys occurs by penetration of hydrogen through the oxide films into the zirconium. As such, it is important to understand hydrogen uptake through the oxides especially in the presence of radiation. Radiation effects on Zr alloys using high-energy protons and neutrons have been studied in the past. Neutron irradiation studies suggest that there is a significant change in hydrogen uptake in Zr alloys due to the irradiation-induced microstructural change in the material. Irradiation causes partial or full amorphization of $Zr(Fe,Cr)_2$ and $Zr_2(Fe, Ni)$ precipitates in the protective oxide layer of zirconium alloys. Also, it is not clear whether the ion-cut process using hydrogen implantation and thermal treatment can be utilized in many other oxide single crystals to generate thin oxide films. Hence, understanding the cleavage of thin films in yttria-stabilized zirconia single-crystals is an additional benefit of this study.

The current study investigates the effects of hydrogen implantation, implantation damage, and subsequent annealing in yttria-stabilized ZrO_2 (100) using Rutherford backscattering spectrometry in channeling geometry (RBS/C), nuclear reaction analysis (NRA), and scanning electron microscopy (SEM). Single-crystal ZrO_2 (100) samples were implanted using 40 keV H^+ ions to the fluences of $5.0x10^{16}$ and $1.0x10^{17}$ at the temperature of 120 K. Isochronal annealing of the hydrogen-implanted Y-ZrO_2 single-crystals was performed for 20 min in high vacuum, applied at each temperature step. The annealing temperatures were varied from 370 to 870 K at 100 K intervals with $\pm$ 5 K uncertainty in the temperature. After each annealing step, the sample was cooled

down, and the RBS/C and hydrogen NRA measurements were carried out at a sample temperature of 300 K using 2.0 MeV He^+ and 6.40 to 8.04 MeV F^{3+} ions. At the end of 770 K annealing, the samples were removed from the ion scattering chamber, and the SEM measurements were performed using a LEO 982 SEM instrument.

In Figure 3.19, we present the channeling spectra measured from the irradiated and virgin regions of the crystal (implanted with $1.0x10^{17}$ H^+/cm^2) for several annealing temperatures along with a random spectrum. Although the ion irradiation produced damage on both the Zr and O sublattices, only the damage created on the Zr sublattice is followed. The hydrogen concentration profiles, determined using the hydrogen NRA, are presented in Figure 3.20 for annealing up to 770 K. The as-implanted hydrogen profile is peaked at a depth of 300 nm, and a small shoulder is visible around 150 nm from the surface. Annealing the sample to 370 K resulted in an increase in the backscattering yield from the Zr sublattice near the damage peak. This finding suggests that there is some increased disordering of Zr atoms during
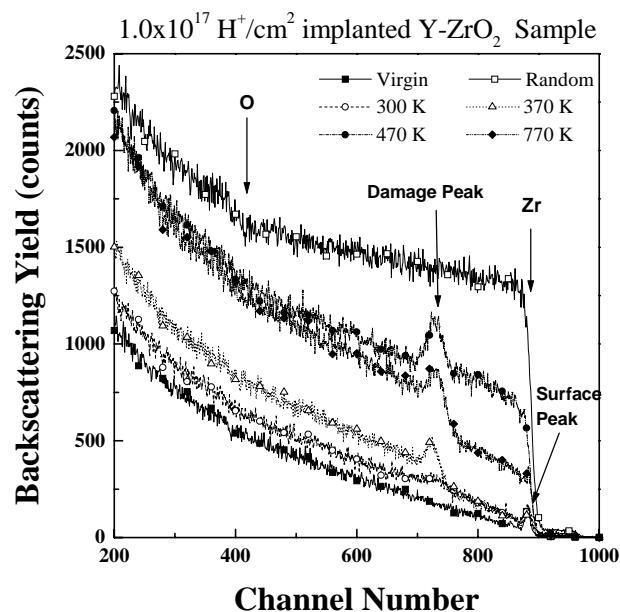
Figure 3.19. Ion scattering/channeling spectra for 2-MeV He^+ ions on virgin and $1x10^{17}$ H^+/cm^2 implanted Y-ZrO_2(100) single-crystal sample, for selected isochronal annealing temperatures as indicated in the figure. The energies of the Zr, O surface peak, as well as the damage peak of the Zr, are indicated by the arrows.
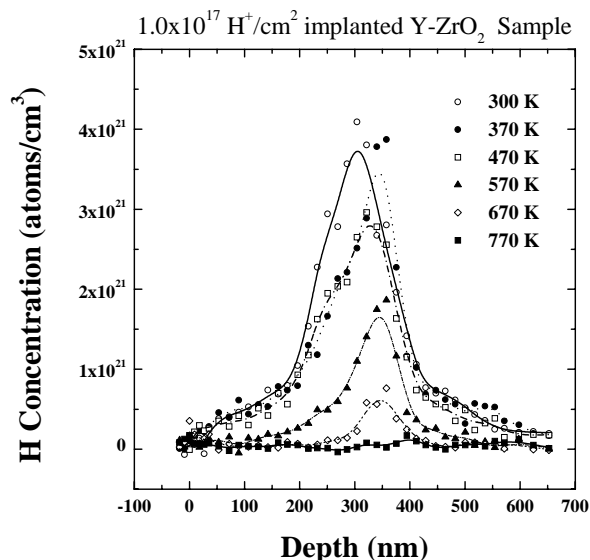
Figure 3.20. The hydrogen depth profiles measured by the resonant $^1H(^{19}F,\alpha\gamma)^{16}O$ nuclear reaction for the 1×10^{17} H$^+$/cm^2 implanted Y-ZrO$_2$(100) single-crystal sample are presented. The profiles were taken after 300, 370, 470, 570, 670, and 770 K isochronal annealing.

annealing due to the possible interaction of H with the structure or the formation of defect clusters or bubble nuclei. The hydrogen profile data show a peak shift toward a larger depth with almost the same hydrogen diffusion toward the surface as seen in the room temperature hydrogen profile. The channeling spectrum looks similar to the random spectrum with the height near the surface region at approximately 50% of the random height. One possibility for the unusual increase in the backscattering yield from the near surface region is the strain and deformation induced by the formation of hydrogen defect clusters or hydrogen blisters in this region after annealing at 470 K. Further annealing at 570 K and 670 K significantly reduces the amount of hydrogen in the analysis region. Further annealing at 770 K reduced the total

amount of hydrogen to the background level. The damage, including the deformation of the surface region, appears to decrease as a result of this annealing. Although virtually no hydrogen is present in the system, within the detection limits, some deformation of the surface region still remains after annealing at 770 K. Scanning electron microscopy (SEM) measurements were carried out on the sample annealed at 770 K to understand the morphology and microstructural changes in the material due to hydrogen interaction with the material and defects during the annealing.

The SEM image obtained from an irradiated region after 770 K annealing is shown in Figure 3.21. The irradiated region shows blisters and bubbles of several-micron diameters. It is also clear from the figure that some of the hydrogen blisters are ruptured during the annealing.
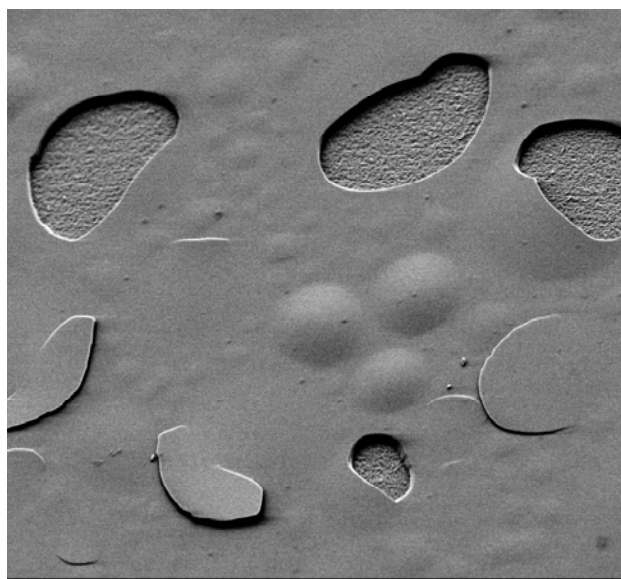
Figure 3.21. SEM image from a 1×10^{17} H$^+$/cm^2 implanted Y-ZrO$_2$(100) single-crystal sample.

Ion Beam Induced Slicing of Single-Crystal Oxide Thin Films

S. Thevuthasan, V. Shutthanandan, W. Jiang[a,b], and W. J. Weber[a,c]

Supported by the U.S. Department of Energy Office of Basic Energy Sciences.
(a) EMSL User.
(b) Postdoctoral Research Fellow.
(c) PNNL Energy Science and Technology Division.

Thin-film cleaving using hydrogen implantation and subsequent thermal treatment was first reported by Bruel for Si in 1995. Since this invention, there has been a growing interest in lifting thin films of semiconductors using this method. In this method, hydrogen, helium, or a combination of the two are incorporated into the material through the use of implantation. Subsequent thermal, pressure, or etching treatment will cleave the film somewhere in the region where the implanted species rest in the material. The sliced film can be transferred to another substrate using material bonding. The advantage of this method is that the dissimilar materials can be integrated regardless of the lattice mismatch between the materials. Also, the thickness of the integrated materials can be controlled by choosing the ion energy that can be translated as a depth range in the material. In the recent past, this method has been shown to be effective for achieving heterogeneous integration of many semiconductor integrated systems. Although the application of the ion-slicing method has been extensively studied for conventional semiconductor materials, a fundamental understanding of the basic mechanisms controlling the crystal slicing is still lacking. In addition, the studies related to thin-film liftoff in oxide and ceramic areas are limited in the literature.

In recent years, a number of techniques including molecular beam epitaxy (MBE) and chemical vapor deposition (CVD) have been used to grow single-crystal epitaxial oxide thin films on various substrates including silicon. However, because of large lattice mismatch and the reactive nature of Si to oxygen, it is very difficult to obtain single-crystal oxide thin films on silicon. Since the conventional dielectric materials that are used in semiconductor devices reach their dimensional limits in device technology, alternative high dielectric materials have received much attention in recent years. Thin-film processing of perovskite materials such as $SrTiO_3$, $BaTiO_3$, and $(Ba,Sr)TiO_3$ is on the rise because of their high dielectric properties. Although there has been some success in growing highly textured, single-crystal perovskite materials on silicon, many of the electrical and electrooptical properties reported generally are not comparable to those of bulk single-crystal materials. In these cases, the ion-slicing method could be effectively applied if the processes and mechanisms associated with this technique were established. The application of this method to $SrTiO_3$ single crystals has been demonstrated at the EMSL accelerator facility.

Hydrogen implantation at 120 K to a fluence of 40 KeV 5.0×10^{16} H^+/cm^2 was carried out on an $SrTiO_3(100)$ substrate at Implant Science Corporation. Isochronal annealing for 20-minute time periods was performed at temperatures from 370 to 870 K at 100 K intervals with ± 5 K uncertainty in the temperature. After each annealing step, the sample was cooled, and the RBS/C and hydrogen NRA measurements were carried out at a sample temperature of 300 K. At the end of 870 K annealing, the sample was removed from the ion scattering chamber, and SEM experiments were performed.

Figure 3.22 presents a planar view of a large region of the sample that shows the boundary between the irradiated and unirradiated surface after annealing at 870 K. It is evident from the figure that the entire

Unirradiated

Irradiated

200 μm
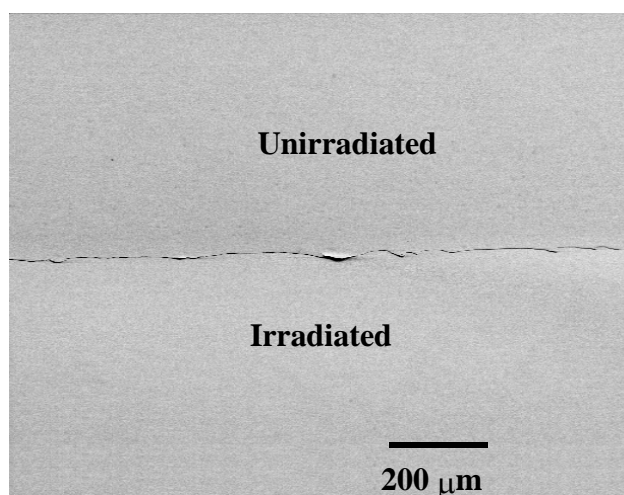
Figure 3.22. SEM micrograph from an irradiated (fluence ~ 5.0×10^{16} H^+/cm^2) and annealed sample after 870 K annealing.

surface layer has been removed in the irradiated region. As discussed previously, it is believed generally that clustering of vacancies in the irradiated material traps the gas and that these gas-vacancy clusters then become nuclei for bubbles. Further investigations are needed to determine the chemical effects, if any, associated with the cleavage process.

The transferred film to a Si substrate through ceramic adhesive is shown in Figure 3.23. The film thickness is approximately 0.3 microns, and the film surface appears to be rough due to the combination of the cleaving process and the particle size (few microns) in the ceramic adhesive. Some portions in the transferred film appear to be flaky due to the particle size in the ceramic adhesive. Material bonding issues need to be addressed for the success of a complete transfer of the film to other substrates.
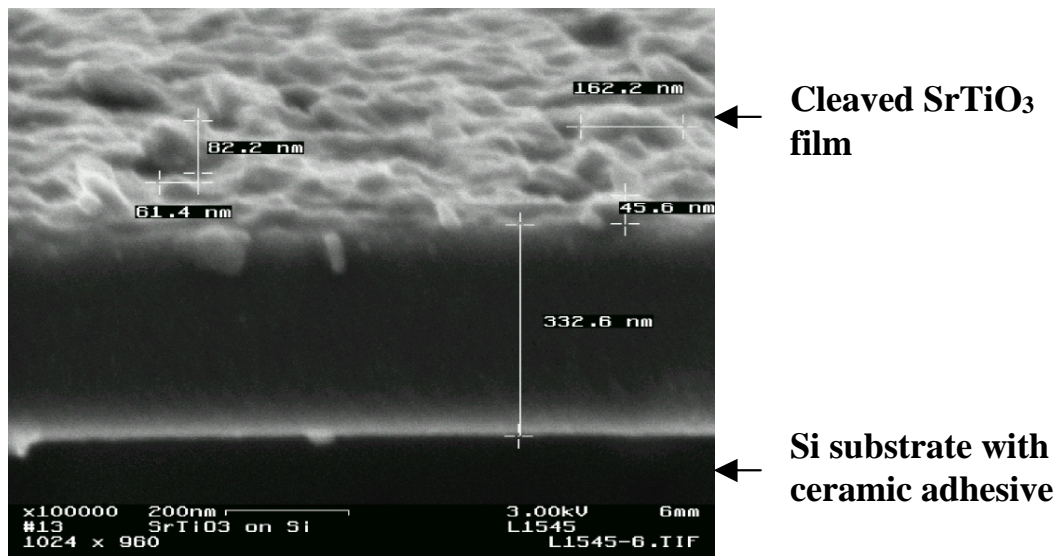
Figure 3.23. SEM micrograph that shows the transferred film to a Si substrate using ceramic adhesive.

Accumulation and Thermal Recovery of Disorder in Au^{2+}-Irradiated $SrTiO_3$

S. Thevuthasan, W. Jiang[(a,b)],
V. Shutthanandan, and W. J. Weber[(a,c)]

(a) EMSL User.
(b) Postdoctoral Research Fellow.
(c) PNNL Energy Science and Technology Division.

Irradiation of materials with energetic ion beams can alter the physical, chemical, electrical, and optical properties of the materials in the surface region. Ion irradiation and implantation have been routinely used not only to transform crystalline materials into either fully or partially amorphous materials but also to perform low-level doping in the semiconductor industry. Often, the irradiation-induced defects and disorder can be fully or partially recovered by subsequent thermal annealing of the irradiated materials.

There is a growing interest in $SrTiO_3$ because of its unique dielectric and structural properties. Because of its high dielectric properties, $SrTiO_3$ is being extensively studied as an alternative dielectric material for conventional silicon dioxide in the semiconductor industry. Also, many perovskite materials are known to be proton conductors when the tetravalent cations such as Ti^{4+} are replaced by trivalent materials such as Sc^{3+}. Furthermore, for purposes of waste stabilization and immobilization, the structure of perovskites including $SrTiO_3$ allows incorporation of both fission products and actinides. In the case of stabilizing high-level nuclear wastes in perovskite materials, the prediction of near- and long-term performance of these materials in the high-radiation environment provided by the decay of fission products and actinides is a challenging task. A fundamental understanding of radiation effects in these materials is critical to such performance predictions.

The goal of the present study is to investigate the ion-beam-induced disordering and recovery processes on $SrTiO_3$ with various ion species and fluences using Rutherford backscattering spectrometry and channeling (RBS/C) techniques. Several irradiation studies of $SrTiO_3$ with H^+, He^+, O^+, and Au^{2+} have been

previously reported by the authors. This report discusses some portion of these studies related to the damage accumulation and subsequent thermal recovery in $SrTiO_3$(100) irradiated with 1.0 MeV Au^{2+}. The ion fluences varied from 0.10 Au^{2+}/nm^2 to 0.40 Au^{2+}/nm^2, and the ion irradiations were performed at a sample temperature of about 170 K and 300 K. The relative disorder, which is the ratio of the damage peak height to the random height, was determined from the spectra by assuming a linear dechanneling yield for each ion fluence. Subsequently, isochronal annealing was performed at temperatures from 370 to 870 K at 100 K intervals. After each annealing step, the sample was cooled, and the RBS/C measurements were carried out at a sample temperature close to room temperature using 2.0 MeV He^+ ions.

The channeling spectra from the irradiated and virgin regions are shown, along with the random spectrum, in Figure 3.24 for the irradiation experiments performed at 170 K. Although irradiation-induced disorder was produced on all three sublattices, only disorder created on the Ti and Sr sublattices is shown. At an ion fluence of approximately 0.30 Au^{2+}/nm^2, the dechanneling yield at the damage peak reaches the random level, suggesting that a completely amorphous state has formed in this region. Similar channeling spectra for the irradiation experiments performed at 300 K show slightly broader damage profiles than the
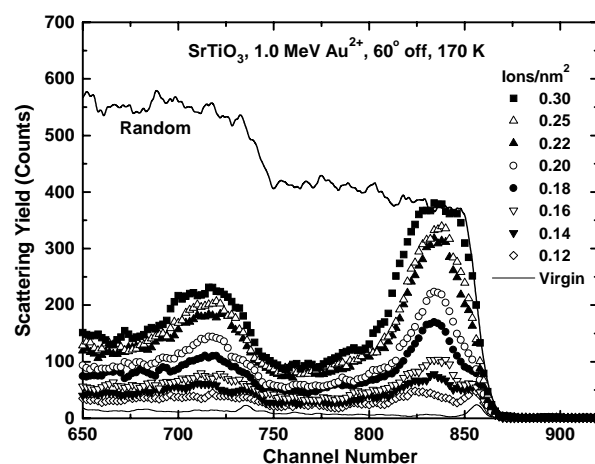
Figure 3.24. The channeling spectra from the virgin and 1.0-MeV Au^{2+} (fluences in the range of 0.12 to 0.30 Au^{2+}/nm^2) irradiated region from $SrTiO_3$ are presented. The irradiations were performed at 170 K, and 2.04-MeV He^+ ions were used to generate these spectra.

damage profiles for the samples irradiated at 170 K, possibly as a result of some diffusion of defects at 300 K. Complete amorphization in the damage peak region at 300 K appears to occur at a fluence of 0.4 $Au2^+/nm^2$, which is slightly higher than the fluence required at 170 K.

The accumulation of relative disorder at the damage peak for both the Sr and Ti sublattices is presented as a function of ion dose (dpa) in Figure 3.25. The relative disorder on both the Sr and Ti sublattices at irradiation temperatures of 170 and 300 K exhibits a strong sigmoidal dependence on the ion dose.

The damage recovery as a function of temperature for various ion fluences is shown in Figure 3.26. The relative disorder at the damage peak in the irradiated regions decreases as a function of increased annealing temperature. After annealing to 870 K, the disorder in the low fluence samples, especially up to a fluence of 0.27 Au^{2+}/nm^2, was almost completely recovered. For the higher fluences starting from 0.27 to 0.30 Au^{2+}/nm^2, it appears that the relative rate of recovery (not shown for 0.29 and 0.30 Au^{2+}/nm^2) started to slow down in the temperature range between 550 and 870 K.
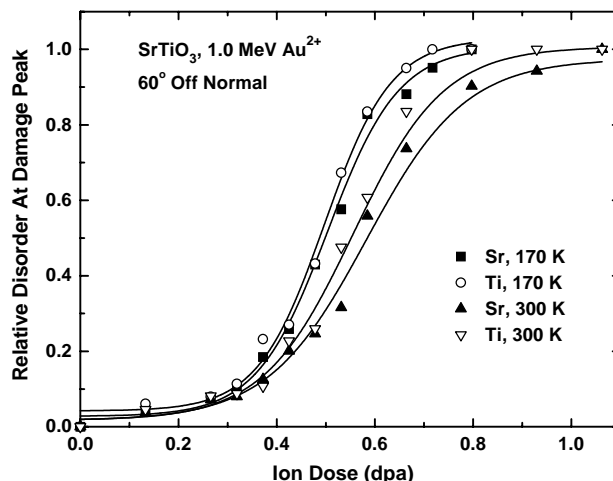
Figure 3.25. Relative disorder at the damage peak from Sr and Ti sublattices in $SrTiO_3$ irradiated at 170 and 300 K with 1.0-MeV Au^{2+} ions.
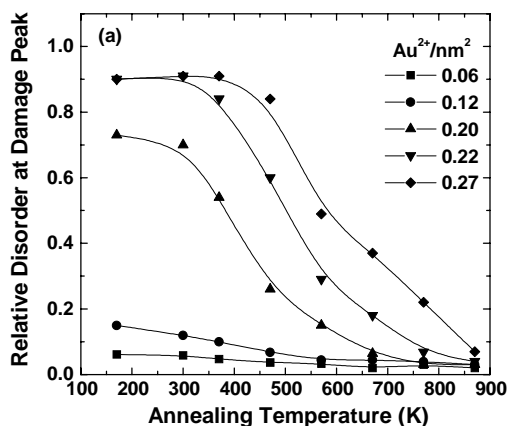
Figure 3.26. Isochronal recovery of the relative disorder in the Sr sublattices as a function of annealing temperature from 0.06, 0.12, 0.20, 0.22, and 0.27 Au^{2+}/nm^2 irradiated regions is presented.

4. Nanoscale Materials

Low Cost Synthesis of Nanocrystalline Titanium Aluminides

E. G. Baburaj[a], F. H. Froes[a],
V. Shutthanandan, and S. Thevuthasan

Supported by internal funding from Institute for
   Materials and Advanced Processes,
   University of Idaho.
(a) EMSL User, University of Idaho.

The collaborative program between the University of Idaho (UI) and the EMSL is aimed at the development of nanocrystalline titanium aluminide intermetallics for structural applications. Intermetallic compounds are a unique class of materials, consisting of ordered alloy phases formed between two or more metallic elements where the different atomic species occupy specific sites in the crystal lattice. Titanium aluminide intermetallics are potential candidates for applications in aerospace systems and automobiles because of their low density and high temperature strength properties. In spite of the combination of excellent properties, the use of these intermetallics is limited because of their prohibitively high cost.

The present collaborative work involves the synthesis of nanocrystalline titanium aluminide by a low-cost process of mechanical alloying of TiH_2 with Al followed by a low-temperature consolidation at the University of Idaho (UI) and hydrogen measurements at the EMSL. The use of hydrogen as a temporary alloying element is advantageous because of the following reasons: 1) hydrogen can act as a temporary alloying element while processing and can be removed from the lattice by vacuum annealing, 2) hydrides can be easily milled to ultrafine size by the mechanical alloying process, thereby enhancing the formation of nanocrystalline alloys in short processing times, and 3) the presence of hydrogen in the lattice has the potential to modify the microstructure of the alloy and thereby tailor the properties of the alloy. The alloys thus produced will have enhanced mechanical properties as compared to the conventional alloys because of the nanoscale grain structure and will open up a new area in the processing of Ti-Al alloys with enhanced properties and low cost.

Experiments were carried out by milling stoichiometric amounts of TiH_2 and Al to form a TiAl intermetallic compound. Initial experiments on milling and heat treatment experiments indicated the possibility of controlling the kinetics of alloy formation and concentration of hydrogen in the intermetallic compound. Heat treatments of the mechanically alloyed powder at 750° C in an argon atmosphere resulted in the formation of a two-phase (TiAl + Al_3Ti) mixture, while consolidation by hot isostatic pressing (HIP) at the same temperature in sealed containers gave rise to a single-phase TiAl containing hydrogen in its lattice. Hydrogen measurements were carried out on the HIP samples, after heat treatments under vacuum.

Hydrogen depth profile measurements were done using $H(^{19}F, \alpha\gamma)^{16}O$ resonant reaction that uses the sharp resonance peak in the reaction cross-section to depth profile the hydrogen concentration. The number of gamma rays produced by this reaction is proportional to the hydrogen concentration (at a particular depth).

The hydrogen content in the intermetallic compound after consolidation qualitatively revealed an inverse proportionality with milling time. This result is consistent with the decrease in particle size and consequent increase in specific surface area, which reduces the number of interstitial sites for hydrogen in the TiAl lattice.

Hydrogen depth profiles obtained from samples milled for 1 hr, consolidated by HIP, and heat treated under vacuum at different temperature-time combinations are given in Figure 4.1. All the heat-treated samples show increasing hydrogen concentration with depth from the surface and a minimum level of hydrogen concentration at the surface as a function of temperature. The observation of low hydrogen concentration in depths up to about 0.2 μ indicates the ease of hydrogen removal when the particle size of individual crystals is in nanoscale.

The microstructure of the TiAl sample has been examined at the UI to establish the nanoscale grain size. The sample was heat treated under vacuum at an arbitrarily chosen high temperature of 950° C for 2 hr.
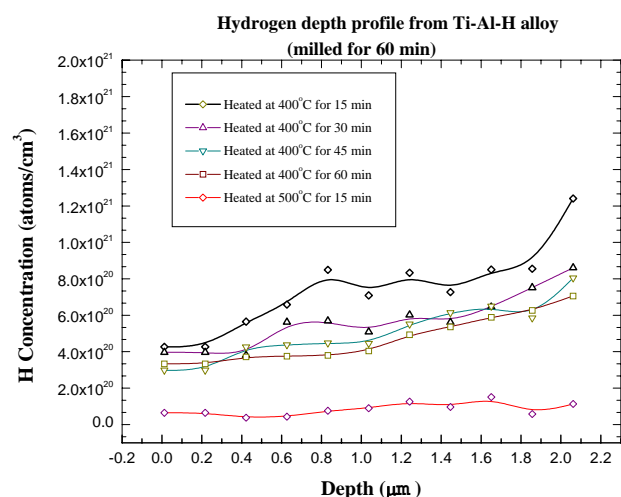
Figure 4.1. Hydrogen depth profiles from Ti-Al-H samples after annealing.

Figure 4.2. Nanocrystalline structure of TiAl. Largest grain in the figure is about 100 nm.

The microstructure (Figure 4.2) shows single-phase TiAl and the absence of hydride phases. Further experiments on kinetics of hydrogen desorption by nuclear techniques are necessary to develop a correlation between hydrogen content as a function of temperature, pressure (vacuum level), additional alloying elements, and grain size.

Diffusion of Pt Nanoclusters on Highly Corrugated Anatase TiO$_2$(001)-(1x4) Surface

S. Gan[a], A. El-Azab, and Y. Liang

Supported by PNNL Laboratory Directed Research and Development funding.

(a)   Postdoctoral Research Fellow.

Kinetic processes such as diffusion of atoms and clusters can influence the structure and performance of metal-on-oxide systems. For example, cluster diffusion strongly affects the spatial and size distribution of clusters on the surface. Many studies have been conducted to advance the understanding of metal diffusion in homoepitaxial systems. Most of the reported studies have dealt with diffusion of atoms or small clusters. Relatively fewer studies, however, have focused on heteroepitaxial systems.

We examined a novel heterogeneous system consisting of Pt on a highly corrugated anatase TiO$_2$(001) surface by scanning tunneling microscopy (STM). Pt forms three-dimensional nanoclusters with a narrow size distribution on the anatase TiO$_2$(001)-(1x4) surface (Gan et al. submitted; Liang et al. in press). We found that Pt on this surface forms a unique system. In contrast to Pt on rutile TiO$_2$ surfaces, Pt clusters on the anatase terraces and step edges do not coalesce under the experimental conditions considered. At elevated temperatures, clusters on the terraces diffuse as a whole mostly along the atomic row direction to the step edges, thus mimicking the diffusion of adatoms on a surface with strongly anisotropic atomic corrugation. To the best of our knowledge, this is the first time that anisotropic diffusion of large three-dimensional metal clusters on oxide surfaces has been reported.

Figure 4.3 shows an STM image of the anatase TiO$_2$(001)-(1x4) surface after depositing 0.2-ML Pt at 300 K, followed by annealing at 470 K in UHV. The atomic rows, which are 16 Å apart, are oriented along the [010] and [100] directions, thus constructing a double-domain surface. The surface contains predominantly single-atomic-layer (2.4 Å) high steps. The bright spots seen in the image are three-dimensional Pt nanoclusters. It could be seen that these clusters spread over the entire surface, with the majority of
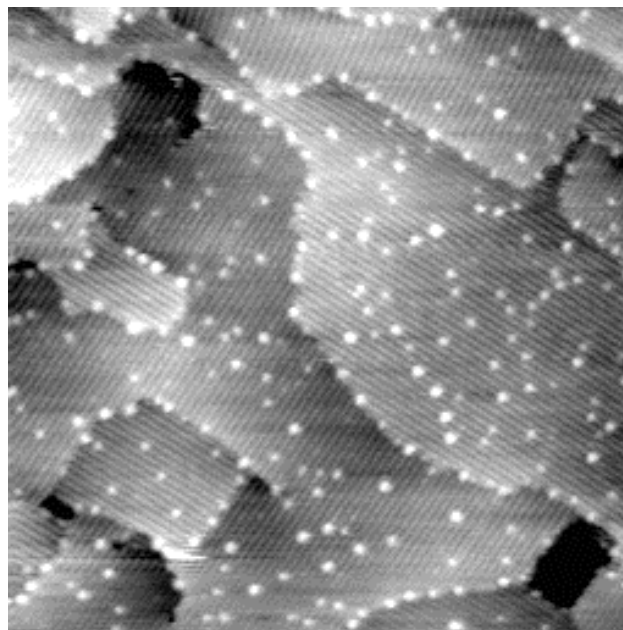
Figure 4.3. An STM image of an anatase TiO$_2$ (001)-(1x4) surface covered by 0.2-ML Pt after annealing in UHV at 470 K.

them occupying the terraces and the remainder occupying the step edges. As the annealing temperature was increased, more clusters were found at the step edges, while the number of clusters on the terraces decreased. Through statistical counting of clusters in STM images at each temperature, we found that the total number of Pt clusters on the surface remains constant at approximately $2.70 \times 10^{-4}/\text{Å}^2$ during annealing in vacuum at temperatures up to 670 K. The number of clusters occupying the step edges increased during annealing at the expense of the cluster population on the terraces. This observation demonstrates that cluster-cluster coalescence did not occur in the temperature range we investigated.

To confirm this conclusion, we constructed a set of autocorrelation images for the inter-cluster separation vectors after annealing at different temperatures. Results showed, from one annealing period to the next evolution of the shape of the denuded zone from a nearly square shape, with sides parallel and perpendicular to the atomic rows (for the as-deposited cluster population), to an elliptical shape, with the major axis increasing and gradually becoming oriented along the direction of the atomic rows. This mode of denuded zone evolution confirms that cluster diffusion takes place primarily along the direction of the atomic rows.

Based on the arguments presented above, a one-dimensional model for cluster diffusion on the terraces is considered to be sufficient for describing cluster diffusion on the terraces and for extracting the diffusion coefficient at different annealing temperatures from the temporal behavior of the cluster population. In this model, cluster diffusion is assumed to obey Fick's law. By solving the diffusion equation under proper boundary conditions, the time-dependent cluster density can be expressed as $N(t)/N(0) \sim (8/\pi^2)\exp(-\pi^2 Dt/L^2)$. Hence, it suffices to count the total number of clusters on a terrace of *fixed dimensions* and substitute them in the above equation to recover the cluster diffusion coefficient at the end of each annealing period. Figure 4.4 shows an Arrhenius

plot for the cluster diffusion coefficient versus the inverse of the annealing temperature obtained through the one-dimensional model described above. The diffusion coefficient at the corresponding temperature was averaged over several values. The error analysis indicates a standard deviation for these calculated diffusion coefficients. The linearity of the fitted line suggests that the simple model described here is adequate. The slope of the curve yields the activation energy E_a for Pt cluster diffusion of 0.27 eV, and a pre-exponential factor D_0 [$D = D_0 \exp(-E_a/kT)$] of 400 $Å^2$/s (Gan et al. submitted; Liang et al. in press).

References

Gan, S., A. El-Azab, and Y. Liang, "Anisotropic Diffusion of Pt nanoclusters on highly corrugated anatase TiO_2(001)-(1x4) surface", *Phys. Rev. Lett.*, submitted.

Liang, Y., S. Gan, S. A. Chambers, and E. Altman, "Surface Structures of Anatase TiO_2 (001): Reconstruction, Atomic Steps, and Domains", *Phys. Rev. B*, in press.

Figure 4.4. The Arrhenius plot of experimentally determined cluster diffusion constant versus the annealing temperature. The diffusion barrier was obtained from the slope of the fitted line.

The Effect of Pt Nanocluster Size and Titania Surface Structure Upon CO Surface Chemistry on Pt Supported TiO$_2$ (110)

S. Gan[a], Y. Liang, D. R. Baer,
M. R. Sievers[a], G. S. Herman, and
C. H. F. Peden

> (a)   Postdoctoral Research Fellow.

Titanium dioxide is a key material for photocatalysis and has a wide range of other technological applications. As a model metal oxide, studies using supported-metal clusters on TiO$_2$ surfaces can shed light on the metal-oxide interface and how it influences the catalytic activity of a metal surface. In particular, when metal clusters are only a few atomic layers thick, the size of clusters and surface structure of the oxide can have a significant impact on the chemisorptive properties of the metal. Among a variety of metals (Pt, Pd, Rh, Cu, Al, etc.) that can be supported on TiO$_2$ surfaces, platinum has the highest work function and is expected to enhance the photocatalytic activity of TiO$_2$. To date, only a few studies have been carried out to investigate Pt thin films on single-crystal rutile TiO$_2$ surfaces.

We have investigated (Gan et al. in press) the adsorption chemistry of CO on clean and Pt-supported TiO$_2$ (110). Figure 4.5 shows STM images of the (1x2) and (1x1) (inset) TiO$_2$ surfaces after Pt deposition. The Pt coverages in the main and inset portions of the figure are 0.1 ML and 0.3 ML, respectively. The STM images clearly show that Pt forms three-dimensional clusters on both TiO$_2$ (110) (1x1) and (1x2) surfaces. The average cluster size was measured to be 8 and 14 Å in the main and inset portions, respectively. We found that, at fractional monolayer coverages, Pt adsorbs on top of Ti atomic rows on the (1x2) surface, while on the (1x1) surface, the Pt clusters were randomly distributed. It was found that the surface structure of TiO$_2$ plays an important role in the chemistry that takes place at the surface. On the reduced (1x2)-reconstructed surface, CO desorbed at 140 and 170 K, while only desorption at 140 K was observed on the stoichiometric (1x1) surface. Additionally, CO
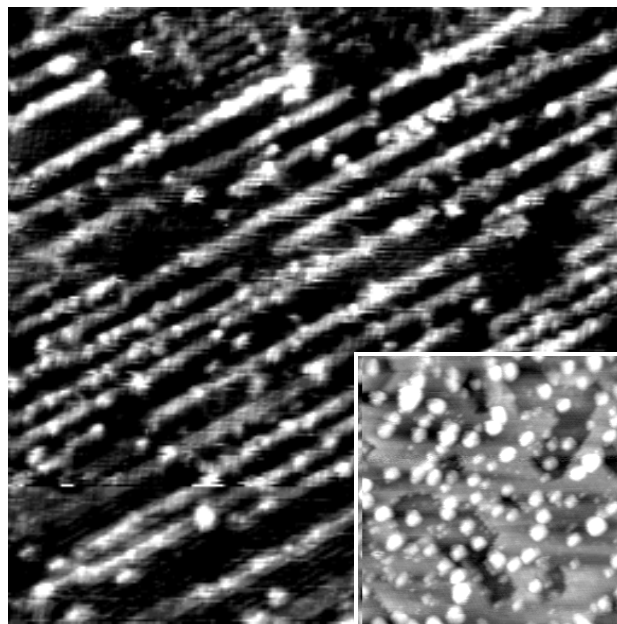
Figure 4.5. Scanning tunneling micrographs of TiO$_2$ (110) surfaces covered by 0.1-ML Pt deposited on the (1x2) and (1x1) (the inset) surface. The image size is 400x400 Å^2.

dissociation, possibly due to the reduction by Ti^{3+}, was observed on the Pt-supported (1x2) surface.

On the Pt-covered surfaces, the chemistry of CO adsorption and desorption strongly depends on the size of Pt nanoclusters. TPD spectra obtained subsequent to 1L CO doses to the Pt-supported TiO$_2$ surfaces are shown in Figure 4.6a. From the bottom to the top, the size of Pt nanoclusters in the corresponding spectra is estimated to be 8, 14, and 45 Å, respectively. The abbreviations SC and BC stand for "small cluster" and "big cluster." Two sets of desorption peaks can be seen in this figure—peaks at approximately 150 K and those near 500 K. Based on a comparison of the TPD spectra shown in Figure 4.6a with spectra obtained from clean surfaces, we believe that the peaks at 500 K can be readily assigned to CO desorption from Pt clusters. This is consistent with previously reported work. Furthermore, for small Pt clusters, only a single CO desorption peak was observed at approximately 510 and 490 K on the corresponding (1x2) and (1x1) surfaces, respectively. The peak position on both surfaces is independent of the CO dosages for small clusters. As an example, the inset in Figure 4.6 shows the TPD spectra for various CO doses to the (1x2) surface covered by Pt clusters
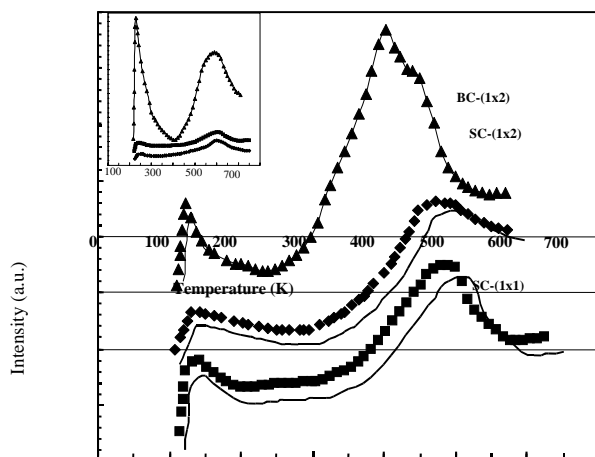
Figure 4.6. TPD spectra of CO desorption from Pt-deposited TiO$_2$ (110) surfaces. BC and SC refer to big (diameter >40 Å) and small (diameter <20 Å) clusters. The inset shows TPD spectra of the SC-(1x2) surface at 0.1, 0.3 and 5 L CO dosages.

of 8 Å in diameter on the (1x2) surface. It can be seen that the peak position does not shift when the CO dosage increases from 0.1 to 5 L. However, when

the cluster size increased significantly to 45 Å, CO was found to desorb at 415 and 470 K, on both the Pt/(1x1) and Pt/(1x2) surfaces. With a decrease in cluster size, CO was found to desorb at higher temperatures. This unusual desorption chemistry is likely related to quantum-size effects of Pt nanoclusters. Scanning tunneling spectra revealed that clusters below 20 Å in diameter exhibited nonmetallic behavior while those above 40 Å were metallic. This transition of the properties of Pt nanoclusters from metallic to nonmetallic as the cluster size decreases correlates with stronger interaction of CO with Pt observed in temperature-programmed desorption spectra.

Reference

Gan, S., Y. Liang, D. R. Baer, M. R. Sievers, G. S. Herman, and C. H. F. Peden, "The effect of Pt nanocluster size and titania surface structure upon CO surface chemistry on Pt supported TiO$_2$ (110)", *J. Phys. Chem. B. Lett.*, in press.

A Novel Nano-Dot System for Electron-Hole Pair Separation: Self-Assembled Cu_2O Dots on $SrTiO_3$(001)

Y. Liang, D. Baer, S. Lea, D. McCready, J. Daschbach, and J. Meethunkij[(a,b)]

(a) EMSL User.
(b) Student, Yale University.

Self-assembled nano-dots have attracted a great deal of attention recently due to their artificial atom-like electronic and optical properties. Two technical challenges in the development of nano-dot applications are the structural stability and property controllability. Since conventional semiconductor nano-dots often exhibit less desirable chemical and thermal stability, we address these issues using oxide-based materials.

We have successfully synthesized Cu_2O nano-dots on $SrTiO_3$ substrates using oxygen-plasma-assisted molecular beam epitaxy. We found that the initial formation of the nano dots occurred after a few mono-layers of Cu_2O deposition due to the large compressive lattice mismatch between Cu_2O and $SrTiO_3$. The structure and composition of the Cu_2O nano-dots were characterized using x-ray diffraction (XRD), x-ray photoelectron spectroscopy (XPS), high-resolution scanning Auger microscopy (SAM), and atomic force microscopy (AFM).

Figure 4.7 is an AFM image of Cu_2O dots grown on an $SrTiO_3$(001) substrate after 20 ML of Cu_2O deposition. Results showed that all the dots had the same orientations, thus suggesting a good structural coherency among these dots. XRD confirmed that the dots grown on $SrTiO_3$ had the Cu_2O characteristic lattice structure. Four types of quantum-dot related structures were found under different synthesis conditions: elongated huts, square pyramids, multifaceted domes and corral-like rings.

While the first three kinds resemble the morphology observed for SiGe quantum dots, the ring structure mimics that of CdTe/ZnSe.

In addition to AFM and XRD, XPS was used to determine the valence and conduction band offsets between
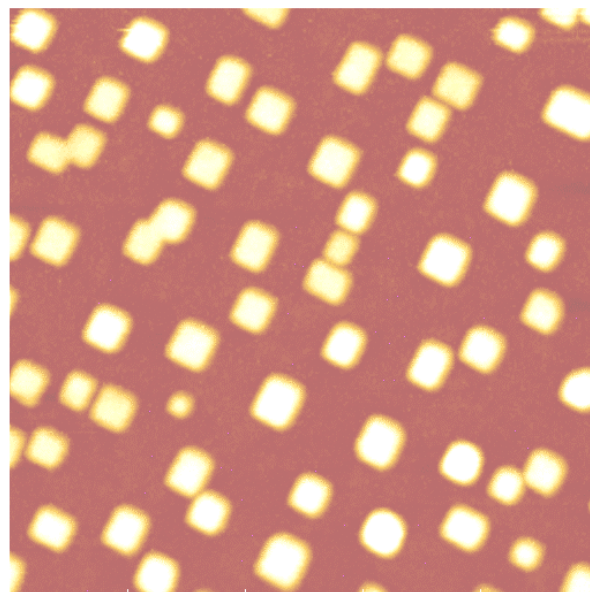
Figure 4.7. An AFM image showing self-assembled Cu_2O dots grown on an $SrTiO_3$(001) substrate. The size of the image is 0.5x0.5 μ^2.

Cu_2O and $SrTiO_3$. Results showed that the $Cu_2O/SrTiO_3$ interface exhibited the so-called type-II heterojunction with both the valence and conduction bands of Cu_2O higher than those of $SrTiO_3$ (i.e., quantum dots for holes but anti-quantum dots for electrons).

High resolution SAM was also used to examine the spatial elemental distribution on $Cu_2O/SrTiO_3$ surfaces. Figure 4.8 shows an SEM image of a $Cu_2O/SrTiO_3$ surface and the corresponding elemental maps of Ti, O, and Cu. Results showed that the amount of interdiffusion between the Cu_2O quantum dots and $SrTiO_3$ substrates was significantly less than several semiconductor-based, quantum-dot systems we investigated, and there was no wetting layer on the $SrTiO_3$ surface in areas between the Cu_2O dots. Therefore, both Cu_2O and $SrTiO_3$ were exposed at the surface. This result, along with the fact that the $Cu_2O/SrTiO_3$ interface has the type-II structure, suggests that, upon above-gap-photon irradiation, photoexcited electrons and holes are spatially separated at the $Cu_2O/SrTiO_3$ surfaces with holes confined to Cu_2O regions and electrons confined to $SrTiO_3$ exposed regions, a property important for photocatalysis and other applications.
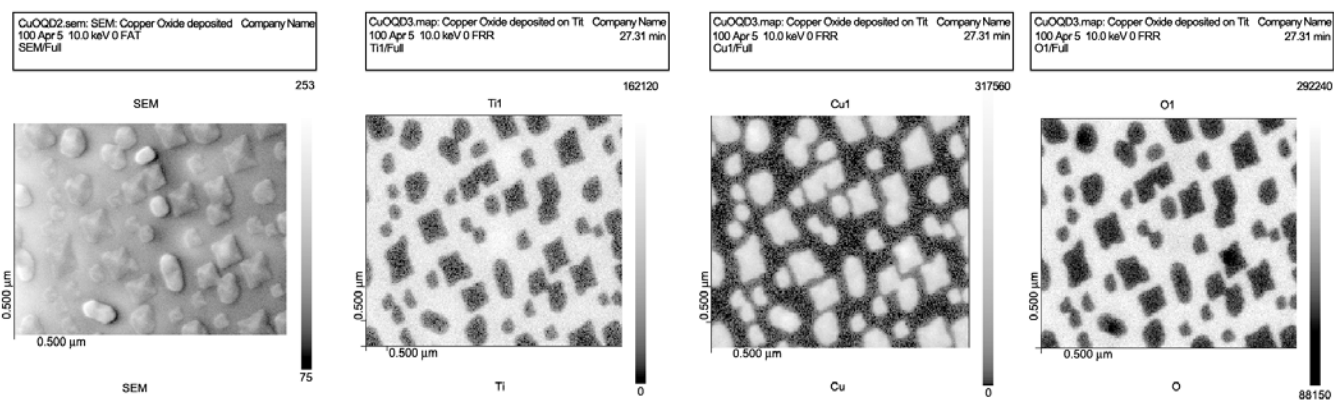
Figure 4.8. An SEM image of a $Cu_2O/SrTiO_3$ surface (a) and the corresponding SAM elemental maps of Ti (b), Cu (c), and O (d) on the surface.

Formation and Characterization of Au Nanoclusters in MgO (100) Using High Energy Ion Beams

B. Koempel-Thomas[a], C. Cooper[a], E. Adams[a], V. Shutthanandan, S. Thevuthasan, Y. Su[b,c], and W. J. Weber[c,d]

Supported by the U.S. Department of Energy Office of Basic Energy Sciences.
(a) EMSL Student.
(b) EMSL Matrixed Staff.
(c) PNNL Energy Science and Technology Division.
(d) EMSL User.

Ion irradiation induced relative disorder has been studied for many years in MgO single crystals. Recently, it has been reported that irradiation with heavy ions such as Au, Cu, and Ag in MgO single crystals followed by thermal treatment generated Au, Cu, and Ag nanoclusters inside the MgO medium. Because of these nanoclusters, the optical properties of the host media are different as compared to the unirradiated samples. As a step towards understanding the nucleation and growth of these nanoclusters in the host media, we initiated Au irradiation work with MgO single crystals at the EMSL accelerator facility. As a first step in the current study, 8-Mev Au ions to about 7×10^{16} ions/cm^2 and 2-MeV Au ions to about 1.4×10^{17} ions/cm^2 were implanted into MgO(100) single crystals. The implantation damage was characterized, and samples were annealed to evaluate the nanocluster formation. The implantation produced visible changes in the optical properties of the MgO. Further optical changes were exhibited after annealing at temperatures of 800° C for 30 min and 1000° C for 10 hrs due to the redistribution of the implanted gold atoms in the MgO. Additional characterization studies are required to confirm the formation of Au nanoclusters, and such studies using optical absorption and TEM are in progress. Thermal recovery of the implantation damage caused by the 8-MeV and 2-MeV implantation was confirmed using Rutherford backscattering spectrometry (RBS) and channeling. A comparison of the expected implantation profile of Au^{2+} ions implanted in single-crystal MgO (100) at 2 MeV and 8 MeV was carried out using TRIM, which is a Monte Carlo simulation.

In Figure 4.9, we compare an optical micrograph from a 2-MeV Au^{2+} irradiated and annealed MgO(100) single-crystal sample to an irradiated sample without annealing. Because of the difference in absorption of light at the surface plasmon resonance wavelength due to the nanocluster formation, the annealed sample is a darker color than the unannealed sample. Figure 4.10 shows the Raman spectra from a 2-MeV Au^{2+} irradiated and annealed MgO(100) single-crystal sample and an irradiated sample without annealing. For comparison purposes, we also show the Raman spectra from a clean, unirradiated MgO(100) crystal.
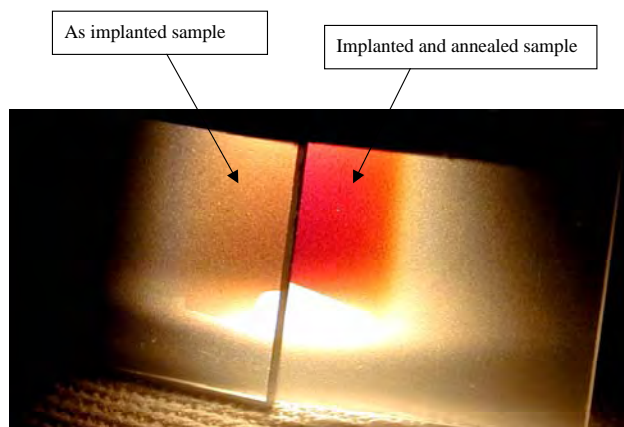
Figure 4.9. Optical micrograph of annealed and unannealed Au$^+$-implanted MgO samples. The annealed sample clearly shows the color change due possibly to the formation of the nanoclusters.
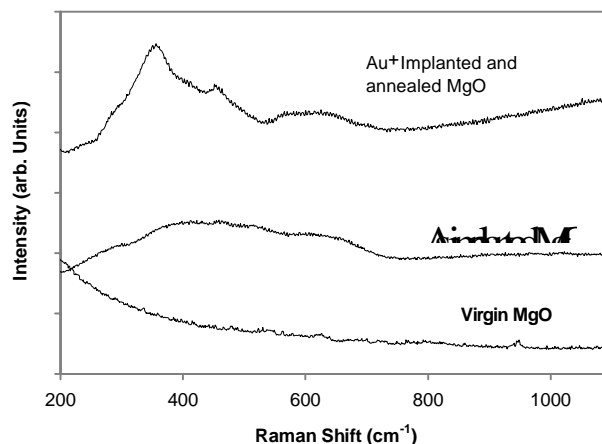
Figure 4.10. Raman spectra from annealed and unannealed Au$^+$ implanted MgO samples. For comparison purposes, Raman spectrum from unimplanted MgO sample is also shown.

While the unirradiated sample does not show any features in the Raman spectrum, the as-implanted sample (without any annealing) shows a very broad feature centered around 500 cm^{-1}. However, the Raman spectrum from the annealed sample clearly shows three distinct peaks at 375 cm^{-1}, 450 cm^{-1}, and 625 cm^{-1}, respectively. We believe that the origin of these three new peaks is somewhat related to the formation of the gold nanoclusters inside the MgO crystal. Further investigations are necessary to confirm that these peaks are related to gold nanocluster formation in MgO. Optical absorption measurements on both samples have been completed and the analysis of the results is currently in progress.

The Discovery of New Crystalline Metal Oxide Materials

Scott Elder and Yali Su[a,b]

(a) EMSL Matrixed Staff.
(b) PNNL Energy Science and Technology Division.

The focus of this project was to develop new molecule-by-molecule synthetic routes for the preparation of nanocrystalline metal oxide powders. The objective was to systematically control nanoparticle size and nanoarchitecture through a rational chemical approach and to determine how size quantification and unique nanostructural features influence photophysical and magnetic properties. We discovered a synthetic route to make stable nanocrystalline metal oxide powders with tailorable size and architecture. We studied and elucidated the reaction mechanism for the synthesis of nanoarchitectured transition metal oxides, and we studied the thermochemical properties of nanoarchitectured transition metal oxides to fundamentally understand the key thermodynamic features that contribute to their stability. Our fundamental investigation enabled us to understand the critical nanoscopic issues that govern the photophysical and magnetic properties of nanoparticle metal oxides.

We have synthesized a series of new nanocrystalline TiO_2-$(MoO_3)_x$ core-shell materials whose photoabsorption energy (PE, the energy required to excite TiO_2-core valence band electrons to MoO_3-shell conduction band states) properties are correlated with both the nanoparticle size and the degree of chemical interaction between the TiO_2 core and the MoO_3 shell. The TiO_2-(MoO_3) nanoparticle size can be readily adjusted from 80 to 40 Å, and, in this series, the PE decreases from 2.88 to 2.60 eV with decreasing particle size. The systematic PE red-shift exhibited by the core-shell materials is due to the change in the relative position of the MoO_3-shell conduction band as it evolves from less than a monolayer to a two-monolayer shell.

The TiO_2-$(MoO_3)_x$ core-shell material powders are synthesized by co-nucleation of metal oxide clusters at the surface of surfactant micelles. Specifically,

after $(NH_4)_2Ti(OH)_2(C_3H_4O_3)_2$ (Tyzor LA) was combined with cetyltrimethylammonium chloride (spherical CTAC micelles) and then diluted with water, nucleation of TiO_2 nanocrystallites occurred at the surface of flexible, rod-like micelles, thus representing a heterogeneous nucleation of nanocrystals from a homogeneous solution. The cross-section view shown in Figure 4.11 demonstrates the nucleation of TiO_2 nanocrystallites at the surface of CTAC micelles. Removal of the organics (in Figure 4.11a) by heat treatment at 450° C will result in crystal growth. However, in the presence of metal oxide spacers, such as MoO_3 (Figure 4.11b), particle size and architectural features are stabilized due to interfacial diffusional barriers at the nanoscale. Figure 4.12 shows the entropies of nanoarchitectured materials and nanoparticle mechanical mixture relative to bulk rutile TiO_2 and bulk baddelyite ZrO_2. The two sets of entropy data are similar, indicating that the stability of the nanoarchitectured materials is due primarily to the presence of diffusion barriers (see Figure 4.11b). The
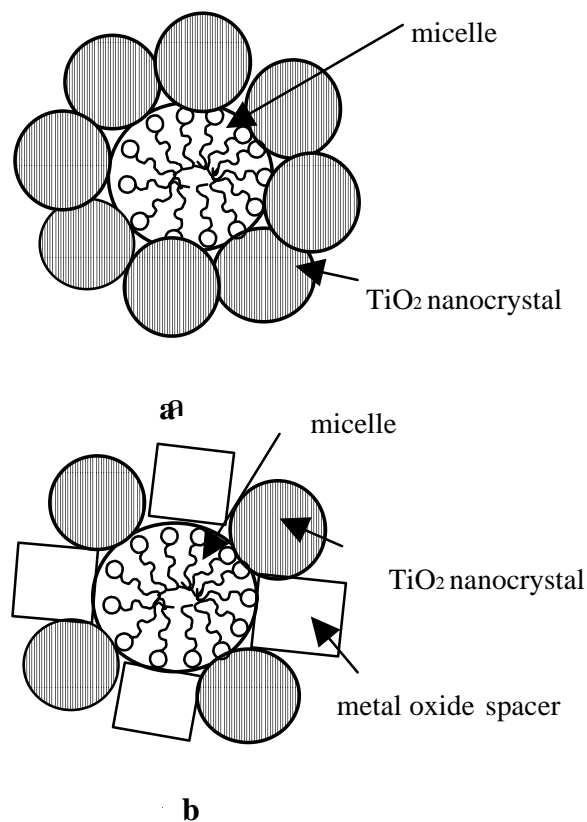
Figure 4.11. A cross-section view of nucleation of TiO_2 nanocrystallites at the surface of CTAC micelles: (a) TiO_2 only, (b) with metal oxide spacer.
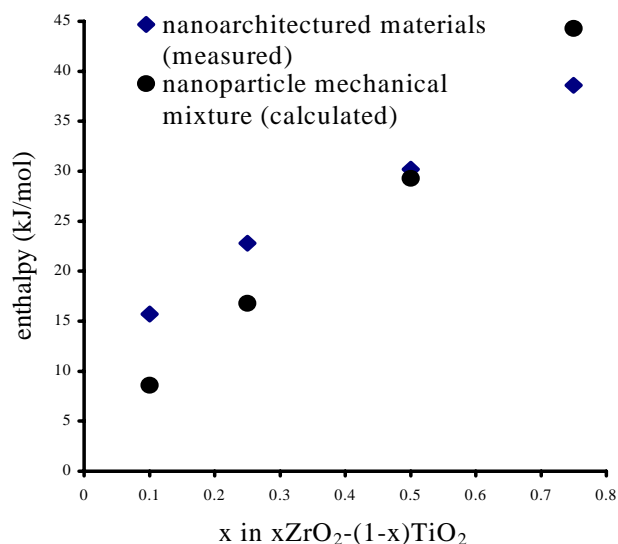
Figure 4.12. Comparison of entropies of nanoarchitectured materials and nanoparticle mechanical mixture relative to bulk rutile TiO_2 and bulk baddelyite ZrO_2.

TiO_2-(MoO_3) compounds are potentially a significant step in the right direction for understanding how to synthesize and design advanced metal oxides with fundamentally new physical and chemical properties.

References

Elder, S. H., F. M. Cot, Y. Su, S. M. Heald, A. M. Tyryshkin, M. K. Bowman, Y. Gao, A. G. Joly, M. L. Balmer, Ana C. Kolwaite, K. A. Magrini, and D. M. Blake, "The Discovery and Study of Nanocrystalline TiO_2-(MoO_3) Core-Shell Materials", *J. Am. Chem. Soc.* **122**, 5138-5146 (2000).

Advanced Thin Film Materials Based on Functionalized Carbon Nanotube Composites

Y. Gao, J. W. Grate, J. H. Sukamto[a,b],
D. A. Nelson[a,b], S. Thevuthasan, and
G. S. Herman

Supported by PNNL Laboratory Directed Research and Development funding.
(a) EMSL Matrixed Staff.
(b) PNNL Environmental Technology Division.

We investigated functionalized carbon nanotube (CNT) composite materials with the aim of exploring their chemical and physical properties. The proposed research was based on our recently developed novel synthesis technique for producing CNT thin films with controlled properties, together with our expertise in metal decoration and polymer derivatization of various surfaces. The scope of the work encompasses fundamental studies on the growth and modification of CNT films, patterning, characterization of inter-active properties, and exploratory experiments to demonstrate the functionality of these novel materials in applications such as hydrogen storage.

Carbon nanotubes are emerging as a new, advanced material for the next century. Because of the combi-nation of their high mechanical strength, tailorable electronic properties, very high surface area, light weight, and excellent chemical and thermal stability, CNTs exhibit a variety of potential applications including hydrogen storage, electronic nano-devices, fuel cells, and batteries. To date, most of the fundamental research on CNTs has been focused on their growth mechanism and direct measurements of various physical properties. Modifying the surfaces of CNTs with functional materials exhibiting useful chemical and physical properties will add a new aspect of promise for the application of this family of novel materials. However, the fundamental study of such advanced composite materials is absent in the literature, and their tremendous potential is yet to be realized.

Following an approach similar to one described by Li et al. (1996), support substrates for CNTs were initially coated with a thin film of porous silica impregnated with metal catalysts (e.g., Fe, Ni, or Co). CNTs were subsequently grown by CVD techniques employing ethylene as the carbon source. The result-ing CNT films were typically characterized by SEM and/or TEM. For hydrogen storage studies, we used an element-specific, ion-beam technique developed at PNNL based on nuclear reaction analysis for deter-mining the concentration of absorbed H_2.

Aligned and crack-free CNT films are critical for many applications (e.g., field emission devices). We have successfully grown aligned CNT films on stainless steel foils as shown in Figures 4.13a, b, and c. A stainless steel foil was first coated with a thin film of porous silica impregnated with iron. The CNTs were subsequently grown on the substrate at 750º C using ethylene as the carbon source. The cracks seen in Figure 4.13a are possibly caused by cracks on the porous silica film. Additional studies are underway to determine conditions required to grow crack-free CNT films.

(a)   **(b)**   **(c)**
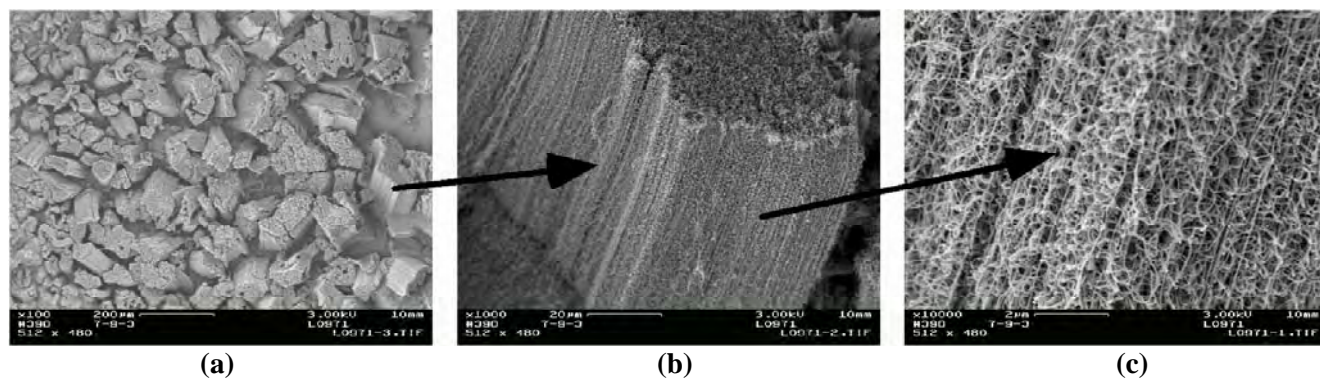
Figure 4.13. (a) – (c) Successive magnification of CNTs grown on a stainless steel substrate.

Two types of surface modification activities were pursued in FY 2000: 1) decoration of CNTs with noble metals (e.g., Pt) and 2) derivatization of CNTs with polymers. Shown in Figure 4.14 is the secondary electron image from the in-lens detector of a CNT sample that has been decorated with Pt. The Pt was deposited electrochemically (5-second deposition period) using the electronically conductive CNTs as electrodes. Thus, we have successfully demonstrated that CNT surfaces can be electrochemically modified with metal nanoparticles (approximately 10-nm Pt particles).

Pt deposits on CNTs are of interest to a wide range of applications from catalysis in general to hydrogen storage. The use of CNTs for catalyst support is of interest because of the uniformity of CNT surfaces (i.e., defect-free CNTs are single crystals), and their high thermal and electrical conductivities. The possibility of storing hydrogen in the hollow centers of CNTs has sparked interest worldwide. Because noble metals (such as Pt) are known to dissociate molecular hydrogen into atomic hydrogen, the kinetics of hydrogen uptake and release may be improved.

The high surface area of CNT films makes them viable support materials for electrodes. Commercial polyvinylferrocene (PFV) from Polysciences Inc. was coated on CNT films using a solvent casting technique where the PVF was dissolved in dichloromethane.

The cyclic voltammogram of the PVF-coated CNT film was obtained in a solution of 0.5-M $NaNO_3$; the result was then compared to the cyclic voltammogram of a PVF-coated carbon cloth electrode (GC-14 from the Electrosynthesis Co.). The integrated charges passed as a function of time for both electrodes are shown in Figure 4.15a. The PVF-coated CNT electrode exhibited a higher surface charge density. Furthermore, there was no difference in electrode accessibility (i.e., solution mass transport rates) between the two electrodes. This is evident from Figure 4.15b, where the charge passed has been normalized to the maximum charge passed. That is, the same amount of time is required for passing the same relative amount of charge. Therefore, CNT films provide additional surface area with negligible mass transfer limitations.
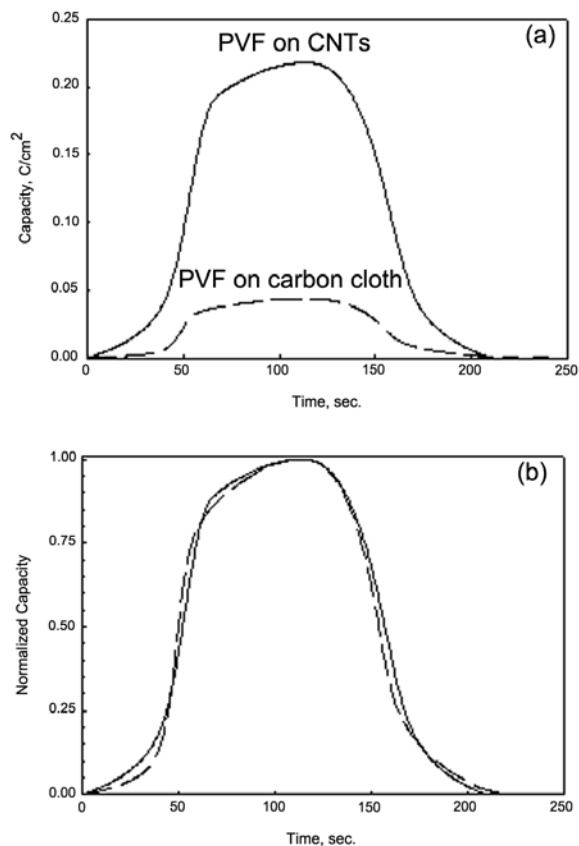
Figure 4.15. (a) Integrated charge passed from cyclic voltammogram of PVF-coated CNT thin film measured in 0.5-M $NaNO_3$ at 5 mV/sec. Time = 0 corresponds to beginning of the potential scan. (b) Same as (a) but normalized to the maximum charge passed.

Figure 4.14. Secondary electron image from the in-lens detector for a 5-second deposition time of Pt.

We have verified the feasibility of using a nuclear reaction analysis to directly measure the amount of H_2 absorbed in CNTs. Briefly, a beam of ^{19}F with a specific energy is imparted on CNT samples. The nuclear reaction, $^{19}F + {}^1H \rightarrow {}^{16}O + \gamma$, occurs only when the ^{19}F has a specific energy (i.e., the resonant energy). Because the reaction is very specific to $^{19}F + {}^1H$, a measure of the γ yield provides a measure of the concentration of H_2. In addition, variation of the ^{19}F energy gives us the ability to obtain the concentration of H_2 as a function of depth (the ^{19}F must expand sufficient energy before the resonant nuclear reaction will take place). Figure 4.16 shows the H_2 content of a virgin CNT sample and the same sample after it has been dosed with H_2 at 1 atmosphere for 1 hour. The amount of H_2 is approximately 0.2 wt%. This is consistent with published reports on the H_2 content of CNTs that have undergone similar treatments. Because this technique is a direct spectroscopic measure of H_2 in CNTs, it provides an unambiguous measure of H_2 content. It is especially useful for studying H_2 uptake and release by means of pressure swings.
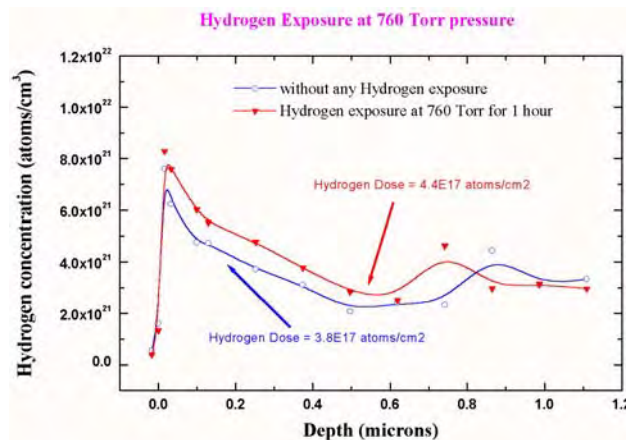
Figure 4.16. H_2 concentration determined using nuclear reaction analysis.

References

Li, W. Z., S. S. Xie, L. X. Qian, B. H. Chang, B. S. Zou, W. Y. Zhou, R. A. Zhao, and G. Wang, "Large-Scale Synthesis of Aligned Carbon Nanotubes", *Science* **274** 1701 (1996).

Ion Beam Synthesis of Au Nanoclusters in Telluride Glasses

M. Haller[a,b], S. K. Sundaram[a,c], S. Thevuthasan, V. Shutthanandan, and Y. Su[d,e]

(a) EMSL User.
(b) Graduate Student, University of Washington.
(c) PNNL Environmental Technology Division.
(d) PNNL Energy Science and Technology Division.
(e) EMSL Matrixed Staff.

Table 4.1. Experimental Implantation Doses and Temperatures

Glass Sample	Dose (Au^{2+} ions/cm^2)	Temperature (^{o}C)
TeNaLa Glass		
1	$4*10^{15}$	-77
2	$7*10^{15}$	0
3	$7*10^{15}$	60
4	$1*10^{16}$	10
5	$2*10^{16}$	
TeNaNd Glass		
6	$1.9*10^{15}$	140
7	$1.8*10^{15}$	
8	$5*10^{15}$	20
9	$1*10^{16}$	-30
10	$5*10^{16}$	-25

The purpose of this project was to determine the effect of heavy ion beam damage and formation of Au nanoclusters on the optical properties of telluride glasses for photonics application. This work involved the preparation of glasses, generation of local damage using the beam facility, synthesis and characterization of nanoclusters, and characterization of the change in optical properties. Raman spectroscopy measurements were performed to analyze any structural changes within the irradiated region of the sample. The refractive index and transmission electron microscopy (TEM) measurements were not completed due to time constraints. These measurements will be performed in FY 2001.

Ten-gram batches of telluride glasses were prepared. The target glass composition (in normalized weight percent) was $TeO_2 = 95.79$, $Na_2O = 7.2$, and Nd_2O_3 or $La_2O_3 = 2$. The samples doped with Nd_2O_3 were placed in the furnace for 1 hr at 750° C, then air quenched to cool. The La_2O_3-doped samples were melted at 800° C for 1 hr, then air quenched to cool at room temperature. All of the samples were melted in platinum crucibles. The glass samples were cut into small pieces and polished for implanting. The samples were implanted at various doses of Au^{2+} ions at different temperatures as listed in Table 4.1. After irradiation, Rutherford backscattering spectrometry (RBS) and Raman spectroscopy measurements were carried out to investigate the changes in the material.

A Gaussian distribution of the Au profile was obtained from TRIM simulations for both glasses. These profiles are shown in Figures 4.17a and 4.17b.

Figure 4.17. Au profile in (a) La_2O_3-doped glass and (b) Nd_2O_3-doped glass.

The depth range for Au in Nd_2O_3- or La_2O_3-doped samples were 4 and 5 microns, respectively. If the current used during implantation was less than 200 nA, no crystallization related problems occurred within the glass. If the current was greater than 200 nA, crystallization occurred. Crystallization occurred in samples 3, 5, 6, and 7. As an example, we present a picture of crystallized sample 3 in Figure 4.18. A bubble was formed on the surface, and the irradiated region changed in color to gray. RBS was performed on the highest dose samples, the non-implanted samples, and the crystallized samples. This data reiterated that the gold was in the sample as were the correct elements. Au profiles from RBS measurements are consistent with Figures 4.17a and 4.17b. Raman spectroscopy measurements were made and the analysis of the data is currently in progress.

Figure 4.18. Sample 3 after Au irradiation.

Polarized UV Light Emission from Nanoscale Oxide Heterostructures

A. C. Tuan[a], S. Thevuthasan, Y. Liang,
G. Dunham, J. W. Rogers, Jr.,
R. F. C. Farrow[b], R. M. Macfarlane[b],
B. T. Jonker[c], C. L. Aardahl[d,e], and
S. A. Chambers

Supported by PNNL Laboratory Directed Research and Development funding.
(a) Graduate Student, University of Washington.
(b) IBM Almaden Research Center, San Jose, CA.
(c) Naval Research Laboratory.
(d) PNNL Environmental Technology Division.
(e) EMSL Matrixed Staff.

Although the idea of utilizing an electron's spin in modern electronic and optical devices has existed for decades, the recent discovery of ferromagnetism in semiconductor materials (Story et al. 1986; Munekata et al. 1989), as well as advances in epitaxial growth techniques, now provide the enabling science and technology that allow for the investigation of spin behavior in controlled systems (Dietl et al. 2000). A significant ramification of these investigations will be rapid evolution in the area of quantum spin electronics and photonics. Sometimes called spintronics, this field encompasses polarized light emission, spin field effect transistors (spin FETs), and spin resonant tunneling devices. One of the most attractive means of adding the spin degree of freedom described above is by spin injection and transport in structures involving ferromagnetic metals and/or diluted magnetic semiconductors (DMS) as the spin source. However, ferromagnetic metal spin sources have thus far been uniformly unsuccessful, producing spin polarizations of only ~1% in semiconductor quantum well structures (Jia et al. 1996; Hirohata 1999). In contrast, the diluted magnetic semiconductors $Be_yMn_xZn_{1-x-y}Se$ and $(Mn, Zn)Se$ have been utilized as efficient spin injectors, with spin polarizations between 40% and 50%, into $(Al, Ga)As/GaAs/(Al, Ga)As$ quantum well structures (Fiederling et al. 1999; Jonker et al. 2000). However, because of the very low ferromagnetic ordering temperature of this material, as well as almost every other DMS, this dramatic polarization was only achievable at cryogenic temperatures.

This research takes an entirely different approach to achieve efficient, near-room temperature spin injection into a high-bandgap oxide material that will readily be processed into polarized UV light emitting device structures. Such devices are not currently available, but will be of great importance in a number of 21st century technologies. The spin source material of choice is heavily nitrogen-doped p-$Mn_xZn_{1-x}O$, which according to recent theoretical calculations should exhibit a Curie temperature of approximately 320 K (Dietl et al. 2000). Using the p-$Mn_xZn_{1-x}O$ layer as a robust source of spin-polarized holes, and injecting into a ZnO quantum well, electron-hole recombination with electrons entering from an aluminum doped n-$Mn_xZn_{1-x}O$ layer will result in circularly polarized UV light at or near room temperature (Figure 4.19).

Material growth is carried out by plasma-enhanced metalorganic vapor phase epitaxy (MOVPE) in a cold-wall, vertical flow reactor with a high-speed rotating disk. Thus far, the focus has been on the development of processing conditions for reliable control of film composition, so films have only been deposited on readily available, disordered substrates, such as SiO_2 (Spectrosil). Using bis(2,2,6,6-tetramethyl-3,5-heptanedionato) zinc and tris(2,2,6,6-tetramethyl-3,5-heptanedionato) manganese as precursors, the optimal substrate temperatures at a chamber pressure of
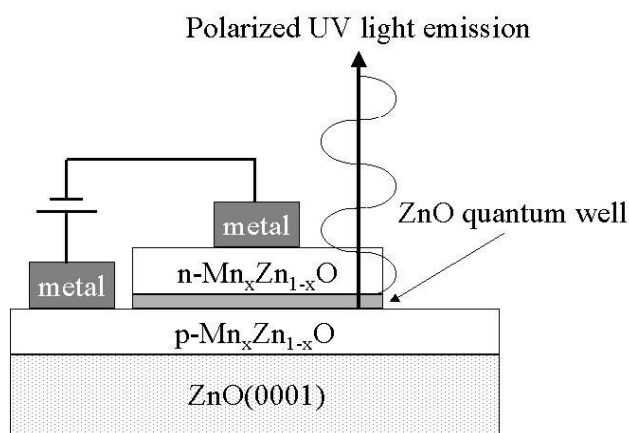
Figure 4.19. ZnO-based surface-emitting LED structure. Spin-polarized holes enter the quantum well from the p-$Mn_xZn_{1-x}O$ layer and recombine with electrons from the n-$Mn_xZn_{1-x}O$ layer to emit circularly polarized UV light.

40 Torr lie between 300º and 500º C. Above 500º C, the quality of the crystallinity and the composition of the film become difficult to control, which most likely is due to premature homogeneous reactions between precursor gases. Chemical analysis by x-ray photo-electron spectroscopy (XPS) and Rutherford back-scattering (RBS) provides evidence that the Mn content is tunable up to $Mn_{0.35}Zn_{0.65}O$ by varying the precursor delivery ratio and/or the substrate temperature. Furthermore, the lack of MnO_x peaks in x-ray diffraction (XRD) spectra indicates the absence of phase separation. Initial attempts at nitrogen incorporation using ammonia also show a great deal of promise. Analysis of TOF-SIMS spectra shows the existence of nitrogen-containing fragments in films processed both by on-surface cracking and by microwave plasma.

Once a reliable method has been developed for control of film composition, the research effort will shift to growth of high-quality epitaxial films on single-crystalline ZnO substrates. The result of this emphasis in materials synthesis will be the footing necessary for the successful fabrication of a surface-emitting LED structure (Figure 4.19) by established clean-room techniques.

References

Dietl, T., H. Ohno, F. Matsukura, J. Cibert, and D. Ferrand, *Science* **287**, 1019 (2000).

Fiederling, R., M. Kelm, G. Reuscher, W. Ossau, G. Schmidt, A. Waag, and L. W. Moelkamp, *Nature* **402**, 787 (1999).

Hirohata, A., *Journal of Applied Physics* **96**, 5804 (1999).

Jia, Y. Q., R. C. Shi, and S. Y. Chou, *IEEE Trans. Magn* **32**, 4707 (1996).

Jonker, B. T., Y. D. Park, B. R. Bennett, H.-D. Cheong, G. Kioseoglou, and A. Petrou, *Physical Review B*, to appear (2000).

Munekata, H., H. Ohno, S. von Molnar, A. Segmuller, L. L. Chang, and L. Esaki, *Physical Review Letters* **63** (17), 1849 (1989).

Story, T., R. R. Galazka, T. B. Frankel, and P. A. Wolff, *Physical Review Letters* **56**, 777 (1986).

5. Interfacial Properties and Reactivity

Local Reactions on Carbonate Surfaces: Structure, Reactivity, and Solution

D. R. Baer and J. E. Amonette

The purpose of this program is to develop a fundamental, microscopic understanding of the structure and chemistry of carbonate surfaces, including the interactions with adsorbates. This project involves an interdisciplinary theoretical and experimental effort designed to gain a fundamental, molecular-level understanding of carbonate mineral surface structure and chemistry. Carbonate minerals are particularly important in the global carbon dioxide cycle and in subsurface contaminant migration processes. The availability of large, single crystals allows fundamental measurements to be made on well-defined surfaces. By linking experimental studies of geochemical reactions on single-crystal surfaces with first-principle, quantum-mechanical model calculations to describe the surface and interfacial structure and chemistry, a systematic study of the factors controlling the surface chemistry of carbonate minerals can be made. In particular, the effects of substitutional impurities and other point-chemical defects on the structure and geochemical reactivity of carbonate mineral surfaces and interfaces can be isolated and quantified. Moreover, this improved microscopic understanding will eventually provide insights into the behavior of these materials in natural systems.

The approach to meeting program goals involves three interdependent efforts: 1) developing *ab initio* and mechanistic models for interpreting experimental observations regarding the structure and chemistry of the calcite cleavage surfaces; 2) studying the structure and chemistry of the cleavage surface in solution and vacuum; and 3) measuring the reaction kinetics and local nano-scale surface topology during calcite dissolution, using scanning probe microscopy and optical microscopy methods.

During the past year, a terrace ledge kink model was applied to measurements of the influence of various cations on calcite dissolution. The aqueous dissolution of the $(10\bar{1}4)$ surface of calcite had been observed at pH near 9 using an atomic force microscope (AFM) equipped with a fluid cell. The influences of carbonate (CO_3^{2-}), strontium (Sr^{2+}), and manganese (Mn^{2+}) ion concentrations on the rates of step motion were measured. Carbonate ions were shown to have a step-specific effect on calcite dissolution. At low levels ($<1\ \mu M$) of CO_3^{2-}, the retreat rate of the more structurally open $[441]_+$ steps was faster than the retreat rate of the structurally confined $[441]_-$ steps, leading to anisotropic dissolution. Increasing the CO_3^{2-} level to as high as 900 μM decreased the rate of retreat of both steps, but the $[441]_+$ step was slowed to a much greater extent changing the degree of dissolution anisotropy. This decrease in step velocity at high CO_3^{2-} levels was attributed to a corresponding increase in the back reaction (i.e., precipitation) as the solution approached saturation with respect to calcite. Strontium cations were also shown to have a step-specific effect on calcite dissolution similar to that of CO_3^{2-}. Manganese cations, on the other hand, slowed the rate of retreat of the $[441]_-$ step to a greater extent than Sr^{2+}.

The dissolution rate and etch-pit morphology are highly dependent on the presence of cationic impurities and CO_3^{2-} ions in solution. While we cannot directly determine the exact mechanisms or species involved, solution reactions and the observed concentration behaviors indicate that the changes in dissolution rate and etch-pit morphology are kinetically driven by the arrival rates of ions or ion pairs at the calcite surface. Kink propagation is retarded by adsorption of the ions or ion pairs along steps and at single-kink sites.

All of our observations can be understood by considering how "impurity" ions sorbed on kink and step sites "block" dissolution. Although there are many assumptions and approximations in the model, the essence is that the adsorbing species can both influence the formation of double-kink sites and block (or at least inhibit) the dissolution of single-kink sites. At low concentrations, retardation of double-kink formation is the dominant process. At higher concentrations, retardation of single-kink dissolution along the step is dominant. A sharp change in step-edge migration velocities is predicted at the threshold concentration where rate control shifts from double-kink formation to single-kink dissolution. This change is clearly shown in the AFM measurements of step movement (Figure 5.1).
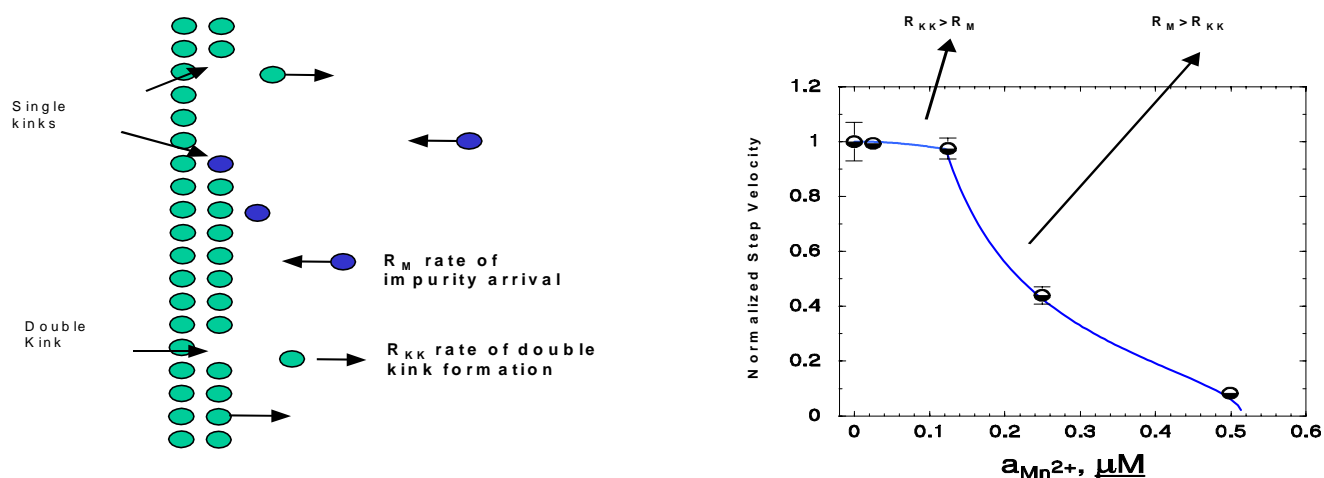
Figure 5.1. Impurity blocking of dissolution at steps on a surface. The major impact of impurities occurs when the rate of impurity arrival is faster than the generation of new kink sites. This is a dynamic process where impurity arrival perturbs or blocks normal dissolution events.

The structure of the calcite water interface was studied using synchrotron based x-ray diffraction by graduate student Phillip Geissbühler and Professor Larry Sorensen from the University of Washington and Neil Sturchio of Argonne National Laboratory. This work found that the surface-carbonate groups of calcite are rotated into the surface relative to the bulk structure and that water above the surface is ordered into an apparent "epitaxial" structure.

In a new series of experiments conducted in collaboration with Professor Luttge at Rice University, vertical-scanning interferometry experiments were made of calcite dissolution and pit formation. Our scanning probe measurements and the optical interferometry observations provide a complementary picture of the surface processes. While the optical measurements offer a wider field of view, the AFM observations allow higher spatial resolution and a more detailed look at the surface.

Hydration of Passive Oxide Films on Aluminum

B. C. Bunker[a,b], G. C. Nelson[a,b], K. R. Zavadil[a], J. C. Barbour[a], F. D. Wall[a], J. P. Sullivan[a], C. F. Windisch Jr., M. H. Engelhard, D. R. Baer, and C. H. F. Peden

Supported by the U.S. Department of Energy Office of Basic Energy Sciences.
(a) Sandia National Laboratories, Albuquerque.
(b) EMSL User.

Models for the corrosion and pitting of passive metals such as aluminum usually involve the migration of point defects through the native oxide film as the rate limiting step (Chao et al. 1981). Hydration of the surface oxide could also influence the protective nature of the film, or contribute to uniform corrosion (Alwitt 1976). Experiments were conducted at the EMSL user facility to investigate how water influences the composition and properties of the native oxide on aluminum using secondary ion mass spectrometry (SIMS). The experiments involved exposing aluminum samples to aqueous solutions that were isotopically labeled with either deuterium or ^{18}O and monitoring the rate at which species from the water (protons, oxygen, and dissolved species such as chloride ions) penetrated the passive oxide film using SIMS depth profiling. A critical aspect of the experiments involved the ability to conduct electrochemical experiments in a special cell that was attached directly to the SIMS apparatus. Use of such a cell allowed us to expose samples to isotopically-labeled water and analyze the samples directly without having to worry about whether the samples exchanged isotopes with the water and oxygen found in typical laboratory environments.

Results of the SIMS experiments (Bunker et al. submitted) revealed that hydration is more rapid and pervasive than is generally recognized, and that reactions with water create hydroxide ion defects within the passive film that may dominate the kinetics of corrosion and pitting. In the absence of an applied voltage, water hydrolyzes Al-O bonds to form hydroxide ions within the film. The SIMS results (Figure 5.2) show that hydration promotes reactions between water and the underlying aluminum, causing the passive oxide to thicken with time as the passive nature of the film is compromised. In hot water, up to 6% of the oxygen in the oxide is
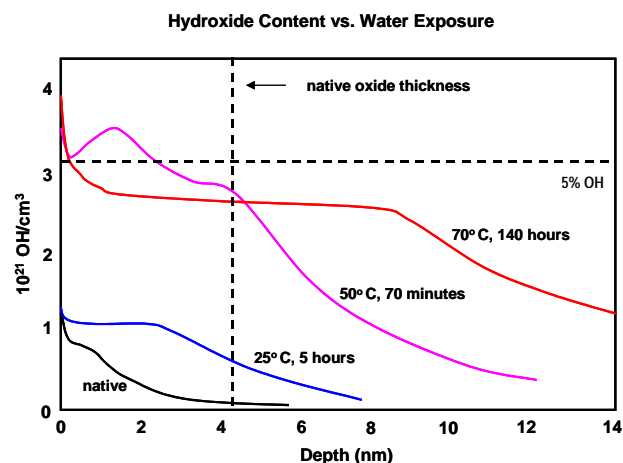
Figure 5.2. SIMS profiles obtained for the mass 17 (OH) species for thermal oxides on Al exposed to water for times and temperatures indicated.

eventually converted into hydroxide ions. Cathodic polarization has little effect on the kinetics of hydration. However, SIMS results show that anodic polarization results in rapid film growth and hydration (Figure 5.3). Anodically-polarized samples can exhibit hydroxide contents as high as 50%, which is consistent with the formation of boehmite films. The SIMS experiments show that when it comes to reactions with water, the thermal oxide on aluminum may be "passivating," but it is certainly not inert. Isotopic exchange of the oxygen in the film is almost 100% after only a few days at room temperature. The SIMS results suggest that ionic transport and diffusion through the passive films ($D = 10^{-19}$-10^{-17} cm^2/sec) is rapid enough to account for the kinetics of both corrosion and pitting.
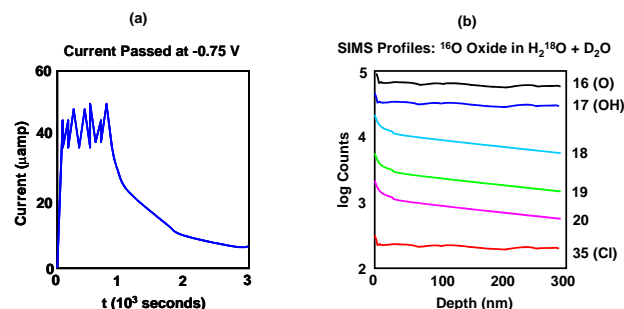
Figure 5.3. a) Current passed through Al sample anodized above the pitting potential at -0.75 V vs. a Pt pseudo-reference electrode, b) SIMS profiles for a range of ionic and isotopic species in the thick oxide film on the same sample.

References

Alwitt, R. S., "The Aluminum-Water System",
  Chapter 3 in *Oxides and Oxide Films*, J. W.
  Diggle and A. K. Vinjh, Eds., Marcell Dekker,
  Inc., New York (1976).
Bunker, B. C., G. C. Nelson, K. R. Zavadil, J. C.
  Barbour, F. D. Wall, J. P. Sullivan, C. F.
  Windisch Jr., M. H. Engelhard, and D. R. Baer,
  submitted to *J. Phys. Chem. B.*
Chao, C. Y., F. Lin, and D. D. Macdonald,
  J. Electrochem. Soc. **128**, 1187 (1981).

Scanning Auger Microscopy Studies of an Ancient Bronze

E. Paparazzo[(a,b)], A. S. Lea,
D. R. Baer, and P. J. Northover[(c)]

Supported by NATO Collaborative Research Grant.
(a) EMSL User.
(b) Istituto di Struttura della Materia del CNR, Italy.
(c) University of Oxford, United Kingdom.

Bronze is one of the materials most commonly found in ancient artifacts. Deterioration of these artifacts through long-term exposure to the environment is a result of corrosion phenomena that occur within the bronze material. Detailed knowledge of the bronze corrosion mechanisms not only provides insight into the deterioration process, but also can aid in the preservation and restoration of these artifacts. For many years, bronze corrosion was considered to be similar to pure copper corrosion. However, the work of Robbiola et al. (1998) demonstrated that bulk corrosion of bronze differs substantially from that of pure copper. While the mechanisms governing bulk corrosion phenomena and how they affect the chemical composition of the bulk (i.e., depth ≥ 1 µm) of ancient objects are reasonably well understood, far less is known about the local and surface (i.e., depths ~0.5 to 3 nm) corrosion processes.

Here we report on a scanning Auger microscopy (SAM) analysis of a fragment cut from a bronze belt from the Urartian kingdom in northeastern Syria originating in the early first millennium B.C. The main objective is to derive a detailed microchemical insight into the object's surface and interface composition. This study has relevance to both the manufacturing procedures used to make the object, as well as to the modifications it underwent as a result of chemical attack by the environment. The manufacturing of bronze involves thermal treatments that may contribute to either altered elemental composition of the surface relative to the bulk, lateral segregation of elements to form second phases, or accumulation of elements at grain boundaries. As a consequence, surface corrosion mechanisms, mostly induced by the chemical agents present in the burial site, likely differ from those in bulk. Since it is often the local corrosion processes that lead to the object's degradation, it is useful to know as much as possible about the local structure and second-phase composition of the artifact. Moreover, the surface layers are of crucial importance in phenomena that have general relevance to archaeometry.

The main results may be summarized as follows:

1. With the exception of lead, none of the bulk metals of the bronze (i.e., Cu, Sn, and Zn) are present in the original patina. Indeed, this region mostly contains Ca-silicates (deriving from the burial site), as well as carbonaceous and N-bearing species, the latter tentatively interpreted as being related to amine-like organic residues from the soil.

2. While the metal side of the surface is otherwise flat, it contains some grains with a highly textured morphology. Point-spectra and images showed that the hollow regions of a grain are SnO_2-rich, whereas the flat regions are Cu_2O-rich. These species are indicators of a locally imperfect mixing of Cu and Sn, and, as such, they bear witness to the "pre-archaeological" chemical modifications the bronze underwent during the alloying stage of the two metals.

3. Intergranular and transgranular corrosion patterns were imaged with a spatial resolution of ~200 nm. In particular, the grain boundaries are rich in S, but deficient in Sn, whereas the external borders of the grain boundaries are rich in both Sn and Zn.

4. Cu and Sn lateral heterogeneities were highlighted with a spatial resolution of ~15 nm. Figure 5.4 shows the microchemical detail that stands distinctly unprecedented among archaeometric studies (using either bulk methods or surface-specific methods) performed on bronze so far.

These results provide new information and hopefully anticipate a wider use of SAM analysis in the study of the surface and interface microchemistry of metallurgical archaeomaterials.

| (a) | (b) | (c) |
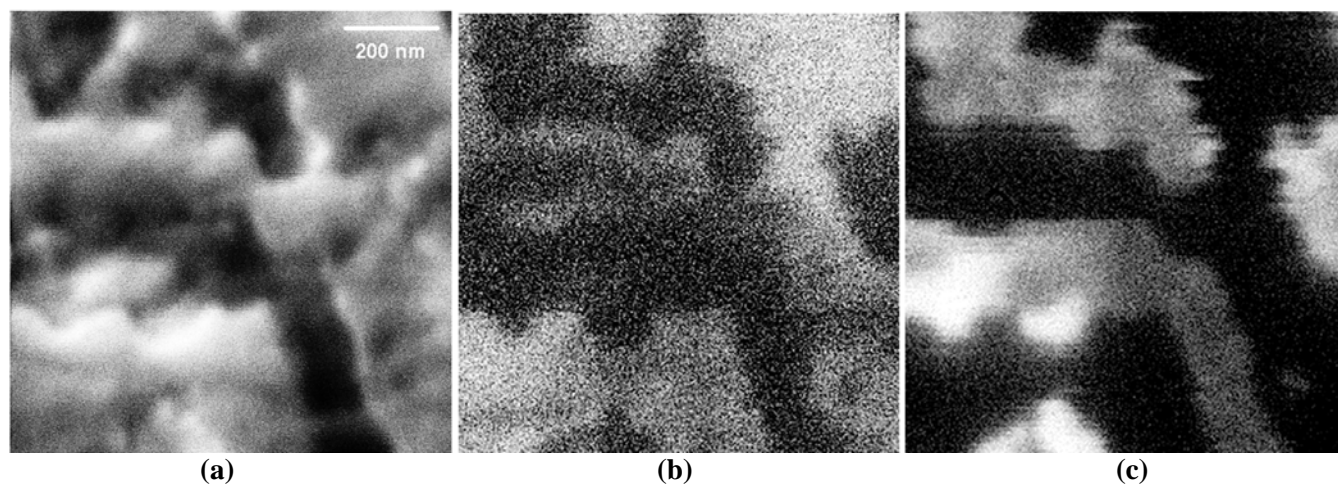
Figure 5.4. SEM and SAM images (100,000X) show the high spatial resolution capable for determining lateral distribution of Sn and Cu in a grain on the bronze surface. a) SEM; b) Cu; c) Sn.

Reference

Robbiola, L., J. M. Blengino, and C. Fiaud,
   "Morphology and mechanisms of formation of
   natural patinas on archaeological Cu–Sn alloys",
   Corros. Sci. **40**, 2083-2111 (1998).

Investigation of Surface and Interface Properties of Iron Oxide Thin Films Grown on Sapphire Substrates Using Ion Channeling and Monte Carlo Simulations

S. Maheswaran[a], S. Thevuthasan, V. Shutthanandan, and E. M. Adams[b]

Supported by the U.S. Department of Energy Environmental Management Science Program and Nepean Seed Grant Scheme.
(a) EMSL User, School of Science, University of Western Sydney-Nepean, Australia.
(b) Student.

Synthesis of model oxides as thin films on various oxide and metal substrates to obtain high-quality surfaces is a growing interest in the scientific community. High-quality iron oxide films have applications in several areas including heterogeneous catalysis, magnetic thin films, surface geochemistry, corrosion, and integrated microwave devices. The aim of the present study is to investigate the disordering at the α-Fe$_2$O$_3$ (0001)/α-Al$_2$O$_3$ (0001) interface using Rutherford backscattering spectrometry and channeling (RBS/C) techniques and Monte Carlo simulations. Channeling measurements were carried out on a pure sapphire substrate and on 0.7- , 7- , and 70-nm-thick, epitaxially grown, high-quality iron oxide films to systematically study the surface and interface properties. Computer simulations were performed using the "VEGAS" program, which uses Monte Carlo calculations, and the surface peak (SP) and interface peak (IP) areas determined from the simulations were compared to the corresponding experimental values.

As an example for experimental data, in Figure 5.5, we show the aligned and random RBS spectra for a 70-nm-thick film. The minimum yield (χ_{min}) was found to be 1.56% for Fe in the film and 5.98% for Al in the substrate. The value of the minimum yield of Fe (1.56%) indicates that the film has a high crystalline quality. Five peaks are visible in the aligned spectrum. The first peak at the high-energy side is the surface peak at the front of the film (Fe – SP). The second peak is attributed to some Fe atoms
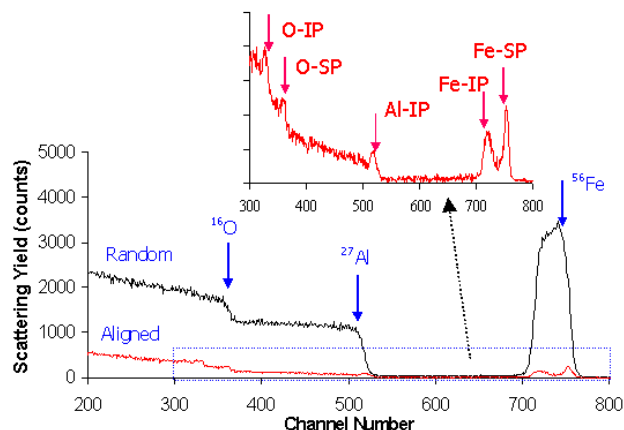
Figure 5.5. Aligned and random RBS spectra from epitaxially grown 70-nm-thick α-Fe$_2$O$_3$(0001) film on α-Al$_2$O$_3$(0001) substrate. Incident energy of the He$^+$ was 2.04 MeV, and the scattering angle was 150°. Magnified version of the aligned spectrum is presented in the insert.

visible to the ion beam at the interface (back surface of the film – Fe - IP). Ion beam measurements also show some Al atoms (substrate surface) at the interface as indicated by the third peak (Al – IP). The fourth peak is related to the backscattered ion contribution due to the surface oxygen atoms (O – SP) of the film, and the fifth peak is due to the visibility of oxygen to the ion beam at the interface (O – IP). Since the Fe, O, and Al atoms are visible to the ion beam at the interface, there must be some disordering at the interface. Although mixing of the substrate and the film is possible at the interface, no evidence for mixing has been observed in the random spectrum within the experimental resolution and the uncertainties. Since similar systems [e.g., $\alpha-$Cr$_2$O$_3$ (0001)/α-Al$_2$O$_3$ (0001)] show misfit dislocations at the interface, we believe this interface [α-Fe$_2$O$_3$ (0001)/α-Al$_2$O$_3$ (0001)] also has misfit dislocations and, as a result, interface is disordered.

Regarding simulations, bulk-like sapphire clusters with appropriate surface terminations and relaxations were used to simulate the experimental surface peak area obtained for Al from the clean substrate. Isotropic thermal vibrational amplitudes of 0.08 A^o and 0.085 A^o for Al and O, respectively, were used in these simulations. The simulated SP area of 6.2 atoms/row for Al agrees very well with the experimental value of 6.2 atoms/row. In the case of

thin iron oxide films, about six bulk-like monolayers with appropriate surface terminations and relaxations and a bulk-like sapphire cluster were used for the simulations. Again, isotropic thermal vibrational amplitudes of 0.07 A^o, 0.08 A^o, and 0.085 A^o for Fe, Al, and O, respectively, were used. The simulated SP areas for Fe and Al are 1.9 and 6.2 atoms/row, respectively. Although the simulated SP area for Fe agrees well with the experimental value (2.0 atoms/row), there is a significant difference between the experimental (7.0 atoms/row) and simulated (6.2 atoms/row) SP areas for Al. This indicates that more Al atoms were visible to the ion beam compared to the Al atoms, which can be visible with just bulk-like sapphire structures. It appears that some of the surface Al atoms are displaced due to the growth of the thin iron oxide film. In the case of the 70-nm-thick film, the experimental SP and IP areas for Fe are 3.9 and 4.3 and the experimental IP area for Al is 7.3 atoms/row. The simulated SP area

of 3.8 atoms/row for Fe agrees well with the experimental value. The IP area of 7.3 atoms/row appears to be slightly higher than the Al atoms visible (7.0 atoms/row) in the case of the 0.7-nm-thick film. This increase may be due to either more displaced Al atoms at the interface, dechanneling in the iron oxide film, or a combination of both. Regarding the experimental IP area for Fe (4.3 atoms/row), it would be very difficult to simulate this using the VEGAS code since both interface disordering and dechanneling contribute to the Fe IP. Since these results are consistent with the interface disordering due to misfit dislocations, a cluster with misfit dislocations at the interface was used in the simulation of IP areas for Fe and Al. Although the VEGAS code cannot accommodate large clusters, the simulations with smaller clusters indicate the possibility for an existence of an interface with misfit dislocation for this system. Detailed simulations are currently in progress.

Corrosion of Mg- and Cu-Implanted Al in 3.5% NaCl Solution

C. F. Windisch Jr.[a], D. R. Baer,
M. H. Engelhard, M. J. Danielson[a], and
R. H. Jones[a]

Supported by the U.S. Department of Energy Office of Basic Energy Sciences.
  (a) PNNL Energy Science and Technology Division.

The intergranular stress corrosion cracking (IGSCC) of Al alloys containing Mg has been related to the presence of Al_3Mg_2 at grain boundaries (Spidel and Hyatt 1972). Similarly, Cu is believed to influence Al corrosion when present as Al_2CuMg particles (Buchheit et al. 2000). In both cases, however, the role of intermetallic phases at grain boundaries is insufficient to explain IGSCC in Al alloys because these phases are not generally continuous along the grain boundary surfaces. It appears that part of the mechanism of IGSCC of Al alloys also involves Mg and Cu segregated to grain boundary surfaces but still in solution with the Al matrix. In a series of experiments designed to mimic the composition and conditions of these surfaces, pure Al samples implanted with Mg or Cu were electrochemically treated in 3.5% NaCl solution and then analyzed with x-ray photoelectron spectroscopy (XPS) using a UHV transfer system. Experiments were performed as a function of pH and polarization conditions.

Earlier measurements in neutral 3.5% NaCl solution showed that pure Al and Mg- and Cu-implanted Al samples gave identical potential responses as a function of time (Baer et al. 2000). Because these tests in neutral 3.5% NaCl indicated that the strong propensity of Al to passivate under neutral conditions masked any effects of the Mg and Cu, additional studies were undertaken at conditions where passivation would be inhibited. Both buffering to acidic (pH=3) and alkaline (pH=10) conditions destabilized the film to some extent and appeared to contribute to observed differences in both electrochemical behavior and the composition of the resulting films. However, the samples exposed to acidic conditions tended to show more localized corrosion sites than those tested under alkaline conditions. Therefore, a series was undertaken in

alkaline (pH=10) solutions where the passive oxide films appear to be sufficiently destabilized so that the effects of the Mg and Cu could be observed.

Pure Al and the Mg- and Cu-implanted Al samples exhibited very different behavior when polarized slightly anodic (100 mV vs. the original OCP) for 500 seconds in 3.5% NaCl solution adjusted to pH=10 with NaOH. As shown in Figure 5.6, the resulting current for pure Al reached a steady-state value rapidly after polarization. The Mg-implanted sample gave more anodic (negative) current than pure Al, and this current gradually dropped over the course of 500 seconds until it reached a value close to pure Al. The Cu-implanted sample exhibited anodic current at first but then the current lessened, becoming cathodic (positive) after about 300 seconds. These results clearly indicate that, unlike the tests in neutral solution, experiments using alkaline media reveal distinct effects of the implanted elements on corrosion. The NaOH destabilized the oxide films so the rates of passivation and corrosion were similar enough to permit the influence of the implanted elements to be observed within the time frame of the experiments.

Depth profiling by XPS on samples polarized and then transferred under UHV to the XPS revealed important differences between the samples that could be related to the differences observed in the electrochemical responses. As shown in Figure 5.7, the depth profile for the Mg-implanted sample indicates the presence of a relatively thick (≈ 100 nm)
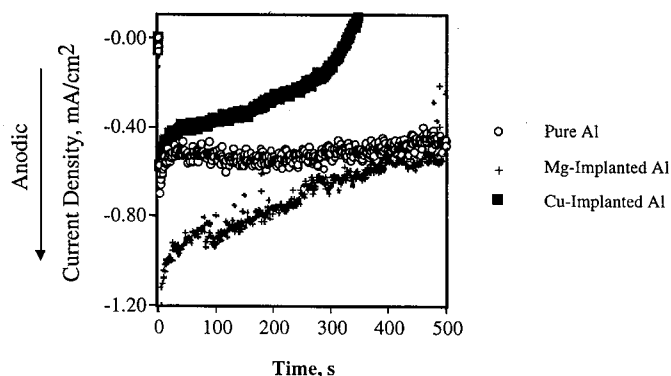
Figure 5.6. Current responses for Al, Mg-implanted Al, and Cu-implanted Al specimens after a potential step 100 mV anodic to OCP in 3.5% NaCl adjusted to pH=10.
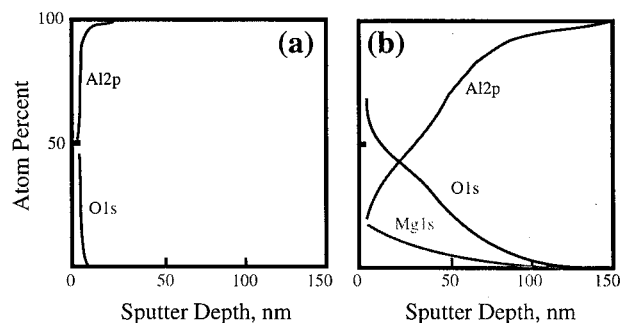
Figure 5.7. XPS depth profiles for (a) pure Al and (b) Mg-implanted Al.

Figure 5.8. XPS depth profiles for Cu-implanted Al after potential step 100 mV anodic to OCP in 3.5% NaCl adjusted to pH10.

oxide layer compared to the thin (<10 nm) layer on pure Al treated under the same conditions. Furthermore, the data show that essentially all of the Mg originally implanted into the metal was oxidized, either dissolved into solution or incorporated into the film. The Cu-implanted samples gave very different XPS depth profiles as shown in Figure 5.8. These profiles showed a thin oxide layer similar to that observed on pure Al. The Cu has largely been removed from the metal as a result of polarization but, unlike Mg in the Mg-containing samples, accumulated in a thin layer between the oxide and the metal surface. The peak Cu concentration in this layer was enriched to about 8 at. %, compared to the peak concentration originally in the metal (1 at. %).

The results of this work clearly indicate that both Mg and Cu can have an effect on the corrosion of Al when dissolved in the Al at grain boundaries, but only under conditions when the metal is not fully passivated. In this work, this condition was achieved by using alkaline solutions; whereas, in a crack, the situation may exist immediately after the crack is opened and prior to passivation. Under

these conditions, both Mg and Cu appear to enhance corrosion. The effect of Cu appears to be galvanic (i.e., accelerating corrosion) under open circuit conditions.

At slightly positive potentials (relative to the initial OCP), however, the galvanic influence on Al oxidation is suppressed because the surface becomes enriched in Cu metal and the electrochemically driven oxidation reactions shift to the counter electrode.

References

Baer, D. R., C. F. Windisch Jr., M. H. Engelhard, M. J. Danielson, R. H. Jones, and J. S. Vetrano, *J. Vac. Sci. Technol. A* **18**, 131 (2000).

Buchheit, R. G., M. A. Martinez, and L. P. Montes, *J. Electrochem. Soc.* **147**, 119 (2000).

Spidel, M. O. and M. V. Hyatt, in *Advances in Corrosion Science and Technology Vol. 2,* edited by M. G. Fontana and R. W. Staehle, p. 115, Plenum Press, New York (1972).

6. Microanalytical Separations and Sensing

Microfabricated Sensor Arrays

J. W. Grate, D. A. Nelson [(a,b)],
N. Anheier [(a,c)], *and J. Price*

Supported by the U.S. Department of Energy, Office of Nonproliferation Research and Engineering.
(a) EMSL Matrixed Staff.
(b) PNNL Environmental Technology Division.
(c) PNNL National Security Division.

The use of microfabricated sensor arrays is a promising approach for the development of field analytical instruments for chemical vapor detection. These instruments are needed for a variety of environmental and national security applications.

The ultimate objective of a field analytical instrument is to provide chemical information about samples of interest. Sensor arrays offer greater chemical information than single sensors, with improved selectivity and the potential for analyzing multiple species in a mixture simultaneously. These arrays are designed by applying chemically interactive sorbent coatings on microfabricated transducers. The transducers provide measurable signals in response to changes in the physical properties of the sorbent layer upon interaction with chemical species. The use of several such sensors in an array, each with an interactive layer with distinct selectivity, gives rise to response patterns that can be used to distinguish one compound from another.

Development of sensor array-based instrumentation is a multidisciplinary effort. We are involved in a number of research areas designed to advance the performance of array-based instruments for chemical analyses. These include crosscutting areas that can be applied to a variety of sensor device technologies, as well as advances in the specific area of acoustic wave sensors. Crosscutting areas include developments in polymeric sensing materials, new pattern recognition approaches, and analyte preconcentration. This work is performed by understanding vapor/polymer interactions that are systematically characterized using linear solvation energy relationships (LSERs), a form of linear free energy relationship.

In the acoustic wave sensor field, we are developing array-on-a-chip detection methods using flexural plate wave (FPW) devices. When coated with polymeric

sorbent layers, these devices detect mass increases and polymer modulus decreases that occur when vapors are absorbed by the polymer. We recently published a comprehensive review of "Acoustic Wave Microsensor Arrays for Vapor Sensing" in a special issue of *Chemical Reviews* about chemical sensors (Grate 2000).

Using hydrosilylation as the bond-forming reaction, we have developed a versatile and efficient approach to developing sorbent polymers with diverse interactive properties for sensor applications. Both the chemical and physical properties of these polymers are predictable and tunable by design. Hydrosilylation polymerization method is capable of incorporating a variety of organic structures and functional groups into a polymeric structure. Diverse polymers with various functional groups have been prepared, and the resulting polymers exhibit low glass-to-rubber transition temperatures. These are useful sensing materials for a variety of sensing platforms, including acoustic wave and optical sensors. We use these polymers in our sensing studies, and have supplied samples to other researchers in the sensor field. For example, one of our polymers, for which we recently received a patent (Grate and Kaganove 2000), has been used in lab-on-a-chip applications for chemical agent detection. Our approach has recently been described in detail in an article on "Carbosiloxane Polymers for Chemical Sensors" in *Chemical Innovations* (Grate et al. 2000).

We have also shown that hydrosilylation chemistry can be used to crosslink, graft, and photopattern polymer layers. Photopatterning is achieved by incorporating an initially inactive catalyst in the prepolymer formulation. Upon exposure to ultraviolet light, the catalyst in the film is activated and hydrosilylation reactions occur in the film. The films can be formulated so that these reactions cause polymerization, crosslinking, and covalent grafting to surface functional groups. These reactions result in film domains whose solubility is different from unexposed prepolymers. Unexposed regions can be dissolved away, leaving a pattern of the exposed material. An example is shown in Figure 6.1. The ability to photopattern sensing materials into discrete domains on microfabricated structures is important for obtaining useful chemical sensors from microfabricated electromechanical systems (MEMS). Given an array of polymer-coated sensors, the response patterns to

Figure 6.1. Lines of a photopatterned chemical sensing polymer on a silicon wafer with a nickel placed for size comparison.

vapors can be processed using statistical pattern recognition techniques or neural networks to classify the detected vapor. In conventional pattern recognition, the observed patterns are compared with patterns found on training the array against known compounds at calibrated concentrations. We set out to advance the field of pattern recognition by using the found patterns to estimate the chemical properties of the

unknown vapor, even if the specific vapor has not been used in training (Grate et al. 1999). The sensor array pattern vector is converted into another vector containing vapor descriptors. These descriptors are those that are used in linear solvation energy relationships, and they provide measures of properties such as dipolarity, polarizability, hydrogen-bond basicity, and hydrogen-bond acidity. By analogy, an infrared spectrum can be used to characterize an unknown in terms of functional groups, even if no reference spectrum for the specific compound is available for comparison.

Polymer synthesis, polymer photopatterning, and new pattern recognition techniques are just a few highlights from this interdisciplinary microanalytical project.

References

Grate, J. W., B. M. Wise, and M. H. Abraham, *Anal. Chem*, **71**, 4544-4553 (1999).

Grate, J. W., *Chem. Rev.,* **100(7)**, 2627-2647 (2000).

Grate, J. W. and S. N. Kaganove, "Strongly Hydrogen Bond Acidic Polymer and Methods of Making and Using", U.S. Patent, 6,015,869, January 18, 2000.

Grate, J. W., S. N. Kaganove, and D. A. Nelson, *Chemical Innovations*, **30(11)**, 29-37 (2000).

Microfluidic Renewable Sensing

J. W. Grate, C. J. Bruckner-Lea, D. Holman[a], and R. M. White[b]

The objective of this project is to develop microanalytical methods for trace chemical detection in liquid phases. Unlike conventional chemical sensors requiring chemoselective materials whose interactions with analytes are reversible, this project is focused on automated delivery of chemoselective interfaces on microsphere surfaces to and from the active area of the detector. The microspheres can be delivered in suspension, captured in the detection zone, perfused with sample and reagents, and then released prior to the next sample. Then a fresh suspension of microspheres can be used for the next sample. In this way, the sensing surface is renewed for each measurement.

This project has two parallel approaches to implementing renewable surface sensing. In one approach, the delivery and manipulation of reagents, samples, wash solutions, and bead suspensions is carried out using a computer-operated sequential injection (SI) system. Sequential injection is a recent variant of flow-injection methods that provides greater precision and versatility while being more compatible with computer control. This approach is an open architecture fluid handling method giving the experimentalist complete control over system design, materials, and operation. At PNNL, we have designed a variety of flow cells for automated capture and release of microspheres. A method for automating enzyme-amplified immunoassays using antibody-derivatized magnetic beads has been demonstrated using TNT as the test analyte.

Our second, more speculative approach for manipulating bead suspensions involves the use of flexural plate wave devices. These acoustic wave devices can pump fluids and microsphere suspensions by an acoustic streaming method. This novel fluid drive mechanism stands in contrast to more common electro-osmotic pumping methods, providing reversible fluid flow at low voltages. In addition, unlike most microfabricated pumps with check valves, the FPW technique permits the pumping of suspensions of beads. This work is being carried out in collaboration with the Berkeley Sensor and Actuator Center at the University of California, Berkeley. Recent work has focused on methods to manipulate and concentrate microspheres in microchannels using these devices.
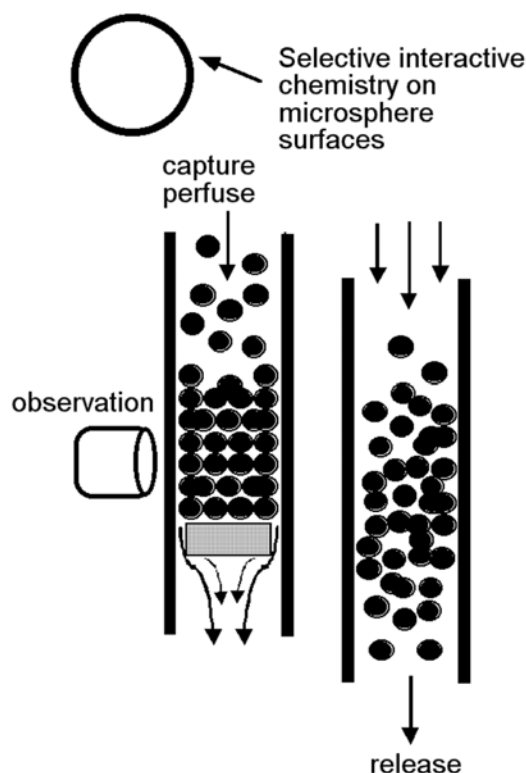
Figure 6.2. Conceptual scheme for renewable surface methods. The barrier to microspheres can be removed mechanically or fluidically. Observations can be made on the trapped bead surfaces (sensing) or downstream (separations).

Integrated Systems for DNA Sample Preparation and Detection in Complex Sample Matrices

C. J. Bruckner-Lea, D. Chandler[a], J. W. Grate, B. Dockendorff[b], S. Gunaratnam[b], D. Holman[c], J. Kim[c], J. Stults[a], J. Price, J. Follansbee, D. Hopkins, T. Tsukuda[d,e], M. Kingsley[d,e], J. Posakony[d,f], and L. Bond[d,f]

Supported by PNNL Laboratory Technology Research, NASA, and the Office of Naval Research.
(a) PNNL Fundamental Science Division.
(b) Student.
(c) Postdoctoral Research Fellow.
(d) EMSL User.
(e) PNNL Environmental Technology Division.
(f) PNNL National Security Division.

The rapid detection of specific microorganisms or gene sequences is required in many areas of basic and applied research in both clinical and environmental science. Applications range from pathogen detection in environmental and food samples to disease diagnosis and drug screening. Nucleic acid analysis in complex samples typically includes some combination of sample collection, sample concentration, cell lysis, nucleic acid target amplification, and analyte detection processes. A fully integrated system for detection and characterization of nucleic acids must likewise embody these functions. We are working on several projects focused on developing different DNA sample preparation modules that can be tailored to meet specific biodetection needs, depending upon the sample type. Our recent projects have focused on developing an automated system as a 'front-end' for biological warfare detectors, for detection of bacterial DNA in soil samples for monitoring microorganisms in recycled water used on space stations, and for monitoring health hazards on U. S. Navy submarines. These projects involve the use of equipment and capabilities within the Sensor Laboratories of the Interfacial Chemistry and Engineering Group of the EMSL.

The most common approaches to bioanalytical automation are robots that can automate manual manipulations (e.g., pipeting, mixing, centrifugation, filtration, and incubation) or integrated "chips" that perform all manipulations in nanoliter volumes. These technologies are very advanced, but are either too large and cumbersome for point-of-use application, or too small to process sample types and volumes typifying many practical biodetection problems. For example, the sample may consist of a large volume of chicken wash solution being tested for the presence of biological pathogens, a soil extract with high biomass content being tested for DNA present at low concentration, or a blood sample being tested for infected white blood cells present at low concentration. In these situations, even for highly-sensitive detection systems such as DNA probe assays, large sample volumes (milliliters) must be interrogated for statistically meaningful results. In addition to concentration of DNA, the sample preparation system must remove compounds that interfere with subsequent detection systems (e.g., PCR inhibitors such as humic acid in soil or red blood cells in a blood sample).

We are developing DNA sample preparation systems for handling sample sizes ranging from many milliliters down to a few microliters. The systems include renewable microcolumns for sample concentration and purification. Microbeads with a specific surface chemistry are trapped and perfused within the fluid path. After the purification/detection is complete, the microbeads are flushed from the system. This approach is attractive because the delivery of different microbeads is automated for reproducible, real-time, analytical testing. Furthermore, the microbeads are used only one time, which makes it possible to include irreversible binding chemistries and analyze complex sample matrices that inevitably lead to surface fouling. The systems are well suited for reversible sensing applications, automated serial assays, on-column or off-column detection, and biological or chemical separations/detection.

Technology Components

Cell Concentration. We have developed and demonstrated a novel electromagnetic flow cell for sample preconcentration utilizing immunoreagents or non-specific binding interactions between target cells and magnetic particles. Novel features of the electromagnetic flow cell include uniform field gradients throughout the flow path and the ability to trap and perfuse nanoparticles in addition to standard particles.

Flow rates up to 200 µl/s are possible without loss of matrix from the system. Successful on-line immuno-captures have been performed at 10 cells/ml with comparable performance to batch capture protocols.

Cell Lysis. In keeping with the integrated system concept and the need to process complex/recalcitrant cell types, we have developed a flow-through physical lysis system and demonstrated >99% lysis of Bacillus globigii spores. DNA liberated from the spores is available and intact for PCR and other molecular-based detection components.

Nucleic Acid Purification. With a judicious choice of microbead surface derivatization, nucleic acids can be purified free from PCR inhibitors from a sample as complex as garden soil. We have isolated and purified 1 attamole (8.3 fM) target DNA from a crude soil extract in 18 minutes, using a single pass purification protocol. Benchtop methods require more than 4 hours to achieve comparable purification efficiencies with this reagent.

DNA Amplification and Detection. For low-copy number detection problems, target amplification is required to generate enough analyte for even the most sensitive (nucleic acid) detectors. We are currently developing reusable flow cells that utilize either polymerase chain reaction (PCR) or strand displacement amplification (SDA) for amplifying DNA. We are currently investigating methods for eliminating DNA carryover between samples to allow reuse of the flow cell. EMSL surface analysis equipment is being used to characterize the internal surfaces of fluidic system components, so that we can understand and optimize the surface chemistry to eliminate DNA carryover between samples. DNA detection is achieved by the incorporation of fluorescent probes during the DNA amplification process.

Integrated System Development. We also are developing an integrated DNA sample preparation system in collaboration with the Instrument Development Group in the EMSL. The initial prototype device, shown in Figure 6.3, has a footprint the size of notebook paper, and includes cell concentration, cell lysis, and DNA amplification and detection modules for processing liquid samples ranging in size from 100 microliters to 100 milliliters.
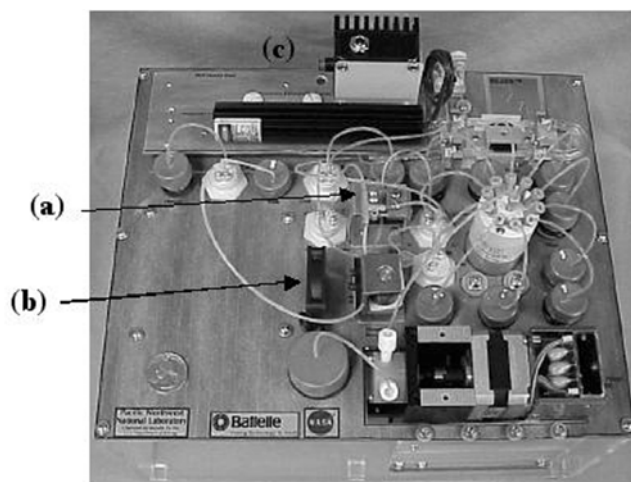
Figure 6.3. Photo of the first integrated system prototype for processing 0.1 to 100 ml aqueous samples for DNA-based detection. Cell concentration is at (a), then beads with attached cells are moved to (b) for on-bead amplification. Fluorescence detection of the PCR product is at (c).

Supporting Publications

Bruckner-Lea, C. J., D. A. Holman, B. L. Schuck, F. J. Brockman, D. P. Chandler, "Strategies for automated sample preparation, nucleic acid purification, and concentration of low target number nucleic acids in environmental and food processing samples", *SPIE Proceedings*, **3544**, 63-71 (1999).

Bruckner-Lea, C. J., M. S. Stottlemyre, J. W. Grate, D. A. Holman, F. J. Brockman, and D. P. Chandler, "Rotating rod renewable microcolumns for automated, solid-phase DNA hybridization studies", *Anal. Chem*, **72**, 4135-4141(2000).

Bruckner-Lea, C. J., N. C. Anheier, Jr., D. Holman, T. Tsukuda, M. T Kingsley, F. J. Brockman, J. M. Price, J. W. Grate, and D. P. Chandler, "Integrated systems for DNA sample preparation and detection in environmental samples", *SPIE Proceedings,* **4200**, *in press* (2001).

Chandler, D. P., B. L. Schuck, F. J. Brockman, and C. J. Bruckner-Lea, "Automated nucleic acid isolation and purification from soil extracts using renewable affinity microcolumns in a sequential injection system", *Talanta*, **49**, 969-983 (1999).

Chandler, D. P., F. J. Brockman, D. A. Holman, J. W. Grate, and C. J. Bruckner-Lea, "Renewable microcolumns for solid-phase nucleic acid separations and analysis from environmental samples", *Trends Anal. Chem.*, **19**, 314-321 (2000).

Biomolecular Interaction Assay

C. J. Bruckner-Lea, J. W. Grate,
B. Dockendorff[a], D. Holman[b], J. Kim[b],
E. Ackerman[c,d], and L. Iachoucheva[c,d]

(a) Student.
(b) Postdoctoral Research Fellow.
(c) PNNL Fundamental Science Division.
(d) EMSL User.

Understanding protein-protein and protein-DNA interactions is integral to understanding the function of living organisms and how organisms respond to insults such as environmental exposure to chemicals and radiation. We are using capabilities in the Sensors Labs of the Interfacial Chemistry and Engineering Group to develop methods for rapidly measuring the interactions between biomolecules (e.g., proteins and DNA) and multiple protein complexes. This project advances our ability to rapidly measure biomolecular interactions and therefore understand biological systems.

Renewable surface sensing techniques are being developed for monitoring biomolecule binding events. In this approach, a suspension of surface derivatized beads is introduced into a flow system and then automatically trapped by a barrier that stops the beads but allows the fluid to proceed (Chandler et al. 2000; Ruzicka and Scampavia 1999; Ruzicka 1998). This produces a small microcolumn of beads (only about a microliter in volume) in a location for observation. The beads can then be automatically perfused with reagent or sample solutions to perform separations or surface reactions. Detection methods can be used to observe optical changes (absorbance or fluorescence) on the bead surfaces. At the completion of the observation, the beads can be flushed from the observation area and disposed. A new bed of beads can then be packed for the next assay. This new bead bed has a fresh surface, hence the name renewable surface sensing.

The key advantages of this approach for monitoring protein binding events are that the experiments are rapid, automated, and require small sample volumes. Typical sample volumes currently used are 50 µl and the perfusion rate is 0.5 µl/s, so that sample perfusion and washing can occur in less than 5 minutes. These volumes and time could be scaled down even further by using smaller syringe pumps. In addition, this approach does not require fluorescent labeling and is suitable for the detection of protein complexes containing multiple proteins. This is in contrast to surface sensitive methods for monitoring protein binding such as surface plasmon resonance devices (e.g., BiaCore), in which the measurement sensitivity falls off exponentially with film thickness. When general nonspecific binding is a concern, the spectral information can be used in some cases to distinguish between molecules. The on-column measurement of absorbance as a function of wash stringency conditions can also be used to investigate the conditions required for removing non-specifically adsorbed molecules.

Two custom renewable surface flow cells were designed and evaluated: 1) a piston flow cell and 2) a rotating rod flow cell. Both flow cells included a microcolumn volume of about 1 µl and a path length of 1 mm. The fluidic system allowed automated packing of a microcolumn from a stirred slurry, followed by perfusion of the column with various sample and wash solutions (all automated). Optical fibers leading to the flow cell were used to monitor the microcolumn absorbance during column delivery and protein binding to the microcolumn during sample perfusion. The reproducibility of column packing and absorbance baseline noise were identical for both devices; however, the rotating rod design (Figure 6.4) was more reliable and rugged over many months of use.

The detection of the binding of multiple proteins was demonstrated using the renewable microcolumn system. Microcolumns that are 1 µl in volume were automatically formed from a slurry of Sepharose beads. Sepharose beads were derivatized with Protein G, and absorbance spectra were collected during and Sepharose 4B beads (Zymed) was estimated to be
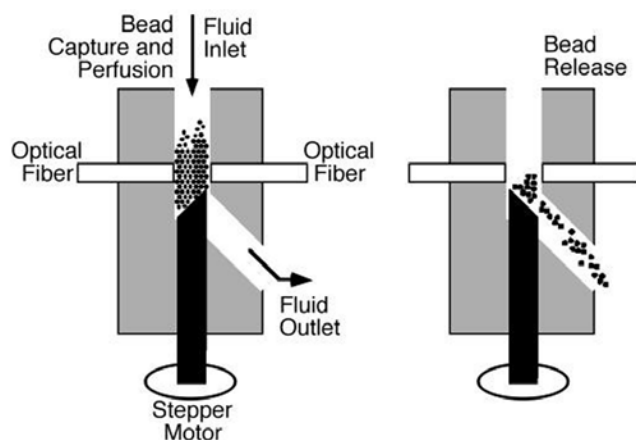
Figure 6.4. Rotating rod renewable surface system with optical detection. Small microcolumns (about 1-μl packed bed volume) are automatically captured and perfused with samples such as cell extracts. Optical fibers are used to monitor the UV-Vis absorbance during protein binding. After perfusion, the beads are automatically released (right) to allow detection of proteins with low absorbance. Currently, we are incorporating on-column fluorescence detection and using the automated biomolecular interaction assay system to study DNA-protein interactions.

in situ binding of human IgG and goat anti-human-IgG. The data showed that the renewable micro-column system can detect *in situ* binding of multiple proteins (Figure 6.5). The detection limit of the renewable microcolumn system that included a 1-mm path length 5 ng of protein bound to the beads (as measured using commercial IgG antibody proteins). However, fluorescence detection (rather than absorbance) will be necessary in some cases for increasing sensitivity to allow detection of proteins with low absorbance. We are currently incorporating on-column fluorescence detection and using the automated biomolecular interaction assay system to study DNA-protein interactions.
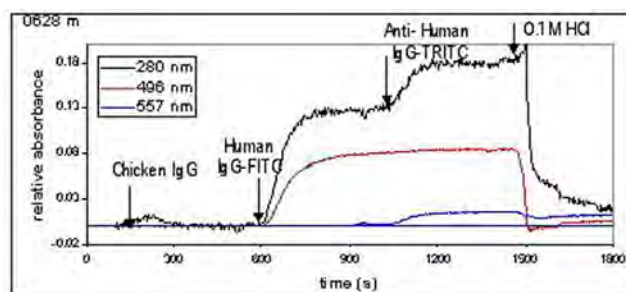
Figure 6.5. Automated renewable microcolumn protein binding experiments demonstrating the selective binding of multiple proteins. On-column absorbance data are shown at three wavelengths. The column is perfused at 0.5 μl/s with three proteins (40 μg/ml, 50 μl). Each injection is followed by 150-μl PBS (0.5 M HCl, pH 7.4). Chicken IgG does not bind to the protein G Sepharose beads (demonstrates negligible non-specific protein binding), but subsequent injections of human IgG and goat anti-human IgG bind to the microcolumn. The protein binding can be monitored in the UV region (due to aromatic amino acids) and also at the wavelengths of specific labels on the proteins (fluorescein = 496 nm and tetramethyl-rhodamine = 557 nm).

Supporting Publications

Chandler, D. P., F. J. Brockman, D. A. Holman, J. W. Grate, and C. J. Bruckner-Lea, "Renewable microcolumns for solid-phase nucleic acid separations and analysis from environmental samples", *Trends Anal. Chem.* **19**, 314-321 (2000).

Ruzicka, J., "Bioligand interaction assay by flow injection absorptiometry using a renewable bio-sensor system enhanced by spectral resolution", *Analyst* **123**, 1617-1623 (1998).

Ruzicka, J. and L. Scampavia, "From flow injection to bead injection", *Anal. Chem.* **71**, 257A-263A (1999).

Microfluidics/Electrochemical Sensors for Monitoring of Environmental Exposure to Complex Chemical Mixtures

Y. Lin[a], K. Thrall[b], C. Timchalk[a,b], R. Zhao[c], and J. Wang[d]

Supported by PNNL Environmental Health Initiative Laboratory Directed Research and Development funding.
  (a) EMSL Matrixed Staff, PNNL Environmental Technology Division.
  (b) PNNL Fundamental Science Division.
  (c) Postdoctoral Research Fellow.
  (d) New Mexico State University.

The ultimate goal of the proposed work is to develop a miniaturized analytical system based on a micro-fluidics/electrochemical detection scheme. The system will be used for the on-site characterization and real-time monitoring of toxic chemical mixtures in waste sites and eventually for non-invasive monitoring of biological samples from workers. The development of this instrument will greatly enhance ongoing efforts to improve the health protection of workers in the field.

Microfluidics/Electrochemical Sensor System

The fabrication scheme for the microfluidic platform was based on a multi-layer lamination method. With the exception of the detector module, all components were fabricated from fluorinated ethylene propylene (FEP) or polyimide. All in-plane microchannels, including the mixing/reaction channel, were produced by sandwiching laser-machined, adhesive-backed polyimide gaskets between layers of the device. Individual components, such as the microfabricated piezoelectrically-actuated pumps, the sample and reagent reservoirs, and microelectrochemical flow cell were designed as plug-in parts, allowing for rapid change-out and repair if necessary. The base dimensions of the microfluidic device were 5.0 x 8.0 cm. The overall height of the device was approximately 2.5 cm. The analytical system was controlled using a laptop computer.

Non-Invasive Biomonitoring of Lead

The integrated microfluidic analytical system was used for the detection of lead using square wave anodic stripping voltammetry (SWASV). For lead detection, a constant potential of -1.10 V is applied on a glassy carbon mercury-film electrode. When sample solution flowed through the electrode surface, Pb^{2+} was reduced and accumulated. After accumulation for 3 min, the potential of the mercury film electrode was scanned from -1.10 V to -0.10 V for stripping analysis. The linear range for the calibration curve is 1 to 200 ppb Pb^{2+}. The detection limit for Pb^{2+} is 0.2 ppb using a 3-min preconcentration period.

One aim of this work was to demonstrate the use of the microanalytical system for field application in non-invasive biological monitoring of occupational exposure to lead for workers involved in cleanup of waste sites. Groups of rats were used for animal studies to evaluate the relationship between Pb concentration in blood and saliva. Our results indicated that the relationship followed a biphasic curve. In general, the Pb concentration in whole blood was 1 to 2 orders of magnitude greater than that in the saliva. A physiologically based pharmacokinetic (PBPK) model was developed to predict blood Pb concentration based on analyzed saliva Pb levels. The results indicate that it is feasible to detect the occupational exposure to lead by analyzing Pb levels in saliva.

Environmental Monitoring of Chlorophenol

A simple sample pretreatment was used to convert chlorophenols into the simple product, phenol, for the purposes of detection and analysis. In preliminary experiments in which we collaborated with Prof. Cheng at the University of Idaho, chlorophenols were shown to convert into phenol by a simple dechlorination reaction under an Mg/Pd catalyst. The reaction was completed rapidly:
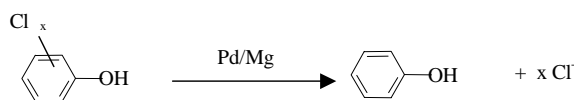
By detecting the end product, phenol, we can detect the chlorophenols.

The electrochemical biosensor developed for phenol was designed and fabricated based on the immobilization of an enzyme, tyrosinase, onto an electrode and the amperometric detection of the enzymatically formed quinone product (Figure 6.6).

The remarkable specificity of biological recognition of tyrosinase led to a high selectivity for phenol detection. Amperometric detection of phenol was carried out with the microanalytical system. The buffer reservoir contained a 0.02-M phosphate buffer (pH 7.0). The flow rates of both buffer and sample solutions were 20 μL/min. A constant potential of -0.20 V versus Ag/AgCl was applied to the working electrode. The response to phenol was linear in the concentration range of 1×10^{-7} to 1×10^{-4} mol/L. The detection limit was determined to be 5×10^{-8} mol/L.
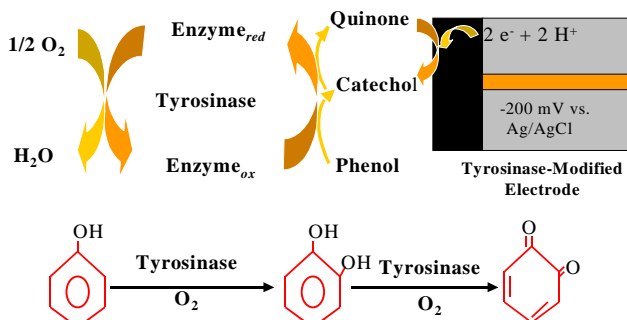
Figure 6.6. Principles of biosensor for phenol detection.

The above results indicate that by combination of selective catalytic dechlorination for sample pretreatment, the microfluidics/electrochemical sensor system could be applied for on-site screening of various highly chlorinated phenols in contaminated biological and environmental samples.

The detection of chlorophenols using microfabricated capillary electrophoresis/electrochemical detection is in progress in collaboration with New Mexico State University.

Supporting Publications

Lin Y., C. Timchalk, D. W. Matson, H. Wu, and K. D. Thrall, "Integrated Microfluidics/ Electrochemical Sensor System for Environmental Monitoring of Chlorophenols", *Biomedical Microdevices*, submitted (2000).

Lin Y., D. W. Matson, W. D. Bennett, K .D. Thrall, and C. Timchalk, "Integrated Microfluidics/Electrochemical Sensor System for Field-Monitoring of Toxic Metals", in *Microreaction Technology: Industrial Prospects*, W. Ehrfeld, ed., pp. 588-596, Springer-Verlag (2000).

Lin Y., R. Zhao, K. D. Thrall, C. A. Timchalk, W. D. Bennett, and D. W. Matson, "Integration of microfluidics/electrochemical system for trace metal analysis by stripping voltammetry", *Proceedings of SPIE*, **3877**, 248-256 (1999).

Timchalk, C., T. S. Poet, Y. Lin, K. K. Weitz, R. Zhao, and K. D. Thrall, "Development of an Integrated Micro-Analytical System for Lead in Saliva and Linkage to a Physiologically Based Pharmacokinetic Model Describing Lead Saliva Secretion", *American Industrial Hygiene Association Journal*, in press (2000).

Laser-Machined Microfluidic Devices for Bioanalytical Applications

Y. Lin[(a,b)], K. Tang, D. W. Matson[(c)], and R. D. Smith

   (a) EMSL Matrixed Staff.
   (b) PNNL Environmental Technology Division.
   (c) PNNL Energy Science and Technology Division.

The development of capabilities to miniaturize analytical devices and components offers a number of potential benefits. Among these are the ability to reduce sample sizes; the development of low-cost, single-use disposable devices; and increased sample throughput. Extensive work has been done on producing such microdevices on silicon or glass substrates using processes commonly employed in electronic chip manufacturing. For many analytical applications, however, common polymeric materials provide acceptable substrates from which to produce microfluidic devices. In this work, we have developed several polymer microfluidic devices using laser-micromachining technology and have successfully demonstrated the application of these microfluidic devices for rapid and automatic cleanup, fractionation, and separation of complex biological samples.

Single-Stage and Dual-Stage Microdialysis Devices for On-Line Cleanup and Fractionation of Complex Biological Samples

Microfabricated single-stage and dual-stage microdialysis devices were developed for fast and efficient cleanup and fractionation for electrospray mass spectrometric (ESI-MS) analysis of complex biological samples. The sample channel (60-μm deep, 150-μm wide) was machined directly into the polymer chip (30x30x6 mm) by using multiple parallel laser passes. A 500-μm-wide buffer channel was machined from 225-μm-thick polyimide with a silicone adhesive on one side. The adhesive was used to attach the buffer channel to a flat polymer chip. Two microdialysis

membranes are sandwiched between three polymer chips with microfabricated serpentine channels to form a dual-stage microdialysis device. This novel design makes the dual-microdialysis device highly compact and rugged, eliminating the tubing for the connection of two stages of microdialysis units. For analyzing complex biological samples, initial sample fractionation and cleanup can simplify analytical procedures. On-line, dual-dialysis using the microfabricated device is a fast and efficient means to achieve this. The molecular weight range selected for analysis by dual-microdialysis can be controlled by the selection of appropriate MWCO membranes at both stages. The application of dual-microdialysis/ ESI-MS for the identification of "biomarkers" of crude *E. coli* whole cell lysate has been successfully demonstrated.

Microfabricated Isoelectric Focusing (IEF) Device for Protein Separations

Capillary isoelectric focusing (CIEF) is a technique for high-resolution separation of proteins. However, conventional CIEF using fused silica capillary tubing commonly suffers from poor reproducibility that results from inconsistent sample handling and poor hydrolytic stability of the capillary coatings. Isoelectric focusing (IEF) devices microfabricated on polymer chips can circumvent some of these limitations and can potentially be integrated with similarly miniaturized injection and interfacing components, thus enabling much more rapid and automated analyses. In the present investigation, microfabricated IEF chips on polymer substrates (polycarbonate, polyimide) were used for the separation of proteins. Electroosmotic flows in microchannels directly laser-machined on these polymers are typically lower than those in a fused silica capillary. This suggests that isoelectric focusing experiments may be performed directly in these microfabricated IEF chips without the need for coating of the microchannels, allowing for improved reproducibility in this microchip IEF mode. To reduce the dead volume in the interface between the microchip and the mass spectrometer and improve both speed and sensitivity, an electrospray emitter was directly fabricated into the end of the device. Preliminary experiments have been conducted for the separation of a protein mixture with a concentration of 0.05 mg/mL for each protein. Good separation of myoglobin and carbonic anhydrase was achieved

without coating of the flow channel. The results indicate that electrospray directly from the sharp-edge microchip is feasible for separation and detection of proteins with microfabricated IEF/ESI-MS.

Microdevice with High-Density Micronozzle Arrays for Improving Sample Throughput

Multiplexing is one aspect of microchip-mass spectrometor coupling that offers great potential for high-throughput mass spectrometer analysis. The ability to handle multiple samples using microchip devices is one of the most significant advantages offered by the microfluidic network. Plastic microchips containing arrays of laser-micromachined electrospray nozzles were developed in this work for interfacing multichannel, microfluidic devices with a mass spectrometer. The number of micronozzles can be easily expanded to 96 if necessary. For different applications, micronozzles with various diameters can be readily fabricated. Nozzles with diameters as small as 40-μm O.D. and 15-μm I.D. for the generation of nanosprays from chips have been fabricated using this method.

Supporting Publications

Lin, Y., D. W. Matson, D. E. Kurath, J. Wen, F. Xiang, W. D. Bennett, P. M. Martin, and R. D. Smith, "Microfluidic Devices on Polymer Substrates for Bioanalytical Applications", in *Microreaction Technology:Industrial Prospects,* W. Ehrfeld, ed., pp. 451-460. Springer-Verlag (2000).

Lin, Y., K. Tang, and R. D. Smith, "Laser-Machined Microdevices for Mass Spectrometry", in *Mass Spectrometry and Hyphenated Techniques in Neuropeptide Research*, J. Silberring and R. Ekman, ed., John Wiley & Sons, Invited paper, submitted.

Lin, Y., N. Xu, D. W. Matson and R. D. Smith, "Microfabricated Dual-Microdialysis and Capillary Isoelectric Focusing Devices for Cleanup and Separation/Mass Spectrometric Analysis of Biomolecules", in the *Micro Total Analysis Systems,* D. J. Harrison and A. V. den Berg, ed., pp. 343-346; Kluwer Academic Publishers (1998).

Martin, P. M., D. W. Matson, W. D. Bennett, Y. Lin, and D. Hammerstrom, *J. of Vacuum Science and Technology A,* **17**, 2264-2269 (1999).

Martin, P. M., D. W. Matson, W. D. Bennett, Y. Lin, and D. Hammerstrom, *Proceedings of SPIE*, **3680**, 826-833 (1999).

Matson, D. W., P. M. Martin, W. D. Bennett, D. E. Kurath, Y. Lin, and D. Hammerstrom, "Fabrication Processes for Polymer-Based Microfluidic Analytical Devices", in the *Micro Total Analysis Systems*, D. J. Harrison and A. V. den Berg, ed., pp. 371-374, Kluwer Academic Publishers (1998).

Tang, K., Y. Lin, D. W. Matson, T. Kim, and R. D. Smith, "Generation of Multiple Electrosprays Using Micro Fabricated Emitter Arrays for Improved Mass Spectrometric Sensitivity", *Anal. Chem.*, submitted.

Wen, J., Y. Lin, F. Xiang, D. Matson, and R. D. Smith, *Electrophoresis,* **21**, 191-197 (2000).

Xiang, F., Y. Lin, J. Wen, D. W. Matson, and R. D. Smith, *Anal. Chem.,* **Accelerated Article, 71**, 1485-1490 (1999).

Xu, N., Y. Lin, D. W. Matson, C. J. Call, and R. D. Smith, *Anal. Chem.*, **70***, 3553-3556 (1998).

Radionuclide Sensors for Water Monitoring

J. W. Grate, O. B. Egorov, and T. A. DeVol[a]

Radionuclide contamination in the soil and groundwater at U. S. Department of Energy sites is a severe problem requiring monitoring and remediation. Radionuclide measurement techniques are needed to monitor surface waters, groundwater, and process waters. Typically, water samples are collected and transported to the analytical laboratory where costly radiochemical analyses are performed. To date, there has been very little development of selective radionuclide sensors for alpha- and beta-emitting radionuclides such as ^{90}Sr, ^{99}Tc, and various actinides of interest.

The objective of this program is to investigate novel sensor concepts and materials for sensitive and selective determination of beta- and alpha-emitting radionuclide contaminants in water. To meet the requirements for low-level, isotope-specific detection, the proposed sensors are based on radiometric detection. As a means of addressing the fundamental challenge of the short ranges of beta and alpha particles in water, our overall approach is based on localization of preconcentration/separation chemistries directly on or within the active area of a radioactivity detector, using automated microfluidics for sample manipulation and sensor regeneration or renewal.

The outcome of these investigations will be the knowledge necessary to choose appropriate chemistries for selective preconcentration of radionuclides from environmental samples, new materials that combine chemical selectivity with scintillating properties, new materials that add chemical selectivity to solid-state diode detectors, new preconcentrating column sensors, and improved instrumentation and signal processing for selective radionuclide sensors. This new knowledge will provide the basis for designing effective probes and instrumentation for field analytical chemistry.

An ongoing effort is directed at the investigation of the preconcentration column sensor concepts, development and characterization of the selective scintillating microspheres (SSMs), development of the new scintillation detection systems, and investigation of the chemically modified diode detectors. The preconcentrating minicolumn radionuclide sensor is based on the use of dual-functionality bead materials. These materials are designed to incorporate both selective separation chemistry for analyte preconcentration and localization within the detector, and scintillating fluors, so that radioactivity of retained species can be transduced to a measurable light output. To date we have achieved progress in SSM materials prepared by co-immobilization of selective organic extractants and scintillating fluors within inert polymeric beads. Scintillating microspheres selective for Tc, Sr, and actinides were prepared. Using pertechnetate selective scintillating beads, we have demonstrated the feasibility of a renewable preconcentrating column sensor concept in successful application toward ^{99}Tc determination in contaminated groundwater samples from the Department of Energy's Hanford site. To avoid sensor material degradation during the regeneration step, the sensor column was renewed via fluidic bead replacement. Using a 50-mL sample volume and 30-minute counting time, the detection limit for ^{99}Tc was 0.37 dpm/mL (9.8 pg/mL). This detection limit is below the maximum permissible drinking water level of 2 dpm/mL. This study is a subject of a recent publication (Egorov et al. 1999).

In addition to the technetium selective sensor, research has commenced on a combined extraction chromatographic and scintillation resin in a solid support for on-line and off-line monitoring of radiostrontium in aqueous solutions. This extractive scintillator resin has been realized as 1) a mixture of extraction chromatographic resin and granular scintillator, 2) extraction chromatographic material coated on the surface of a scintillating glass, and 3) inert polystyrene chromatographic resin impregnated with a proprietary extractant and organic fluors. Characterization of the detection efficiency, minimum detectable concentration, selectivity, loading capacity, capacity factor, and regeneration capability of the extractive scintillator resin continues. In addition, we are evaluating a number of solid-phase and inorganic sorbent materials for the purpose of Sr capture from

large volumes of groundwater. Several recently developed materials showed strong Sr uptake from Hanford groundwater matrices. The feasibility of ^{90}Sr sensing in groundwater samples was demonstrated using a mixture of selective sorbent and scintillator beads. Detection efficiencies as high as 50% were achieved. The feasibility of sensor regeneration, as necessary for reuse, was also demonstrated.

The development of a photodiode-based scintillating microsphere detection system continues. The photodiode-based system offers several advantages over commercially available photomultiplier-based systems to include better pulse shape discrimination capability, higher sensitivity at certain scintillation wavelengths, compactness, and reduced power requirements.

Reference

Egorov, O. B., S. K. Fiskum, M. J. O'Hara, and J. W. Grate, "Radionuclide Sensors Based on Chemically Selective Scintillating Microspheres: Renewable Column Sensor for Analysis of ^{99}Tc in Water", *Anal. Chem.* **71**, 5420-5429 (1999).

[99]Tc Monitor Development and Testing

O. B. Egorov

   Supported by BNFL Inc. and CHG.

Operations of a high-level tank waste processing plant to be built at the Hanford site requires an on-line/at-line monitor to measure the total ^{99}Tc in column effluents during technetium removal from the aqueous fraction of the waste. The monitor must achieve detection limits of 1×10^{-8} Ci/mL (0.6 μg/mL), and measurements must be done in near real time, with analysis frequency of ~15 minutes or faster. The monitoring technology must be sufficiently simple and robust for unattended operation at the plant settings. Currently, there is a lack of measurement technologies suitable for this task.

Recent work at the EMSL, funded by the Department of Energy Office of Basic Energy Research has been directed at the development of the automated, computer-controlled instrumentation and analytical procedures for the analysis of several important radionuclides in Hanford nuclear wastes (Grate and Egorov 1998). Automated fluidics is used to execute required chemical separation steps using radionuclide-selective extraction chromatographic or solid-phase extraction resins. The separated radionuclide fractions are delivered to an on-line scintillation detector for quantification. Specifically, we have recently developed an automated [99]Tc(VII) analyzer with stopped-flow radiometric detection. Pertechnetate separation was accomplished using TEVA-resin, which selectively retains pertechnetate from low acidity solutions (Egorov et al. 1998). Interfering species are not retained and were removed with a short column wash. The separated [99]Tc(VII) was eluted using nitric acid solution and delivered to the flow cell of an on-line liquid scintillation detector. To enhance analysis sensitivity, quantification was carried out using stopped-flow detection. The method was validated using diluted AN-107 tank waste samples treated with crystalline silicotitanate for ^{137}Cs and ^{90}Sr removal.

An on-going research effort is directed at evaluating the possibility of using automated radiochemical

Table 6.1. Method validation using acidified AW101 and AN107 samples treated with $Na_2S_2O_8$

Sample ID	Description	ICP MS, ^{99}Tc ppm	Radiometric Monitor, ^{99}Tc ppm[a]
AIR-PS-TR	processed AW101 sample	1.66±0.17	1.65±0.05 (1.53±0.05)
AIR-PS-TR-S	spiked processed AW101 sample	2.79±0.28	NA (2.57±0.13)
AN107-PS-TR	processed AN107 sample	0.706±0.007	0.610±0.06 (0.625±0.06)
AN107-PS-TR-S	spiked processed AN107 sample	1.81±0.18	NA (1.82±0.05)

(a)   Obtained using standard addition approach. Results in parentheses were obtained using 33% analysis efficiency from the previous analyzer calibration. Sample volume 0.25 mL.
1 ppm=629 Bq/mL= 1.7×10^{-5} Ci/L

analyzer methodology for the purpose of total ^{99}Tc monitoring in the diluted feed matrices (Egorov and Kurath 2000). Automated separation procedures for the analysis of acidic and caustic samples were tested using on-line radiometric detection. The automated radiochemical analysis method requires that Tc is present in the sample as pertechnetate. Manual sample oxidation procedures to convert all Tc to Tc (VII) were therefore developed and tested. AW101 and AN107 samples were oxidized using developed procedures, and resulting solutions were analyzed using automated analyzer and ICP MS techniques. The analytical results obtained using radiochemical analyzer techniques were in excellent agreement with the ICP MS total Tc data, as shown in Table 6.1. The detection limits that can be achieved using an automated radiochemical analyzer are a factor of 40 below the target detection limit of 1×10^{-8} Ci/mL. We are now developing automated prototypical instrumentation that integrates on-line sample oxidation and analysis procedures in a single functional unit. Software, instrumentation, and analytical procedures are being investigated for testing under conditions that emulate plant operation.

References

Egorov, O. B. and D. E. Kurath, "Automated ^{99}Tc Analysis in AW-101 and AN-107 Diluted Feed Matrixes", PNNL Report PNWD-3014 (2000).

Egorov, O. B., M. J. O'Hara, J. Ruzicka, and J. W. Grate, "Sequential Injection System with Stopped Flow Radiometric Detection for Automated Analysis of ^{99}Tc in Nuclear Waste", *Anal. Chem.*, **70**, 977-984 (1998).

Grate, J. W. and O. B. Egorov, "Automating Analytical Separations in Radiochemistry", *Anal. Chem.*, **70**, 779A-788A (1998).

Spectroelectrochemical Sensor for Technetium Applicable to the Vadose Zone

T. L. Hubler [(a,b)], S. A. Bryan [(b,c)],
W. R. Heineman [(c,d)], and C. J. Seliskar [(c,d)]

(a) EMSL Matrixed Staff.
(b) PNNL Environmental Technology Division.
(c) EMSL User.
(d) University of Cincinnati.

The general aim of this project is to continue the design and implementation of a new sensor technology that offers the unprecedented levels of specificity needed for analysis of the complex chemical mixtures found at Department of Energy sites nationwide. The new sensor concept combines the elements of electrochemistry, spectroscopy, and selective partitioning into a single device that provides three levels of selectivity. The specific goal of this project is the development of a sensor for technetium (Tc) that is applicable to characterizing and monitoring the vadose zone and associated subsurface water at the Hanford site. Consistent with this goal is the design of a sensor that determines technetium in the chemical form pertechnetate (TcO_4^-).

Efforts at PNNL have been focused primarily on development of the selective partitioning films for the Tc sensor. For an analyte to be detected, it first must partition into the selective coating (ion-exchange process) and then be electrolyzed at the potential applied to the electrode with the reduced species being selectively ligated. Either the analyte or its electrolysis product then absorbs light at the wavelength chosen. Selectivity for the analyte relative to other solution components is obtained by choice of coating material, electrolysis potential, and wavelength for optical monitoring.

As shown in Figure 6.7, TcO_4^- partitions into an anion-exchange coating (metal cations are thus excluded from the film). Application of an appropriate potential reduces the Tc(VII) to Tc(VI) or Tc(V), which is then selectively chelated into the preorganized binding site. This binding site has been designed to give an optimal signal for visible spectroscopy. The electrochemical process is reversible so the analyte can be expelled to "reset" the sensor for the next measurement.

A basic synthetic strategy has been adopted for covalent binding of the selective ligands into the polymer matrix. For PDMDAAC (polydimethyldiallylammonium chloride) polymer systems, this
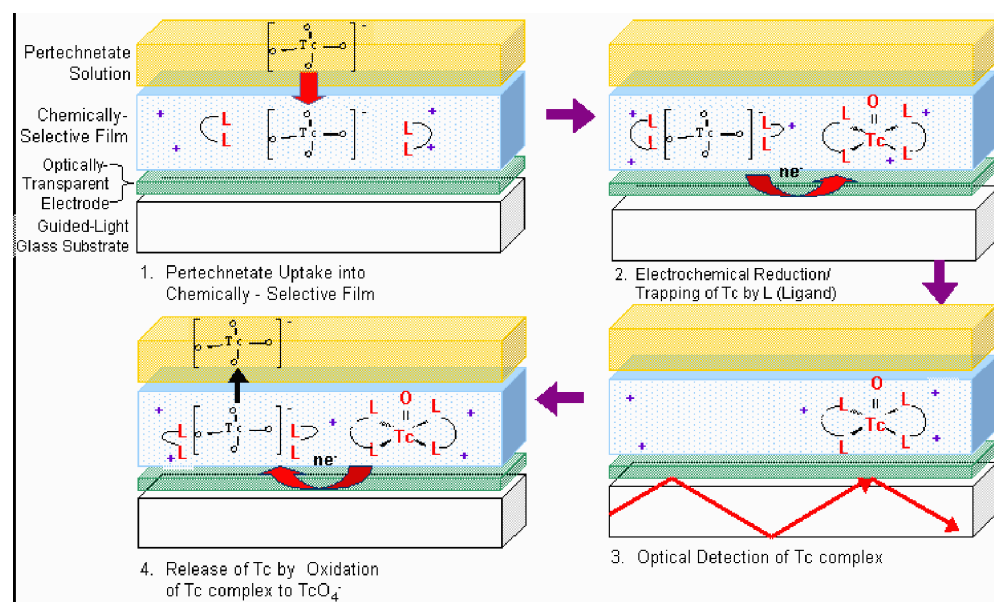
Figure 6.7. Schematic representation showing the three modes of selectivity for the spectroelectrochemical sensor.

strategy consists of preparation of diallylamides that can undergo cyclopolymerization with the DMDAAC monomer to become an integral part of the PDMDAAC polymer (the ligand set is covalently bound to the rest of the polymer). Diallylamides are prepared generally from carboxylic acids with diallylamine via DCC (dicyclohexylcarbodiimide) coupling or direct reaction of the amine with an acid chloride derivative. For example, tris-(DMSA)Re(VI) was reacted with diallylamine using DCC to give the hexaamide (each carboxylic acid group of the DMSA ligands is amidated). The per-amidated Re complex was then copolymerized with DMDAAC to give a polymer with a templated ligand set for Re. This co-polymer was immobilized on quartz crystal micro-balance slides (with Pt electrodes) using a silica sol gel. Electrochemical studies of the films thus created showed a reversible oxidation wave in the region from 0 to 1.2 V (SCE). An associated reversible mass gain/loss was also observed concurrently with the cyclic voltammogram. This indicates a redox cycle between Re(VI) and Re(VII) (presumably as ReO_4^-), with uptake of water from the surrounding solution as a reason for the increase in mass of the film. One consequence of this interpretation is that apparently ReO_4^- is not exiting the ion-exchange film. Other ligands have been examined including catechols and phenanthrolines. These materials can also be derivatized with diallylamine and co-polymerized with PDMDAAC.

Examination of these films and several other ligands will be tested at PNNL with TcO_4^- to verify that the polymer films and the sensor platform, including the conductive ITO layer (indium tin oxide), will perform satisfactorily. Key experiments performed on ReO_4^- and/or MnO_4^- will be repeated with TcO_4^- to verify that complications in forming the required complex in the sensing film are due to the difference in the electrochemistry of the cold surrogates, ReO_4^- and MnO_4^-, compared to TcO_4^-.

7. Environmental Studies — Waste Separations, Forms, and Chemistry

Aluminosilicate Precipitates from High-PH, High-Ionic-Strength, Al-Bearing Solutions Exposed to Quartz Sand

B. R. Bickmore[a,b], K. L. Nagy[b], and J. S. Young

Supported by the University of Colorado at Boulder.
(a) EMSL User.
(b) University of Colorado at Boulder.

At the Hanford site, high-pH, high-ionic-strength fluids with a significant amount of Al have leaked into the subsurface sediments. In order to predict the transport and fate of the radionuclides present in the leaked fluids, it is necessary to know what reactions might occur between the leaked fluids and the sediments, as well as the kinetics of these reactions. We have performed batch kinetics experiments with high-pH (11-12), high-ionic-strength (0-2m $NaNO_3$) solutions with varying amounts of Al (0.0001-0.01 m) exposed to quartz sand at 89° C. As the quartz dissolves, the dissolved Si concentration increases until, in some of our solutions, an aluminosilicate phase precipitates. We utilized the personnel and facilities at the EMSL to identify and characterize the precipitates, as well as characterize their relationship to the quartz surfaces. Using both an x-ray diffracto-meter and a field emission scanning electron microscope, EMSL personnel examined several samples. It was found that a nitrate-cancrinite precipitated with a peculiar ball-shaped morphology onto the quartz sand surfaces, often cementing the grains together. The cancrinite appears to nucleate as a film on the quartz surface, after which the ball-shaped crystal aggregates can form on top of the film.

The Influence of Calcium Carbonate Grain Coatings on Contaminant Reactivity in Vadose Zone Sediments

T. Droubay[a] and S. A. Chambers

(a)   Postdoctoral Research Fellow.

Cr(VI) has become an important environmental concern at the U.S. Department of Energy sites and elsewhere because of its high toxicity at low concentrations and its high mobility in groundwater. In contrast, Cr(III) typically forms insoluble oxides and is considerably less toxic to humans, animals, and plants than Cr(VI). Historically, remediation of chromium contamination was excavation/ encapsulation, but recently geochemical and micro-biological processes that reduce Cr(VI) to Cr(III) are becoming the methods of choice for cost and liability issues. We (Kendelewicz et al. 1999) have shown that aqueous Cr(VI) can be reduced to Cr(III) when it interacts with single-crystal iron oxides that contain Fe(II) in the near-surface region. The influence of natural calcium carbonate coatings on the ability of iron oxides present in the soil to adsorb Cr(VI) will affect the mobility of chromium through the vadose zone or affect the lifetime of remediation efforts utilizing the sorbing ability of Fe.

Work carried out in three separate areas highlights the advantages of utilizing x-ray photoemission spectroscopy (XPS) and oxygen-plasma-assisted molecular beam epitaxy (OPA-MBE) to better understand the influence of calcium carbonate coatings grown by metalorganic molecular beam epitaxy (MOMBE) on aqueous chromate reactivity. These three areas include the design and construction of a novel liquid introduction system, design and construction of a metalorganic gas delivery system, and research into a better understanding of photoemission lineshapes of transition metal oxides and compounds.

The design and construction of a chamber for controlled reactions between aqueous solutions and well-characterized epitaxially grown substrates or UHV-cleaned single crystals should minimize the possibility of surface contamination prior to reaction with aqueous Cr(VI). The liquid introduction chamber can be brought from UHV pressures up to the atmospheric pressure of nitrogen. Reaction between a liquid droplet and the substrate then can occur under atmospheric pressure conditions before being pumped down to UHV. This chamber is connected to the MBE in the EMSL. Growth and characterization of several Fe oxide surfaces done by Chambers and coworkers (Chambers and Joyce 1999; Chambers et al. 1999) forms one of the baselines for the present experiments. A direct test of the feasibility and a necessary starting point is to examine the changes induced at the surface of $Fe_3O_4(001)$ when reacted with distilled water. Photoemission examination of the water-reacted magnetite surface confirms hydroxide formation with the appearance of a third peak in the O 1s spectrum with a binding energy of 2.4 eV above the primary oxygen peak (Figure 7.1). A surprising result is that the magnetite surface becomes rich in Fe(III) as evidenced by an increase in the Fe(III) satellite (Figure 7.1a) and a decrease in the $2p^{3/2}$ shoulder attributed to Fe(II) (Figure 7.1b). The oxidation is probably caused by dissolved oxygen.

The second area of experimentation deals with the design and construction of a doser to deliver metal-organic precursor to the sample growth position in the MBE chamber. In principle, it should be possible to deposit calcium carbonate films epitaxially on the Fe oxide surfaces. Thus far, only submonolayer coverages of $CaCO_3$ have been grown by using $Ca(tmhd)_2$ as a precursor (tmhd = 2,2,6,6-tetramethyl-3,5,heptanedione).

The final area of research involves a melding of experimental x-ray absorption near-edge spectroscopy (XANES) and atomic multiplet calculations to help explain the complex metal 2p photoemission line-shapes measured for the Fe oxides. Comparison of the XANES spectra with the XPS spectrum from hematite displays the similarities between the relative peak positions. This striking similarity points to a multiplet dominated spectra described by ($2p^6d^n \rightarrow 2p^5d^{n+1}$) albeit for very different reasons. XANES involves the excitation of an electron from the 2p core level into the 3d valence band; whereas, in photoemission, the 2p electron is ejected, and through charge transfer the ligand donates an electron into the 3d shell. Since an atomic multiplet theory yields very good agreement with experimental XANES spectra for an appropriate site symmetry, we are utilizing the calculation for the energy separations for the
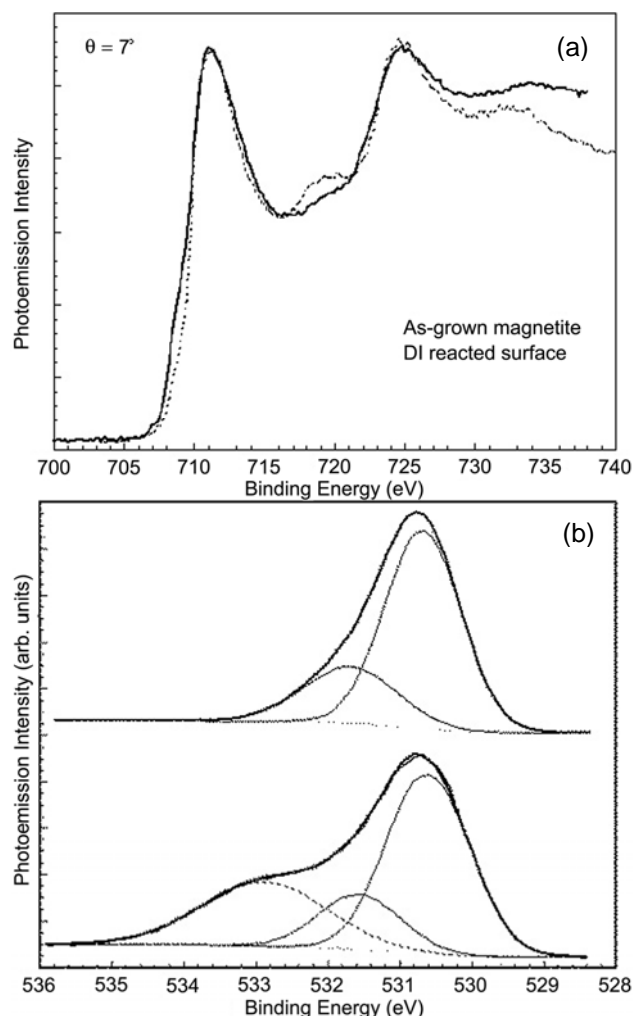
Figure 7.1. High-resolution x-ray photoemission spectroscopy (XPS) of as-grown and water-reacted surface of Fe_3O_4/MgO(001).

multiplets themselves. To ease the complexity of the calculation, we limit the number of allowed multiplets to best represent the experimental x-ray absorption spectra. With the use of limited multiplets, the experimental 2p core-level photoemission spectra are simulated using the value of the crystal field (10Dq) and the symmetry as parameters. Utilization of this method has enabled us to reproduce and explain the subtle Fe 2p photoemission lineshape differences between two different geometries, specifically bulk-dominated normal emission geometry and surface-sensitive glancing emission geometry. Once the reduced symmetry (C_{3v}) of the terminal Fe atoms is taken into account, the lineshape differences are explained by a reduction of the crystal field value from 10Dq = 1.8eV in bulk to 10Dq = 1.5eV at the surface of α-Fe_2O_3(0001).

References

"Hanford Site Environmental Report", U.S. Department of Energy, Richland, WA (1994).

Chambers, S. A. and S. A. Joyce, *Surface Science*, **420**, 111-122 (1999).

Chambers, S. A., S. Thevuthasan, and S. A. Joyce, *Surface Science* (1999).

Kendelewicz, T., P. Liu, C. Doyle, G. Brown, E. Nelson, and S. A. Chambers, *Surface Science*, **424**, 219-231 (1999).

Radiation Resistance of the Gd$_2$(Ti$_{1-y}$Zr$_y$)$_2$O$_7$ Compositional Series Pyrochlores

N. J. Hess[a,b], B. D. Begg[a,c], D. E. McCready, P. Gassman, S. Thevuthasan, and W. J. Weber[a,d]

Supported by the U.S. Department of Energy Office of Basic Energy Sciences.
(a) EMSL User.
(b) PNNL Fundamental Sciences Division.
(c) ANSTO, Menai, New South Wales, Australia.
(d) Energy Science and Technology Division.

Pyrochlore is one of a number of materials proposed for the immobilization of actinide-rich wastes and surplus plutonium. Actinide-bearing waste forms will experience extensive α-recoil radiation damage, so it is important to understand the effect of radiation damage on the structure. Considerable work has been carried out characterizing the irradiation-induced, crystalline-to-amorphous transformation observed in titanate-based pyrochlores (Weber et al. 1985, 1986; Weber and Hess 1993). More recently, pyrochlores of Gd$_2$(Ti$_{1-y}$Zr$_y$)$_2$O$_7$ stoichiometry have been investigated that display a systematic decrease in susceptibility to

radiation-induced amorphization with increasing Zr content (Wang et al. 1999a, 1999b) commensurate with a phase transition from an ordered pyrochlore structure to a defect fluorite structure. The Gd$_2$Zr$_2$O$_7$ end member retained the defect fluorite structure even at 25 K (Wang et al. 1999a, 1999b).

Powder x-ray diffraction and reflection FTIR data were collected on Gd$_2$(Ti$_{1-y}$Zr$_y$)$_2$O$_7$ pyrochlores prior to and following irradiation with 2-MeV Au^{2+} ions to an ion fluence of 5 ions/nm^2. The expected structural phase transition from an ordered pyrochlore structure to a defect fluorite structure with increasing Zr substitution in the unirradiated samples was clearly evident in the XRD and vibrational data (Figure 7.2a). Upon irradiation, the XRD data indicated loss of the ordered pyrochlore structure for compositions in the range 0<y<0.75 and retention of the defect fluorite structure for y=1.0 composition. Vibrational spectra of the irradiated samples over the compositional range exhibited similar spectra characteristics to the unirradiated Gd$_2$Zr$_2$O$_7$ end member (y=1.0) (Figure 7.2b). These results suggest that one effect of ion-beam irradiation is the creation of cation and anion disorder on symmetrically equivalent sites that also defines the structural phase transition from the ordered pyrochlore structure to the defect fluorite
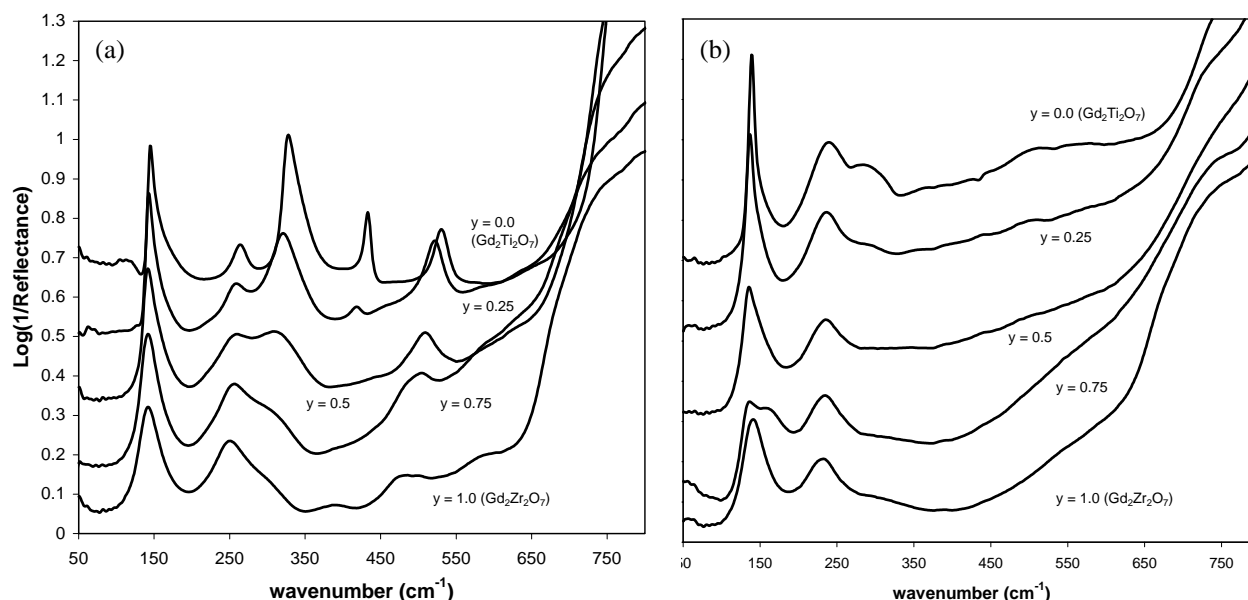
Figure 7.2. FTIR spectra of the Gd$_2$(Ti$_{1-y}$Zr$_y$)$_2$O$_7$ compositional series (a) prior to ion-beam irradiation (the Gd$_2$Ti$_2$O$_7$ (y=0) end member displays several distinct absorption bands that decrease in number and shift in position with increasing Zr substitution) and (b) following ion-beam irradiation. There are strikingly similar characteristics in the FTIR spectra for all compositions upon irradiation. The change is most significant for the Gd$_2$Ti$_2$O$_7$ (y=0) end member and systematically less with increasing Zr substitution.

structure. The radiation resistance of the $Gd_2Zr_2O_7$ end member (y=1.0) may be in part the result of this structure to accommodate cation and anion disorder without a change in symmetry.

References

Wang, S. X., B. D. Begg, L. M. Wang, R. C. Ewing, W. J. Weber, and K. V. Govidan Kutty, *Journal of Materials Research*, **14**:4470-73, (1999a.)

Wang, S. X., L. M. Wang, R. C. Ewing, and K. V. Govindan Kutty, "Microstructural Processes in Irradiated Materials", *Materials Research Society Symposium Proceedings*, **540**:355-360 (1999b).

Weber, W. J. and N. J. Hess, "Ion beam modification of $Gd_2Ti_2O_7$", *Nuclear Instruments and Methods in Physics Research*, **B80/81**:1245-1248 (1993).

Weber, W. J., J. W. Wald, and Hj. Matzke, "Self-radiation damage in $Gd_2Ti_2O_7$", *Materials Letters*, **3**:173-180 (1985).

Weber, W. J., J. W. Wald, and Hj. Matzke, "Effects of Self-Radiation Damage in Cm-doped $Gd_2Ti_2O_7$ and $CaZrTi_2O_7$", *Journal of Nuclear Materials*, **138**:196-209 (1986).

Surface Properties and Crystalline Defects of Hydrogen-Implanted SrTiO₃ Using High Energy Ion Scattering Techniques

S. Maheswaran[a,b], V. Shutthanandan,
E. M. Adams[c], and S. Thevuthasan

(a) EMSL User.
(b) School of Science, University of Western Sydney-Nepean, Australia.
(c) Student.

Perovskite materials, such as $SrTiO_3$, have been recommended as alternate materials for stabilization and immobilization of high-level wastes containing fission products and actinides. The prediction of near- and long-term performance of these materials in the high-radiation environment provided by the decay of fission products and actinides is a challenging task. The fundamental scientific understanding of radiation effects on these materials is crucial for such predictions. In addition, there is a renewed interest in the use of ion implantation to alter the near-surface properties of $SrTiO_3$ related to current activities in the semiconductor industry. Many of the potential semiconductor technology applications require thermal annealing to remove the damage introduced by ion implantation. Furthermore, it has been shown that thin single-crystal $SrTiO_3$ films can be cleaved using hydrogen implantation and subsequent annealing. The ability to cleave such implanted surfaces for mounting on other substrates could have a significant impact on the fabrication of electrooptical devices.

The goal of the present study is to determine the structure of the clean surface of $SrTiO_3$, and to measure changes in structure and defects induced by the hydrogen implantation. The $SrTiO_3(001)$ surface was irradiated with 40-keV H^+ ions at 120 K with ion fluence of 7.5×10^{16} atoms/cm². High-energy ion backscattering and channeling spectrum, including angular yield curves, were measured from the virgin and hydrogen-implanted regions using 1.0- to 3.0-MeV He^+ ions.

The channeling spectra from the irradiated and virgin regions are presented, along with the random spectrum, in Figure 7.3. Although the damage was created as a result of ion irradiation on all three sublattices, for simplicity we only show the damage created on the Ti and Sr sublattices. Figure 7.4 summarizes the surface peak area of Sr as a function of incident beam energy for both clean and irradiated $SrTiO_3$ samples. The surface peak areas are higher for H^+ irradiated samples
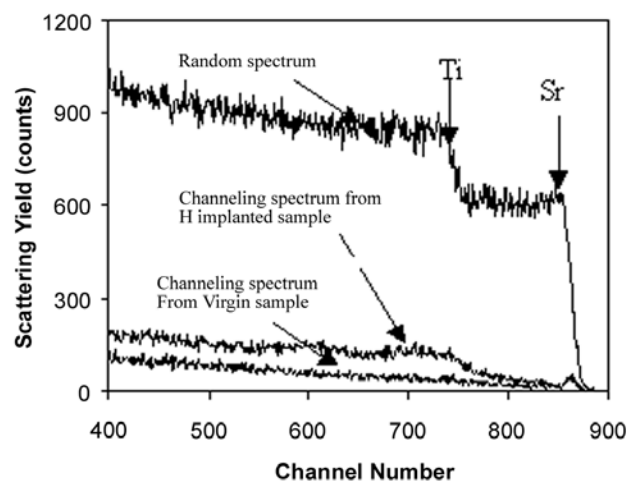
Figure 7.3. Channeling and random spectra from virgin and 7.5×10^{16} atoms/cm² H^+-implanted $SrTiO_3$ (100).
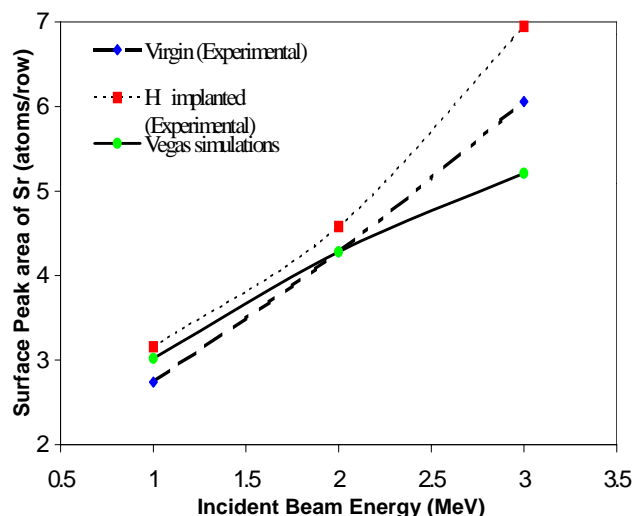
Figure 7.4. Sr surface peak area as a function of incident ion beam energy for virgin and H^+-implanted $SrTiO_3$ (100) samples. Simulated surface peak area using VEGAS simulation is also presented.

as compared to unirradiated samples. In all the aligned spectra, dechanneling appears to be higher for H^+ irradiated samples. These results indicate that the defect density increased due to H^+ irradiation. VEGAS simulations are carried out using $SrTiO_3$ bulk-like clusters. The simulated surface peak areas appear to be smaller for higher energies compared to the experimental values from virgin samples, possibly due to the intrinsic defects in the crystals.

The defect-dechanneling factor has a different dependence on the type of defects in the material. By studying the defect-dechanneling factor as a function of energy, one can predict to the first order what type of defects exist in the crystal. The defect dechanneling factor σ_D is defined as:

$$\sigma_D = A(1/E^2 \ \varphi_{1/2})^2 \qquad (1)$$

where $A = C_c \pi Z_1^2 Z_2^2 e^4$, E is the incident energy of the projectile, and $\psi_{1/2}$ is the critical angle, which can be determined from the angular yield curves. The average number of atoms in a defect cluster is indicated by C_c, and Z_1 and Z_2 represent the atomic numbers of the projectile and the target atom, respectively. If the defects are interstitial atoms and amorphous clusters, the defect-dechanneling factor is expected to decrease as a function of energy. In this study, a clean substrate and one irradiated region were selected to investigate the type of defects using the dependence of the defect-dechanneling factor on the incident energy. First, the critical angles need to be determined using angular yield curves at different energies. Five different incident energies such as 1.0, 1.5, 2.0, 2.5, and 3.0 MeV were selected to generate the angular yield curves. These angular yield curves were generated from the variation of integrated yield over a small region near the surface peak in the clean substrate and

around the damage peak in the irradiated regions as a function of tilt or polar angle. The critical angles were determined from these curves, and the defect-dechanneling factor, σ_D, was calculated using these values.

Figure 7.5 presents the defect-dechanneling factor as a function of energy for a clean substrate and a 7.5×10^{16} atoms/cm^2 irradiated region, respectively. As expected, a smooth decreasing curve for the clean substrate (solid line) indicates that the defects in the clean substrate are mostly point defects, such as vacancies and/or interstitial atoms. The trend in the defect-dechanneling factor (dotted line) of the irradiated regions also indicates the defects are mostly point-scattering centers. However, if more than one type of defect is present in the system, in general, a quantitative separation of the type of defects may not be possible.
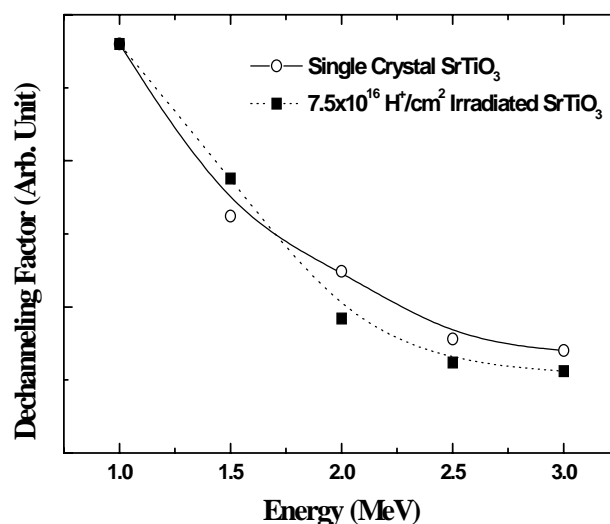
Figure 7.5. Dechanneling factor as a function of incident ion beam energy for virgin and 7.5×10^{16} atoms/cm^2 H^+-implanted $SrTiO_3$ (100) samples.

High-Energy Ion Beam Studies of Ion Exchange in a Na₂O-Al₂O₃-SiO₂ Glass

V. Shutthanandan, D. R. Baer,
S. Thevuthasan, E. M. Adams[a],
S. Maheswaran[b,c], M. H. Engelhard,
J. P. Icenhower[b,d], and B. P. McGrail[b,d]

   Supported by the U.S. Department of Energy
      Environmental Management Science Program
      and Nepean Seed Grant Scheme.

    (a)   Student.
    (b)   EMSL User.
    (c)   School of Science, University of Western
        Sydney-Nepean, Australia.
    (d)   PNNL Energy Technology Division.

In part, because of the planned use of vitrification as a means to stabilize nuclear waste, many studies have been conducted on glass/water reaction processes for glass compositions ranging from simple binary and ternary silicate glasses to complex waste glasses with 30 or more components. The general picture of the glass-corrosion process in water can be summarized as follows: upon initial contact by water, alkali is extracted by ion exchange in what is thought to be a diffusion-controlled process and, simultaneously, hydrolysis and dissolution of the glass network occurs. Although previous studies have provided critical insights into the mechanism of ion exchange in glasses, the test conditions have focused on reactions for which there was general dissolution of the glass matrix. However, in a disposal system, particularly water-unsaturated disposal systems, glass matrix dissolution is minimal. Measurements suggest that Na continues to be released, presumably by ion exchange, at a rate in excess of the rate of matrix dissolution. The work reported here is part of a study funded by the Department of Energy Environmental Management Research Program. This project, entitled "*Ion Exchange Processes and Mechanisms in Glasses,*" is designed to help us understand the ion exchange process when matrix dissolution is minimal and formulate glasses for which ion loss is minimized. Separate publications provide more detailed information about glass formulations and the results of kinetic measurements. This discussion focuses on ion beam measurements related to the release of Na from a Na₂O-Al₂O₃-SiO₂ glass with 10 mol % Al₂O₃

exposed to a solution containing $D_2{}^{18}O$ and saturated with respect to amorphous silica.

Glass reaction experiments were carried out using a single-pass, flow-through (SPFT) apparatus. Following exposure to solution, sample coupons were carefully removed from the SPFT reactors and carbon coated to avoid charging during the ion beam experiments. The ion beam experiments were carried out in the accelerator facility at the EMSL. Rutherford backscattering spectrometry (RBS) and nuclear reaction analyses (NRA) measurements were carried out to determine Na loss to the solution and D and ^{18}O uptake in the glass. Ion beam measurements were carried out on 1-, 2-, 3-, 4-, and 5-day reacted glasses.

Figure 7.6 summarizes the Na loss and D and ^{18}O uptake results from a 3-day reacted glass sample. The amount of ^{18}O incorporated into the glass increases with solution exposure time, and the depth of penetration increases such that the concentration maximum gets slightly deeper with longer exposure times. The amount of Na loss roughly mirrors the oxygen uptake, both in shape and magnitude. The deuterium incorporated into the reacted glass is at a
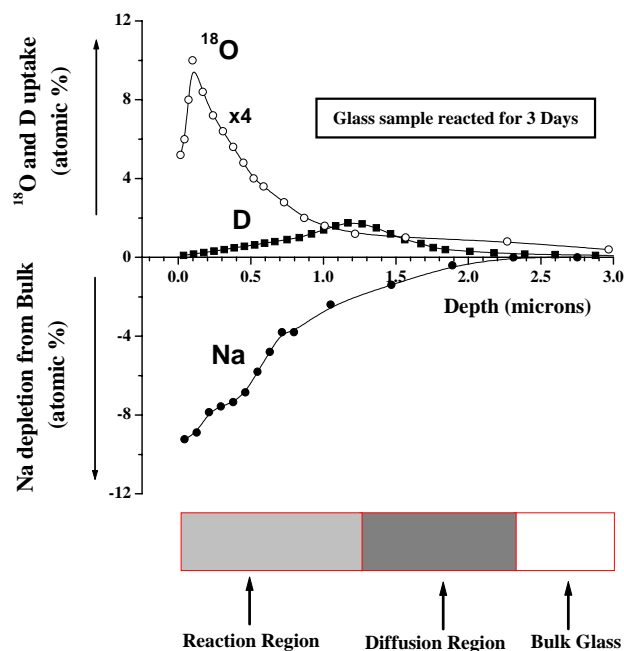
Figure 7.6. Na depletion profile, D uptake profile, and ^{18}O uptake profile for 3-day reacted glass sample are presented as a function of depth.

significantly different depth than the ^{18}O. Although the depth of the maximum ^{18}O concentration occurs around 0.25 μm, the peak of the D concentration appears near one-micron depth. The deuterium accumulates in the region where the Na concentration is increasing toward the bulk value. The data support a view that the region containing the largest amount of ^{18}O near the surface involves the reaction of the labeled water with the silica backbone of the glass and with the non-bridging oxygen. This part of the profile is identified as the reaction region. If the thickness is defined as the depth in which the ^{18}O drops to 50% of the maximum value, the reacted layer thickness would have been somewhat less than 0.5 μm.

The region closest to the undisturbed glass region in the glass contains significantly less ^{18}O, the maximum amount of D and an increasing amount of Na. We believe that the dominant process in this region is some type of ion diffusion and this region is identified as a diffusion region. The ratio of ^{18}O uptake to D in this region is in the range of 0.3 to 0.5. This ratio is generally quite consistent with H_3O^+, but some H^+ and H_2O may also be present.

It is important to remember that these studies involved time scales that are very short relative to those associated with waste storage or long-term operation of a repository. It is often observed that there are surface influences, transitory effects, and other artifacts that have an initial influence on the Na release. When we examine the glass surface regions, we are examining the region altered during these initial processes as well as any changes that continue with time. When reaction rates become very small, there may be little change with time, and they may occur at depths relatively deep into the material. The types of measurements achieved by the ion beam techniques provide the sample context for understanding solution measurements of ion exchange rates. The Na release from a glass reaction layers is confirmed. Solution studies often assume a diffusion-limited ion exchange process and use solution data to calculate a depth of Na depletion. Such calculations are usually based upon the total removal of Na. The ion beam work shows that less than half of the Na is removed even in the surface reaction layer so that such a calculation would severely underestimate the depth into the glass from which some material is removed.

Chemical and Thermal Stability Studies of Cs-loaded IE-911

Y. Su[(a,b)], L. Li[(c)], J. S. Young, and M. L. Balmer

An inorganic ion exchanger based on crystalline silicotitanate (CST), IE-911, is currently being considered for Cs separation at the Department of Energy, Savannah River site. While the performance of this ion exchanger has been well characterized under normal operating conditions, the stability of the material at slightly elevated temperatures, such as those that may occur during a process upset, is the subject of current evaluations. Recent reports indicated that after exposure to Savannah River site supernate simulant at 80° C and 120° C, the Cs exchange capacity of the ion exchanger was severely compromised. The purpose of this study is to determine the time and temperature profiles at which irreversible desorption of Cs from the CST occurs and to determine the cause of the apparent reduced Cs capacity of the CST.

In this study, Cs from the simulant was loaded onto IE-911 at room temperature, then the simulant/ exchanger mixture was held at ambient temperature, 55° C, and 80° C, for periods of 1 hour, 1 day, 3 days, 5 days, 7 days, 10 days, 14 days, and 30 days. A small amount of Cs desorbed from IE-911, as shown in Figure 7.7. The desorbed Cs concentration increases with the increase of the heat-treatment time and temperature. After each of these time periods, the batches were returned to ambient temperatures to reload any Cs that was desorbed. Figure 7.8 shows the Cs reloading curve after heat-treatment at 55° C and 80° C. For all exposure times up to 30 days at 55° C and 80° C, the Cs was readsorbed by IE-911 after the temperature was lowered to ambient. However, the reloading rate decreases with increasing time at high temperature. The lowest reloading rate that is observed after exposure to 55° C for 30 days is slower than the reloading rate observed after exposure to 80° C for 30 days, as shown in Figure 7.8.
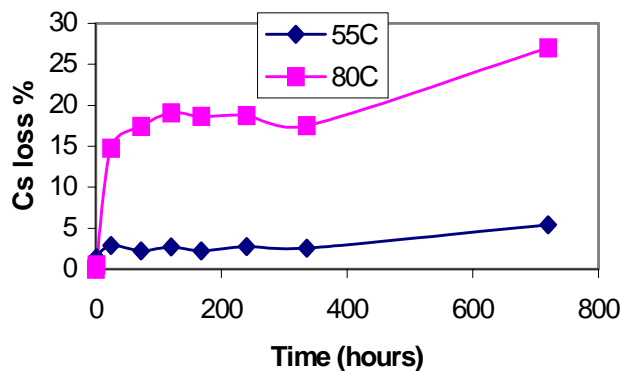
Figure 7.7. Cs leaching test at 55° C and 80° C.
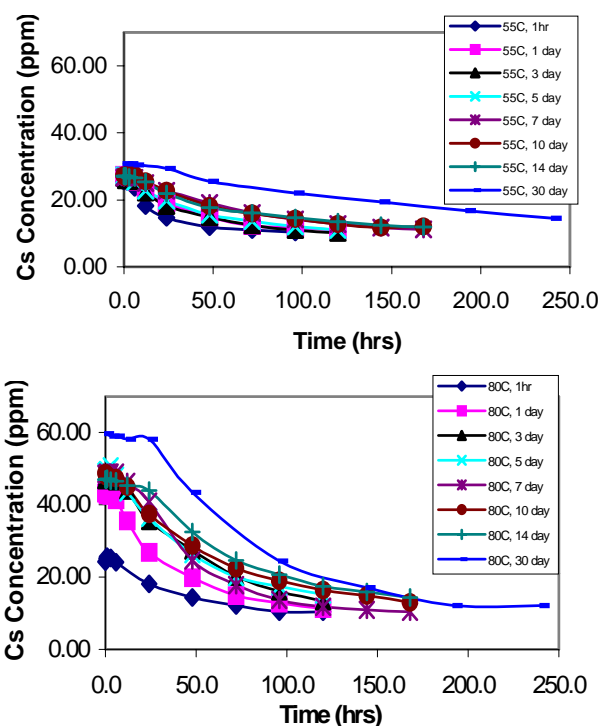
Figure 7.8. Cs reloading test at room temperature after heat-treatment at 55° C and 80° C.

XRD analysis showed that a hexagonal nitrate cancrinite-type sodium aluminosilicate, similar to PDF-38-513: $Na_8Al_6Si_6O_{24}(NO_3)_2 \bullet 4H_2O$, precipitated from simulant/IE-911 mixtures after exposure to 55° C and 80° C. Additionally, scanning electron microscopy (SEM) analysis showed that a sodium aluminosilicate coating formed on beads of IE-911 after exposure to simulant at 55° C and 80° C. However, the morphology of the coating after 55° C and 80° C treatment is quite different. At 55° C, a uniform layer composed

of fine plates grows up to 1-μm thick after 30 days heat-treatment. The maximum coating thickness was observed at ~10 days with no further growth up to 30 days. At 80° C, larger, non-uniform lower-density spheres composed of plate-like grains form on top of a thin layer (up to 2-μm thick) of denser, plate-like cancrinite. The growth rate of the coating cannot be quantified due to irregularities in thickness; however, regions up to 10 μm exist. The morphology of the flake-like precipitates at 55° C is similar to the coating morphology at 80° C. These differences in coating morphology can be explained by differences in nucleation and growth rates at the two different temperatures. A high-nucleation, low-growth regime is present at 55° C, whereas a high-growth rate and low-nucleation rate is present at 80° C. Differences in the rate of Cs uptake for samples treated for the same amount of time at 55° C and 80° C may be due to differences in the density of the coatings.

New Silicotitanate Waste Forms: Development and Characterization

M. L. Balmer, Y. Su[(a,b)], D. McCready, A. Navrotsky[(c,d)], H. Xu[(c,d)], T. Nenoff[(e)], M. Nyman[(e)], R. Roth[(f)], and R. Ewing[(g)]

Supported by the U.S. Department of Energy Environmental Management Science Program.

(a) EMSL Matrixed Staff.
(b) PNNL Energy Science and Technology Division.
(c) EMSL User.
(d) University of California, Davis.
(e) Sandia National Laboratories.
(f) National Institute of Standards and Technology.
(g) University of Michigan.

The objective of this program is to identify new waste forms and disposal strategies specific to crystalline silicotitanate (CST) secondary waste that is generated from Cs and Sr ion exchange processes. Waste forms that are developed in this work will offer an alternative to current disposal plans. The goals of the program are to reduce the costs associated with CST waste disposal, to minimize the risk of contamination to the environment during CST processing, and to provide the U.S. Department of Energy with technical alternatives for CST disposal. The technical objectives of the proposed work are to fully characterize the phase relationships, structures, and thermodynamic and kinetic stabilities of crystalline silicotitanate waste forms and to establish a sound technical basis for understanding key waste form properties, such as melting temperatures and aqueous durability, based on an in-depth understanding of waste form structures and thermochemistry.

Research performed on this program has fulfilled the above objectives. To date, studies have been performed to 1) determine the durability of waste forms synthesized by heat treating the UOP CST IE-911, 2) investigate the stable and metastable phase formation, especially the cesium-containing phases resulting from heat-treated CST and from model 3-component systems, and 3) investigate thermodynamic stabilities of compounds related to the ion-exchanged CST and the thermally converted oxides. Leach tests have shown that durabilities of waste

forms resulting from a simple heat treatment of the Cs-loaded CST *with no additives* in the range of 800° to 1000° C were orders of magnitude higher than that of baseline borosilicate glass. Cs volatilization was found to be approximately 3 wt% at temperatures as high as 1000° C. In addition, heat treatment reduces waste volume by approximately 40% and simultaneously coarsens fines, thus reducing inhalation risks. Heat treatments above 800° C completely removes molecular water and hydroxyl groups so that the possibility of radiolytic hydrogen production during storage is eliminated.

A number of new phases appear when IE-911 is heat-treated. Nuclear magnetic resonance (NMR), x-ray diffraction (XRD), and transmission electron microscopy (TEM) results indicate that major phases in thermally converted CST are $Cs_2ZrSi_3O_9$, $Na(TiNb)O_3$, and $Na_2Ti_6O_{13}$. Rietveld refinement of x-ray powder diffraction data showed that $Cs_2ZrSi_3O_9$ has a hexagonal structure (space group P63/m) with lattice parameters a=7.2303(2) Å and c=10.2682(4) Å. The high aqueous durability of $Cs_2ZrSi_3O_9$ can be explained by its small channel size (smaller than a Cs ion), which precludes facile migration of Cs. Radiation stability studies by gamma irradiation in the PNNL ^{60}Co source, as well as by *in situ* TEM electron beam with the collaboration of Professor Rod Ewing at the University of Michigan, were completed. For the gamma irradiation studies, both Cs-loaded IE-911 and the Cs-containing phase $Cs_2XSi_3O_9$ were exposed to gamma irradiation at a dose rate of approximately $9x10^5$ Rad/hr at various temperatures (50° to 200° C). The total absorbed dose was $5.2x10^{10}$ Rad. XRD analysis indicates there is no radiation-induced damage or amorphization. These results suggest that $Cs_2ZrSi_3O_9$ and IE-911 have good radiation stability and are suitable for waste form applications. In contrast, preliminary results from *in situ* TEM electron irradiation show amorphization after an electron fluence of $1.1x10^{22}$ e/cm^2.

A second new phase discovered by TEM (Na, Ti, Nb, oxide) has a structure similar to the perovskite $NaNbO_3$. In order to determine the extent of titanium substitution in this mixed phase, a series of compounds with up to 20% Ti substitution were synthesized using a sol-gel technique. A systematic shift of the lattice parameter as a function of Ti substitution has been observed. Comparison of the heat-treated

IE-911 with the synthesized compounds revealed that this phase in IE-911 has 15% Ti substitution in the lattice.

In the course of Na_2O-TiO_2 hydrothermal phase searches, a novel Na/Ti/Nb/O class of molecular sieves was found. These phases show high selectivity for divalent cations over monovalent cations, which is a useful characteristic for numerous applications including extraction of ^{90}Sr or Pb from mixed wastes. Additionally, direct thermal conversion of these ion exchangers produces a perovskite, which is a durable phase. Structural characterization of these phases is currently underway.

Phase equilibria and single-crystal growth experiments on the three-component Cs_2O-TiO_2-SiO_2 system have revealed several new compounds. SNL-A and SNL -B were synthesized hydrothermally at Sandia National Laboratories, and $Cs_2TiSi_6O_{15}$ and $CsTiSi_2O_{6.5}$ by sol-gel methods at PNNL. A complete solid substitution series of $Cs_2TiSi_6O_{6.5}$ and $CsAlSi_2O_6$ has been synthesized. Substitution of Ti for Al in pollucite results in stabilization of the cubic structure at low temperatures (to 100 K). The standard molar enthalpies of formation from Ti-substituted pollucites with the composition $CsTi_xAl_{1-x}Si_2O_{6+0.5x}$ have been determined at the University of California - Davis by solution-drop calorimetry. As Ti^{4+} substitutes for Al^{3+} in pollucites, the enthalpies of formation become more endothermic and show exothermic mixing within the composition ranging from x=0.3 to 1. This non-ideal mixing behavior is consistent with the trend seen in the lattice parameters, and we interpret it to be a result of the short-range order associated with the framework cations Al^{3+}, Si^{4+}, and Ti^{4+}. The enthalpies of formation for pharmacosiderite analogues with the composition $(K_{1-x}Cs_x)_3Ti_4Si_3O_{15}(OH)\cdot4H_2O$ become more exothermic as Cs/(Cs+K) increases. This result indicates that the incorporation of Cs in these phases is thermodynamically favorable, although kinetic factors may play a role as well.

Supporting Publications

Balmer, M. L., Y. Su, H. Xu, E. R. Bitten, D. E. McCready, and A. Navrotsky, "Synthesis, Structure Determination, and Aqueous Durability of $Cs_2ZrSi_3O_9$", *Journal of the American Ceramic Society* (2000).

Nyman, M. D., B. X. Gu, L. M. Wang, R. C. Ewing, and T. M. Nenoff, "Synthesis and Characterization of a New Microporous Cesium Silicotitanate (SNL-B) Molecular Sieve", *Journal of Microporous and Mesoporous Materials* **34**, 301 (2000).

Nyman, M. D., F. Bonhomme, D. M. Teter, R. S. Maxwell, B. X. Gu, L. M. Wang, R. C. Ewing, and T. M. Nenoff, "Integrated Experimental and Computational Methods for Structure Determination and Characterization of a New, Highly Stable Cesium Silicotitanate Phase, $Cs_2TiSi_6O_{15}$ (SNL-A)", *Chem. Mater.* (2000).

Su, Y., M. L. Balmer, and B. Bunker, "Raman Spectroscopic Studies of Silicotitanates", *J. Phys. Chem. B* **104**, 8160-8169 (2000).

Xu, H., A. Navrotsky, M. D. Nyman, and T. M. Nenoff, "Thermochemistry of microporous silicotitanate phases in the Na_2O-Cs_2O-SiO_2-TiO_2-H_2O System", *Journal Materials Research* **15(3)**, 815 (2000).

Xu, H., A. Navrotsky, M. L. Balmer, Y. Su, and E. Bitten, "Energetics of substituted pollucites along the $CsAlSi_2O_6$-$CsTiSi_2O_{6.5}$ join: A high-temperature calorimetric study", *Journal of the American Ceramic Society* (2000).

Electroactive Materials as Mass Separation Agents

J. H. Sukamto[a,b], T. L. Hubler[a,b], and M. A. Lilga[b]

Supported by the U.S. Department of Energy Environmental Management Science Program.
(a)   EMSL Matrixed Staff.
(b)   PNNL Environmental Technology Division.

Many contaminants of interest to the U.S. Department of Energy exist as anions. These include the high-priority pollutants chromate, pertechnetate, and nitrate ions. In addition, there are also industrial and urban applications where the separation of anionic species from aqueous streams is critical. Examples include industrial water recycle and waste-water treatment (e.g., chloride ion removal for the pulp and paper industry, borate ion in the chemical and nuclear industries) and drinking water and agricultural waste treatment (e.g., nitrate removal).

In the proposed research, ^{99}Tc is chosen as the target pollutant. Because of its half-life of 213,000 years, ^{99}Tc presents a long-term hazard for waste disposal. Much of the ^{99}Tc in the tank wastes is present as pertechnetate (TcO_4^-), thus accounting for its high solubility and mobility in aqueous systems. Several sorbents are available for removing TcO_4^- from alkaline waste brines, but each has important drawbacks. The use of commercial ion exchange (IX) resins to extract TcO_4^- [e.g., Reillex™-HPQ (Reilly Industries) and ABEC 5000 (Eichrom Industries)] generates significant secondary waste. The elution of TcO_4^- from Reillex™-HPQ resins requires either concentrated nitric acid or a concentrated caustic solution of ethylene-diamine containing a small amount of tin chloride. This eluant has a short shelf life requiring frequent preparation, and the ^{99}Tc is delivered in a complexed, reduced form. While TcO_4^- can be eluted from ABEC 5000 resins using deionized water, the much-reduced capacity of ABEC 5000 resins in comparison to the Reillex™-HPQ resins leads to a low-column capacity. In general, unwanted secondary wastes are generated because 1) the only effective eluant happens to be hazardous and/or 2) the IX material has a low capacity or selectivity for the target ion, resulting in more frequent elution and column replacements.

Alternative IX materials that have high capacities, can be regenerated easily, and are highly selective for TcO_4^- would avoid these problems. Electrochemically active IX media meet these criteria. Such an IX system uses electrically induced changes in the media to expel sorbed ions through a charge imbalance rather than requiring chemical eluants to "strip" them. Therefore, this medium eliminates the need to prepare, store, and dispose of many of the process chemicals normally required for IX operations.

The focus of the project is to develop a fundamental understanding of how the physical and chemical properties of electroactive ion exchange (EaIX) materials control their efficiency when used as mass separation agents. Specifically, the desirable characteristics of EaIX materials for separation applications are 1) high reversibility, 2) high selectivity, 3) acceptable physical and chemical stability, 4) rapid intercalation and de-intercalation rates, and 5) high capacity. Because of these requirements, EaIX materials share many properties in common with conventional ion exchangers and electroactive polymers. For example, EaIX materials require the selectivity typically found in ion exchangers; they also require the redox reversibility of electroactive polymers. The results of this work will allow the rational design of new materials and processes tailored for the separation of specific anions.

The two components of the project are 1) synthesis and 2) characterization of EaIX materials. The monomer constituents of the electroactive polymer ultimately control the desirable characteristics described earlier. We have focused our efforts on the synthesis of monomers that have the appropriate functional groups and that are stable under highly alkaline conditions. We have recently synthesized new ferrocene-containing polymers that, under alkaline conditions, exhibit more stability than commercially available polyvinylferrocene (PVF). Figure 7.9 compares the characteristics of PNNL-synthesized and commercially available PVF polymers; the commercial PVF is deactivated in less than 2 cycles.

Although PNNL PVF-11 is deactivated mainly after 20 cycles, our study (where we are systematically modifying the basic ferrocene units to make the resulting polymer more stable in alkaline conditions)
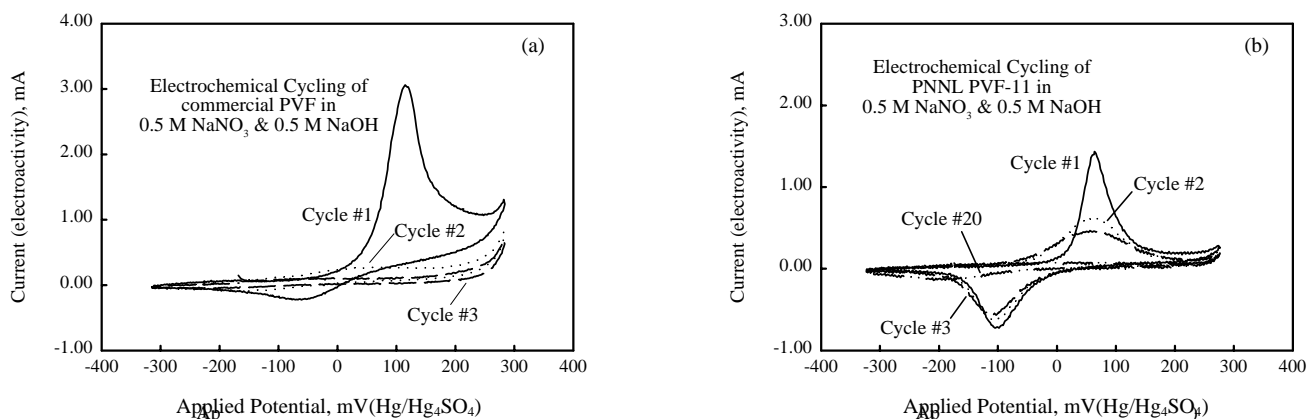
Figure 7.9. Cyclic voltammetry for (a) commercial polyvinylferrocene (PVF) and (b) PVF-11 (prepared at PNNL) in alkaline solultions. PVF-11 shows significantly enhanced stability in alkaline solution and remains electroactive through 20 cycles in comparison to a single cycle for commercial PVF coatings.

is not completed. Therefore, we are hopeful that we will successfully synthesize alkaline-stable electro-active polymers. We have successfully synthesized vinyl-ether ferrocene monomers; these monomers will allow us to systematically study the effects of charge site mobility and molecular weight on characteristics listed earlier (mainly #3 and #4). Initial attempts of using phase-inversion techniques with commercial PVF for making high-capacity electrodes (#5 above) have failed; this has been attributed to the inability to make highly concentrated solutions. In addition, variables in commercially available PVF have made systematic studies of the process conditions difficult. PNNL currently is synthesizing polymers to overcome both of these difficulties. Studies on the application of phase-inversion techniques for making high capacity electrodes are continuing using model polyaniline polymers.

The methods for obtaining *in situ* x-ray absorption spectroscopy (XAS) on PVF electrodes in perrhenate (ReO_4^-) electrolytes have been refined and improved. Most of the problems in collecting spectra at the Fe K edge accrued from the large background from the ReO_4^- ions, which has been resolved by reconfiguring the electrodes in the spectroelectrochemical cell. It was necessary to optimize the x-ray optics in two separate x-ray scans to obtain good near edge (XANES) and extended fine structure (EXAFS) spectra. Spectra have also been obtained *ex situ* at the Fe K edge on several electrodes prepared from polymer materials synthesized at PNNL. XAS and electrochemical studies were also done on ferrocenium perrhenate, dimethylferrocenium perrhenate, and ferrocenium nitrate, which were synthesized at Brookhaven National Laboratory. The electrochemical studies indicated a stronger interaction of the perrhenate anion with the ferrocenium cation than that seen with the nitrate anion.

Plasma Functionalization of Electroactive Polymers

J. H. Sukamto[a,b], *T. Hubler*[a,b], *and M. Lilga*[b]

The project objective is to provide the basis for using electroactive ion exchange materials to remove anionic contaminants from high-level wastes (HLW) and process streams. An ion exchange process using electroactive materials sorbs contaminants selectively and then expels (elutes) them electrochemically by changing the charge balance through redox reactions in the sorbent as opposed to requiring the addition of a chemical eluant. Such processes theoretically can remove anions (e.g., pertechnetate and chromate) and concentrate them in a separate product stream without adding process chemicals. A practical implementation in HLW process facilities would be a breakthrough in the ability of the Department of Energy to economically minimize waste and prevent pollution at its sites. To enable this, our work focuses on manipulating specific properties of redox polymers to control the hydrophobicity and ion-pair properties pertinent to the reversibility, selectivity, stability, intercalation/deintercalation rates, and capacity of the polymers. This involves determining the density of charged sites, mobility of charged sites, degree of cross-linking, and polymer chain length. The work will be performed by PNNL (synthesis and characterization of polymers), Brookhaven National Laboratory (direct characterization of ion-pair interactions), and the University of Minnesota (synthesis and characterization of high capacity polymers).

Plasma functionalization of the electroactive polymers mentioned above was explored to address stability issues: 1) delamination of the polymer from the electrode surface during electrochemical cycling and 2) chemical degradation of the electroactive moieties due to exposure to highly alkaline solutions. We are particularly interested in enhancing the stability of ferrocene-containing polymers. Because ferrocinium is soluble in aqueous solutions, delamination of polyvinylferrocene (PVF) from a PVF-coated electrode due to extended electrochemical cycling in an aqueous solution is not surprising. It is also known that ferrocinium in alkaline solutions will degrade to form iron hydroxide.

One means to minimize delamination is to reduce the solubility of the polymer, which can be achieved by increasing the molecular weight of the polymer (e.g., through plasma cross-linking). Our initial results indicate that plasma treatment using an inert gas (e.g., nitrogen or helium), which is believed to cross-link the polymer strands, can effectively minimize delamination. Extended (> 8 hours) electrochemical cycling of a PVF-coated high-surface-area carbon electrode resulted in coloration of the contacting solution. On the other hand, the solution in contact with a similar electrode that had been plasma treated remained colorless. More quantitative studies of the effect of plasma cross-linking in minimizing delamination are underway.

All attempts in using plasma treatment to increase the chemical stability in highly alkaline solutions have not been successful.

Ion Beam Modification of Spinel Crystals in Glass Medium

*M. Haller[a,b], S. K. Sundaram[c], S. Thevuthasan, V. Shutthanandan, and Y. Su[d,e]*

(a) EMSL User.
(b) Graduate Student, University of Washington.
(c) PNNL Environmental Technology Division.
(d) PNNL Energy Science and Technology Division.
(e) EMSL Matrixed Staff.

The main objective of this project was to determine the effect of radiation on the stability of spinel crystalline phases in waste glasses. Ideally the project would have demonstrated the amorphization of spinel phase in a glass matrix using ion beam radiation. The project involved careful preparation and characterization of glass samples containing spinel crystals and the exposure of these samples to ion beam radiation. Once the samples were implanted, scanning electron microscopy (SEM) and Raman spectroscopy were used to characterize the irradiated samples. Samples of a high-level waste (HLW) glass (MS-7) were obtained from the Applied Process Engineering Laboratory (APEL) spinel research team. The glass first was melted in platinum crucibles, and then poured on a metallic surface and allowed to quench to room temperature. The glass samples were pretreated at 1200° C for 1 hour, heat treated at 959° C for 2.25 hours, and then air quenched. The samples were cut into small pieces and polished for implanting. The samples were implanted by various doses of Au^{2+} as listed in Table 7.1. Irradiation experiments were carried out at temperatures ranging from 200 to 270 K. After implantation, the samples were removed from the implantation chamber for *ex situ* SEM and Raman spectroscopy measurements.

Table 7.1. Experimental Implantation Doses

Spinel Sample	Dose (Au^{2+} ions/cm^2)
1	$5*10^{15}$
2	$1*10^{16}$
3	$3*10^{16}$
4	$1.25*10^{17}$

An SEM micrograph of an unirradiated glass sample with spinel crystal inclusions is presented in Figure 7.10. Small spinel inclusions are clearly visible in this micrograph. Top and side views of the irradiated (dose- 1.25×10^{17} Au^{2+}/cm^2) sample are shown in Figures 7.11 and 7.12, respectively. Although there were no significant visual changes in the spinel inclusions, significant changes were observed in the glass medium after the irradiation at this dose. Slight compositional changes were observed in both the spinel inclusions and glass medium [confirmed by the energy-dispersive spectroscopy (EDS) data]. No significant changes were observed either in the spinel inclusions or in the glass medium for the smaller doses (doses 1-3). Raman spectroscopy measurements were made on all the irradiated samples along with an unirradiated reference sample. Analysis of these data is currently in progress. TEM data will also be collected on selected samples to support any structural changes observed by the Raman data.
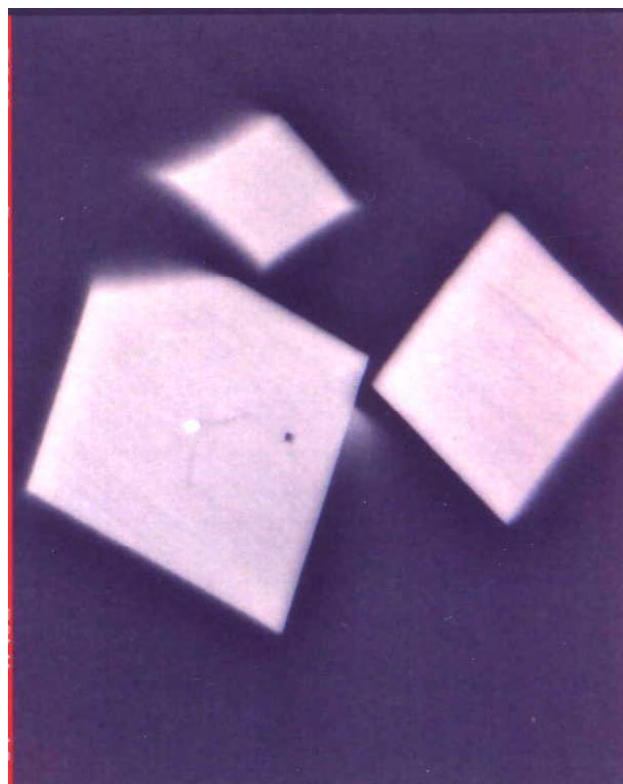
Figure. 7.10. SEM image of unirradiated glass sample (spinel crystal inclusions; × 5000).
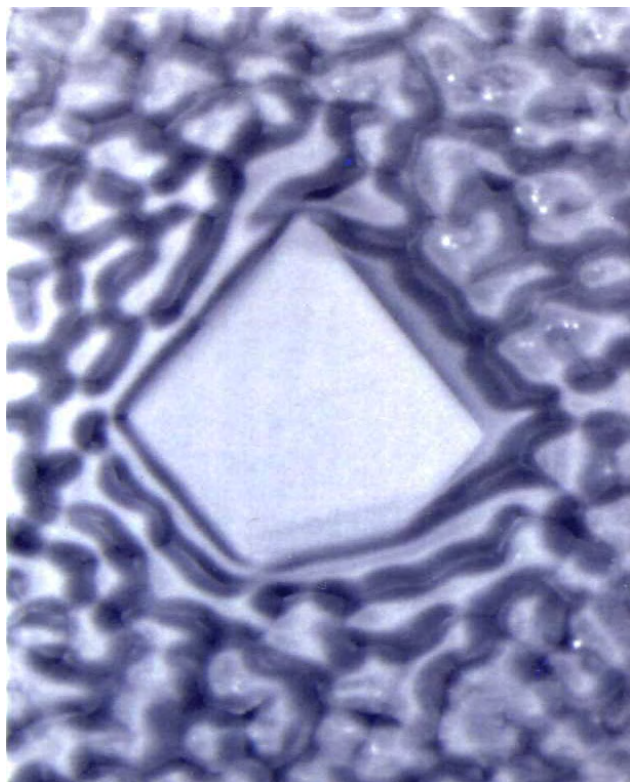
Figure 7.11. SEM image of irradiated glass sample (dose 4 – 1.25x10^{17} Au^{3+}/cm^2; spinel crystal inclusions; top view; $\times$ 5000).
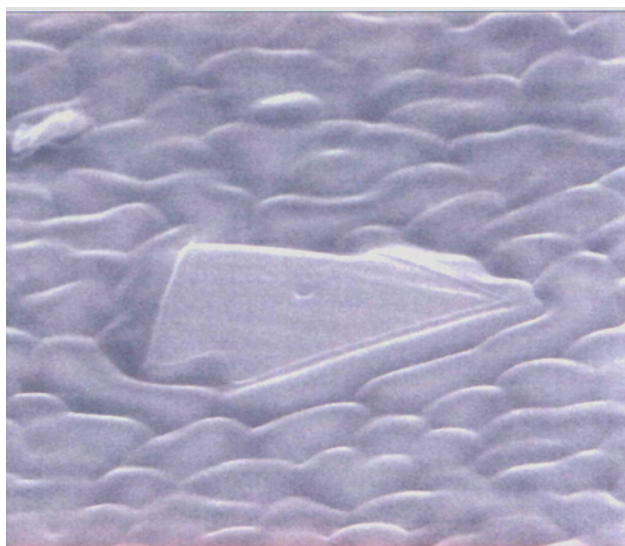
Figure 7.12. SEM image of irradiated glass sample (dose 4 – 1.25x10^{17} Au^{3+}/cm^2; spinel crystal inclusions; side view, $\times$ 10000).

8. Analysis and Characterization

Introduction of Environmental Samples for Analysis by Inductively Coupled Plasma and Ion Trap Mass Spectroscopy

M. L. Alexander, A. Hedges[a], J. Davis[a], D. Weir[b], J. T. Dickinson[c,d], M. T. Taylor[c,e], G. Cardell[c,e], T. Moeller[c,f], P. Irving[c,f], C. Driver[g], and C. Aardahl[g]

(a) Student.
(b) Postdoctoral Research Fellow.
(c) EMSL User.
(d) Washington State University.
(e) Jet Propulsion Laboratory, NASA.
(f) InnovaTek, Inc., Richland, WA.
(g) PNNL Environmental Technology Division.

The work in our laboratory has centered around the general theme of exploring various means of sample introduction for analysis by ion trap mass spectrometry (ITMS) or by inductively coupled plasma mass spectrometry (ICP-MS). The main areas are summarized below.

Laser Ablation ICP-MS for Chemical Analysis of Radioactive Waste from Plutonium Production Operations

This project focused on the specific physical and chemical processes involved in laser ablation of solid waste forms found at Hanford and other Department of Energy sites. Several types of particulates were identified in this ablation process and related to the accuracy and precision of subsequent elemental analysis by ICP-MS. This work also sparked collaboration with EMSL users from the NASA Jet Propulsion Laboratory. Their interests are in using laser ablation for remote sampling and analysis on Mars. During this collaboration, we demonstrated that laser ablation of geological samples within an ion trap could be used to obtain elemental compositions in excellent agreement with those obtained by ICP-MS. A sample mass spectrum is shown in Figure 8.1. Plans are underway to use these results to develop a miniature ITMS for deployment on future Mars missions.
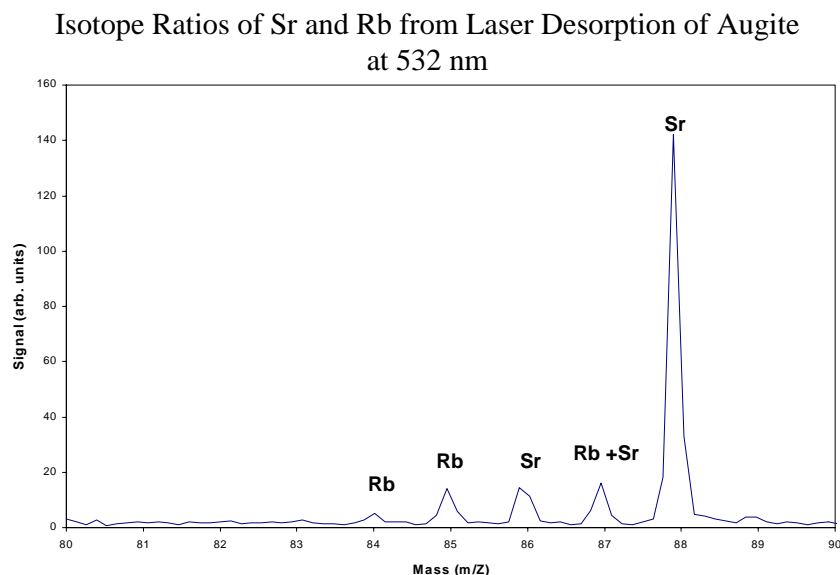
Figure 8.1. Isotope ratios of Rb and Sr determined by laser ablation ion trap mass spectrometry of Augite.

Laser Desorption of Atmospheric Aerosols for Analysis of Semi- and Involatile-Organic Compounds Using Membrane Introduction Ion Trap Mass Spectrometry (MINITMS)

This research investigated the feasibility of using laser desorption to transfer semi- and involatile-organic components from solid, particulate samples into the gas phase, transport them across a semi-permeable membrane, and detect them in an ITMS. The concept was demonstrated on samples spiked with PAH compounds. The system was then deployed in Houston for two weeks as part of the Texas2000 Air Quality Study. The membrane system also was used to monitor gas-phase compounds simultaneously with the collection of particulate samples.

Optical Detection of Single Aerosol Particles for Analysis by Laser Desorption Ion Trap Mass Spectrometry

In this project, we utilized laser light scattering to characterize individual particulates both by their aerodynamic size and their optical size. We were able to distinguish particles with varying densities and optical properties that were indistinguishable using only one measurement. Continuing work on this system involves mounting the optical detection system on an ITMS equipped for laser desorption. The optical system will be used to pre-select aerosols of interest such as biological particles for subsequent interrogation by laser desorption ITMS.

Detection and Identification of Surrogate Chemical Warfare Agents and Their Breakup Compounds

The ITMS system was used with both the MIMS interface and a capillary interface for the detection of compounds resulting from the plasma decontamination of surfaces that had been treated with simulant compounds for chemical warfare (CW) agents. The result of these studies determined that the compounds being released were themselves not toxic, and was able to determine when decontamination was complete. The results are being applied to the development of a portable system for field use in decontamination activities. Related studies involved the observation of breakdown of CW surrogates in the PNNL wind tunnel facility.

Elemental Analysis of Astrosclereids in Needles of Old-Growth Douglas Fir Trees

M. Apple[a,b], B. Bond[a], J. Young, and D. McCready

Supported by private funding.
(a) Department of Forest Science, Oregon State University.
(b) EMSL User.

Needle anatomy changes with increasing tree age in Douglas fir trees. Thus, morphological differences between old growth and sapling [*Pseudotsuga menziesii*, (Mirb.) Franco] Douglas fir trees extend to differences in needle anatomy. We used microscopy and image analysis to compare and quantify anatomical parameters in cross-sections of previous year needles of old growth and sapling Douglas fir trees at the Wind River Canopy Crane in Washington and at three sites in the Cascade Mountains of Oregon. We also compared needle anatomy across a chrono-sequence of 10-, 20-, 40-, and 450-year-old Douglas fir trees from the Wind River site. Anatomy differed significantly between needles of old growth and sapling Douglas fir trees at all sites. Needles of saplings had proportionately smaller vascular cylinders, larger resin canals, and few hypodermal cells. In contrast, needles of old-growth trees were shorter, had proportionately larger vascular cylinders, smaller resin canals, and numerous hypodermal cells. Needles of old-growth trees had an average of 11.2% less photosynthetic mesophyll area than needles of saplings. The percentage of non-photosynthetic area increased significantly with increasing tree age in needles from the chrono-sequence of 10-, 20-, 40-, and 450-year-old trees at the Wind River site. This reduction in photosynthetic area may contribute to decreased growth rates in old trees.

Astrosclereids are large cells found in the mesophyll of Douglas fir needles (Figure 8.2). Astrosclereids were scarce in needles of saplings but abundant in needles of old-growth trees. They sequester carbon as lignin in their secondary cell walls and occupy space otherwise filled by photosynthetic cells. Examination of astrosclereids in cryofractured needles with a Leo 982 field emission scanning electron microscope (FESEM) and energy dispersive x-ray spectroscopy (EDS) demonstrated that astrosclereid walls are composed of carbon, hydrogen, and oxygen, elements consistent with lignin composition. These needles also contained crystals in the phloem and on mesophyll cell surfaces. The composition of these crystals corresponded with that of calcite ($CaCO_3$) and whewellite ($C_2CaO_4 \cdot H_2O$), as determined with x-ray diffraction. Knowledge of astrosclereid and crystal composition is valuable in increasing our understanding of tree physiology and carbon dynamics in ancient forests.
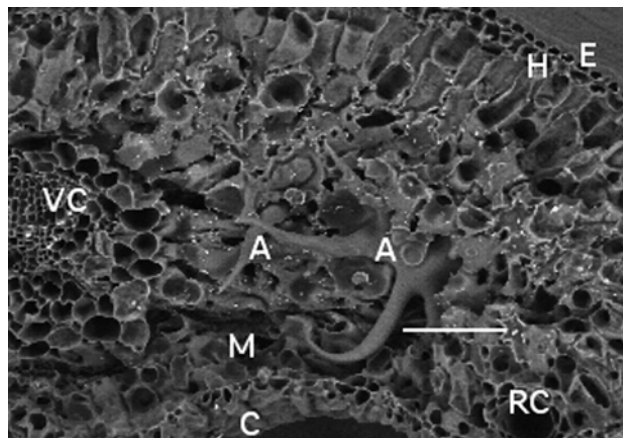
Figure 8.2. Scanning electron micrograph of a freeze-fractured and carbon-coated needle of a 450-year-old Douglas fir tree. A = Astrosclereid, C = Cuticle, E = Epidermis, H = Hypodermis, M = Mesophyll, RC = Resin Canal, and VC = Vascular Cylinder. Scale bar = 100 µm.

Sub-Millimeter Study of C and N Assimilation in Soils Using TOF-SIMS

J. B. Cliff[(a,b)], P. J. Bottomley[(a)], D. J. Gaspar, and D. D. Myrold[(a)]

Supported by a USDA CSREES grant.
(a) Oregon State University.
(b) EMSL User.

Our research has focused on understanding C and N cycling at sub-millimeter scales in soils using time-of-flight secondary ion mass spectrometry (TOF-SIMS). We have used TOF-SIMS to detect C and N assimilation in gram-negative and gram-positive bacteria and fungal biomass labeled with ^{13}C or ^{15}N. Further, we have documented single-cell detection of C and N assimilation in gram-negative bacteria and fungal hyphae. Single-cell detection of bacteria was verified by matching fluorescence images of cells stained with the DNA specific fluorophore DAPI with $^{26}CN^-$ ($^{12}C^{14}N^-$), $^{27}CN^-$ ($^{12}C^{15}N^-$ and $^{13}C^{14}N^-$), and $^{28}CN^-$ ($^{13}C^{15}N^-$) ion images.

We have extended this work to explore factors that differentially affect NO_3^- versus NH_4^+ assimilation in soil systems. In one system, manure and straw were placed in close proximity on pure kaolin clay, $^{15}NO_3^-$ was added, and a Si contact slide was placed on the soil. Atom % ^{15}N in fungal biomass was estimated from the $^{27}CN^-$:$^{26}CN^-$ ratio of region of interest analyses of the hyphae. These studies have shown that ratios of NH_4^+ and NO_3^- assimilation may vary over very small distances. Where manure was separated from straw by a distance of about 500 μm, the ^{15}N abundance of a single fungal hyphae changed from 20 atom % ^{15}N in a region of kaolin to 10 atom % ^{15}N near a piece of manure and within a distance of 200 μm. In an area where manure and straw overlapped, fungal biomass changed from 19 atom % ^{15}N

under the straw to about 10 atom % ^{15}N under the manure over a distance of 40 μm.

In a separate study, a Si contact slide was placed in a clay soil in a riparian area. The soil was labeled with 99 atom % $^{15}NH_4^+$ and natural abundance NO_3^-. The contact slide showed bacteria and fungi in close spatial proximity with widely varying ^{15}N signatures. In one case, a bacterium that was approximately 40 atom % ^{15}N and a fungal hyphae that was 7 atom % ^{15}N were less than 15 μm apart (see Figure 8.3). These data show that the environmental and biological factors that control N assimilation by microorganisms potentially act at the sub-millimeter scale.
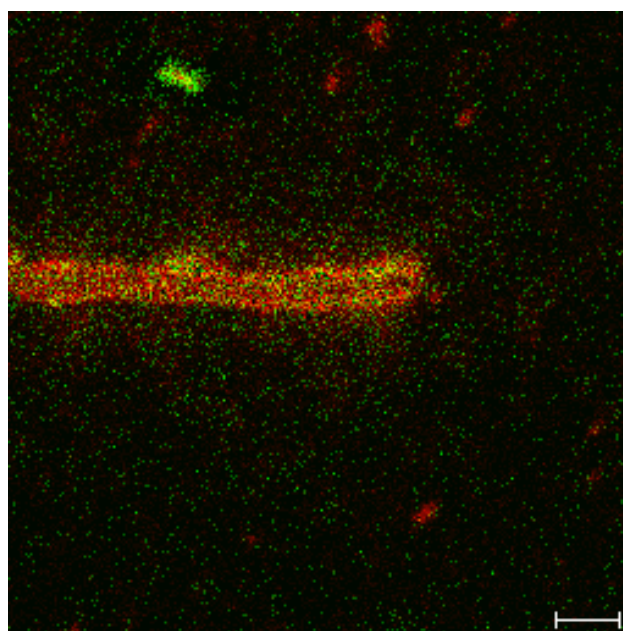
Figure 8.3. TOF-SIMS image overlay of $^{26}CN^-$ and $^{27}CN^-$ ion images of a Si contact slide that had been buried in a clay riparian soil and labeled with $^{15}NH_4^+$. The image shows a fungal hyphae and a bacterium that have different affinities for $^{15}NH_4^+$ despite being in close spatial proximity. Green represents $^{27}CN^-$, red represents $^{26}CN^-$, bar represents 5 μm.

Plasma Lysis of Bacterial Spores

V. K. Kenning[a,b], and J. M. Monteith[a,b]

Supported by DARPA SPO.
(a) EMSL User.
(b) MesoSystems, Inc., Richland, WA.

For more than 100 years, scientists have reported that direct and alternating electrical currents can kill or inhibit the growth of bacteria and yeast (Cohn and Mendelsohn 1879, Tracey 1932). Repetitive high voltage pulses have been recommended for continuous sterilization of liquid streams (Qin et al. 1998, Grahl and Markl 1996). However, researchers report that cells killed by pulsed electrical fields are not disintegrated, and bacterial spores, molds, and viruses are relatively insensitive to high voltage pulsing (Dunne 1999). A plasma discharge, however, has been shown to affect the spectra obtained from spores using matrix-assisted laser desorption ionization mass spectrometry (MALDI-MS) (Birmingham et al. 1999). In order to better understand the effect of the plasma on the spores, a series of scanning electron micrograph (SEM) images were obtained. The conditions of plasma treatment were varied (duration, voltage, etc.). Samples of treated spores as well as

spores to which matrix (a crystal forming solution used in the MALDI process) was added were observed using the SEM. The images have been valuable in showing the shape and distribution of the matrix crystals and spores, the quality of the spore preparations, and the effect of the treatment on the spores. Examples of the images obtained in this effort are shown in Figures 8.4 and 8.5.

References

Birmingham, J., P. Demirev, Y. P. Ho, J. Thomas, W. Bryden, and C. Fenselau, *Rapid Commun. Mass Spectrom.* **13**:604-606 (1999).

Cohn, F. and B. Mendelsohn, *Beitr. Biologie der Pflanzen* **3**, no. 141 (1879).

Dunne, P., "Pulsed Electric Fields for Pasteurization of Food", ElectroMed 99 Concurrent Presentation: First Inter. Conf. on Nonthermal Medical/ Biological Treatments Using Electromagnetic and Ionized Gases, April 12-14, 1999, Norfolk, VA.

Grahl, T. and H. Markl, *Appl. Microbiol. Biotechnol.*, **45**, no. 148 (1996).

Qin, B. L., G. B. Barbosa-Canovas, and B. S. P. Pedrow, *IEEE Trans. on Industry Applications*, **34**, no. 43 (1998).

Tracey, R., *J. Bacteriology* **24**, no. 423b (1932).
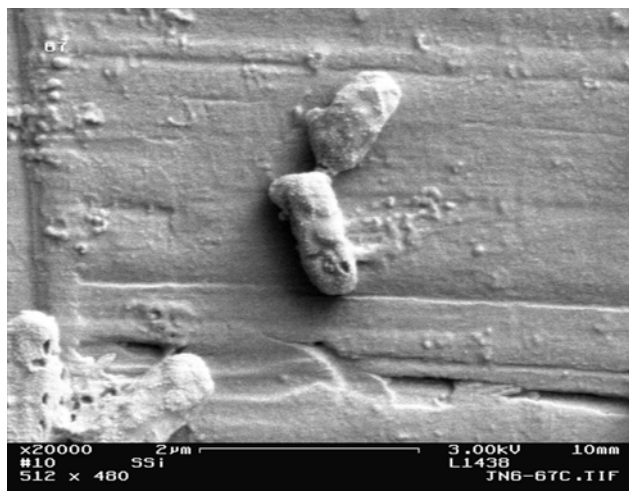
Figure 8.4. Scanning electron micrograph of untreated Bg spores.
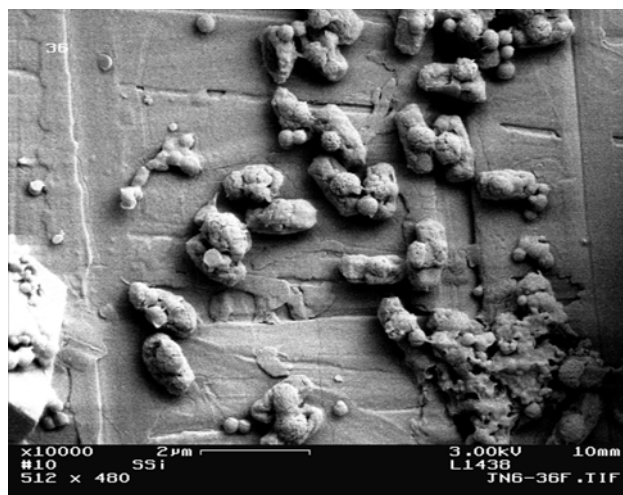
Figure 8.5. Scanning electron micrograph of plasma-treated Bg spores.

Analysis of Gases Produced During Plasma Treatment of Surfaces Contaminated with Chemical and Biological Agent Simulants and the Effects of Treatment on These Surfaces

M. Alexander, T. M. Moeller[a,b], and M. Luna[a,b]

Supported by PNNL Small Business Assistance Program and U.S. Air Force Office of Scientific Research, SIRTI.
(a)   InnovaTek, Inc.
(b)   EMSL User.

InnovaTek, Inc. is developing a portable, hand-held plasma flare gun (patent pending) that operates at atmospheric pressure and low temperatures. The device employs a high-voltage, corona plasma to create active species that destroy or detoxify chemical and biological weapons materials. The active plasma species generated by this device are brought into contact with a contaminated surface to effectively break down both chemical and biological contaminants. Plasma chemical processes are highly effective in promoting oxidation, enhancing molecular dissociation, and producing free radicals to enhance chemical reaction. The focus of the proposed research is to demonstrate the feasibility of a portable plasma surface decontamination system with real time off-gas monitoring by building on our experience with cold plasma systems.

Aluminum coupons inoculated with DMMP, a simulant for the chemical agent Sarin, were positioned below the exit of a plasma flare prototype and treated for up to 10 minutes. A minimum concentration of approximately $0.5 \ g/m^2$ of DMMP was placed on the samples before exposure. Each treatment was replicated three times on aluminum coupons. GCMS data indicate that greater than a four $\log_{10}$ destruction of the DMMP on the aluminum surface was achieved in a 10-minute treatment with the plasma flare (Figure 8.6). The temperature in all tests remained below 105° C.

During the chemical simulant tests, an ion-trap mass spectrometer (ITMS) was used to collect time-resolved data on the off-gases produced during plasma treatment. Figure 8.7 shows mass spectra for the off-gas products of DMMP compared to the mass spectrum of DMMP dissolved in acetone.

The off-gas mass spectrum differs significantly from the pure DMMP mass spectrum. The off-gas spectrum has no components either at the DMMP parent mass of 124 or at 109, which represents the loss of one methyl group. The predominant mass is at 79, corresponding to PO_3. This demonstrates unequivocally that the cold plasma decontamination is not simply volatilizing the DMMP, but is breaking it down. These results indicate that the cold plasma can reduce toxic compounds into harmless by-products during the course of decontamination. Figure 8.8 shows the time-resolved intensity of two of the mass peaks, 79, corresponding to PO_3, and 47, corresponding to PO.
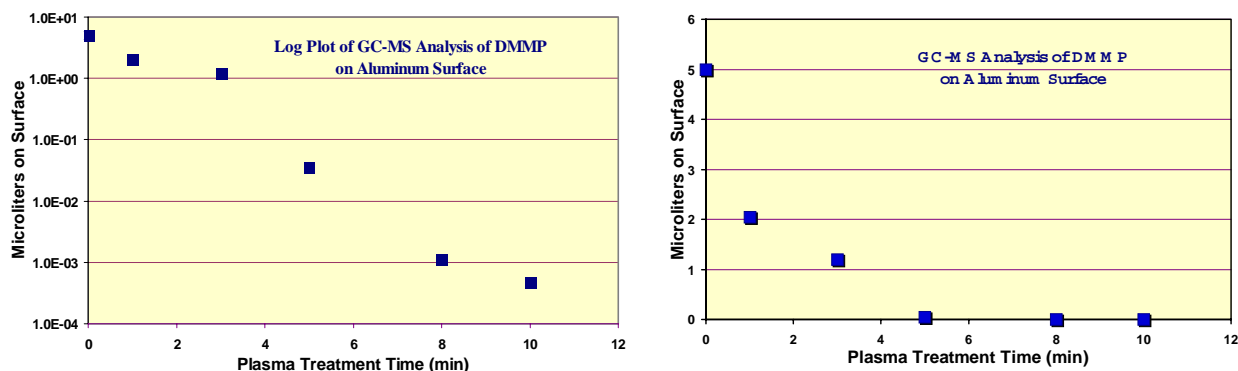
Figure 8.6. Chemical agent decontamination efficiency of DMMP, a Sarin simulant, on an aluminum surface treated with InnovaTek's plasma flare gun. Left: log plot; Right: normal plot.
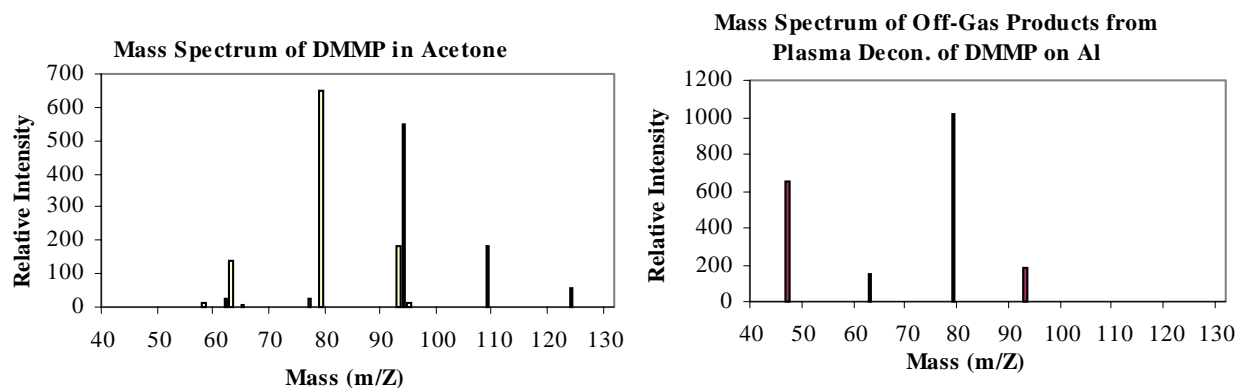
Figure 8.7. Mass spectra for the plasma off-gas products of DMMP (right) and DMMP dissolved in acetone (left).
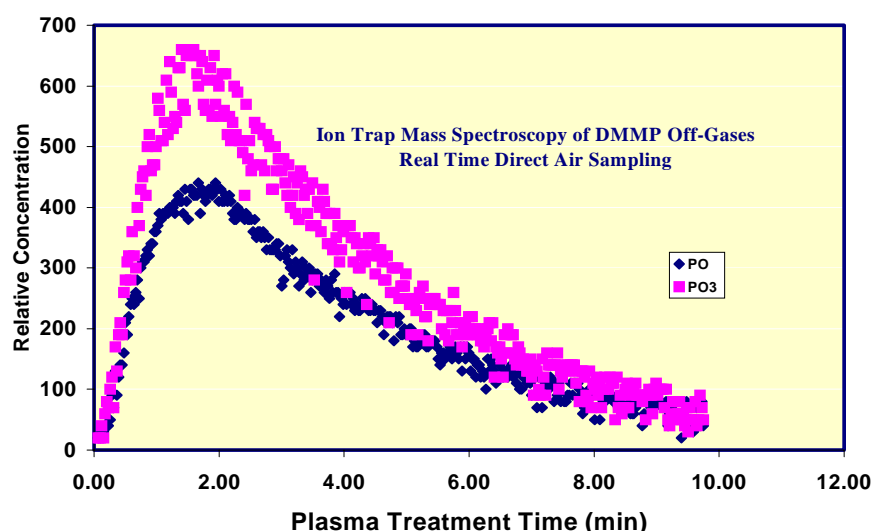
Figure 8.8. Time-resolved intensity of PO and PO_3 in the plasma off-gas.

There is an apparent induction time of approximately 2 minutes followed by a decay period until levels have returned to baseline levels at about 10 minutes. Although the signal-to-noise was far from optimal in this effort, it clearly demonstrates the potential for use of the ITMS system in monitoring off-gas products from plasma decontamination.

The analysis of the off-gases has led to an important new finding of this effort. There appears to be a correlation between the concentration of components of broken down DMMP in the treatment off-gases

and the amount of DMMP remaining on the surface. If a reliable correlation can be established, monitoring the off-gases for fragments of contaminants could be used as a real-time monitor of the degree of surface contamination. The end result would be a monitoring system that tells the operator when the surface decontamination is complete.

Testing with simulants of biological warfare agents, performed by Innova-Tek in its own laboratory, resulted in 99% kill rates in 60 seconds or less.

Thermal Analysis of Polymeric Materials

L. S. Sapochak[a,b], P. E. Burrows[c,d], G. L. Graff[c], and T. Hart[d,e]

(a) EMSL User.
(b) Visiting Faculty, University of Las Vegas, Nevada.
(c) PNNL Energy Science and Technology Division.
(d) EMSL Matrixed Staff.
(e) PNNL Environmental Technology Division.

Polymeric coating materials were analyzed by thermal analysis techniques coupled to mass spectrometry (MS) and Fourier-transform infrared spectroscopy (FTIR). Differential scanning calorimetry (DCS) and thermal gravimetric analysis (TGA) were run simultaneously on UV-cured polymer films. Under a nitrogen atmosphere, TGA traces showed ~3-4% weight loss between 140° and 200° C accompanied by an inflection point in the DSC, before film decomposition at ~400° C. The mass spectral analysis of evolved gases suggested that unreacted monomer and/or photoinitiator was degassing from the film. Gas chromatography (GC)/MS experiments were conducted to determine the nature of the degassing species.

Solid samples were placed directly into the injection chamber of the GC and heated at a constant temperature during the GC/MS run. Samples were first heated at 140° C and then 170° C. GC traces and MS library matches were generated for each major peak run at both temperatures. Excess photoinitiator was identified. This information is important for understanding how to improve the processing conditions and resulting physical properties of the target polymeric coating materials.

Characterization of Ti-6Al-4V Forged and Heat Treated Specimens

F. H. Froes[a,b], O. N. Senkov[a,b], S. V. Senkova[a], M. Cavusoglu[a,c], and D. E. McCready

Supported by University of Idaho funding.
(a) University of Idaho.
(b) EMSL User.
(c) Student.

The effect of the cooling rate from 975° C (upper part of the alpha+beta range) on the microstructure and texture of Ti-6Al-4V forging was studied using optical microscopy (OM), transmission electron microscopy (TEM), and x-ray diffraction (XRD). Longitudinal (*LD,* parallel to the forging axis) and transverse (*TD,* perpendicular to the forging axis) cross-sections were studied. The morphology of the phases, the sizes of primary alpha particles, and the volume percentage of the primary alpha particles were determined using OM methods. The fine microstructure, phases, and chemistry were analyzed using TEM/EDS. The amounts of alpha and beta phases and the texture of the alpha (hcp) phase were determined using XRD.

The specimens had a duplex microstructure consisting of elongated primary alpha particles and secondary finer alpha lathes with some residual beta phase between them. This type of microstructure is typical of the Ti-6Al-4V alloy processed and/or heat treated in the (alpha + beta) field. The average length and width of the primary alpha particles decrease and the aspect ratio increases when the cooling rate is increased (Table 8.1). The volume fraction of the primary alpha particles decreases when the cooling rate increases, which could be described by a power law equation $VF = 1.67 (CR)^{-0.36}$, where VF is the volume fraction and CR is the cooling rate. The prior beta grain size was 0.21 ± 0.02 mm and did not depend on the cooling rate.

Two different microstructural morphologies were observed using TEM. Alpha phase was present as large equiaxed grains consisting of smaller equiaxed subgrains, and lenticular plates (lamellae) with the beta-phase layers between the lamellae. The average lamellar spacing decreases from about 1 µm to 0.3 µm when the cooling rate increases from 25° C/minute to 490° C/minute (Figure 8.9).

EDS analysis showed that the alpha phase contained 3.8 to 5.8 wt.% and 1.4 to 2.1%V, while the beta phase contained 1.4 to 2.5 wt.% Al, 12 to 18 wt.% V.

Table 8.1. Length, width, aspect ratio, and volume fraction of the primary alpha particles in specimens cooled with different cooling rate.

Sample ID and Cross-Section Type	Cooling Rate °C/min	Primary Alpha Particle Length µm	Primary Alpha Particle Width µm	Aspect Ratio of Primary Alpha Particles	Volume Fraction of Primary Alpha Particles
45, *LD*	25	16.5	9.6	1.7	0.61
45, *TD*	25	15.9	8.6	1.8	0.53
28, *LD*	50	16.5	8.5	1.9	0.38
28, *TD*	50	20.0	9.8	2.0	0.36
30, *LD*	108	13.6	7.4	1.8	0.32
30, *TD*	108	19.2	8.5	2.2	0.34
26, *LD*	113	16.3	7.2	2.3	0.28
26, *TD*	113	19.7	7.6	1.7	0.29
20, *LD*	185	14.8	8.8	2.6	0.34
20, *TD*	185	15.3	6.9	2.2	0.24
52, *LD*	250	12.8	6.6	1.9	0.27
52, *TD*	250	15.8	8.0	2.0	0.23
31, *LD*	326	14	8.1	1.7	0.18
31, *TD*	326	15.4	7.0	2.2	0.23
40, *LD*	490	15.3	5.7	2.7	0.19
40, *TD*	490	15.1	7.4	2.0	0.17

and 1.5 to 2.4 wt.% Fe. In the alpha phase, the concentration of Al increases and the concentration of V changes only slightly with an increasing cooling rate (Figures 8.10 and 8.11). In the beta phase, the concentration of Al slightly increases, while the concentration of V decreases as the cooling rate is increased (Figures 8.12 and 8.13). These trends suggest that slower cooling rates allowed both the alpha and beta phases to reach chemistry levels closer to equilibrium.

Table 8.2 shows the amount of the β phase ($n_β$ in %) and lattice parameters (a and c in Å) of the eight different Ti-6Al-4V forging samples as calculated

Figure 8.11. Effect of cooling rate on vanadium composition of the α-lamellae.

Figure 8.9. Effect of cooling rate on the lamellae spacing.
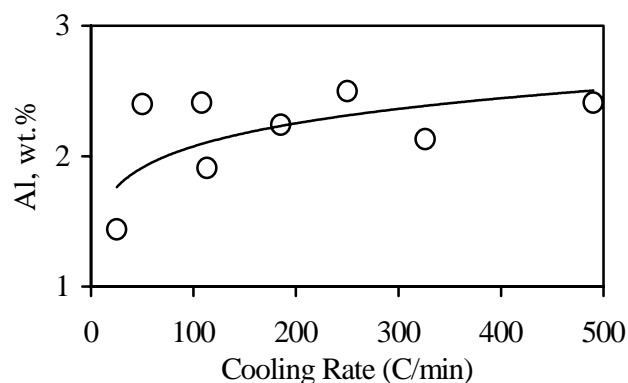
Figure 8.12. Effect of cooling rate on the Al composition in the β layers.

Figure 8.10. Effect of cooling rate on aluminum composition in α-lamellae.
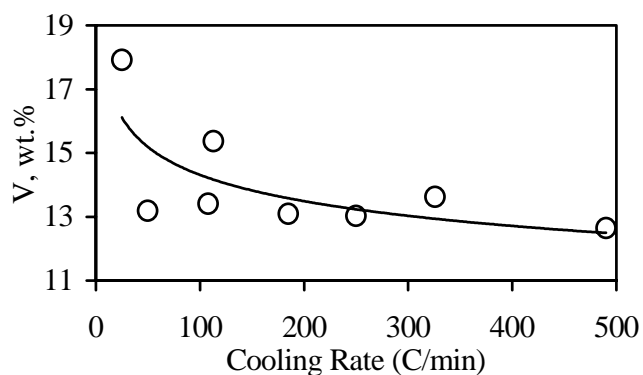
Figure 8.13. Effect of cooling rate on the vanadium composition in the beta layers.

Table 8.2. Percentages of beta phase and lattice parameters (a and c).

Sample #	Cooling Rate (°C/min)	n_β (%)	a(Å)	c(Å)
45	25	5.96	2.9394	4.6673
28	50	12.31	2.9387	4.6826
30	108	7.18	2.9332	4.6877
26	113	11.13	2.9447	4.6751
20	185	6.88	2.9295	4.6759
52	250	5.86	2.9166	4.6499
31	326	6.45	2.9334	4.6913
40	490	4.32	2.9293	4.6755

using XRD. The lattice parameters of pure titanium, according to the ASTM standard, are a=2.9500 Å and c=4.6860 Å. The volume fraction of the beta phase was observed to decrease with increasing cooling rate. Lattice parameter 'a' of the dominant alpha phase was observed to decrease with increasing cooling rate, while lattice parameter 'c' of this phase appeared to increase slightly as the cooling rate was increased.

The as-forged sample had a very weak (0001) texture in a forging plane. Annealing at 975° C followed by cooling with different cooling rates showed only a little effect on the texture.

Lanthanum Chromite Materials: Characterization and Development

S. P. Simner[a,b], J. S. Hardy[b], L. A. Chick[b], J. W. Stevenson[b], and T. M. Armstrong[b]

Several studies have been undertaken to characterize and develop lanthanum chromite materials. Each of these studies is summarized below.

Cost Reduction of Lanthanum Chromite Materials

S. P. Simner, J. S. Hardy, L. A. Chick, and J. W. Stevenson

Acceptor-doped lanthanum chromite ($LaCrO_3$) has long been the interconnect material of choice for high temperature solid oxide fuel cells (SOFCs), typically operating at 1000° C. However, lanthanum chromite is relatively expensive, and many developers are currently pursuing SOFCs operating at lower temperatures. As the operating temperature is lowered, metal interconnects (e.g., ferritic steels or chromium alloys) become increasingly viable, but they have their own unique problems (including Cr-oxide formation and Cr volatilization); it is therefore likely that uncoated metals cannot be used at temperatures greater than 700° C. For intermediate operating temperatures (700° to 800° C), the application of protective oxide coatings may allow the use of metal interconnects (if such coatings can be applied cost-effectively), but lanthanum chromite may offer better long-term performance. While the electrical conductivity of lanthanum chromite does decrease as temperature decreases, the conductivity at 800° C is only about 10% less than the conductivity at 1000° C.

In this study, the authors have investigated the viability of replacing pure La in the acceptor-doped $LaCrO_3$ with a less expensive mixed lanthanide (Ln) precursor containing La^{3+} as the principal cation, but also with Ce^{4+}, Nd^{3+}, and Pr^{3+} in significant proportions. Typical compositions investigated were of the formula $Ln_{0.85}Sr_{0.15}Cr_{1-y}M_yO_3$, where $0.02 \leq y \leq 0.1$ and M = Co, Cu, Ni, and V. Samples were studied with respect to sinterability in air, thermal expansion, conductivity in air and at low pO_2, phase stability, and dilation under reducing atmospheres. The most promising of the materials investigated was a $Ln_{0.85}Sr_{0.15}Cr_{0.95}Cu_{0.05}O_3$ composition, which could be sintered to >90% theoretical density at 1250° C, exhibited conductivities >20 S/cm in air and >5 S/cm at $pO_2 = 10^{-16}$ atm, and indicated no phase change from 25° to 1000° C. The TEC (25° to 1000° C) of the material, 9.4×10^{-6} °C^{-1}, was somewhat lower than that of the YSZ electrolyte (10.5×10^{-6} °C^{-1}). The isothermal expansion at a pO_2 of 10^{-16} atm and 1000° C was 0.12%, only slightly higher than the targeted maximum of 0.10%.

Sintering and Property Characterization of Strontium-Doped Lanthanum Chromite

S. P. Simner, J. S. Hardy, J. W. Stevenson, and T. R. Armstrong

The sintering of $La_{0.85}Sr_{0.15}CrO_3$ (LSC-15) SOFC interconnect material can be significantly enhanced by doping with transition elements, such as Cu, Co, V, and Ni, on the chromium B-site. Optimized compositions yielded densities greater than 93% theoretical after sintering at 1550° C for 2 hours, compared to <70% theoretical for undoped stoichiometric LSC-15. Detailed XRD and DTA was used in an attempt to establish phenomena responsible for sintering, in particular the presence of low melting temperature second phases. High-density materials were also evaluated for thermal expansion and electrical conductivity in air.

Optimizing Lanthanum Chromite Interconnects For Solid Oxide Fuel Cells

T. R. Armstrong, S. P. Simner, J. S. Hardy, and J. W. Stevenson

Optimizing the composition of strontium-substituted lanthanum chromites to minimize expansion is not straightforward and must be done carefully to avoid compromising sinterability, electrical conductivity, and mechanical strength. In this study, a variety of lanthanum strontium chromites were modified with V, Cu, and Mg to allow densification in air at 1500° C, and their material properties were evaluated. Both additives ($\approx$5 mole% V and 2 mole% Cu) resulted in full densification of Sr substituted (10 and 15 mole%) lanthanum chromite. Of the compositions evaluated, only $La_{0.85}Sr_{0.15}Cr_{0.95}V_{0.05}O_3$ appeared to be a promising interconnect material, showing <0.1% expansion at 10^{-16} atm. While the coefficient of thermal expansion was less than that of stabilized zirconia, small additions of Co (1 mole%) increased the CTE to 10.1 ppm °C^{-1}. The results of this study indicated that Cu acted as an acceptor when added to lanthanum chromite, increasing both the electrical conductivity and expansion upon reduction. The effects of vanadium additions were twofold. First, it acted as a donor in the chromite lattice effectively reducing the overall acceptor concentration. Second, during sintering, V reacted with Sr to form $Sr_3(VO_4)_2$, an effective sintering aid for lanthanum chromite, and further reduced the acceptor level by removing Sr from the perovskite lattice.

Results presented and published at "Solid Oxide Fuel Cells VI", Hawaii, *The Electrochemical Society Proceedings Series*, Pennington, New Jersey, p. 706-715 (October, 1999).

Sintering Mechanisms in Strontium-Doped Lanthanum Chromite

S. P. Simner, J. S. Hardy, J. W. Stevenson, and T. R. Armstrong

The sintering behavior of $(La_{0.7}Sr_{0.3})_xCrO_3$ (0.95≤x≤1.05) is investigated to compare liquid phase sintering phenomena occurring in stoichiometric and non-stoichiometric compositions. Shrinkage analysis revealed marked contrast between the densification characteristics of the A-site enriched (x>1.00) and A-site depleted (x<1.00) materials. A-site depleted samples typically exhibited a single-liquid phase sintering event at 1250° C attributed to the melting of an exsouled $SrCrO_4$ phase. A-site enriched samples indicated two rapid shrinkage events due to the melting of $SrCrO_4$, and a $Sr_{2.67}(CrO_4)_2$ phase with a melting temperature of 1450° C. $Sr_{2.67}(CrO_4)_2$ was shown to evolve from a decomposition reaction between $SrCrO_4$ and La_2CrO_6, detected together in A-site enriched samples from 800° to 1000° C. Maximum densities (93% theoretical density) were achieved for $(La_{0.7}Sr_{0.3})_xCrO_3$ x=1.00 and x=1.01 after sintering at 1700° C for 2 hours.

Results published in *Journal of Materials Science*, **34** [23] 5721-5732 (1999).

Sintering of Lanthanum Chromite Using Strontium Vanadate

S. P. Simner, J. S. Hardy, J. W. Stevenson, and T. R. Armstrong

Small proportions (5 and 10 wt%) of strontium vanadate $[Sr_3(VO_4)_2]$ were added to strontium-doped lanthanum chromite $(La_{0.85}Sr_{0.15}CrO_3)$ to produce high-density, fuel-cell interconnect materials in air at 1550° C without adversely affecting the desirable properties of the material. Compositions investigated were shown to have good electrical conductivity at SOFC operating temperatures in air and reducing environments, phase stability from room temperature to 1000° C, negligible thermal expansion mismatch with yttria-stabilized zirconia electrolytes, and relatively low dilation at pO_2 10^{-16} atm.

Results published in *Solid State Ionics* **128** 53-63 (2000).

Porous Silicon as a Versatile Platform for Laser Desorption/Ionization Mass Spectrometry

Z. Shen[a,b], J. J. Thomas[c], C. Averbuj[b,d], K. M. Broo[c], M. Engelhard, J. E. Crowell[a], M. G. Finn[c], and G. Siuzdak[b,c]

Supported by National Institute of Health.
(a) Department of Chemistry and Biochemistry, University of California, San Diego.
(b) EMSL User.
(c) Departments of Chemistry and Molecular Biology and The Skaggs Institute for Chemical Biology, The Scripps Research Institute.
(d) Mass Consortium Corporation.

Desorption/ionization on porous silicon mass spectrometry (DIOS-MS) is a novel method for generating and analyzing gas phase ions that employs direct laser vaporization. The structure and physicochemical properties of the porous silicon surfaces are crucial to DIOS-MS performance and are controlled by the selection of silicon and the electrochemical etching conditions. Porous silicon generation and DIOS signals were examined as a function of silicon crystal orientation, resistivity, etching solution, etching current density, etching time, and irradiation. Pre- and post-etching conditions were also examined for their effects on the DIOS signal, as were chemical modifications to examine stability with respect to surface oxidation. Pore size and other physical characteristics were examined by scanning electron microscopy (SEM), atomic force microscopy (AFM), and Fourier transform infrared (FTIR) spectroscopy, and correlated with the DIOS-MS signal. Porous silicon surfaces optimized for DIOS responses were examined for their applicability to quantitative analysis, organic reaction monitoring, post-source decay mass spectrometry, and chromatography.

Cavitation Damage with the Dual Reflector Lithotripter

D. L. Sokolov[a,b,c], M. R. Bailey[b], and L. A. Crum

Supported by National Institute of Health and National Science Foundation Graduate Research Fellowship.
(a) Student, Department of Bioengineering, University of Washington.
(b) Applied Physics Laboratory, Center for Industrial and Medical Ultrasound, University of Washington.
(c) EMSL User.

Most patients treated for kidney stones undergo extracorporeal shock wave lithotripsy (ESWL), a method by which high-pressure shock waves are focused at the site of the stone. Although ESWL is the most favored method for treating stones, there is evidence to indicate that substantial damage may be occurring to healthy tissue during treatment. A primary mechanism for damage to both stone and soft tissue may be shock-wave-induced cavitation, the violent growth and collapse of microscopic bubbles. When a cavitation bubble collapses near a rigid surface, it generates a jet of water directed toward the surface with enough force to cause damage even to hard metals (Crum 1988). A conventional spark-gap lithotripter generates a cavitation field in water approximately 2 cm in diameter and 10 cm in length. A similar pattern of damage is observed in pig kidneys exposed to clinical doses of shock waves (Connors et al. 2000).

The current project explores methods for cavitation control. Extensive *in vitro* experiments as well as numerical calculations indicate that two confocal lithotripters, fired simultaneously, may localize the region of most intense cavitation to a spot size of less than 1 cm (Sokolov et al. 1999). It is hypothesized that a cavitation field modified in this way may accelerate stone fragmentation while mitigating damage to surrounding tissue.

All experiments are carried out in an experimental electrohydraulic lithotripter modeled after the Dornier HM3 and modified for the dual-reflector system. A primary method for quantifying the physical effects of the dual reflector lithotripter (DRL) cavitation field involves placing thin sheets of aluminum foil at the focus of the lithotripter and measuring pit depth resulting from cavitation collapse against the foil. Working with Glen Dunham at the EMSL, peak-to-valley (PV) distances were measured in 2.1 mm x 2.8 mm square regions of the foils using a Zygo New View 2000 non-contact profilometer (Zygo Corporation, Middlefield, CT). Measurements were made on foils exposed to both a conventional single reflector lithotripter and the DRL, at the focus, and 2 cm from the focus. Figure 8.14 demonstrates surface profiles for typical pits at each of these locations.

It was found that PV at the focus of the DRL was 1.4 times greater than at the focus of the conventional lithotripter and four times greater than at a region 2 cm from the focus of the dual reflector lithotripter. Subsequent *in vitro* experiments with model stones at the focus and blood 2 cm from the focus demonstrate enhanced stone fragmentation and decreased red blood cell lysis with the DRL (Sokolov et al. 2000). Understanding the shock-wave-bubble interactions and mechanisms for stone
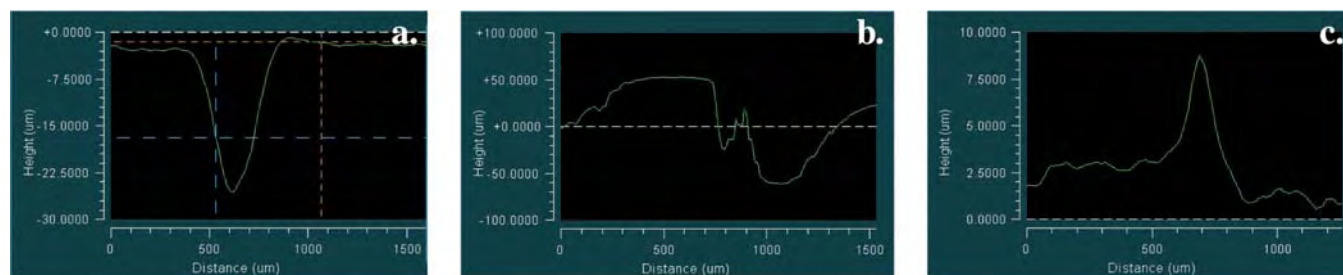
Figure 8.14. Surface profiles for typical pits in foil exposed to (a) conventional lithotripter, at focus, (b) dual-reflector lithotripter, at focus, and (c) dual-reflector lithotripter, 2 cm from the focus. The y-axes indicate respective scales for peak-to-valley distances.

versus tissue damage in the dual-reflector system may lead to the development of a safer and more effective lithotripter.

References

Connors, B. A., A. P. Evan, L. R. Willis, P. M. Blomgren, J. E. Lingeman, and N. S. Fineberg, "The effect of discharge voltage on renal injury and impairment caused by lithotripsy in the pig", *J. Am. Soc. Nephrol*. **11**, pp. 310-318, (2000).

Crum, L. A., "Cavitation microjets as a contributory mechanism for renal calculi disintegration in ESWL", *J. Urol*., **140**, 1587-1590 (December 1988).

Sokolov, D. L., M. R. Bailey, and L .A. Crum, "Use of two pulses to localize and intensify cavitation in lithotripsy", In *Collected Papers of the Joint ASA/EAA/DEGA Meeting*, Berlin, Germany (March 14-19, 1999).

Sokolov, D. L., M. R. Bailey, F. Pulvermakher, and L. A. Crum, "Increased damage to stones without increased damage to cells with a dual-reflector lithotripter", In *Proceedings of the 2000 IEEE International Ultrasonics Symposium*, San Juan, Puerto Rico (October 22-25, 2000).

Coal Surface Charging Property Characterization

S. Trigwell[(a,b)], D. Kumar[(a,b)], and M. K. Mazumder[(a,b)]

(a) Applied Science Department, University of Arkansas at Little Rock.
(b) EMSL User.

Our goal is to advance the fundamental understanding of tribocharging of coal and mineral particles and apply it to dry coal beneficiation and mineral separation. The polarity and amount of charging of coal particles and mineral inclusions is dependent upon the surface work function difference between the particles and the charging medium. At present, high levels of bipolar charging are observed in the coal and mineral particles, which limits the efficiency of the separation technique.

The work function of a surface itself is dependent upon the surface composition, humidity, and contamination. The surface composition of various coal specimens were determined by XPS and AES using the Quantum 2000 ESCA spectrometer and the PHI 680 Field Emission Auger spectrometer. The data showed the surface of the coals to be oxidized to various degrees depending upon the coal maceral content on the surface. The specimens were then sent to Japan where the work functions of the various coal specimens were determined by UPS in air using a Riken Keiki AC2 surface analyzer. The work functions of all the specimens were determined to be much higher (~5.4 eV) than observed for clean coal in vacuum (~3.85 eV). The higher work function on the coal surfaces was probably due to the oxidation of the surface. Various materials (including metals, polymers, and raw compounds found in coal) were then analyzed by XPS and UPS to determine the correlation between surface composition and work function. The data showed that for the metals that were heavily oxidized, the work functions were correspondingly higher than those for clean surfaces measured in vacuum as reported in the literature. For the insulating materials that were

only slightly oxidized after exposure to air, the work functions were close to that reported in vacuum. The work function for oxidized copper in air was measured at 5.11 eV, and that for pure pyrite in air was 5.50 eV. Copper is the material used in the tribocharging of coal powder for beneficiation. It can be observed that the work function for copper in air (5.11 eV) is very close now and lower to that of both coal (~5.4 eV) and pyrite in air (5.50 eV). Within the experimental errors of the measurements for the work function (+/- 0.2 eV), the work functions can be considered similar.

The results indicate that for unipolar charging by triboelectrification, the respective work functions need to be as far apart as possible in the triboelectric series, and that the choice of materials used for the charger depends upon the surface work function corresponding to the environment in which the charging is performed. The implication of the work is that selected materials may then be used as the tribocharging material in on-going trial runs to improve the charging efficiency.

Cross-sectioned specimens of three coal nuggets from different mines (Pittsburgh #8, Illinois #6, and Kentucky #9) were analyzed by electrostatic force microscopy (EFM) to determine the charge distribution on the surface. Differences in the surface topography and charge distribution were observed for all the specimens. However, attempts to identify actual charge distribution by adding positive and negative ion charges by a static charge gun were not conclusive due to blurring of the image. The images started clearing after time, suggesting the effect of the induced charge had diminished. After a period of time, the image returned to its original form. These results warrant further investigation.

Reference

Trigwell, S. M., K. Mazumder, and R. Pellisier, "Tribocharging in Electrostatic Beneficiation of Coal: Effects of Surface Composition on Work Function as Measured by XPS and UPS in Air", Accepted for publication*, Journal of Vacuum Science and Technology*, Nov. 2000.

9. Appendix

Interfacial Chemistry and Engineering

Associate Director, EMSL

J. W. Rogers, Jr.
(509) 375-6452
jw.rogers@pnl.gov

> B.S. University of Texas at Austin 1975; Ph.D. University of Texas at Austin 1979; Research Scientist, Sandia National Laboratories, 1979-1990; Professor, University of Washington 1991-1999; Associate Director, IC&E, PNNL 1999-2000; Associate Lab Director, PNNL, November 2000. Research interests: chemical and surface engineering of materials including chemical vapor deposition of refractory thin films and nanoepitaxy of biomolecules for biomaterials applications.

Interim Associate Director, EMSL

Jay W. Grate
(509) 376-1833
jwgrate@pnl.gov

> B.A. Rollins College 1978; M.S. University of California, San Diego 1980; Ph.D. University of California, San Diego 1983; Postdoctoral Fellow, University of California, Irvine 1983-1984; Scientist, Geo-Centers, Inc. 1984; Research Chemist, Naval Research Laboratory 1984-1992; joined PNNL in October 1992. Research interests: inorganic, organic, and organometallic chemistry; polymers; and surface science.

User Coordinator

Donald R. Baer
(509) 376-1609
don.baer@pnl.gov

> B.S. Carnegie Mellon University 1969; Ph.D. Cornell University 1974; Postdoctoral Fellow, University of Illinois 1974-1976; joined PNNL in 1976. Research interests: solid-solution interfaces; oxide and mineral surfaces; corrosion and stress corrosion; material-environment interactions; surface and interface analysis methods; and scanning probe methods.

Staff

Michael L. Alexander
(509) 376-1576
michael.alexander@pnl.gov

> B.S. University of California, Berkeley 1979; Ph.D. University of Colorado, Boulder 1987; Postdoctoral Fellow 1987-1990; staff scientist, Los Alamos National Laboratory 1990-1993; joined PNNL in June 1993. Research interests: fundamental processes involved in laser ablation of samples for chemical analysis; laser spectroscopy, and laser desorption in an ion trap mass spectrometer.

Mari Lou Balmer

> B.S. The Pennsylvania State University 1987; Ph.D. University of California, Santa Barbara 1993; Ceramic Research Engineer, National Institute of Standards and Technology 1987-1989; Consultant, Statham Division of Mark IV Transducer Corporation 1992-3; Research Scientist, PNNL October 1993-January 2001; now with Caterpiller, Inc. Research interests: metastable and stable phase selection in oxide systems, plasma catalyst development and characterization, and structure-property relationships in titanosilicates.

Cynthia J. Bruckner-Lea
(509) 376-2175
cindy.bruckner-lea@pnl.gov

> B.S. University of California, Davis 1985; Ph.D. University of Utah 1990; Postdoctoral Fellow, University of Utah 1990-1992; joined PNNL in 1992. Research interests: formation and characterization of ultrathin organic films; molecular recognition using organic films; chemical sensor development and flow injection analysis for environmental and biomedical applications.

Chunshe "James" Cao
(509) 376-0293
chunshe.cao@pnl.gov

>B.S. 1990 and M.S. 1993, Tsinghua University, Beijing; Ph.D. City University of New York, 1998; research assistant, The City University of New York 1994-1998; research scientist, ExxonMobile Research and Engineering Company 1998-2000; joined PNNL in August 2000. Research interests: heterogeneous catalysis, chemical process modeling, microchannel reactor system and its applications in industrial chemical processing, transportation, military, environmental restoration, space exploration and carbon management.

Scott A. Chambers
(509) 376-1766
sa.chambers@pnl.gov

>A.B. University of California, San Diego 1973; Ph.D. Oregon State University 1977; Assistant Professor George Fox College 1977-1982; Assistant and Associate Professor of Chemistry, Bethel College 1982-1986; Research Scientist, Boeing High Technology Center 1987-1992; Affiliate Professor, University of Washington 1992-present; joined PNNL in 1992. Research interests: MBE growth, characterization, surface structure determination, and reactivity with small molecules of oxide surfaces; and auger and photoelectron diffraction investigations of oxide surface structures.

Ya-Huei "Cathy" Chin
(509) 376-0134
ya-huei.chin@pnl.gov

>B.S. and M.S. The University of Oklahoma; joined PNNL in 2000. Research interests: heterogeneous catalysis, chemical process modeling, microchannel reactor system and its applications in industrial chemical processing, transportation, military, environmental restoration, space exploration and carbon management.

Robert Dagle
(509) 376-5354
robert.dagle@pnl.gov

>B.S., Washington State University 1999; M.S. Washington State University–Tri-Cities, expected 2002. Research interests: heterogeneous catalysis, with emphasis in steam reforming and catalytic combustion.

John L. Daschbach
(509) 376-2467
john.daschbach@pnl.gov

>B.S. Lewis & Clark College; Ph.D. University of Utah 1989; Postdoctoral Fellow, University of Utah 1990-1; Research Associate, University of Oregon 1991-1993; joined PNNL in January 1994. Research interests: nonlinear spectroscopy of interfaces and carrier dynamics in semiconductors.

Glen C. Dunham
(509) 376-4397
gdunham@pnl.gov

>B.A./B.S. Pacific Lutheran University 1980; M.S. Washington State University 1983; Research Engineer, University of Washington 1983-1989; Research Scientist, Washington State University 1989-1992; joined PNNL 1992. Research interests: electro-optics; solid-state devices for chemical sensing; metalorganic chemical vapor deposition; molecular beam epitaxy; and applications of porous silicon.

Oleg B. Egorov
(509) 376-3485
oleg.egorov@pnl.gov

>M.S. Moscow State University 1992; M.S. University of Washington 1993; Ph.D. University of Washington 1998; Graduate Student Fellowship, PNNL 1994-1998; joined PNNL staff in 1998. Research interests: automated radiochemical methods applied to nuclear waste; radiochemical sensors with application to surface, ground and process waters; and automated medical isotope generation.

Scott H. Elder
B.S. Northwest Missouri State University 1988;
Ph.D. Cornell University 1993; Graduate Student
Fellowship Cornell University 1989-1992;
Postdoctoral Fellow, University of California,
Berkeley 1994-1996; joined PNNL July 1996;
now with Intel Corporation. Research interests:
discovery of new synthetic methodologies for the
preparation of novel materials; materials charac-
terization to understand the relationship between
the crystallographic/surface structure of materials
and the physical/chemical properties they exhibit;
synthesis of nanocrystalline metal oxides with
new electronic, magnetic and photophysical
properties; and the design and preparation of
macrostructured systems with well-defined and
tailorable mesoporosity for electronic device
applications.

Mark H. Engelhard
(509) 376-1664
mark.engelhard@pnl.gov
A.A. Columbia Basin College 1978; joined PNNL
in 1978. Research interests: surface analysis
techniques, including XPS, UPS, AES, TOF-
SIMS, RBS, NRA, PIXE, and EDX.

Gregory J. Exarhos
(509) 375-2440
greg.exarhos@pnl.gov
A.B. Lawrence University 1970; Ph.D. Brown
University 1974; Assistant Professor, Harvard
University 1974-1980; joined PNNL in 1980.
Adjunct Professor (Physics) Washington State
University, Pullman, Washington 1993-present.
Research interests: deposition and post deposition
modification of oxide films; fundamental mea-
surements of the linear and nonlinear optical
response of structured dielectrics; optical charac-
terization of materials by means of laser Raman
spectroscopy and ellipsometry; and molecular
design and synthesis of polymers and advanced
polymer composites.

Sean P. Fitzgerald
B.S. University of Minnesota 1993; Ph.D.
University of Notre Dame 1998; joined PNNL
in 1998; now with Battelle Memorial Institute,
Columbus. Research interests: reaction engineer-
ing, heat exchanger design, and heat and mass
transfer.

Yufei Gao
B.S. University of Science and Technology,
Beijing, China 1982; M.S. Ohio State University
1985; Ph.D. Ohio State University 1989;
Postdoctoral Fellow 1989-1992 and Assistant
Scientist, Argonne National Laboratory 1992;
Assistant Professor, New Mexico Tech
1992-1994; joined PNNL December 1994; now
with Lucent Technologies. Research interests:
metalorganic chemical vapor deposition;
molecular beam epitaxy; ceramic thin films and
surfaces; interface science; transmission and high-
resolution electron microscopy; metal-ceramic
adhesion; ferroelectric thin films; and composites.

Todd R. Hart
(509) 376-4966
todd.hart@pnl.gov
Senior Technician, Pinnell Inc. 1981-1989;
Branch Service Manager, Pinnell Inc. T/C
1989-1991; joined PNNL 1991. Research focus:
electronic, analytical, and process chemistry
equipment, including design and construction of
bench and pilot scale systems.

Michael A. Henderson
(509) 376-2192
ma.henderson@pnl.gov
B.S. Auburn University 1981; M.S. Auburn
University 1984; Ph.D. University of Texas 1988;
Postdoctoral Fellow, University of Pittsburgh
1988-1989; Research Assistant Professor,
University of Pittsburgh 1989-1991; joined PNNL
1991. Research interests: chemical structure,
dynamics, and reactivity of adsorbed species on
single crystal substrates under ultra-high vacuum
conditions with emphasis on the chemistry of
small probe molecules on metal and metal oxide
surfaces.

Gregory S. Herman
B.S. University of Wisconsin-Parkside 1985;
Ph.D. University of Hawaii 1992; Postdoctoral
Fellow, Naval Research Laboratory 1992;
Postdoctoral Fellow, PNNL 1992-1995; joined
PNNL in May 1996; now with Hewlett-Packard
Inc. Research interests: growth of ultra-thin oxide
films and environmentally relevant catalysis with
metal and oxide surfaces.

Jianli "John" Hu
(509) 376-0427
jianli.hu@pnl.gov
> B.S. Tsinghua University, China 1986; Ph.D. Tsinghua University, China 1991; M.B.A. Washington State University expected 2001. Research interests: microtechnology development and microreactor design and catalysis.

Timothy L. Hubler
(509) 373-0249
tim.hubler@pnl.gov
> B.S. Albertson College of Idaho 1984; M.S. University of Idaho 1988; Ph.D. University of Idaho 1992; Postdoctoral Fellow, PNNL 1992; joined PNNL staff in October 1994. Research interests: synthesis of materials with catalytic applications and ion-exchange technology.

Keith D. Keefer
> B.A. Charleton College 1974; Ph.D. Stanford University 1981; Technical Staff, Sandia National Laboratories 1980-1990; Associate Professor, University of Cincinnati 1990-1994; Research Scientist PNNL 1994 to 2001. Research interests: long- and short-range atomic structures and synthesis of crystalline and amorphous materials, particularly oxides and silicates.

Micheal Lamont
> B.S. South Dakota School of Mines and Technology 1997; student PNNL 1997; joined PNNL 1999; now with Battelle Memorial Institute, Columbus. Research interests: microtechnology and environmental protection.

Evan O. Jones
(509) 376-4610
evan.jones@pnl.gov
> B.S. Washington State University 1980; M.S. Washington State University 1986; UOP 198-1987; joined PNNL in 1987. Research interests: technical project management, process design and modeling, equipment design and testing, and chemical process development.

A. Scott Lea
(509) 376-9145
scott.lea@pnl.gov
> B.S. Lehigh University 1981; M. Engr. Rensselaer Polytechnic Institute 1983; Ph.D. University of Utah 1993; Postdoctoral Fellow, PNNL 1993-1996; joined PNNL as staff in 1996. Research interests: geochemical reactions at the mineral water interface, particularly in the presence of heavy metals; investigating the forces between particles in aqueous solutions as a function of solution composition, relating these to the colloidal and rheological behavior of particle suspensions; surface characterization using AFM, STM, and AES.

Yong Liang
(509) 376-8565
yong.liang@pnl.gov
> B.S. Fudan University, China 1982; M.S. Academy of Science, China 1985; Ph.D. University of Notre Dame 1991; Postdoctoral Fellow, University of Pennsylvania 1991-1993; Postdoctoral Fellow, PNNL 1993-1996; joined PNNL as staff in 1996. Research interests: scanning probe methods; electronic materials; oxide films and interfaces; ferroelectric materials; and nanotechnology.

Yuehe Lin
(509) 376-0529
yuehe.lin@pnl.gov
> B.S. Peking University, China 1984; Ph.D. Xiamen University, China 1991; Ph.D. University of Idaho 1997; Postdoctoral Fellow, New Mexico State University 1991-1992; Research Scientist, University of Idaho 1992-1995; Postdoctoral Fellow, PNNL 1997-1998; joined PNNL as staff in 1998. Research interests: development of miniaturized analytical systems for environmental and biomedical monitoring based on micro-fluidics/lab-on-a-chip concept; development of advanced materials and supercritical fluid processing technology for separation and hazardous waste removal.

Jun Liu

    B.S. Hunan University, China 1982; M.S. 1986 and Ph.D. University of Washington 1990; Assistant Professor, University of Washington, 1990-1992; joined PNNL in 1992; now with Lucent Technologies. Research interests: development of novel mesoporous materials, hybrid materials, nanocomposites for environmental, energy, catalytic, and agricultural applications.

Jennifer Marco

    B.S. Washington State University 1996; joined PNNL in 1996; now with Battelle Memorial Institute, Columbus, Ohio. Research interests: reactor design and catalysis, and process control.

David E. McCready
(509) 376-9648
david.mccready@pnl.gov

    B.S. Colorado State University 1985; Optical Coating Engineer, Kirtland Air Force Base 1985-1988; Engineering Technician, Sandia National Laboratory 1988-1989; joined PNNL in 1989. Research interests: structures of solid-state materials, using x-ray diffraction techniques.

David A. Nelson
(509) 376-9587
dave.nelson@pnl.gov

    B.S. Montana State College 1963; Ph.D. Montana State University 1966. Research interests: polymer chemistry and organometallic chemistry.

Daniel Palo
(509) 376-4181
daniel.palo@pnl.gov

    B.S. University of Minnesota 1994; Ph.D. University of Connecticut 1999; joined PNNL in 1999. Research interests: microtechnology/process intensification, reactor design and development, heterogeneous catalysis, homogeneous catalysis, and applications of supercritical fluids.

Charles H.F. Peden
(509) 376-1689
chuck.peden@pnl.gov

    B.A. California State University, Chico 1978; M.A. 1981 and Ph.D. University of California, Santa Barbara 1983; Postdoctoral Fellow, Sandia National Laboratories 1983-1985; Technical Staff, Sandia National Laboratories 1985-1992; joined PNNL in 1992. Research interests: surface and interfacial chemistry of inorganic solids, and heterogeneous catalysis of metals and oxides (reaction mechanisms and materials).

Steven Perry

    B.S. Brigham Young University 1994; M.S. Michigan Technological University 1997; Ph.D. Brigham Young University 1999; joined PNNL in 1999; now with Battelle Memorial Institute, Columbus, Ohio. Research interests: chemical kinetics and reactor design, coal devolatilization chemistry (fuel NOx formation), combustion engineering, and particulates processing/physical separations.

Gary L. Roberts

    A.A. Columbia Basin College 1971; joined PNNL in 1965; now with Battelle Memorial Institute. Research interests: microtechnology, particularly involving design and systems installation.

Robert T. Rozmiarek
(509) 376-9664
robert.rozmiarek@pnl.gov

    B.S. Iowa State University 1999, M.S. Washington State University expected 2003. Research interests: laboratory catalysis research work; coordinate catalyst screening and laboratory activities; MTI GC configuration; reactor design and modification; complete system design and instillation (reactor, peripherals, process control); reactor and catalysis data analysis and troubleshooting.

Ming Kun Shi
B.Sc. Dalian University of Science and Technology, China 1986; Ph.D. University Louis Pasteur, France 1991; Postdoctoral Fellow 1992-1993 and Research Associate, Ecole Polytechnique of Montreal, Canada 1993-1997; Project Engineer, New Interconnection & Packaging Technologies, Inc. 1998; Research Scientist PNNL 1998 to 2000. Research interests: surface modification, thin film deposition, surface/interface characterization, and measurement of optical, electrical and adhesive properties.

Vaithiyalingam Shutthanandan
(509) 376-1928
shuttha@pnl.gov
B.Sc. University of Jaffna, Sri-Lanka 1985; M.S. Montana State University 1990; Ph.D. Montana State University 1994; Assistant Professor, Tuskegee University 1994-1998; Staff Analyst, Charles Evans and Associates 1998-1999; joined PNNL in July 1999. Research interests: surface science, material science, thin films, ion beam technique, photoelectron spectroscopy, Monte Carlo simulation of interfaces, sputtering erosions, low-energy sputtering, and ion mass spectroscopy.

Johanes H. Sukamto
B. S. University of California, Berkeley 1988; Ph.D. University of Minnesota 1993; Postdoctoral Fellow, University of Tokyo, Japan 1993-1994; Postdoctoral Fellow, PNNL 1994-1995; joined PNNL as staff in 1995; now with Novella Systems Inc. Research interests: electrochemistry, separations, and electroactive polymers.

Yali Su
(509) 376-5920
ya.su@pnl.gov
B.S. Peking University, China 1984; M.S. Peking University, China 1987; Ph.D. University of Notre Dame 1994; Postdoctoral Fellow, PNNL 1994-1997; joined PNNL as staff in 1997. Research interests: photocatalysis, silicotitanate waste forms, and nano materials.

Suntharampillai Thevuthasan
(509) 376-1375
theva@pnl.gov
B.Sc. University of Peradeniya, Sri-Lanka 1981; M.Sc. Asian Institute of Technology, Thailand 1984; Ph.D. University of Maine 1989; Postdoctoral Fellow, University of Hawaii 1990-1991; Guest Scientist, Lawrence Berkeley Laboratory 1991-1993; Postgraduate Research, University of Davis 1991-1993; joined PNNL in 1993. Research interests: electron emission holography, x-ray fluorescence holography, and various energetic ion spectroscopies.

Anna Lee Y. Tonkovich
B.S. University of Rochester 1987; Ph.D. University of Minnesota 1992; joined PNNL in 1992; now with Battelle Memorial Institute. Research interests: reaction engineering and catalysis, microtechnology, and process intensification.

David VanderWiel
B.S. Iowa State University 1993; Ph.D. Iowa State University 1998; joined PNNL in 1998; now with Battelle Memorial Institute, Columbus, Ohio. Research interests: heterogeneous catalysis, surface reaction kinetics, and environmental engineering.

Yong Wang
(509) 376-5117
yongwang@pnl.gov
B.S./M.S. Chengdu University of Science & Technology, China; M.S. Washington State University 1992; Ph.D. Washington State University 1993; Postdoctoral Fellow, Washington State University 1994; Postdoctoral Fellow, PNNL 1994-1996; joined PNNL staff in 1996. Research interests: catalyst design and testing, reaction kinetics studies, chemical process development, material structure characterization, and process simulation.

James S. Young
(509) 376-2046
jim.young@pnl.gov
> B.S. Humbolt State College 1966; M.S. Humbolt State College 1969; Fishery Biologist, National Marine Fishery Service 1970-1975; joined PNNL in 1975. Research interests: heavy metals bioavailability, toxicology, marine radioecology, ground water chemistry, scanning electron microscopy, and transmission electron microscopy.

Office Support

Susan Finch (sue.finch@pnl.gov)
Terry Law (terry.law@pnl.gov)
Wendy Owen (gwen.owen@pnl.gov)
Courtenay Turner (courtenay.turner@pnl.gov)

Postdoctoral Fellows

Saemin Choi
(509) 376-6275
saemin.choi@pnl.gov
> B.S. Yonsei University 1989; M.S. Yonsei University 1991; Ph.D. University of Michigan 1998; Postdoctoral Fellow, IC&E with Chuck Peden and Yong Wang 1998-August 2000.

Timothy C. Droubay
(509) 376-7065
tim.droubay@pnl.gov
> B.S. University of Puget Sound 1991; M.S. University of Wisconsin-Milwaukee 1993; Ph.D. University of Wisconsin-Milwaukee 1999; Teaching Assistant and Lecturer, University of Wisconsin-Milwaukee 1991-1993, 1999; Physics Instructor, Waukesha County Technical College 1998-2000; Research Associate, University of Wisconsin-Milwaukee 1993-1998; Postdoctoral Fellow, IC&E with Scott Chambers 2000 to present.

Shupan Gan
(509) 376-8467
shupan.gan@pnl.gov
> B.S. University of Science & Technology, China 1994; Ph.D. University of California, Los Angeles 1998; Research Scientist, University of California, Los Angeles 1998-1999; Postdoctoral Fellow IC&E with Yong Liang May 1999-January 2001.

Fei Gao
(509) 376-6275
fei.gao@pnl.gov
> B.Sc. Lanzhou University, China 1982; M.Sc. Lanzhou University, China 1986; Ph.D. The University of Liverpool, United Kingdom 1994; Research Assistant, The University of Liverpool 1991-1994; Research Associate, The University of Liverpool 1994-1997; Senior Research Fellow, The University of Liverpool 1997-2000; Postdoctoral Fellow, IC&E with William J. Weber 2000 to present.

David Holman
(509) 376-3647
david.holman@pnl.gov
> B.S. University of Wisconsin-Eau Claire 1988; Ph.D. University of Wisconsin-Milwaukee 1994; Postdoctoral Fellow, University of Washington 1994-1997; Postdoctoral Fellow, IC&E with Cindy Bruckner-Lea 1997-March 2001.

Jungbae Kim
(509) 376-4621
jungbae.kim@pnl.gov
> B.S. Seoul National University, South Korea 1986; M.S. Seoul National University, South Korea 1988; Ph.D. University of Iowa 1995; Research Assistant, University of Iowa 1990-1995; Postdoctoral Research Associate, University of Iowa 1995-1998; Research Scientist, Rensselaer Polytechnic Institute 1998-2000; Postdoctoral Fellow, IC&E with Cindy Bruckner-Lea 2000 to present.

Liyu Li
(509) 376-0095
liyu.li@pnl.gov
> B.S Peking University, China 1989; M.Eng. China Institute for Radiation Protection 1992; Ph.D. China Institute of Atomic Energy 1995; Assistant Research Professor, Tsinghua University 1995-1998; Postdoctoral Fellow, PNNL 1998-2000; Postdoctoral Fellow, IC&E with M. Lou Balmer and Yali Su July 2000 to present.

Lydia G. Olson
> B.S. Texas Lutheran University 1992; Ph.D. University of Utah 1998; Postdoctoral Fellow, IC&E with Cindy Bruckner-Lea January to November 1999.

Alexander G. Panov
(509) 376-5941
alexander.panov@pnl.gov
> B.S. Moscow State University 1993; Ph.D. University of Wisconsin-Milwaukee 1998; Postdoctoral Fellow, University of Iowa 1998-1999; Postdoctoral Fellow, IC&E with M. Lou Balmer November 1999-present.

Craig L. Perkins
(509) 376-7107
craig.perkins@pnl.gov
> B.S. University of Florida 1990; Ph.D. University of Illinois at Chicago 1998; Postdoctoral Fellow, IC&E with Michael Henderson 1998-July 2000.

Michael R. Sievers
(509) 376-7043
michael.sievers@pnl.gov
> B.S. Boise State University 1990; Ph.D. University of Utah 1998; Research Assistant, University of Utah 1993-1998; Postdoctoral Fellow, IC&E with Greg S. Herman January 1999-January 2000.

Douglas G. Weir
(509) 376-7214
douglas.weir@pnl.gov
> B.S. University of Alberta, Canada 1986; Ph.D. University of British Columbia 1995; Contract Researcher, Westaim Technologies Inc. 1994-1996; Research Professional, The Westaim Corporation 1996-1998; Postdoctoral Fellow, PNNL 1998-1999; Postdoctoral Fellow, IC&E with Michael Alexander April 1999-April 2000.

Graduate Students

Gregory Anderson
> Worked with T. Hubler, 1998-May 2000.

Eric Bitten
> Worked with M. Lou Balmer, 1999-May 2000.

Tiffany Coulter
> Working with J. W. Rogers, Jr. and Don Baer, July 2000 to present.

Brian Dockendorff
> Worked with Cindy Bruckner-Lea, July 2000 to March 2001.

Ana C. Ebeling
> Working with M. Lou Balmer and Chuck Peden, June 1998-present.

Song He
> Worked with Yufei Gao, 1998-December 1999.

Mohammad Islam
> New Mexico Tech, worked with Yufei Gao, summer 2000.

Pornthep "Joe" Meethunkij
> Yale University, worked with Yong Liang, summer 2000.

Allan Tuan
> Working with J. W. Rogers, Jr. and Don Baer, July 2000 to present.

I. Steven Yoon
> Worked with M. Lou Balmer, 1998-October 2000.

Undergraduate Students

Stephanie Alexander
> Washington State University, worked with Glen Dunham, summer 2000.

Dan Allred
> University of Washington, worked with Bob Rozmiarek, summer 2000.

Ryan Boger
> University of Notre Dame, worked with Dave VanderWiel, summer 2000.

Laura Brown
> Washington State University, worked with Cindy Bruckner-Lea, summer 2000.

J. "Tom" Cleaves
> Washington State University, worked with Tim Hubler, summer 2000.

Chad Cooper
> Yakima Valley Community College, worked with S. Thevuthasan, summer 2000.

Jackson Davis
> University of Washington, worked with Mike Alexander, summer 2000.

Jon Gunther
Harvey Mudd College, worked with Chuck Peden, summer 2000.

Krista Hammack
Columbia Basin College, worked with Tim Hubler and Sam Bryan, summer 2000.

Amanda Hedges
Eastern Oregon University, worked with Mike Alexander, December 1999 and summer 2000.

Tom Hurt
Cornell University, worked with Don Baer, summer 2000.

Monesh Kapadia
Tulane University, worked with Sean Fitzgerald, summer 2000.

Beatrice Koempel-Thomas
Yakima Community College, worked with S. Thevuthasan, summer 2000.

Marino Morra
Worked with Mike Alexander, summer 2000.

Jana Mounts
Columbia Basin College, worked with Tim Hubler, summer 2000.

Ismael Nieves
Universitad de Puerto Rico, Mayaguez, worked with Cindy Bruckner-Lea, January – May 2000.

Yisel Rivera
Universitad de Puerto Rico, Mayaguez, worked with Glen Dunham, January – May 2000.

Michelle Rodriguez
Universitad de Puerto Rico, Mayaguez, worked with Glen Dunham, January – May 2000.

Charles Shawley
Whitworth College, worked with Glen Dunham, Summer 2000.

Adam Still
Columbia Basin College, worked with Tim Hubler, summer 2000.

High School Students

Evan Adams
Richland High School, working with Don Baer and Theva Thevuthasan, 1999-August 2000.

Kyle Littlefield
Hanford High School, worked with Glen Dunham, summer 2000 to present.

Matt Noyes
Hanford High School, worked with Glen Dunham, summer 2000 to present.

Pallavi Shukla
Hanford High School, worked with Glen Dunham, summer 2000 to present.

Ashley Stroud
Pasco High School, working with S. Thevuthasan, August 2000 to present.

Visiting Faculty

Eric I. Altman
Yale University, hosted by Scott Chambers and Yong Liang, June to August 2000.

Jaroslav Koca
Masaryk University, Czech Republic, hosted by Cindy Bruckner-Lea, March to May 2000.

Kwan-Young Lee
University of South Korea, hosted by Chuck Peden and Yong Wang, July 2000 to present.

Brian Palmer
Hanford High School, hosted by Glen Dunham, summer 1999 to present.

Where IC&E Fits in PNNL

Pacific Northwest National Laboratory (L. J. Powell, *Director*)

    Energy Science and Technology Division (D. P. McConnell, *Associate Laboratory Director*)

    Fundamental Sciences Division (J. W. Rogers Jr., *Associate Laboratory Director*)

        Atmospheric Sciences and Global Change Resources (W. T. Pennell)

        Biogeochemistry Resources (H. J. Bolton Jr.)

        Molecular Biosciences Resources (J. G. Pounds)

        Statistics Resources (B. A. Pulsipher)

        W. R. Wiley Environmental Molecular Sciences Laboratory (EMSL) (J. H. Futrell, *Director*)

            Chemical Structure and Dynamics (CS&D) (S. D. Colson)

            Interfacial Chemistry & Engineering (IC&E) (J. W. Grate, *interim*)

            Macromolecular Structure and Dynamics (MS&D) (D. W. Koppenaal)

            Theory, Modeling, and Simulation (TM&S) (D. A. Dixon)

            Environmental Dynamics and Simulation (ED&S) (J. M. Zachara)

            Computing and Information Sciences (C&IS) (M. J. Peterson, *acting*)

    Environmental Technology Division (W. J. Apley, *Associate Laboratory Director*)

    National Security Division (M. Kluse, *Associate Laboratory Director*)